



On Multiphysics Modeling and Control of Marine Current Turbine Systems

Seifeddine Benelghali

► To cite this version:

Seifeddine Benelghali. On Multiphysics Modeling and Control of Marine Current Turbine Systems. Engineering Sciences [physics]. Université de Bretagne occidentale - Brest, 2009. English. NNT: . tel-00521615

HAL Id: tel-00521615

<https://theses.hal.science/tel-00521615>

Submitted on 28 Sep 2010

HAL is a multi-disciplinary open access archive for the deposit and dissemination of scientific research documents, whether they are published or not. The documents may come from teaching and research institutions in France or abroad, or from public or private research centers.

L'archive ouverte pluridisciplinaire **HAL**, est destinée au dépôt et à la diffusion de documents scientifiques de niveau recherche, publiés ou non, émanant des établissements d'enseignement et de recherche français ou étrangers, des laboratoires publics ou privés.



université de bretagne
occidentale



THÈSE / UNIVERSITÉ DE BRETAGNE OCCIDENTALE
sous le sceau de l'Université européenne de Bretagne
pour obtenir le titre de
DOCTEUR DE L'UNIVERSITÉ DE BRETAGNE OCCIDENTALE
Mention : Science pour l'Ingénieur
École Doctorale SICMA

présentée par

Seifeddine BENELGHALI

Préparée au sein de l'EA 4325 LBMS
en collaboration avec l'Ecole Navale

On multiphysics modeling and control of marine current turbine systems

Thèse soutenue le 8 décembre 2009
devant le jury composé de :

Jacques André ASTOLFI

Maître de Conférences HDR, Ecole Navale / *examinateur*

Seddik BACHA

Professeur, Université Joseph Fourier, Grenoble / *président et rapporteur*

Mohamed BENBOUZID

Professeur, Université de Bretagne Occidentale / *directeur de thèse*

Jean Frédéric CHARPENTIER

Maître de Conférences, Ecole Navale / *co-encadrant*

Emmanuel DELALEAU

Professeur, ENIB / *examinateur*

David INFIELD

Professeur, University of Strathclyde, Glasgow / *examinateur*

Mohamed MACHMOUM

Professeur, PolytechNantes, Saint-Nazaire / *rapporteur*

Bernard MULTON

Professeur, ENS Cachan Site de Bretagne, Bruz / *examinateur*

Jean-Jacques HEROU

Docteur Ingénieur, EDF CIH, Le Bourget-du-Lac / *invité*

Acknowledgments

This work has been carried out at the Laboratoire Bretois de Mécanique et des Systèmes (EA 4325 LBMS) at the University of Brest in collaboration with the French Naval Academy (EA 3436 IRENav). The financial support provided by Brest Métropole Océane (BMO) and the European Social Fund is gratefully acknowledged.

I wish to express my gratitude to my main supervisor **Prof. Mohamed BENBOUZID** for help, inspiration, encouragement and guidance throughout the work. I also wish to thank my supervisor **Dr. Jean Frédéric CHARPENTIER** for his valuable comments, discussions and suggestions related to this work.

I wish to thank the pre-examiners **Prof. Seddik BACHA** from the Polytechnic Institute of Grenoble and **Prof. Mohamed MACHMOUM** from Polytech'Nantes for their valuable comments and corrections. I am also grateful to my PhD thesis defense committee members: **Prof. David INFIELD** from the University of Strathclyde, Glasgow, **Prof. Bernard MULTON** from ENS Cachan in Brittany, **Prof. Emmanuel DELALEAU** from ENI Brest, **Dr. Jean-Jacques HEROU** from EDF CIH, and **Dr. Jacques André ASTOLFI** from the French Naval Academy, Brest.

Special thanks are due to **Mr. Khaled JELASSI** for his help and encouragement as well as for giving me the opportunity to discover the research world in French laboratories.

I also wish to thank all my friends; their support has been very important to me.

Special thanks are due to my parents-in-law, **Majda** and **Ismail**, as well as to my brothers-in-law, **Raef** and **Mounib**, for their encouragements.

I am deeply indebted to my parents, **Radhia** and **Mohamed**, as well as to my brothers **Fares** and **Montassar** for their untiring support throughout all the years.

Finally, thanks go to my wife, **Chadha**, who has had to live with me during this project.



List of Publications

Some of the results presented in this thesis have been published in the following publications.

INTERNATIONAL JOURNAL PAPERS

- [1] **S.E. Ben Elghali**, M.E.H. Benbouzid, T. Ahmed-Ali and J.F. Charpentier, “High-order sliding mode control of a marine current turbine driven doubly-fed induction generator,” *IEEE Journal of Oceanic Engineering*, To Appear in June 2010.
- [2] **S.E. Ben Elghali**, M.E.H. Benbouzid and J.F. Charpentier, “Modeling and control of a marine current turbine driven doubly-fed induction generator,” *IET Renewable Power Generation*, vol. 4, n°1, pp. 1-11, January 2010.
- [3] **S.E. Ben Elghali**, R. Balme, K. Le Saux, M.E.H. Benbouzid, J.F. Charpentier and F. Hauville, “A Simulation model for the evaluation of the electrical power potential harnessed by a marine current turbine”, *IEEE Journal of Oceanic Engineering*, vol. 32, n°4, pp. 786-797, October 2007.

NATIONAL JOURNAL PAPERS

- [1] **S.E. Ben Elghali**, M.E.H. Benbouzid et J.F. Charpentier, “Modélisation et commande d’une hydrolienne équipée d’une génératrice asynchrone double alimentation”, *European Journal of Electrical Engineering – EJEE*, April 2010.
- [2] **S.E. Ben Elghali**, L. Drouen, M.E.H. Benbouzid, J.F. Charpentier, J.A. Astolfi et F. Hauville, “Les systèmes de génération d’énergie électrique à partir des courants de marées”, *Revue 3EI*, n°52, pp. 73-85, Mars 2008.

INTERNATIONAL CONFERENCE PAPERS

- [1] **S.E. Ben Elghali**, M.E.H. Benbouzid, J.F. Charpentier, T. Ahmed-Ali and I. Munteanu, “High-order sliding mode control of a marine current turbine driven permanent magnet synchronous generator”, in *Proceedings of the IEEE IEMDC’09*, Miami, Florida (USA), pp. 1541-1546, May 2009.

- [2] **S.E. Ben Elghali**, M.E.H. Benbouzid, T. Ahmed-Ali and J.F. Charpentier, “High-order sliding mode control of DFIG-based marine current turbine”, *in Proceedings of the IEEE IECON’08*, Orlando, Florida (USA), pp. 1228-1233, November 2008.
- [3] **S.E. Ben Elghali**, M.E.H. Benbouzid, and J.F. Charpentier, “Modeling and control of a marine current turbine using a doubly-fed induction generator”, *in Proceedings of the ICOE’08*, Brest (France), October 2008.
- [4] **S.E. Ben Elghali**, M.E.H. Benbouzid, J.F. Charpentier, T. Ahmed-Ali, J.M. Gahéry and A. Denis, “Modeling and MPPT sensorless control of a DFIG-based marine current turbine”, *in Proceedings of the ICEM’08*, Vilamoura (Portugal), pp. 1-6, September 2008.
- [5] R. Balme, K. Le Saux, **S.E. Ben Elghali**, M.E.H. Benbouzid and J.F. Charpentier, “A simulation model for the evaluation of the electrical power potential harnessed by a marine current turbine in the Raz de Sein,” *in Proceedings of the IEEE OCEANS’07*, Aberdeen (Scotland), pp. 1-6, June 2007.
- [6] **S.E. Ben Elghali**, M.E.H. Benbouzid and J.F. Charpentier, “Marine tidal current electric power generation technology: State of the art and current status,” *in Proceedings of IEEE IEMDC’07*, Antalya (Turkey), vol. 2, pp. 1407-1412, May 2007.

NATIONAL CONFERENCE PAPERS

- [1] **S.E. Ben Elghali**, J. Bittard, C. Léon, J.F. Charpentier et M.E.H. Benbouzid, “Etude comparative d’une génératrice asynchrone à double alimentation et d’une génératrice synchrone à aimants permanents pour la génération d’énergie hydrolienne,” *Conférence Electrotechnique du Futur – EF’09*, Compiègne, Septembre 2009.
- [2] **S.E. Ben Elghali**, “Modélisation et commande d’une hydrolienne équipée d’une génératrice asynchrone double alimentation,” *Conférence des Jeunes Chercheurs en Génie Electrique – JCQE’08*, Lyon, Décembre 2008.
- [3] **S.E. Ben Elghali**, M.E.H. Benbouzid et J.F. Charpentier, “Modèle de simulation d'une hydrolienne implantée dans le site du Raz de Sein,” *Colloque Nationale de la Recherche dans les IUT – CNRIUT’07*, Thionville-Yutz (France), Mai 2007.
- [4] R. Balme, K. Le Saux, **S.E. Ben Elghali**, M.E.H. Benbouzid, J.F. Charpentier et F. Hauville, “Modélisation de la ressource et du capteur dans la chaîne de conversion d'énergie d'une hydrolienne,” *Journées de la Section Electrotechnique du Club EEA*, Rennes (France), Mars 2007.

*Earth is not a gift from our parents;
it is a loan from our children.*

CONTENTS

INTRODUCTION	1
CHAPTER I: State of the Art Survey of Marine Current Turbine: Concepts & Technologies.....	3
I.1 INTRODUCTION.....	4
I.2 TIDAL KINETIC ENERGY BACKGROUND.....	4
I.3 TIDAL RESSOURCE.....	7
I.4 KINETIC ENERGY EXTRACTION.....	9
I.5 TURBINE TECHNOLOGIES AND CONCEPTS	9
5.1 HORIZONTAL AXIS TURBINES	11
5.2 VERTICAL AXIS TURBINES	19
5.3 OSCILLATING HYDROFOIL	24
5.4 FLOATING TIDAL ENERGY SYSTEM	25
I.6 DEVELOPMENT OF TIDAL TECHNOLOGIES AND DESIGN OPTIONS	26
I.7 ELECTRIC GENERATOR TOPOLOGIES IN MARINE CURRENT TURBINES.....	27
7.1 FULL RANGE VARIABLE SPEED SYSTEM (WITH GEAR)	27
7.2 FULL RANGE VARIABLE SPEED SYSTEM (WITHOUT GEAR)	28
7.3 LIMITED VARIABLE SPEED SYSTEM	28
I.8 CONCLUSION.....	29
CHAPTER II: Marine Current Turbine Modeling	30
II.1 INTRODUCTION	33
II.2 MODELING REQUIREMENTS	33
II.3 HYDRODYNAMIC MODEL.....	34
3.1 RESOURCE MODELING	34
3.2 THE ROTOR MODELING	42

II.4 MECHANICAL MODEL.....	55
II.5 POWER CONVERTER	57
II.6 TRANSFORMER.....	57
II.7 GENERATOR MODEL.....	57
7.1 DOUBLY FED INDUCTION GENERATOR (DFIG)	57
7.2 PERMANENT MAGNET SYNCHRONOUS GENERATOR (PMSG).....	61
II.8 CONCLUSION.....	63
CHAPTER III: Control Strategies and Evaluation of the Tested Technologies.....	64
III.1 INTRODUCTION.....	67
III.2 PRINCIPALS OF MCT OPTIMAL CONTROL.....	67
2.1 CASE OF FIXED-SPEED VARIABLE-PITCH MCT	67
2.2 CASE OF VARIABLE-SPEED FIXED-PITCH MCT	67
III.3 PI CONTROL.....	71
3.1 CONTROLLER DESIGN	72
3.2 OPTIMAL CONTROL OF MCT DRIVEN DFIG BY PI SPEED CONTROL	74
3.3 OPTIMAL CONTROL OF MCT DRIVEN PMSG BY PI SPEED CONTROL	78
3.4 DISCUSSION.....	81
III.4 HIGH-ORDER SLIDING MODE CONTROL.....	81
4.1 CONTROLLER DESIGN	82
4.2 OPTIMAL CONTROL OF MCT DRIVEN DFIG BY HOSM SPEED CONTROL	85
4.3 OPTIMAL CONTROL OF MCT DRIVEN PMSG BY HOSM SPEED CONTROL	92
4.4 HOSM CONTROL ROBUSTNESS AGAINST PARAMETER VARIATIONS.....	98
III.5 COMPARISON	99
III.6 CONCLUSION	104
CHAPTER IV: Validation and Experimental Analysis	105
IV.1 INTRODUCTION.....	106
IV.2 HARDWARE PECIFICATIONS.....	106
IV.3 CONTROL OF A DOUBLY-FED INDUCTION GENERATOR	108

3.1 EXPERIMENTAL RESULTS FOR A FILTERED RESOURCE.....	109
3.2 EXPERIMENTAL RESULTS FOR A TURBULENT RESOURCE	113
IV.4 CONTROL OF A PERMANENT MAGNET SYNCHRONOUS GENERATOR	116
4.1 EXPERIMENTAL RESULTS FOR A FILTERED RESOURCE.....	116
4.2 EXPERIMENTAL RESULTS FOR A TURBULENT RESOURCE.....	119
IV.5 COMPARISON.....	121
IV.6 CONCLUSION	123
CONCLUSIONS & PERSPECTIVES.....	124
EXTENDED FRENCH ABSTRACT.....	127
I. INTRODUCTION.....	128
II. ETAT DE L'ART SUR LES HYDROLIENNES	129
II.1 PRINCIPE.....	129
II.2 POTENTIEL ENERGETIQUE ET CHOIX DU SITE	130
II.3 HYDROLIENNE: CONCEPTS ET TOPOLOGIES.....	131
III. MODELISATION D'UNE HYDROLIENNE.....	131
III.1 MODELISATION DE LA RESSOURCE	132
III.2 MODELISATION DU CAPTEUR	134
III.3 MODELISATION DE LA CHAINE DE TRANSMISSION MECANIQUE	136
III.4 MODELISATION DE LA GENERATRICE.....	136
IV. LES STRATEGIES DE COMMANDE.....	138
IV.1 COMMANDE PI.....	138
IV.2 COMMANDE NON LINEAIRE PAR MODE GLISSANT D'ORDRE SUPERIEUR	138
V. VALIDATION EXPERIMENTALE	139
VI. CONCLUSION ET PERSPECTIVES	140
REFERENCES	142
APPENDICES.....	149

List of Figures

Fig. I.1. Ebb generating system with a bulb turbine.....	6
Fig. I.2. La Rance tidal power station.....	6
Fig. I.3. Raz Blanchard, Fromveur, and Raz de Sein and sites.....	6
Fig. I.4. Spring and neap tides.....	8
Fig. I.5. Tidal turbine against an offshore wind turbine [© MCT].....	10
Fig. I.6. Fundamental tidal turbine types.....	10
Fig. I.7. Hybrid illustration of the Seaflow turbine [© MCT].....	11
Fig. I.8. The Seagen system illustration [© MCT].....	12
Fig. I.9. The Blue or E-Tide concept [© Strøm AS].....	13
Fig. I.10. The Tidal stream concept [© Tidal Stream].....	14
Fig. I.11. Illustration and front view of the TidEL turbine [© SMD Hydrovision]	14
Fig. I.12. The rim turbine concept.....	15
Fig. I.13. The Open-Centre turbine [© OpenHydro].....	15
Fig. I.14. The Clean Current turbine [© Clean Current TM].....	16
Fig. I.15. The Lunar Energy system illustration [© Lunar Energy].....	17
Fig. I.16. The HydroHelix system illustration [© HydroHelix Energies].....	18
Fig. I.17. The Enermar project [© Ponte di Archimede].....	19
Fig. I.18. The Blue Energy project [© Blue Energy].....	20
Fig. I.19. The Gorlov helical turbine [© GCK Technology].....	21
Fig. I.20. The Achard turbine.....	22
Fig I.21.The Uldolmok pilot tidal current power plant of 1 MW.....	23
Fig. I.22. Gorlov helical turbine with a synchronous generator.....	24
Fig. I.23. The Stingray tidal turbine [© EB].....	25
Fig. I.24. The bioSTREAM concept [© BioPower].....	25
Fig. I.25. The University of Southampton completed tidal mill	26
Fig. I.26. Full range variable speed system.....	28
Fig I.27. Variable speed direct-driven system.....	28
Fig I.28. Variable speed with doubly-fed induction generator.....	29
Fig. II.1. Marine current turbine global scheme.....	33

Fig. II.2. Timescale in a marine current turbine.....	34
Fig. II.3. The marine current turbine expected site of installation.....	36
Fig. II.4. Tidal velocity in the Raz de Sein for the year 2007 and March 2007.....	37
Fig. II.5. Swell characteristics.....	38
Fig. II.6. Raz de Sein site tidal data histogram.....	40
Fig. II.7. Idealized power curve.....	41
Fig. II.8. (a) Increasing rotor diameter reduces the rated tidal speed, emphasizing lower speed tidal. (b) Increasing the generator size increases rated power, emphasizing higher tidal speeds.....	41
Fig. II.9. The actuator disk model.....	44
Fig. II.10. Power coefficient C_p as function of the axial induction factor a	45
Fig. II.11. Annular plane used in BEM theory.....	47
Fig. II.12. Blade element velocities and hydrodynamic forces in the blade local coordinate frame with the chord line as reference.....	49
Fig. II.13. 2 (Seaflow) and 3 (E-tide) blades options [© MCT & Strøm AS].....	50
Fig. II.14. NACA 44 blades derived characteristics.....	52
Fig. II.14. Blades mesh using singularities-code.....	52
Fig. II.15. The marine turbine tested in [71].....	53
Fig. II.16. Model (a) and experimental (b) C_p curves [71].....	53
Fig. II.18. $C_p(\lambda, \theta)$ curves.....	54
Fig. II.19. The estimated extracted power for year 2007.....	55
Fig. II.17. The estimated extracted power for July 2007.....	55
Fig. II.21. Drive train model.....	56
Fig. II.22. Schematic diagram of a DFIG-based generation system.....	59
Fig. II.18. Schematic diagram of a PMSG-based generation system.....	61
Fig. III.1. $C_p(\lambda, \beta)$ curves.....	68
Fig. III.2. Power curves for different tidal current speed.....	68
Fig. III.3. Power coefficient curve (hydrodynamic efficiency).....	69
Fig. III.4. MCT PI control structure: speed control loop case.....	73
Fig. III.5. DFIG model bloc.....	75
Fig. III.6. The inner loop of the DFIG speed control.....	76
Fig. III.7. The DFIG control cascade.....	77
Fig. III.8. Speed-tracking part of the DFIG overall variable speed control scheme.	77
Fig. III.9. The DFIG rotor speed and its reference.....	78

Fig. III.10. The DFIG active power.....	78
Fig. III.11. The PMSG Park model.....	80
Fig. III.12. The PMSG rotor speed and its reference.....	80
Fig. III.13. The PMSG active power.....	81
Fig. III.14. The HOSM control scheme for a DFIG-based MCT.....	86
Fig. III.15. Filtered resource speed.....	89
Fig. III.16. The DFIG rotor speed and its reference.....	89
Fig. III.17. The DFIG active power.....	90
Fig. III.18. Turbulent resource speed.....	91
Fig. III.19. The DFIG rotor speed and its reference.....	91
Fig. III.20. The DFIG active power.....	92
Fig. III.21. The HOSM control scheme for a PMSG-based MCT.....	92
Fig. III.22. Filtered resource speed.....	95
Fig. III.23. The PMSG rotor speed and its reference.....	95
Fig. III.24. The PMSG active power.....	96
Fig. III.25. The PMSG rotor speed and its reference.....	97
Fig. III.26. The PMSG active power.....	97
Fig. III.27. DFIG stator resistance Variation.....	98
Fig. III.28. DFIG rotor speed and its reference.....	99
Fig. III.29. DFIG-based MCT control scheme.....	100
Fig. III.30. The DFIG rotor speed and generated active power for a turbulent resource for cases 1, 2 and 3 (PI control).....	102
Fig. III.31. The DFIG rotor speed and generated active power for a turbulent resource for cases 1 and 4 (HOSM control).....	103
Fig. III.32. The DFIG rotor speed and generated active power for a turbulent resource for cases 1 and 5 (HOSM control).....	103
Fig. III.33. The DFIG rotor speed and generated active power for a turbulent resource for cases 4 and 5 (HOSM control).....	104
Fig. IV.1. Components of the G2Elab test bench	106
Fig. IV.2. MCT emulator part of the test bench [©G2Elab].....	107
Fig. IV.3. Software tools.....	108
Fig. IV.4. Control of the doubly-fed induction generator [©G2Elab].....	109
Fig. IV.5. Filtered resource speed.....	109
Fig. IV.6. DC motor torque reference.....	110

Fig. IV.7. The DFIG rotor speed and its reference.....	110
Fig. IV.8. Experimental DFIG I_{rq} current tracking performances.....	111
Fig. IV.9. The DFIG stator currents.....	111
Fig. IV.10. The DFIG rotor currents.....	112
Fig. IV.11. The DFIG active power.....	112
Fig. IV.12. Turbulent tidal speed.....	113
Fig. IV.13. DC motor torque reference.....	113
Fig. IV.14. The DFIG rotor speed and its reference.....	114
Fig. IV.15. Experimental DFIG I_{rq} current tracking performances.....	114
Fig. IV.16. The DFIG stator currents.....	115
Fig. IV.17. The DFIG rotor currents.....	115
Fig. IV.18. The DFIG active power.....	116
Fig. IV.19. Control of the permanent magnet synchronous generator [©G2Elab].....	117
Fig. IV.20. The PMSG rotor speed.....	117
Fig. IV.21 Experimental PMSG I_q current tracking performances.....	118
Fig. IV.22. The PMSG active power.....	118
Fig. IV.23. Turbulent tidal speed.....	119
Fig. IV.24. The PMSG rotor speed tracking performances.....	119
Fig. IV.25. Experimental PMSG I_q current tracking performances.....	120
Fig. IV.26. The PMSG active power.....	120
Fig. IV.27. Experimental and simulation DFIG rotor speed tracking performances.....	121
Fig. IV.28. Output power: Experiments vs simulation.....	121
Fig. IV.29. Experimental and simulation PMSG rotor speed tracking performances.....	122
Fig. IV.30. Output power: Experiments vs simulation.....	122

I ntroduction

Renewable energy generated from natural resources, sun, wind and water, is being seen as the main promising and enduring source of the future energy. It has long been touted as the ultimate solution to the world energy and environmental problems, offering the potential of virtually unlimited cheap and pollution-free energy. Indeed, the interest in renewable energy is spurred by fears of recurrent fossil energy crises which were engendered either by speculation, demand rise, political tensions or depletion risk of this vital resource. In addition, from the beginning of the new century, the rise of human consciousness about the climate change due to the greenhouse emissions gas has contributed in bringing this renewable non pollutant energy to their centre of interest. Thus, the environment preservation becomes one strong argument in promoting the development of renewable energy. Moreover, this tendency is mainly encouraged by the European Union that requested the diminution of greenhouse emission gas by 20% from now to 2020.

Consequently, the efficiency and reliability of renewable technologies has been continuously improved and an important technological advance has been noted. In the last decades, many new renewable energy sectors are emerging and interesting developments are taking place. The most promoting renewable marine energies are wave and swell energy, thermal marine energy and the marine tidal energy. The most motivating sector is the marine renewable one. Indeed, the potential

of electric power generation from marine tidal currents is very interesting. Thus, tidal currents are being recognized as a resource to be exploited for the sustainable generation of electrical power. The high load factors resulting from the fluid properties and the predictable resource characteristics make marine currents particularly attractive for power generation and advantageous when compared to some other renewable energies. Therefore, several demonstration projects in tidal power are scheduled to capture the marine tidal energy.

However, many difficulties have met the complete successful realization of these projects, especially in what concerns the high cost installations on one hand and their maintenance on the other. Therefore, it is obvious that there is a need to quantify the marine current turbine efficiency and the generated power potential before installation and to determine the best technology choice for each prospective site.

The main objective of this *Ph.D.* thesis is to set up a marine current turbine simulation environment which is intended to be used as a sizing and site evaluation tool. Therefore, the developed simulation model has two purposes: performances and dynamic loads evaluation in different operating conditions and control system development for turbine operation based on pitch and speed control.

The contributions of this thesis are:

- Development of a marine current turbine simulation environment with the possibility of future extensions.
- Comparison between two marine current turbine topologies one based on the doubly fed induction generator and another based on the permanent magnet synchronous one.
- Analysis of two types of control strategy performances.

This thesis is organized as follows:

Chapter I reviews marine tidal power fundamental concepts and main projects around the world. It also report issues regarding electrical generator topologies associated to tidal turbines. Moreover, attempts are made to highlight future issues so as to index some emerging technologies mainly according to relevant works that have been carried out on wind turbines and on ship propellers.

Chapter II deals with the development of a Matlab/ Simulink® model of a marine current turbine system through the modeling of the resource, the rotor, and the generator.

Chapter III proposes a series of control strategies which are analyzed, assessed and compared. The main results, based on the developed marine current turbine simulation tools, are presented along with illustration by case studies and Matlab/Simulink® simulation assessment.

Chapter IV presents the experimental validation of the proposed control strategies.

Chapter I

State of the Art Survey of Marine Current Turbine: Concepts & Technologies

I.1	INTRODUCTION	4
I.2	TIDAL KINETIC ENERGY BACKGROUND	4
I.3	TIDAL RESSOURCE	7
I.4	KINETIC ENERGY EXTRACTION	8
I.5	TURBINE TECHNOLOGIES AND CONCEPTS	9
5.1	HORIZONTAL AXIS TURBINES.....	11
5.2	VERTICAL AXIS TURBINES	19
5.3	OSCILLATING HYDROFOIL	24
5.4	FLOATING TIDAL ENERGY SYSTEM	25
I.6	DEVELOPMENT OF TIDAL TECHNOLOGIES AND DESIGN OPTIONS.....	26
I.7	ELECTRIC GENERATOR TOPOLOGIES IN MARINE CURRENT TURBINES	27
7.1	FULL RANGE VARIABLE SPEED SYSTEM (WITH GEAR).....	27
7.2	FULL RANGE VARIABLE SPEED SYSTEM (WITHOUT GEAR)	28
7.3	LIMITED VARIABLE SPEED SYSTEM.....	28
I.8	CONCLUSION.....	29

I.1 INTRODUCTION

The potential for electric power generation from marine tidal currents is enormous. Tidal currents are being recognized as a resource to be exploited for sustainable generation of electrical power. The high load factors resulting from the fluid properties and the predictable resource characteristics make marine currents particularly attractive for power generation and advantageous when compared to other renewable energies. Moreover, international treaties related to climate control have triggered resurgence in the development of renewable ocean energy technology. Therefore, several demonstration projects in tidal power are scheduled to capture the tidal generated coastal currents. Regarding this emerging and promising area of research, this first chapter reviews marine tidal power fundamental concepts and main projects around the world. It also reports issues regarding electrical generator topologies associated to tidal turbines. Moreover, attempts are made to highlight future issues so as to index some emerging technologies mainly based on relevant works that have been carried out on wind turbines and ship propellers.

I.2 TIDAL KINETIC ENERGY BACKGROUND

Oceans, covering more than 70 % of the earth, have long been appreciated as a vast renewable energy source. The energy is stored in oceans in different and several forms as thermal energy, kinetic energy (waves and currents) and also in chemical and biological products. Therefore, numerous techniques for exploiting and extracting energy from the sea have been suggested, the most prominent ones can be included in one of the following categories: wave energy, tidal current energy, ocean thermal energy, energy from salinity gradients (osmosis), and cultivation of the marine biomass. The kinetic energy available in tidal currents can be converted to electricity using relatively conventional turbine technology.

Harnessing the kinetic energy in waves presents a different set of technical challenges which have pushed engineer to suggest a wide variety of designs. Ocean thermal energy conversion is possible in locations with large temperature differences, by extracting energy with a heat engine. Salinity gradients can be exploited to extract energy through the osmotic process. The cultivation of marine biomass can provide many useful products, including renewable fuels for electricity generation. However, due to technology limitations and economic considerations, osmotic and thermal energy developments are limited [1-3].

Only a fraction of the global ocean energy resource can be found in sites which are economically suitable to explore with available technology. However, this fraction could still make a considerable contribution to electricity supply. This is the reason why the marine renewable sector is currently the focus of much industrial and academic research around the world [4-5]. Sites with attractive wave climate and intense tidal currents are abundant in the vicinity of the European coastline. It has been shown that 48% of the European tidal resource is in the UK, 42% in France, and 8% in Ireland [6]. There are basically two ways of generating electricity from marine tidal currents either by building a tidal barrage across an estuary or a bay in high tide areas, or by extracting energy from free flowing water (tidal kinetic energy).

A tidal barrage applies the same principles as hydro-electric power generation, except that tides flow in both directions and generators are designed to respond to two directional water flows. The simplest generating system for tidal plants is the ebb generating system, which involves a dam, known as a barrage across a bay or estuary (Fig. I.1). Sluice gates on the barrage allow the tidal basin to fill on the incoming high tides and to exit through the turbine system on the outgoing tide (known as the ebb tide). La Rance tidal power plant, generating 240 MW, is the largest operating tidal facility in the world, far bigger than the next largest, the Annapolis facility (20 MW) in Canada. The enclosed estuary of La Rance River in Brittany (France) has a surface area of 22 km² (Fig. I.2) and very large tides with 13.5 m difference between high and low tides during the equinox. There are 24 units of 10 MW which can run during both incoming and outgoing tides [7-8]. The main drawback of this technology is that only a few sites are suitable worldwide. Moreover, this kind of system has an important impact on the local ecosystem.

Within the last few decades, developers have shifted towards technologies that capture the tidally-driven coastal currents or tidal stream. Indeed, very large amounts of energy are available in coastal waters [1], [9-15].

There are many areas of the world in which extreme tidal currents are observed. Three examples in France are shown in Fig. I.3. The Raz Blanchard situated in Cap de la Hague experiences very high tidal currents exceeding 8 knots and leading to a large amount of kinetic energy flux.

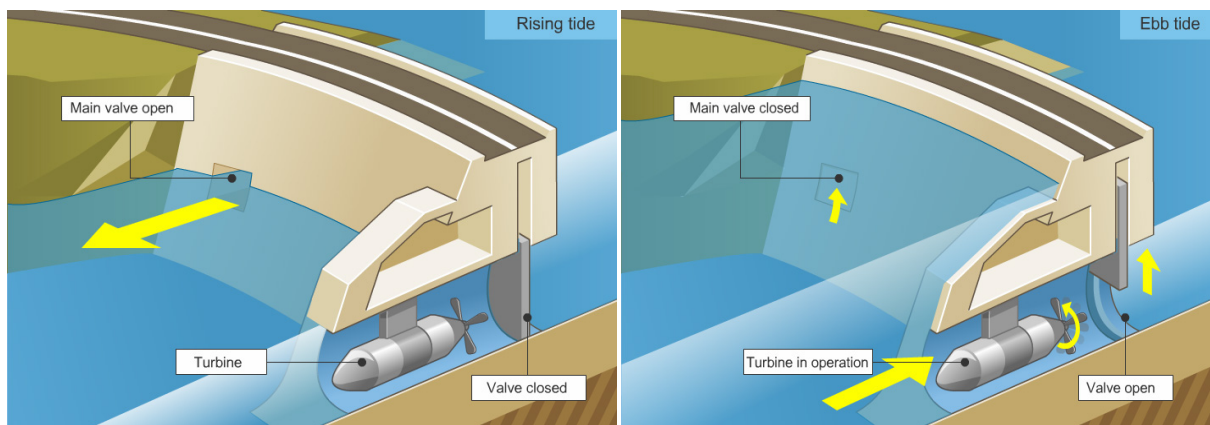


Fig. I.1. Ebb generating system with a bulb turbine.



Fig. I.2. La Rance tidal power station [6].

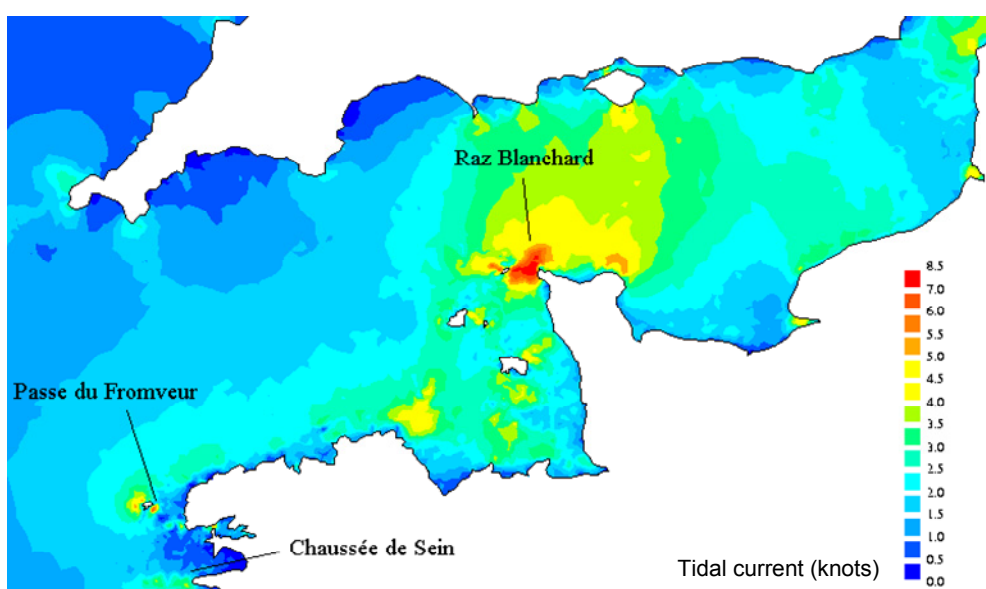


Fig. I.3. Raz Blanchard, Fromveur, and Raz de Sein sites in the French western coast.

I.3 TIDAL RESSOURCE

Nowadays, the attraction of tidal currents for renewable energy developers is obvious. The medium, seawater, is more than 800 times denser than air. Moreover, the astronomic nature of the underlying driving mechanism results essentially in predictable resource. However, it is subjected to weather-related fluctuations.

As a renewable resource, tidal current flow is very predictable, to within 98% accuracy for decades. Tidal charts are accurate to within minutes, for years ahead. Tidal current is mainly independent of prevailing weather conditions such as fog, rain, and clouds that can impact other renewable generation forecasts. Solar generation is impacted by rain, clouds and fog. Wind turbines are impacted by calm weather; tidal cycles are as reliable as the rising of the moon. While solar energy and the wind are valuable renewable resources, neither can be plotted with the predictability of tidal energy. Thus, reliable amounts of tidal power can be forecast with confidence. This predictability is critical to successful integration of renewable resources into the electrical grid [9].

The global marine current energy resource is mostly driven by tides and to a lesser extent by thermal and density effects. Tides cause water to flow inwards twice each day (flood tide) and seawards twice each day (ebb tide) with a period of approximately 12 hours and 24 minutes (a semi-diurnal tide), or once both inwards and seawards in approximately 24 hours and 48 minutes (a diurnal tide). In most locations the tides are a combination of semi-diurnal and diurnal effects, with the tide being named after the most dominant type. The strength of the currents varies, depending on the proximity of the moon and the sun relative to the earth. The magnitude of the tide-generating force is about 68% moon and 32% sun due to their respective masses and distance from the earth. Where the semi-diurnal tide is dominant, the largest marine currents occur at new moon and full moon (spring tides) and the lowest at the first and third quarters of the moon (neap tides). With diurnal tides, the current strength varies with the declination of the moon (position of the moon relative to the equator). The largest currents occur at the extreme declination of the moon and lowest currents at zero declination. Further differences occur due to the changes between the distances of the moon and the sun from earth, their relative positions with reference to earth and varying angles of declination. This phenomena occurs with a periodicity of two weeks, one month, one year or longer, and it is entirely predictable [6], [16]. For illustration, Fig. I.4 shows the sequence of spring and neap tides according to the moon phases. The size of the tide gradually decreases over the course of one week to become neap tides and then gradually increases again.

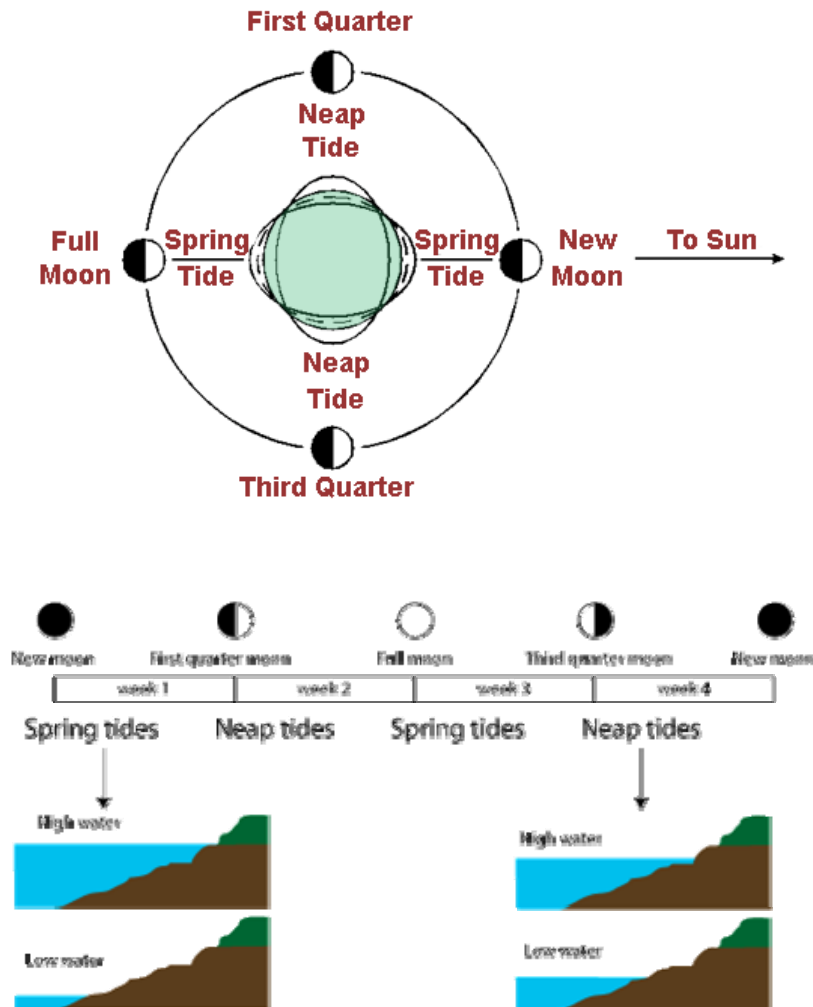


Fig. I.4. Spring and neap tides.

The resource assessment is generally based on oceanographic databases containing data with a fixed grid square resolution. The main key criteria are: maximum spring current velocity; maximum neap current velocity; seabed depth; maximum probable wave height in 50 years; seabed slope; significant wave height; and the distance from land [12], [17-18].

I.4 KINETIC ENERGY EXTRACTION

The total kinetic power in a marine current turbine has a similar dependence as in a wind turbine and is governed by the following equation [6], [19-20]

$$P = \frac{1}{2} \rho A v^3 \quad (I.1)$$

where ρ is the fluid density, A is the cross-sectional area of the turbine and V is the fluid velocity. However, a marine energy converter or a turbine can only harness a fraction of this power due to losses and (I.1) is modified as follows.

$$P = \frac{1}{2} \rho C_p A V^3 \quad (\text{I.2})$$

C_p is known as the power coefficient which is essentially the percentage of power that can be extracted from the fluid stream and takes into account losses due to Betz law and those assigned to the internal mechanisms within the converter or turbine. For wind generators, C_p has typical values in the range 0.25–0.5. The upper limit is for highly efficient machines with low mechanical losses. For marine turbines, C_p is estimated to be in the range 0.35–0.5 [21]. Compared to the largest wind turbines operating today, the output power as well as the size of a classical tidal turbine is extremely promising. Indeed, this is due to the sea water huge density and to the current velocity. For illustration, Fig. I.5 shows a tidal turbine against an offshore wind turbine of the same power rating. Furthermore, with constant or highly predictable marine currents a tidal turbine could not only rival the largest wind turbines in being more manageable in size but also in generating highly predictable power [20], [22],[61].

I.5 TURBINE TECHNOLOGIES AND CONCEPTS

The harnessing of the energy in a tidal flow requires the conversion of kinetic energy in a moving fluid, in this case water, into the motion of a mechanical system, which can then drive a generator. It is not too surprising, therefore, that many developers have proposed to use technology which has been successfully utilized to harness the wind, which is also a moving fluid.

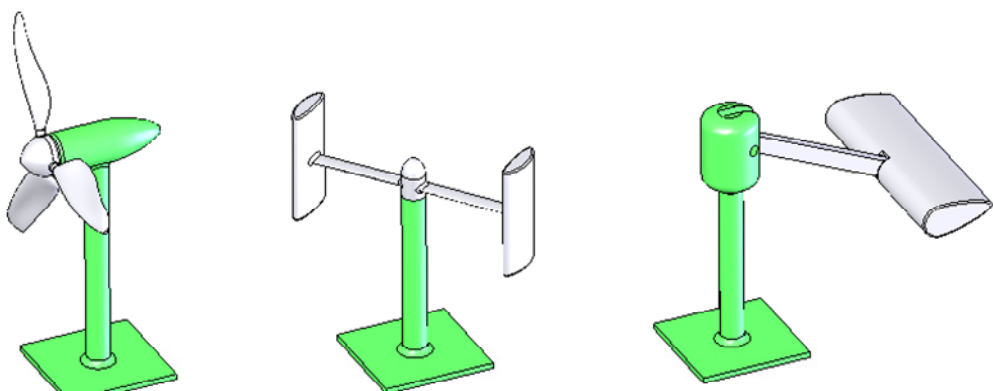


Fig. I.5. Tidal turbine against an offshore wind turbine [© MCT].

Therefore, most devices can be characterized as belonging to three fundamental types [23]. These are (Fig. I.6):

- Horizontal axis systems that have been installed for example in the Bristol Channel between England and Wales [24], or in Hammerfest Strøm, in Norway [25].
- Vertical axis systems such as the device that was tested in the Strait of Messina between Sicily and the Italian mainland [26].
- Variable foil systems such as the device that has been tested in Yell Sound in Shetland, which lies to the North of Scotland and Orkney [27].

An overview of some of the major tidal turbine technologies and concepts is presented below.



Horizontal axis turbine Vertical axis turbine Linear left based device

Fig. I.6. Fundamental tidal turbine types.

5.1 Horizontal Axis Turbines

5.1.1 The Marine Current Turbine (MCT) Projects (UK)

Figure I.7 shows hybrid illustrations of the Seaflow turbine. It has a single 11 m diameter rotor, with full span pitch control, and is installed in a mean depth of seawater of 25 m approximately 1.1 km off the nearest landfall at the Foreland Point lighthouse below Exmoor in North Devon, UK [24]. It has exceeded its 300 kW rated power under favorable flow conditions with a 15 rpm rotor speed. It is not grid-connected but as an experimental test-rig dumps its power into resistance heaters capable of absorbing the maximum power.

A key feature is that it is mounted on a steel tubular tower, 2.1 m in diameter, set in a piled foundation in the seabed and tall enough to always project above the surface of the sea. The entire rotor and power system can be physically raised up the tower above the surface to facilitate maintenance or repairs from a boat, a vital requirement as the use of divers or any other form of underwater intervention which is virtually impossible in locations with such strong currents.

The MCT second project was “*Seagen*”. It was deployed in the Northern Ireland’s Strangford Lough in May 2008. The *Seagen* turbine has its rotors mounted at the outer ends of a pair of streamlined wing-like arms projecting either side of the supporting pile (Fig. 8a).

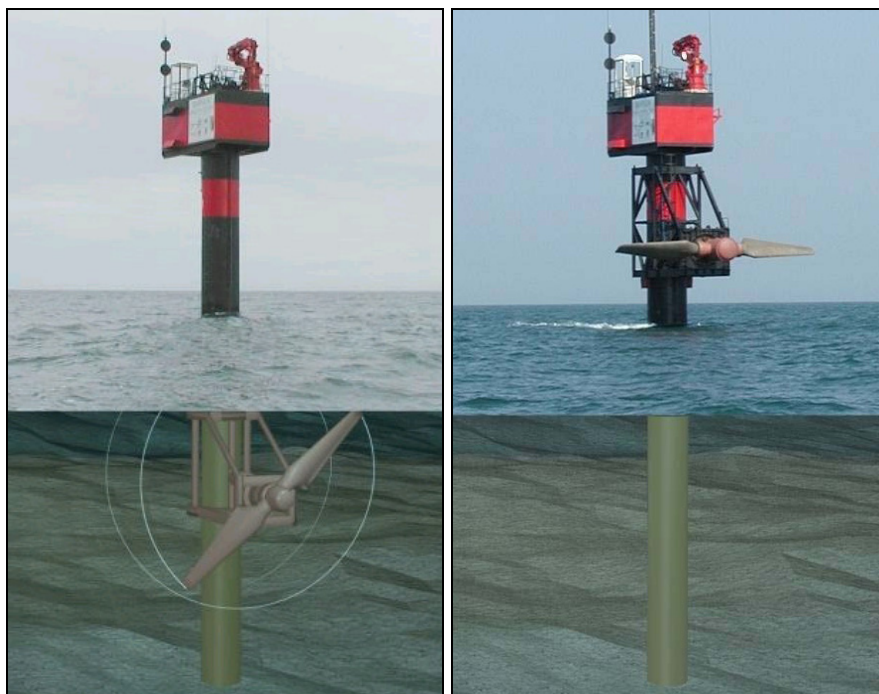
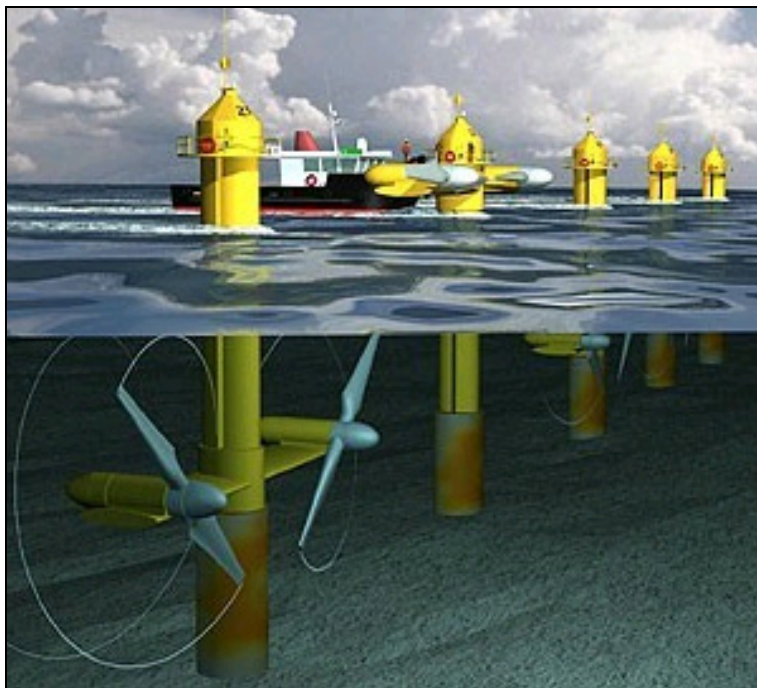


Fig. I.7. Hybrid illustration of the Seaflow turbine [© MCT].



(a) Seagen turbine.



(b) Seagen farm.

Fig. I.8. The Seagen system illustration [© MCT].

Each rotor drives a power-train consisting of a gearbox and generator each rated at around 600 kW. The total rated power is approximately 1.2 MW. This is the highest power so far produced by a tidal stream system anywhere in the world. The *Seagen* project will be followed by a set of similar systems (farm) to be installed in the coast of Anglesey, North of Wales. Seven turbines will be added to provide a total capacity up to 10.5 MW (Fig. I.8b).

5.1.2 The E-Tide project (Norway)

Hammerfest Strøm developed the so-called Blue or E-Tide concept in Kvalsund (Northern Norway) in 2003. The Blue Concept device is a tidal current turbine that can be installed on the seabed offshore or near shore depending on the tidal current strength (Fig. I.9). A 300 kW system was tested and the concept proven during the installation and a larger design is being developed for the same location that will provide 750-1000 kW of power. The turbine blades of 15-16 m are able to pitch on their own axes, allowing the turbine to be optimized to current conditions and also operate in both directions of the tide (pitch control) [25].

5.1.3 The Tidal Stream Energy Project (UK)

The Tidal Stream turbine is shown in Fig. I.10. This configuration is designed for the site of Pentland Firth between the North of Scotland and the Orkney Islands [18]. In the first design (Fig. I.10a), the twin turbine carries two 20 m rotors. This system is rated at 1-2 MW depending on current speed, and operates in 30-50 m water depths. Each rotor runs in clean water upstream of its support arm. The seabed anchorage is now shown with a gravity base, and the swinging arm ball-joint is attached to the base by a three-axis swivel assembly. The swinging arm is hinged at its upper end to the main spar buoy so that it can be stowed easily for installation or removal. During operation, it is held in place by a cranked strut. The Tidal Stream technology is scalable from a twin rotor system - up to 2 MW systems for constrained sites - up to the six-rotor 10 MW platform for deeper water and highly energetic sites (Figs. I.10b and I.10c) [28].



(a) E-tide turbine.

(b) Installation.

Fig. I.9. The Blue or E-Tide concept [© Strøm AS].

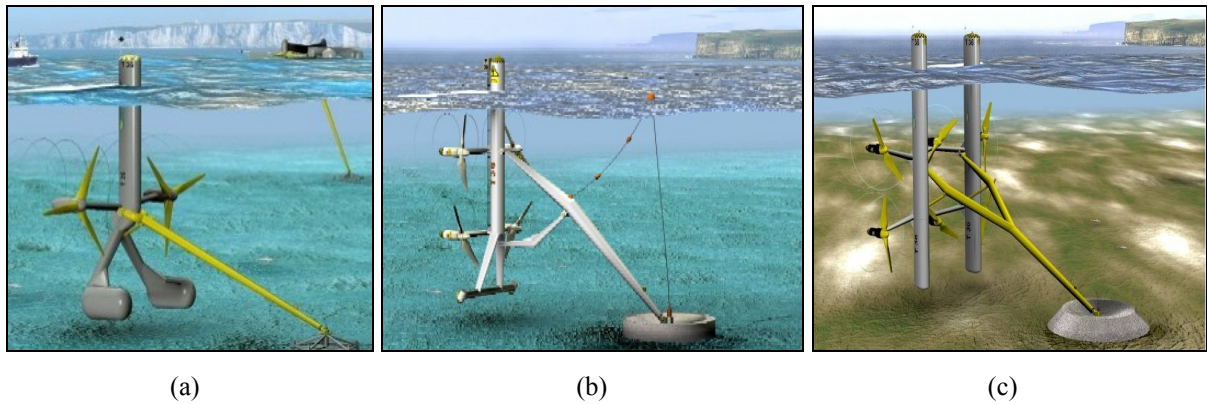


Fig. I.10. The Tidal stream concept [© Tidal Stream].

5.1.4 The SMD Hydrovision TidEL Project (UK)

The TidEl concept consists of a pair of contra-rotating 500 kW turbines, mounted together on a single crossbeam (Fig. I.11). The complete assembly is buoyant and tethered to the seabed by a series of mooring chains. The mooring system allows the turbines to align themselves down stream of the prevailing tidal flow without requiring any external intervention. As the system requires no support structure, it can be fitted in any reasonable coastal water depth. Each of the turbine power trains are driven by 15 m diameter fixed pitched blades and are housed within a pod. The 1 MW units are designed to be mounted in an offshore tidal environment with a peak tidal velocity of 5 knots (2.5 m/sec) or more and a water depth of more than 30 m [29].

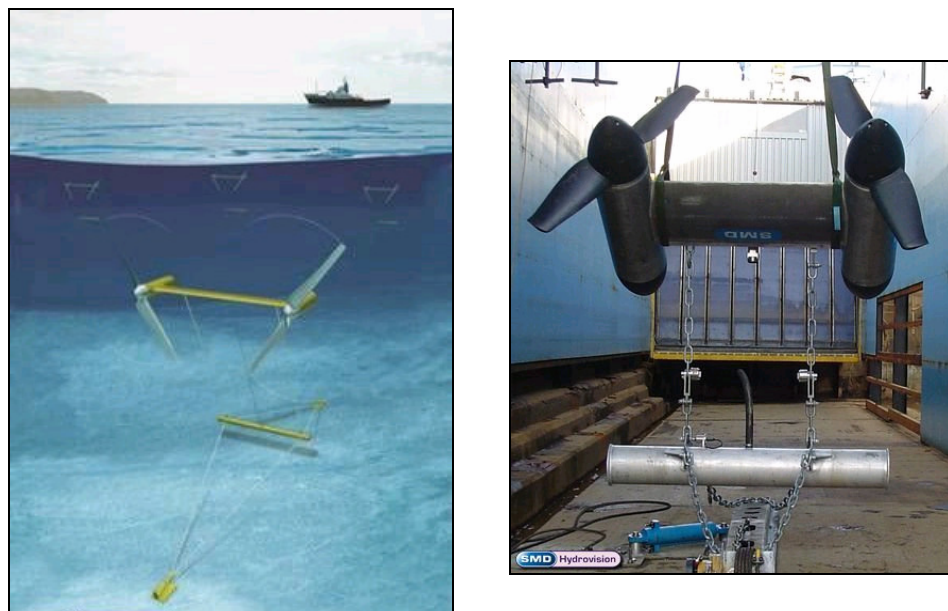


Fig. I.11. Illustration and front view of the TidEL turbine [© SMD Hydrovision].

5.1.5 Ducted Turbine Projects

In another kind of marine horizontal turbines, the turbine blades are surrounded by a duct. The duct captures a large area of the tidal stream and accelerates the flow through a narrowing channel into the turbine [30-31]. Thus, a smaller turbine can be used for a given power output, or alternatively, a larger amount of power can be generated by a turbine of given blade diameter.

The rim tidal turbine can be used to extract tidal current energy [43]. This concept has been already studied for ship propulsion [44] (Fig. I.12). The functionality and survivability of equipment in an underwater environment demands simplicity and robustness. The rim tidal turbine seems to meet these demands, with its slow-moving rotor and lubricant-free construction. The rim turbine, with just one moving part and no seals, is a self-contained rotor with a solid state permanent magnet generator encapsulated within the outer rim. This concept permits in fact the minimization of maintenance requirements. This concept has been adopted by OpenHydro (Ireland) through their Open-Centre Turbine that is shown by Fig. I.13 [45].

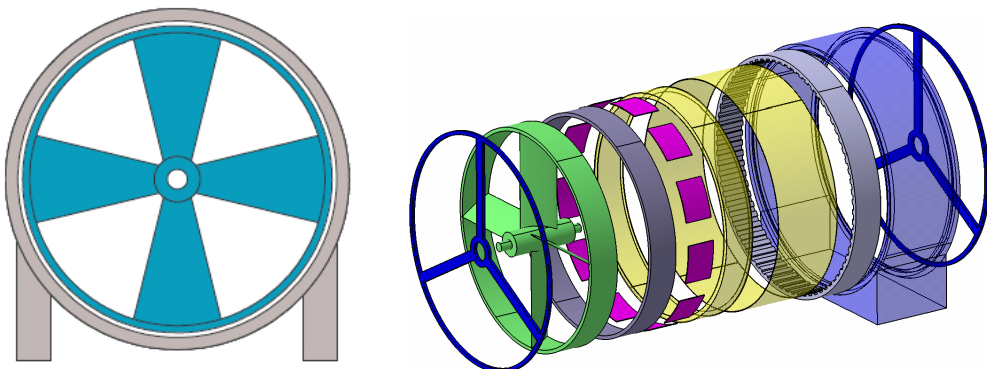


Fig. I.12. The rim turbine concept [44].



Fig. I.13. The Open-Centre turbine [© OpenHydro].

It should be noted that OpenHydro was chosen by EDF to develop the first tidal current demonstration farm in France. The project involves the installation of at least 4 and up to 10 large seabed mounted marine turbines in a tidal farm located in Paimpol-Bréhat (Brittany-France).

Another concept is the Clean Current Turbine. The Clean Current's tidal turbine generator is a bi-directional ducted horizontal axis turbine with a direct drive variable speed permanent magnet generator (Fig. I.14). Operability is enhanced by a simple design that has one moving part - the rotor assembly that contains the blades. There is no drive shaft and no gearbox. The bearing seals will be replaced every 5 years and the generator will be overhauled every 10 years. The service life of turbine generator is 25-30 years [32].

The Clean Current direct drive variable speed permanent magnet generator incorporates features that allow the generator to be configured to produce either alternating or direct current. Moreover, the rotor disks and generator are adapted to be removed as a modular unit such that maintenance and replacement is easily facilitated. Alstom Hydro has signed a licensing cooperation agreement with Clean Current Power Systems Incorporated. Indeed, Alstom plans to commercialize its first tidal stream products by 2012.

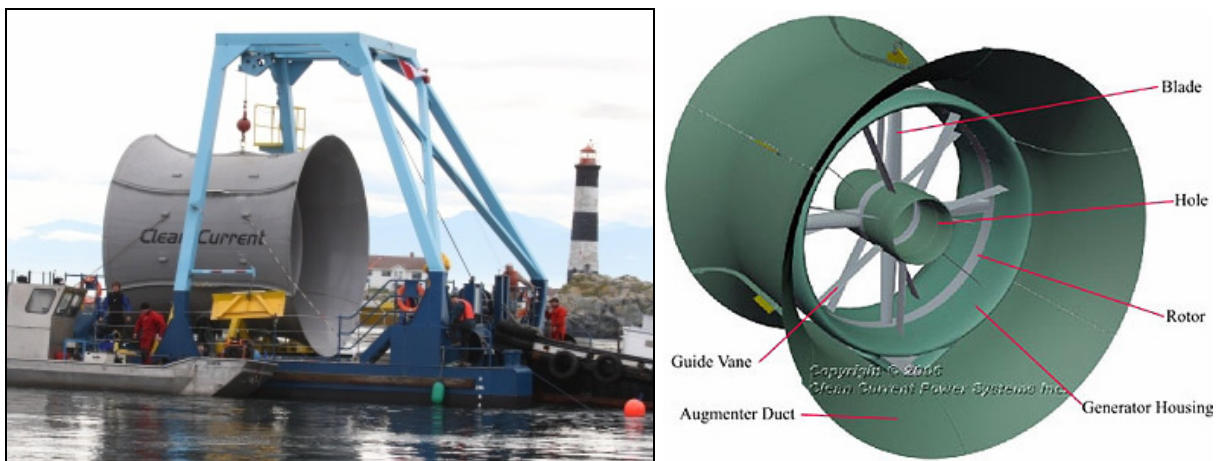


Fig. I.14. The Clean Current turbine [© Clean CurrentTM]

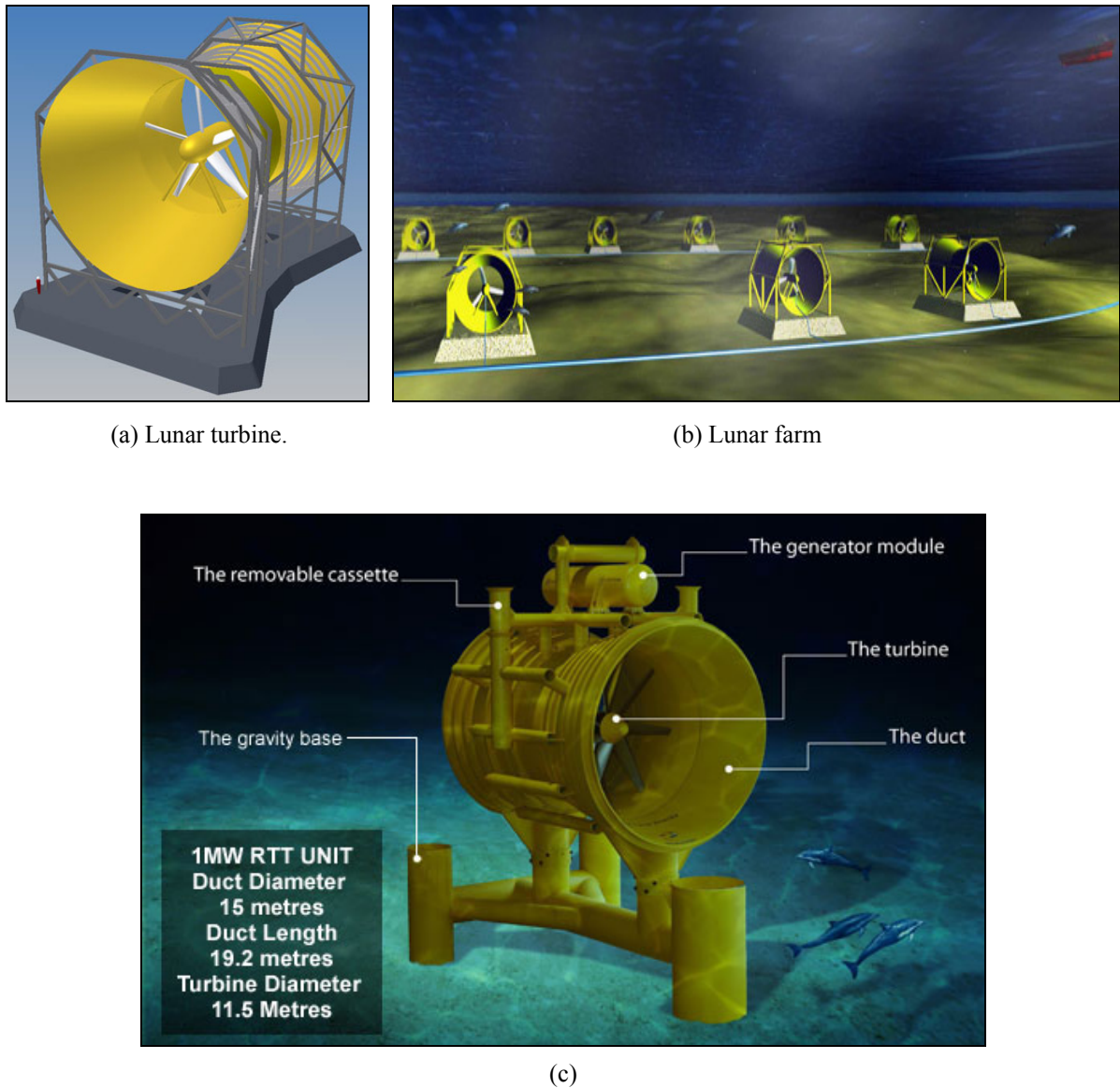


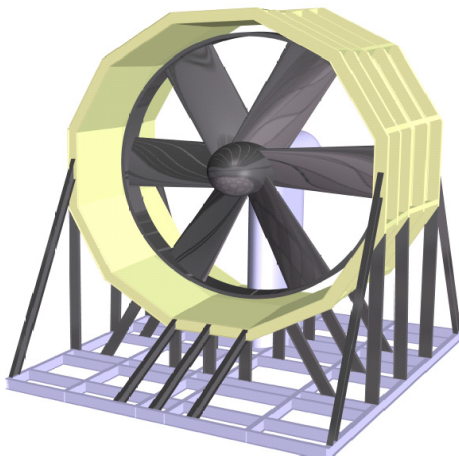
Fig. I.15. The Lunar Energy system illustration [© Lunar Energy].

The Lunar Energy tidal turbine is another ducted system of a symmetrical design. This system is capable of bi-directional operation obviating the need for a pitch or yaw control thus keeping the design simple and more cost-effective (Fig. I.15). The tidal flow can be offset by as much as 40° to the duct axis without affecting the performance. In fact, when operating in flows that come from this $\pm 40^\circ$ sector, the ducted system extracts more power than when the flow is perfectly aligned with the turbine axis. A 1/20th model was tested in 2004, and a 1 MW prototype is expected soon (Fig. I.15c) [33].

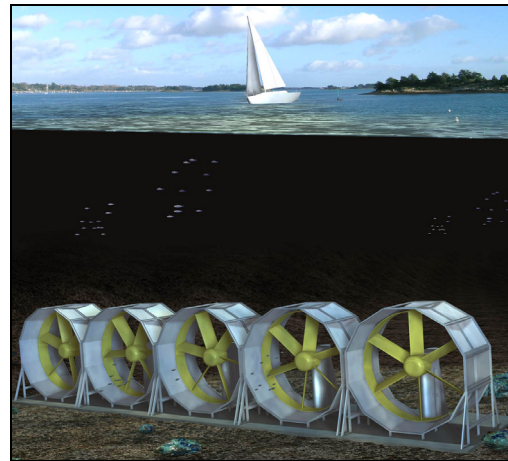
A similar project is the HydroHelix one in France. It consists of a 200 kW turbine as shown in Fig. 16a. The expected tidal energy unit is illustrated by Fig. I.16b with an average output power of 1 MW. A new 10 kW prototype, named Sabella, has been tested near Brest (Odet estuary) in April 2008 (Fig. I.16c) [34].

The ducted configuration presents several advantages: It is more robust since the crown surrounding the blades protects and reinforces them. The duct can improve the hydrodynamic efficiency of the turbine. Moreover, some mechanical or electromechanical solutions to convert the mechanical energy of the rotor can be located in the duct (e.g. gears, straps, non conventional generators).

All these projects or concepts are characterized by a very low speed turbine rotor. The speed range is typically of 10 to 20 rpm, which means that the turbine has a huge torque for a given power.



(a) HydroHelix turbine.



(b) HydroHelix tidal energy unit.



(c) Sabella project.

Fig. I.16. The HydroHelix system illustration [© HydroHelix Energies].

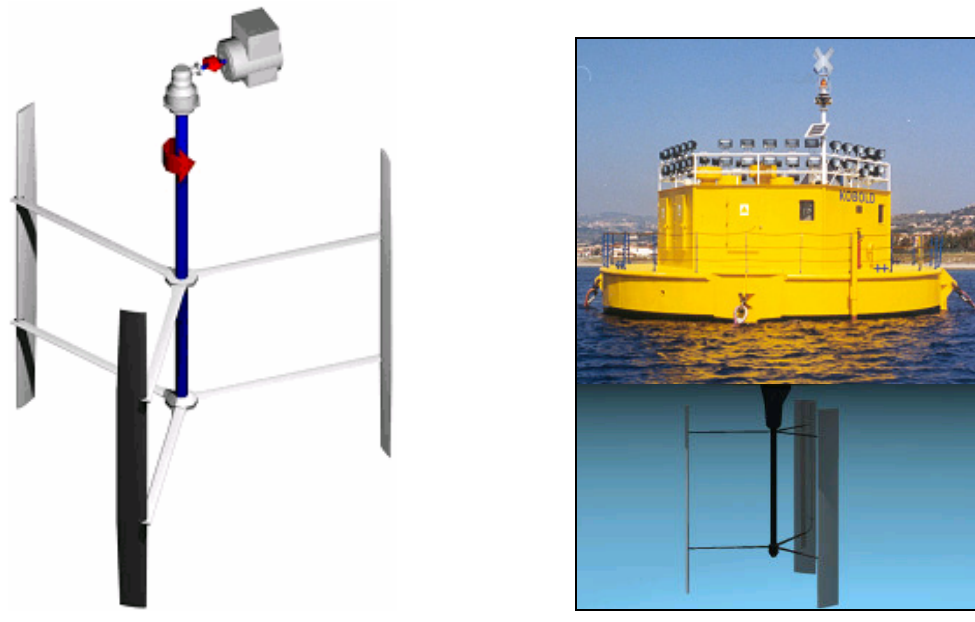
5.2 Vertical Axis Turbines

Vertical axis turbines that operate in marine currents are based on the same principles as the land based Darrieus turbine. The Darrieus turbine is a cross flow machine, whose axis of rotation meets the flow of the working fluid at right angles. In marine current applications, cross flow turbines allow the use of a vertically orientated rotor which can transmit the torque directly to the water surface without the need of complex transmission systems or an underwater nacelle.

The vertical axis design permits the harnessing of tidal flow from any direction, facilitating the extraction of energy not only in two directions, the incoming and outgoing tide, but making use of the full *tidal ellipse* of the flow [35]. In this kind of turbines as in the horizontal axis ones the rotation speed is very low (around 15 rpm).

5.2.1 The Enermar Project (Italy)

The core of the Enermar project is the patented Kobold turbine (Fig. I.17a). Among its main characteristics, the Kobold turbine has a very high starting torque that makes it able to start spontaneously even in loaded conditions. A pilot plant is moored in the Strait of Messina, close to the Sicilian shore in Italy, in an average sea tidal current of about 2 m/sec (Fig. I.17b). With a current speed of about 1.8 m/sec, the system can produce power of 20 kW [26].



(a) Kobold turbine.

(b) Floating platform.

Fig. I.17. The Enermar project [© Ponte di Archimede].

5.2.2 The Blue Energy Project (Canada)

Four fixed hydrofoil blades of the Blue Energy tidal turbine are connected to a rotor that drives an integrated gearbox and electrical generator assembly (Fig. I.18a). The turbine is mounted in a durable concrete marine caisson which anchors the unit to the ocean floor, directs flow through the turbine further concentrating the resource supporting the coupler, gearbox, and generator above it. These are located above the water surface and are readily accessible for maintenance and repair (Fig. I.18b). The hydrofoil blades employ a hydrodynamic lift principal that causes the turbine foils to move proportionately faster than the speed of the surrounding water. The rotation of the turbine is unidirectional on both the ebb and the flow of the tide. A unit turbine is expected to be about 200 kW output power. For large scale power production, multiple turbines are linked in series to create a tidal fence across an ocean passage or inlet [36].

5.2.3 The Gorlov Helical Turbine (USA)

The Gorlov Helical Turbine (GHT) is shown in Fig. I.19a. The turbine consists of one or more long helical blades that run along a cylindrical surface like a screw thread, having a so-called airfoil or airplane wing profile. The blades provide a reaction thrust that can rotate the turbine faster than the water flow itself [37].

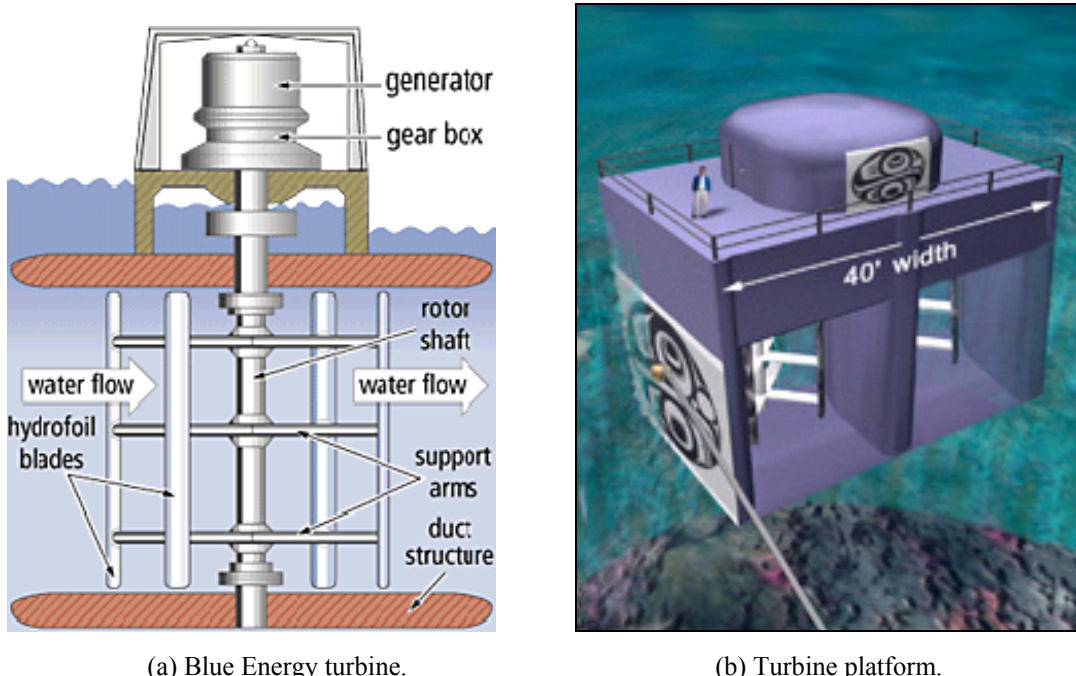
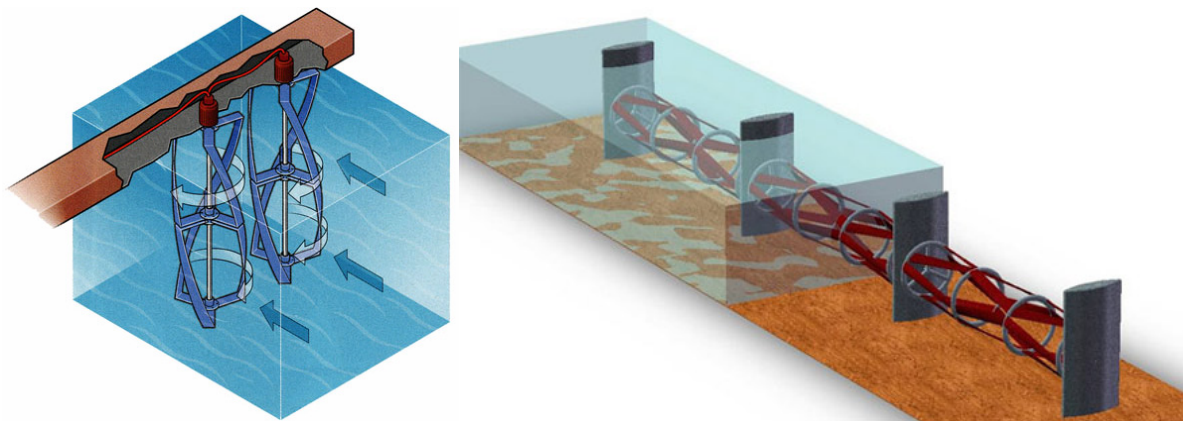


Fig. I.18 The Blue Energy Project [© Blue Energy].



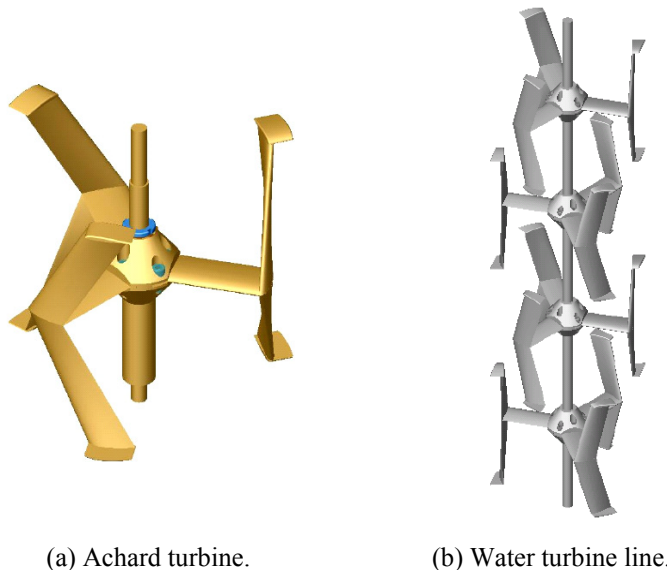
(a) Gorlov turbine.



(b) Expected power plant.

Fig. I.19. The Gorlov helical turbine [© GCK Technology].

The Gorlov helical turbine is self-starting and can produce power from water current flow as low as 1.5 m/sec with power increasing in proportion to the water velocity cubed. Due to its axial symmetry, the GHT always rotates in the same direction, even when tidal currents reverse direction. This is a very important advantage that simplifies design and allows exploitation of the double action tidal power plants. The standard model (1 m in diameter, 2.5 m in length) can be installed either vertically or horizontally to the water current flow [38]. A single Gorlov helical turbine rated power is 1.5 kW for 1.5 m/sec water speed and 180 kW for 7.72 m/sec. Pictorial views of expected power plants with vertically or horizontally aligned turbines are shown in Fig I. 19b. A similar concept to the Gorlov helical turbine is the Achard one also known as the Harvest project in France [39]. In this turbine, blades are in a fixed position with regard to the turbine axis (Fig. I.20a). However, it does not have a squirrel cage shape like in the Gorlov concept. Blades have airplane wing shape and are attached to the turbine axis in their centre. At the blade extremities, some winglets will prevent vortices and induced drag.



(a) Achard turbine.

(b) Water turbine line.



(b) Water turbine Farm.

Fig I.20. The Achard turbine [39].

The arms between blades and axis are airfoil shaped and have a pitch angle which might be different from 0: the lift on the arm can push the turbine up or down, depending on the arm pitch angle. With this turbine concept, a farm structure is also proposed. Several units are stacked, with the same axis then forming a water turbine line (Fig. I.20b). The association of many water turbine lines forms a water turbine farm. The lines will be attached to a floating barge at one extremity and anchored to the ground at the other.

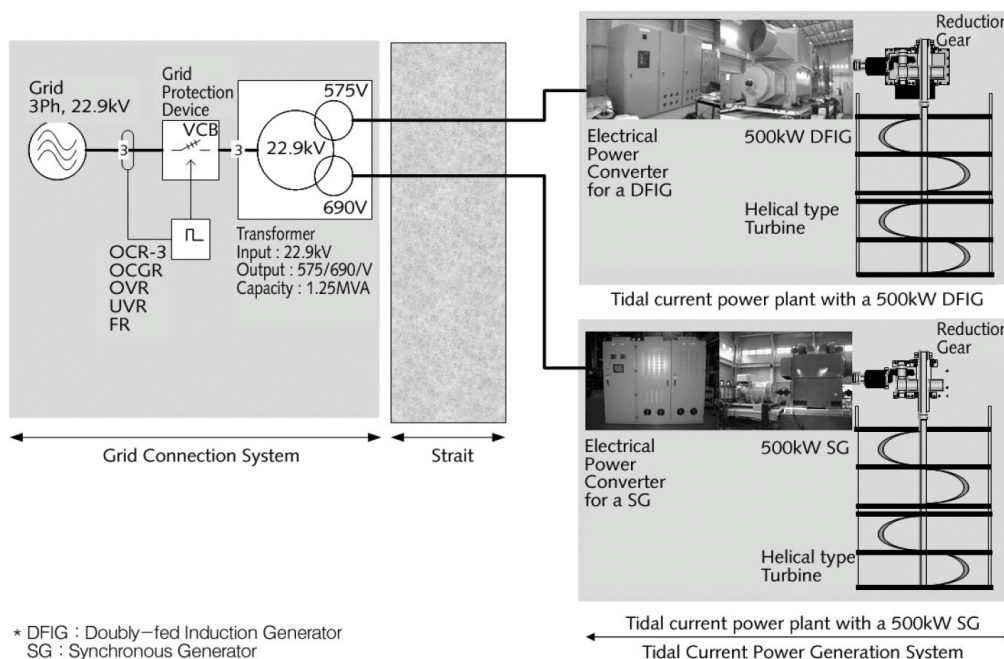
For illustration, the Uldolmok (the strait with the strongest tidal current in Korea, located at the southwestern tip of the Korean Peninsula) pilot tidal current power plant of 1MW is

shown by Fig. I.21. It uses Gorlov helical turbine and two generator topologies: a doubly-fed induction generator (500 kW) and a synchronous generator (500 kW), (Fig. I.21b) [44].

In tidal applications, maintenance is a key feature which is sometimes considered as a barrier to marine turbine development [20]. It is thus recommended to avoid gearbox systems that need regular lubrication and induce additional losses. In this context, direct driven generators are an alternative solution [45].



(a) View of the power plant.



(b) The electrical system.

Fig I.21.The Uldolmok pilot tidal current power plant of 1 MW [44].

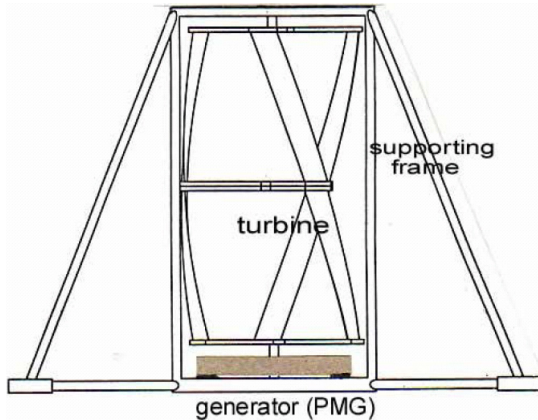


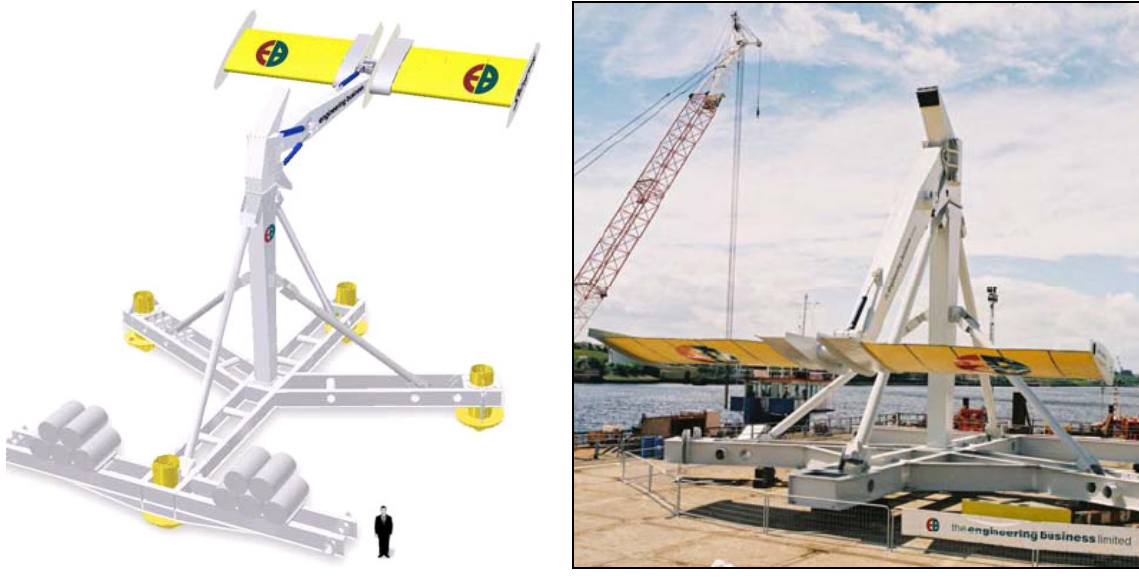
Fig. I.22. Gorlov Helical Turbine with a synchronous generator.

In spite of the similarities to wind turbines, tidal ones present some distinct features such as the blade reduced diameter and maintenance difficulties. These characteristics will push ahead some topologies that are not commonly used for wind turbines. The vertical axis turbine with a synchronous generator is one of these technologies. An advantage of this topology is that the generator can be located under or over the tidal turbine. That means that the size of the generator is not constraint by the turbine size as it is clearly shown by Fig. I.22 in the case of the Gorlov helical turbine.

5.3 Oscillating Hydrofoil

The Stingray concept, developed by Engineering Business (UK), is illustrated by Fig. I.23a. It consists of a hydroplane that has an attack angle relative to the approaching water stream varied by a simple mechanism. This causes the supporting arm to oscillate, which in turn forces hydraulic cylinders to extend and retract. This produces high-pressure oil that is used to drive a generator. The 150 kW rated demonstrator produced 250 kW at peak capacity and averaged 90 kW in a 1.5 m/sec measured current during its initial power cycles (Fig. I 23b). In 2005, this project was put on hold [27].

A quite similar and innovative project is the bioSTREAM in Australia. This system is based on the Thunniform-mode swimming propulsion of some swimming species, such shark, tuna, and mackerel (Fig. I.24). Due to the single point of rotation, this device can align with the flow in any direction, and can assume a streamlined configuration to avoid excess loading in extreme conditions. Systems are being developed for 500 W, 1 and 2 MW capacities to match conditions in various locations [40].



(a) The Stingray turbine.

(b) Deployment for submerged testing.

Fig. I.23. The Stingray tidal turbine [© EB].



(a) The basic concept.

(b) The farm concept.

Fig. I.24. The bioSTREAM concept [© BioPower].

5.4 Floating Tidal Energy System

The concept of floating tidal energy system is based on the use of a moored floating structure (e.g. a catamaran) to support the weight of a wheel/generator system (Fig. I.25). The use of a moored device allows easy access to remote coastal communities where it is often expensive to build a fixed infrastructure, and also facilitates removal to a place of refuge when extreme storm conditions occur. Such systems can also exploit shallow water sites or those with large variations in water level [41].



Fig. I.25. The University of Southampton completed tidal mill [41].

I.6 DEVELOPMENT OF TIDAL TECHNOLOGIES AND DESIGN OPTIONS

At the present time, only one kind of system is being investigated for commercial development: horizontal axis turbines evolved from wind power technology, with two prototypes installed in the coasts of Norway and England [24-25]. Tidal current turbines operate in a more determinate environment than wind turbines. However, some stochastic inputs would arise from the effect of storm surges, bringing increased current velocities and introducing dynamic loading due to surface wave action. Although this requires systematic investigation, sites will be generally close to land so that the fetch for surface wave development will be limited. Incoming turbulence will also generate fluctuating loads, although the range of excursions, particularly in the direction of flow, will be relatively small. For these reasons, research is continuing into determining the operational performance envelope of tidal stream rotors under real operating conditions. The objective is to set tools that enable precise design solutions to be tailored to specific site conditions [42].

It is impossible at this time to predict the optimal configuration of future tidal stream energy conversion devices. However, comparisons with wind energy give some useful pointers. Tidal stream devices are likely to have a cut-in stream velocity, with a period of enforced idleness at slack water. While wind turbines have a cut-out speed to avoid damage in storms, this should not be the case necessary for tidal turbines given the predictable nature of the flow regime. Shut-down procedures would only be executed in emergencies (e.g. loads caused by wave action in stormy conditions might be severe enough to trigger shut-down) [20], [42].

I.7 ELECTRIC GENERATOR TOPOLOGIES IN MARINE CURRENT TURBINES

Marine current turbines can operate with either fixed speed (small speed changes due to the generator slip) or variable speed. Variable speed is here understood as 5% to 100% variation of nominal speed. For fixed-speed turbines, the generator (induction generator) is directly connected to the grid. Since the speed is almost fixed to the grid frequency, and most certainly not controllable, it is not possible to store the turbulence of the tidal resource in form of rotational energy. Therefore, for a fixed-speed system the turbulence of the tidal resource will result in power variations, thus affect the power quality of the grid [50]. This is why the fixed-speed system is not proposed for marine tidal current turbine application. For a variable speed, the generator is controlled by power electronic equipment, which makes it possible to control the rotor speed. In this way the power fluctuations caused by marine current variations can be more or less absorbed by changing the rotor speed [51]. Hence, the power quality impact caused by the marine tidal current turbine can be improved compared to a fixed-speed turbine [52].

Furthermore, one should distinguish two topology categories: the direct and the indirect driven technology. In this section the following marine current turbine concepts will be briefly presented:

1. Full range variable speed system (with gear).
2. Full range variable speed system (without gear).
3. Limited range variable speed system.

There are also some other concepts, which could be considered but they tend to increase the complexity and therefore the tidal turbine cost [53].

7.1 Full Range Variable Speed System (with Gear)

The system presented in Fig I.26. consists of a marine current turbine equipped with an inverter connected to the stator of the generator. The generator could either be a singly-fed induction generator or a synchronous generator. The used inverter has to have active switches in both the grid and the generator side converters, which allow the converter, at the generator side, to supply reactive power, while active power is flowing from the generator.

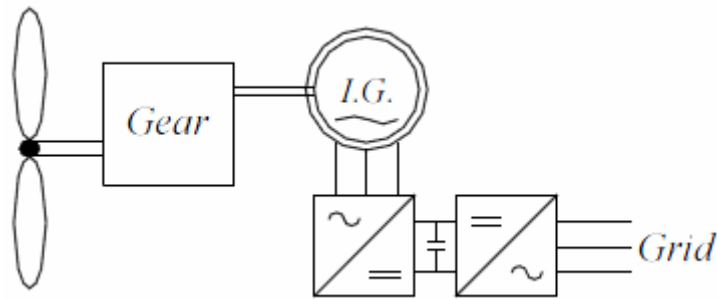


Fig. I.26. Full range variable speed system

The gearbox is designed so that the maximum rotor speed corresponds to the generator rated speed. Since this full-power converter system is commonly used for other applications, one advantage with this system is its well-developed and robust control [54-56]. However, the disadvantage for the full speed range system is that all the power has to be converted in the inverter.

7.2 Full Range Variable Speed System (without Gear)

The generator used here is a multipole synchronous one, either with an excitation system or with permanent magnets. The lack of gear box losses compensates partly the large losses in the full power converters (Fig.I.27).

7.3 Limited Variable Speed System

This system consists of a marine current turbine with a variable speed constant frequency induction generator (Fig I.28). It is also known as the doubly fed induction generator system. This means that the stator is directly connected to the grid while the rotor winding is connected via slip rings to an inverter.

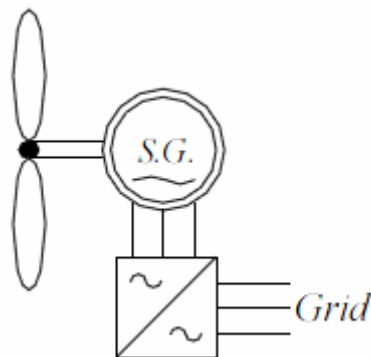


Fig I.27. Variable speed direct-driven system.

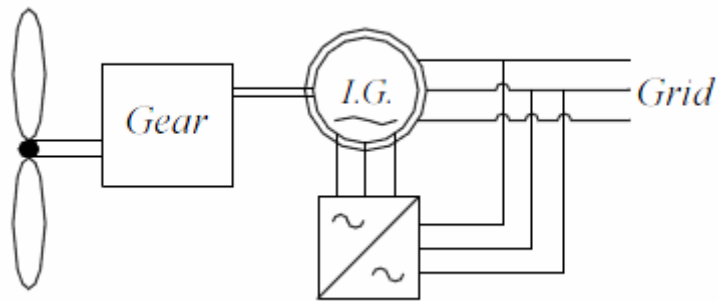


Fig I.28. Variable speed with doubly fed induction generator.

The inverter is designed so that the induction generator can operate in a limited variable speed range. The gearbox ratio is set so that the nominal speed of the induction generator corresponds to the middle value of the rotor-speed range of the marine current turbine. This is done in order to minimize the size of the inverter which will vary with the rotor-speed range. With this inverter it is possible to control the speed (or the torque) and also the reactive power on the stator side of the induction generator.

I.8 CONCLUSION

This chapter has reviewed state of the art of marine tidal turbines. The emphasis has been put on tidal turbine concepts. Indeed, the strength and the weakness of the major tidal turbine technologies have been described. Finally, generator topologies have been presented regarding similarities to wind turbine technology. Finally, attempts have been made to highlight current trends and alternative issues.

It has been shown that technologies for the exploitation of marine tidal currents are still in their infancy stage. It is then obvious that there is a need to quantify the potential to generating electricity from various sites and to compare the different proposed concepts. Next chapter reports then on the development of a practical Matlab/Simulink® simulation tool based on the modeling of the resource, the tidal turbine rotor and the generator.



Chapter
II

Marine Current Turbine Modeling

II.1	INTRODUCTION	33
II.2	MODELING REQUIREMENTS	33
II.3	HYDRODYNAMIC MODEL.....	34
3.1	RESOURCE MODELING.....	34
3.2	THE ROTOR MODELING	42
II.4	MECHANICAL MODEL	55
II.5	POWER CONVERTER.....	57
II.6	TRANSFORMER.....	57
II.7	GENERATOR MODEL.....	57
7.1	DOUBLY FED INDUCTION GENERATOR (DFIG)	57
7.2	PERMANENT MAGNET SYNCHRONOUS GENERATOR (PMSG).....	61
II.8	CONCLUSION	63

NOMENCLATURE

ρ	=	Fluid density;
A	=	Cross-sectional area of the marine turbine;
V_{tide}	=	Fluid speed;
C_p	=	Power coefficient;
C	=	Tide coefficient;
$V_{st} (V_{nt})$	=	Spring (neap) tide current speed;
λ	=	Tip speed ratio;
$s, (r)$	=	Stator (rotor) index (superscripts);
d, q	=	Synchronous reference frame index;
$V(I)$	=	Voltage (Current);
$P(Q)$	=	Active (Reactive) power;
ϕ	=	Flux;
ϕ_m	=	Permanent magnet flux;
$T_{em} (T_m)$	=	Electromagnetic torque (Mechanical torque);
R	=	Resistance;
$L(M)$	=	Inductance (Mutual inductance);
σ	=	Total leakage coefficient, $\sigma = 1 - M^2/L_s L_r$;
θ_r	=	Rotor position;
$\omega (\omega_s)$	=	Rotor electrical speed (electrical synchronous speed);
ω_r	=	Rotor current frequency ($\omega_r = \omega_s - \omega$);
Ω	=	Mechanical speed ($\Omega = \omega/p$);
f	=	Viscosity coefficient;
J	=	Rotor Inertia;
p	=	Pole pair number;
L_{ss}	=	Stator inductance;
M_s	=	Stator mutual magnetizing inductance;
M_{jr}	=	Rotor mutual magnetizing inductance in phase $j, j = a, b$ or c ;
λ_j	=	PMSG rotor flux in phase $j, j = a, b$ or c .

GLOSSARY

MCT	=	Marine Current Turbine;
DFIG	=	Doubly-Fed Induction Generator;
PMSG	=	Permanent Magnet Synchronous Generator;
SHOM	=	French Navy Hydrographic and Oceanographic Service;
BEM	=	Blade Element Momentum;
VSI	=	Voltage Source Inverter;
PWM	=	Pulse Width Modulation.

II.1 INTRODUCTION

This Chapter deals with the development of a Matlab/Simulink® model of a tidal marine current energy harnessing global system through the modeling of the resource, the rotor and the generator. As the developed simulation model is intended to be used as a sizing and site evaluation tool for current turbine installations, it has been applied to evaluate the extractable power from the Raz de Sein (Brittany, France) as an example. A first-order model of the tidal current resource has been developed including perturbations related to the swell effect and turbulences. An algorithm based on the Blade Element Momentum approach is used to establish a hydrodynamic turbine model from the blade geometry description. Moreover, a theoretical model of a Doubly-Fed Induction Generator and a Permanent Magnetic Synchronous generator model are proposed in order to compare different marine current turbine topologies.

II.2 MODELING REQUIREMENTS

Marine Current Turbine dynamic performance analysis requires the use of computational models representing the nonlinear differential-algebraic equations of the various system components (Fig. II.1). However, the main difficulty is to include a variety of sub-models with different timescale for hydrodynamic loads (turbine, mechanical systems, generators, power electronics and other components). The user is therefore concerned with selecting the appropriate models for the problem at hand and determining the data to represent the specific MCT equipment.

Appropriate models choice depends mainly on the timescale of the problem being analyzed. Figure II.2 shows the principal MCT dynamic performance areas displayed on a logarithmic timescale ranging from microseconds to days. The lower end of the band for a particular item indicates the smallest time constants that need to be included for adequate modeling.

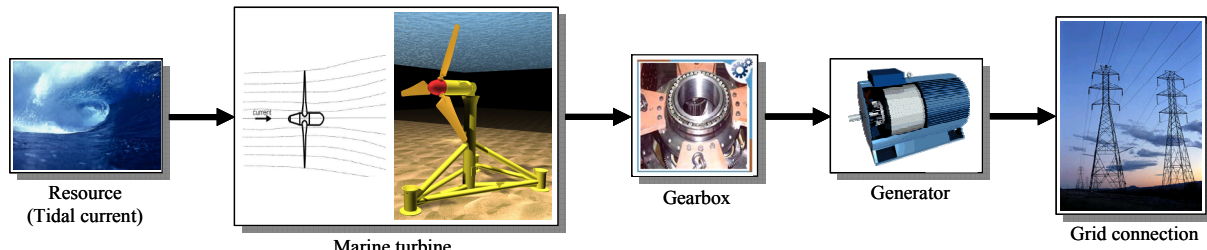


Fig. II.1. Marine current turbine global scheme.

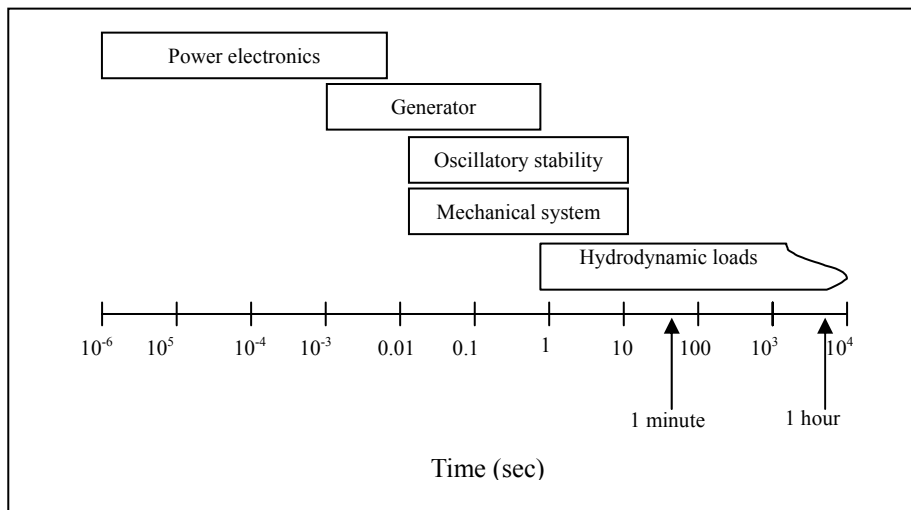


Fig. II.2. Timescale in a Marine current turbine.

The upper end indicates the approximate length of time that must be analyzed. It is possible to build an MCT simulation model that includes all dynamic effects from very fast ones to very slow hydrodynamic loads. However, for efficiency and ease of analysis, normal engineering practice dictates that only models incorporating dynamic effects relevant to the particular performance of the concerned area to be used.

Matlab/Simulink[®], a general-purpose software package for dynamic systems, has been selected to carry out the modeling task for many reasons. Indeed, Simulink is a platform for multi-domain simulation and model-based design for dynamic systems. It provides an interactive graphical environment and a customizable set of block libraries, and it can be extended for specialized application. Accordingly, this makes it the best candidate for accomplishing the objective of fostering interdisciplinary integration (hydrodynamics and electromechanics). Simulink, being integrated with Matlab, provides immediate access to an extensive range of tools for algorithm development, data visualization, data analysis and access, and numerical computation. Moreover, Matlab/Simulink[®] allows automatically generating code for direct implementation and experimental tests.

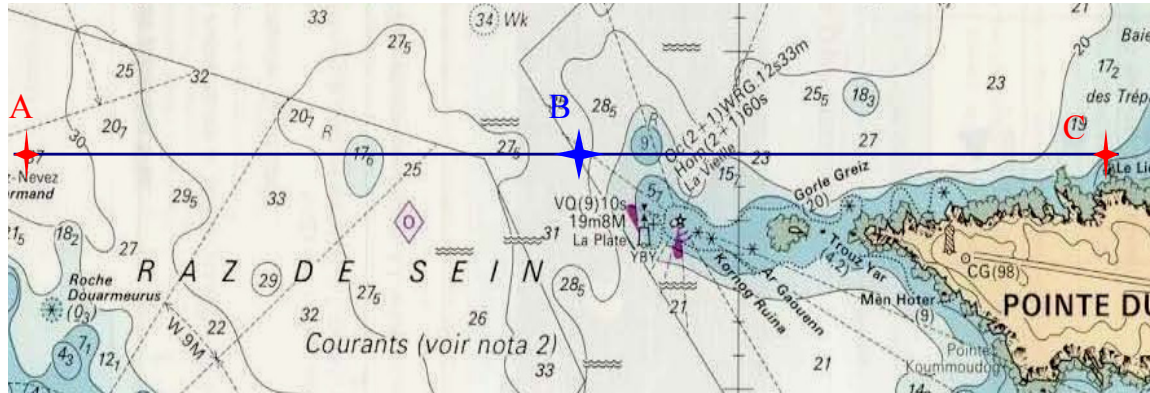
II.3 HYDRODYNAMIC MODEL

3.1 Resource Modeling

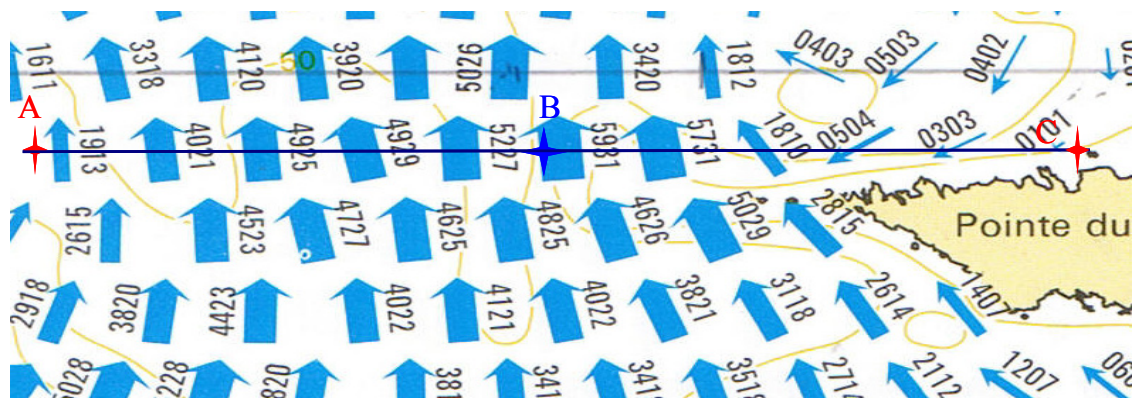
The proposed simulation tool has been applied to assess the extractable power from the Raz de Sein (Brittany, France) as it is one of the more characterized sites in terms of tidal current. The modeling approach can be extended to any other sites.

3.1.1 The Test Case Site

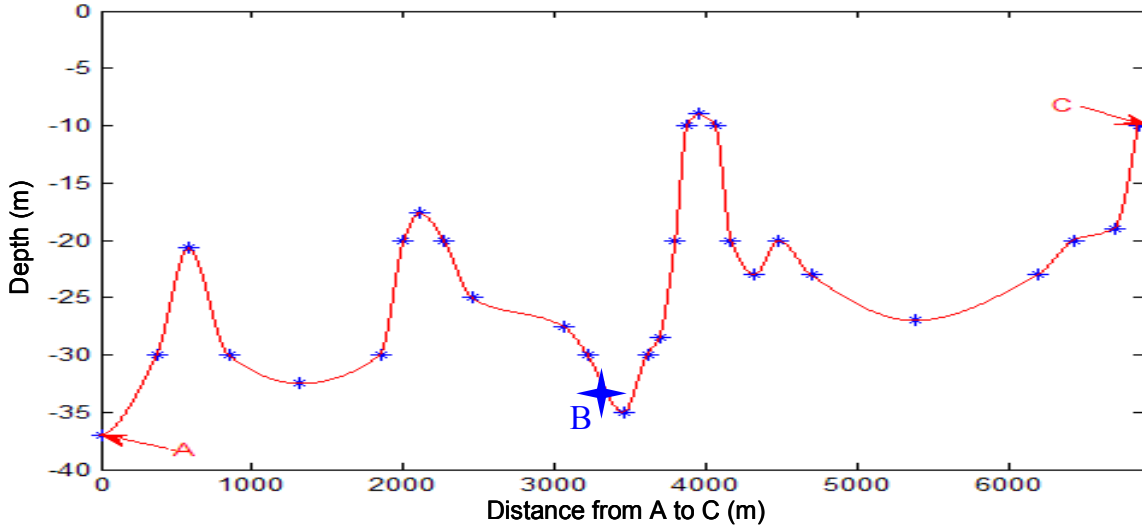
The Raz de Sein site was chosen above several others listed in the European Commission report EUR16683 due to the presence of high velocity current coupled with appropriate depths suitable for marine turbine [57]. Moreover, the marine current velocity distribution for most of the time is greater than the minimum, estimated to be 1 m/sec, required for economic deployment of marine turbines [57-58]. The studied area is shown by Fig. II.3.a, where A and C are the area ends and B the expected installation site for the marine current turbine. Indeed, this site is located in an alternating current area (Fig. II.3.b) where the depth is about 35 m (Fig. II.3.c) which will allow the installation of a marine current turbine with blades of about 20 m diameter (the maximal swell amplitude is about 10 m in this area).



(a)



(b) Direction and tidal current velocity 4 hours before high water.



(c) Depth profile of the site.

Fig. II.3. The marine current turbine expected site of installation.

It should be noted that tidal current data are provided by the SHOM (French Navy Hydrographic and Oceanographic Service) and it is available for various locations in chart form [23].

3.1.2 The Resource Modeling Under Matlab/Simulink®

Considering all the above site data, the resource has been modeled at site B which has the following GPS (WGS84) coordinates.

$$\begin{cases} \varphi_B = 48^\circ 02' 42'' N \\ G_B = 004^\circ 45' 45'' W \end{cases}$$

The SHOM available charts give, for a specific site, the current velocities for spring and neap tides. These values are given at hourly intervals starting at 6 hours before high waters and ending 6 hours after. Therefore, knowing tide coefficients, it is easy to derive a simple and practical model for tidal current velocities V_{tide} .

$$V_{tide} = V_{nt} + \frac{(C-45)(V_{st} - V_{nt})}{95-45} \quad (\text{II.1})$$

Where C is the tide coefficient which characterize each tidal cycle (95 and 45 are respectively the spring and neap tide medium coefficient). This coefficient is determined by astronomic

calculation of earth and moon positions. V_{st} and V_{nt} are respectively the spring and neap tide current velocities for hourly intervals starting at 6 hours before high waters and ending 6 hours after. For example, 3 hours after the high tide in Brest, $V_{st}= 1.8$ knots and $V_{nt}=0.9$ knots. Therefore, for a tide coefficient $C=80$, $V_{tide}=1.53$ knots. This first-order model is then used to calculate the tidal velocity each hour. The implemented model will allow the user to compute tidal velocities in a predefined time range. Figure II.4 shows the model output for a month (March 2007) and for a year (2007). It should be noticed that the current velocity peak values will be taken into account in the choice of the marine turbine.

The first-order model which has been adopted for the resource has several advantages including its modularity not to mention its simplicity. Indeed, the marine turbine site can be changed, the useful current velocity can be adapted, and the time range taken into account can also be adapted from one month to one year.

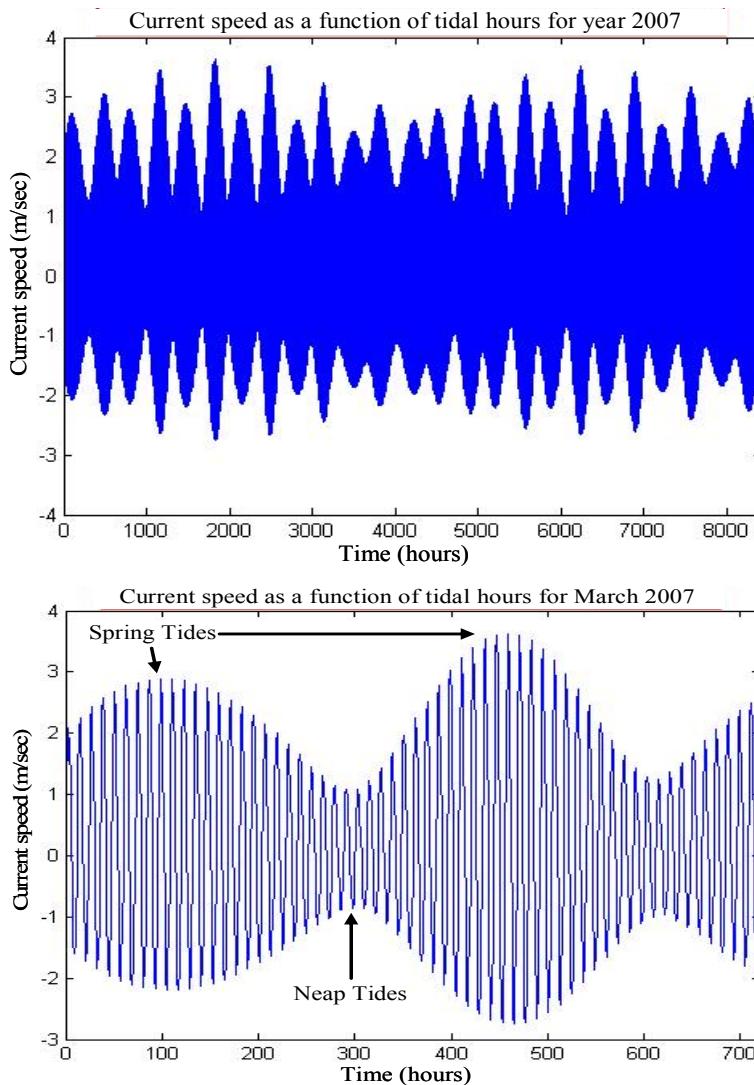


Fig. II.4. Tidal velocity in the Raz de Sein for the year 2007 and March 2007.

3.1.3 Disturbed Resource

In simulations, we consider several waveform cases for the tidal speed (V_{real}) with and without disturbances. To take into account the swell effect, which is considered as the most disturbing one for our resource model, a Stokes model have been used. This model is a very classical first-order model used to predict the swell influence in the sea water column.

For a given swell amplitude H , a period T , a swell length L and ground sea depth d as shown in Fig. II.5, the speed potential Φ can be calculated for each depth z . The water speed created by the swell effect can be deduced by a spatial derivation of this potential [58].

$$\begin{cases} V_{tides} = \text{grad}\phi \\ \phi = -\frac{HL}{2T} \frac{\text{ch}2\Pi\left(\frac{z+d}{L}\right)}{\text{sh}2\Pi\left(\frac{d}{L}\right)} \sin 2\Pi\left(\frac{t}{T} - \frac{x}{L}\right) \end{cases} \quad (\text{II.2})$$

This speed disturbance, calculated for typical intense swell specifications, can be added to the predicted tidal current speed to estimate how the swell can disturb the tidal current values in the turbine disk. It is also possible to add a white noise $b(t)$ to the tidal current value which allows taking into account other turbulence phenomena.

This first-order model does not take into account the coupled interaction between the tidal current and the swell which is indeed a very complex phenomenon. In this model the two phenomenon influence are considered as independent. Moreover, (II.2) shows that the tidal current speed varies according to the sea depth. However, during simulation, the tidal current speed was supposed constant on the turbine surface.

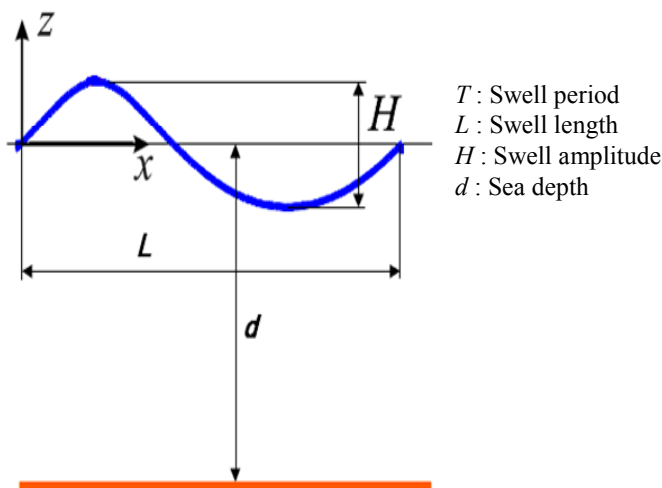


Fig. II.5. Swell characteristics.

3.1.4 Tidal Energy and Specific Marine Current Turbine Performance Calculations

Having presented the equations for power (I.1) and described the essential components of a marine current turbine system, it is time to put the two together to determine how much energy might be expected from an MCT in various tidal regimes, the cubic relationship between fluid kinetic power and tidal velocity shows that the average power in the marine current turbine can not be determined by simply substituting average tidal speed into (II.3). To explore the tidal current nonlinear characteristic, (II.3) is written in terms of average values:

$$P_{avg} = \left(\frac{1}{2} \rho A v^3 \right)_{avg} = \frac{1}{2} \rho A (v_{tide}^3)_{avg} \quad (\text{II.3})$$

In other words, we need to find the average value of the cubed velocity. Indeed, the average tidal speed can be seen as the total marine current that goes through the site, divided by the total time that it took to do so [59].

$$(v_{tide})_{avg} = \frac{\sum_i [v_i (\text{hours @ } v_i)]}{\sum \text{hours}} = \sum_i [v_i (\text{Fraction of hours @ } v_i)] \quad (\text{II.4})$$

Equation (II.3) shows that the quantity of interest in determining the marine resource average power is not the V_{tide} average value, but the V_{tide}^3 average value. The averaging process is the same as in (II.5), yielding the following

$$(v_{tide}^3)_{avg} = \frac{\sum_i [v_i^3 (\text{hours @ } v_i)]}{\sum \text{hours}} = \sum_i [v_i^3 (\text{Fraction of hours @ } v_i)] \quad (\text{II.5})$$

From Raz de Sein site tidal histogram of Fig. II.6, the average kinetic power is deduced by

$$P_{avg} = \frac{1}{2} \rho (v^3)_{avg} = 0.5 \times 1027.68 \times (1.63)^3 = 604.7239 \text{ W/m}^2 \quad (\text{II.6})$$

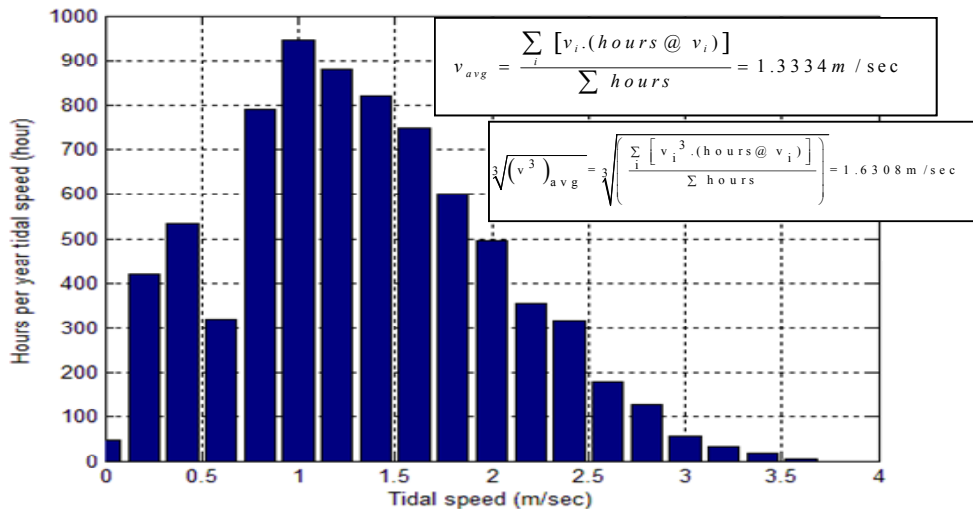


Fig. II.6. Raz de Sein site tidal histogram.

It can be noticed that this power is the average total kinetic power in a unitary cross sectional area. It does not include the power coefficient of the turbine which is usually around 0.4.

The obtained average power will help us to determine the rotor diameter and the generator rated power. Indeed, the most important technical information for a specific marine current turbine specification is the power curve, which shows the relationship between the tidal speed and the generator electrical output. A somewhat idealized power curve is shown in Fig.II.7 where:

Cut-in tidal speed. Low-speed tidal may not have enough power to overcome friction in the turbine drive train and, even if it does and the generator is rotating, the generated electrical power generated may not be enough to offset the power required by the generator field windings. The cut-in tidal speed V_C is the minimum needed to generate net power. Since no power is generated at tidal speeds below V_C , that portion of tidal energy is wasted.

Rated tidal speed. As velocity increases above the cut-in tidal speed, the power delivered by the generator tends to increase proportionally to the cubed tidal speed. When marine current speed reach the rated tidal speed V_R , the generator is delivering as much power as it is designed for. Above V_R , there must be some way to shed some of the tidal power otherwise the generator may be damaged. Three approaches are common on large machines to limit the power on the turbine: an active pitch-control system, a passive stall-control design, and a combination of the two.

Cut-out or Furling tidal speed. At some point the marine current speed is so strong that there is real danger for the MCT. At this tidal speed V_F , called the cut-out tidal speed or the furling one, the machine must be shut down. Above V_F , output power obviously is zero.

The idealized power curve of Fig. II.7 provides a convenient framework to consider the trade-offs between rotor diameter and electrical system size as ways to increase the energy delivered by an MCT.

As shown in Fig. II.8.a, increasing the rotor diameter, while keeping the same electrical power, shifts the power curve upward so that rated power is reached at a lower tidal speed. This strategy increases output power for lower-speed marine current. However, keeping the same rotor and increasing the generator size allows the power curve to continue upward to the new rated power (Fig. II.8.b). For lower-speed tidal, there is not much change but in an area with higher marine current speeds, increasing the generator rated power is a good strategy.

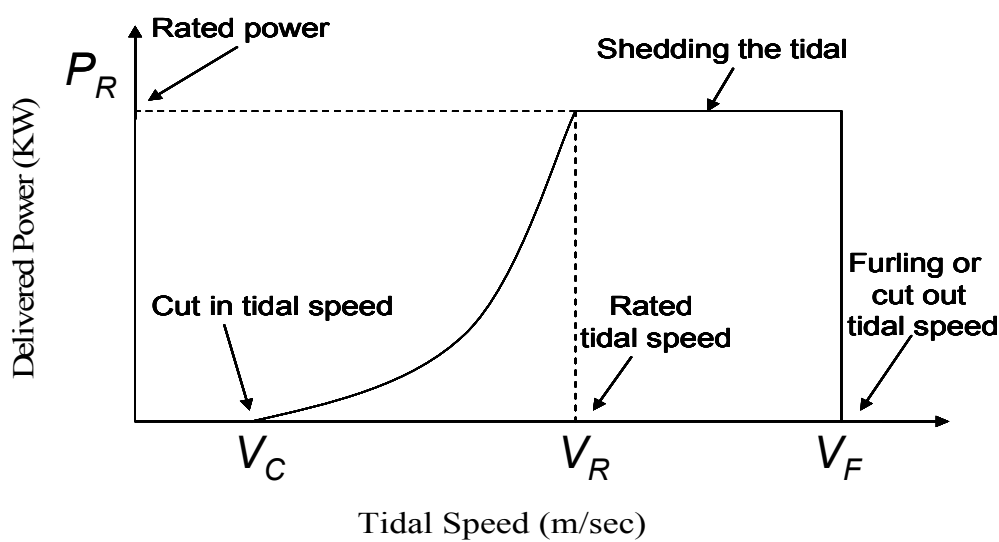


Fig. II.7. Idealized power curve.

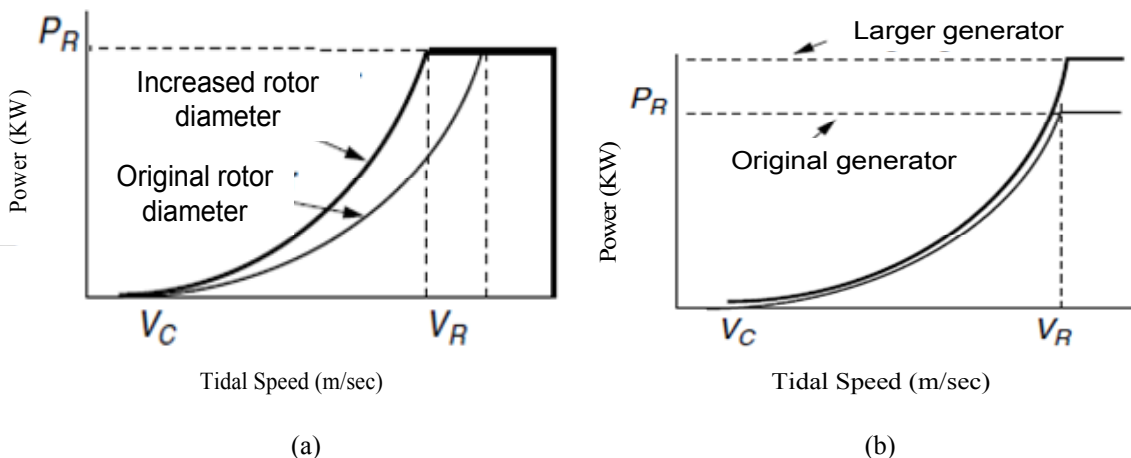


Fig. II.8. (a) Increasing rotor diameter reduces the rated tidal speed, emphasizing lower speed tidal. (b) Increasing the generator size increases rated power, emphasizing higher tidal speeds.

3.2 The Rotor Modeling

The power production from tidal flow requires the kinetic energy conversion to electrical power. To handle this problem, several technologies have been proposed. Most of them have been successfully utilized to harness wind energy [60]. Thus, many systems are based upon the use of horizontal axis turbines [61]. Therefore, many techniques can be transferred from the design and operation of wind turbines [62]. There are, however, a number of fundamental differences in the design and operation of marine turbines. Particular differences entail changes in force loadings, immersion depth, different stall characteristics, and the possible occurrence of cavitations phenomena in the blades. Much information is however available on the cavitations and stall characteristics of marine propellers [63], which can provide useful information for marine turbines [64-65].

3.2.1 Marine Turbine Hydrodynamics

The hydrodynamic design parameters basically entail the choice of diameter, pitch and speed for a particular application. Further design criteria include the pitch or twist distribution across the blade span, the stall characteristics, the blade section choice, and the need to preclude the cavitations occurrence. The hydrodynamic design is further complicated by changes in the non uniform speed and the current direction, the shear profile in the tidal flow, and the influences of water depth and the free surface [65].

Bearing in mind that the simulation model has two purposes: performance and dynamic load assessment in different operating conditions, and further control system development for turbine operation based on pitch and speed control. It is therefore necessary to find a compromise between the simulation model accuracy and the control loop computational speed. Moreover, modeling the turbine rotor is done in two steps: *firstly* performance curve assessments are calculated for the turbine geometry. These performance curves are integrated in a second step into a dynamic simulation environment.

Wind turbine rotor aerodynamics refers to the interaction of the wind turbine rotor with the incoming wind. The treatment of rotor aerodynamics in all current design codes is based on Glauert well-known, and well established Blade Element Momentum (BEM) theory [66].

This theory is an extension of the Rankine-Froude actuator disk model which aims to overcome the unsatisfactory accuracy performance predictions based on this model.

The BEM method has, therefore, been used for the marine turbine rotor modeling. Indeed, it is widely used in the industry as a computational tool to predict aerodynamic loads and the

power of turbine rotors. It is relatively simple and computationally fast meeting the above-mentioned requirements of the simulation model [67].

3.2.2 The Rankine-Froude Actuator Disk Model

In this model the rotor is replaced by an *actuator disk*, which is a circular surface of zero thickness that can support a pressure difference, and thus decelerate the tidal current through the disk. Physically, the disk could be approximated by a rotor with an infinite number of very thin, dragless blades rotating with a tip speed much higher than the tidal current velocity. The actuator disk model is thus an approximation of a real marine turbine rotor (which has only a small number of blades). As a result the flow of the actuator disk will be very different from that of a real rotor, which is unsteady, with a wake of discrete vorticity corresponding to the discrete loading[62], [68].

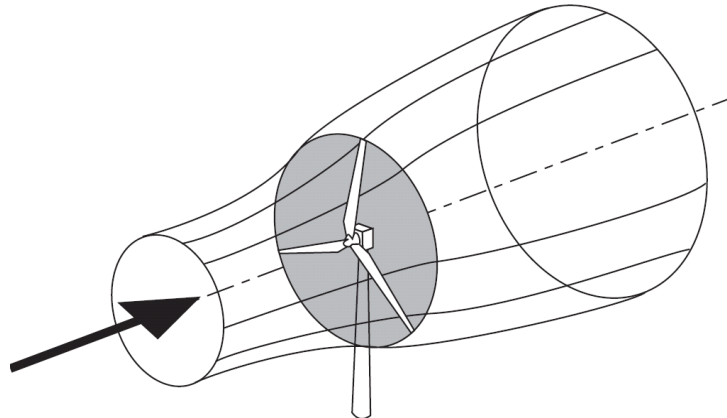
The principal use of the actuator-disk model is to obtain a first estimate of the wake-induced flow, and hence the total induced power loss. Note that the actual induced power loss will be larger than the actuator-disk result because of the non-uniform and unsteady induced velocity. The assumptions on which the Rankine-Froude actuator disk theory is based are well-detailed in [62]. Among these assumptions, one requires that the disk slows the tidal current equally at each radius, which is equivalent to assume uniform thrust loading at the disk. Uniform thrust loading is, in turn, equivalent to consider an infinite number of rotor blades.

Figure II.9 illustrates the one-dimensional flow through the actuator-disk plane for a non-loaded and loaded machine. For instance, for a turbine with zero loading, the current velocity in the rotor plane (V_r) is equal to the undisturbed tidal current velocity (V_{tide}), while an operating and hence loaded turbine slows down the current velocity to a lower value. If the decreased velocity induced by the rotor is V , then the velocity at the disk is $V_{tide} - V = V_r$, while far downstream at section 1 the current has been slowed further to velocity V_∞ . The difference between the axial component of the current velocity and the axial flow velocity in the rotor plane is usually called the *induced velocity*.

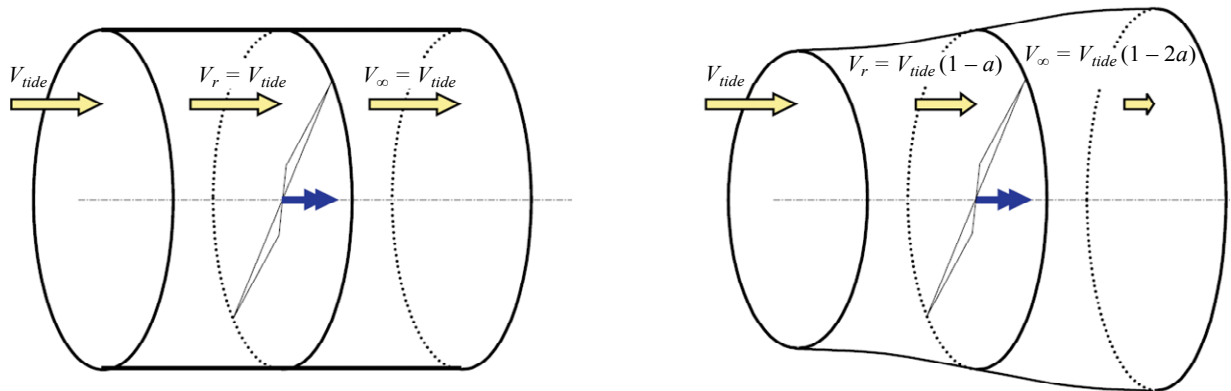
Thus, the velocity at the disk is the average of the upstream and downstream velocities.

Defining an axial induction factor, a , as the fractional decrease in current velocity between the free stream and the rotor plane represented by

$$a = \frac{V}{V_{tide}} \quad (\text{II.7})$$



(a) Energy extracting stream tube of a wind/marine turbine.



(b) Marine turbine with (right) and without (left) loading.

Fig. II.9. The actuator disk model.

It follows that $\begin{cases} V_r = V_{tide}(1-a) \\ V_\infty = V_{tide}(1-2a) \end{cases}$ (II.8)

For $a = 0$, the current is not decelerated and no power is extracted, whereas for $a = 0.5$, the far wake velocity vanishes, and, without presence of flow behind the turbine, no power is generated (Fig. II.10). The power extracted from the tidal current by the rotor is given by

$$P = \frac{1}{2} \rho A V_r (V - V_\infty)(V + V_\infty) \quad (\text{II.9})$$

Substituting V_r and V_∞ from (II.8), we find that

$$P = \frac{1}{2} \rho A V_{tide}^3 4a(1-a)^2 \quad (\text{II.10})$$

A power coefficient C_p is then defined as

$$C_p = \frac{P}{\frac{1}{2} \rho A V_{tide}^3} = 4a(1-a)^2 \quad (\text{II.11})$$

where the denominator represents the global kinetic energy of the free-stream current contained in a stream tube with an area equal to the disk area. The extracted power is expressed by

$$P = \frac{1}{2} \rho C_p A V_{tide}^3 \quad (\text{II.12})$$

The maximum value of the power coefficient C_p occurs when $a = 1/3$. Hence, $C_{p,\max} = 16/27 \approx 0.59259$, $V_r = \frac{2}{3}V_{tide}$, and $V_\infty = \frac{1}{3}V$. Thus the maximum amount of energy extraction equals the 16/27th part of the kinetic energy in the current. This limit is often referred to as the *Betz limit*, or more accurately the *Lanchester-Betz limit*. The power coefficient C_p versus the induction factor a is shown in Fig. II.10.

Additional data that can be derived from this model include the thrust loading on the rotor.

$$D_r = \frac{1}{2} \rho A (V_{tide}^2 - V_\infty^2) = \frac{1}{2} \rho A V_{tide}^2 [4a(1-a)] \quad (\text{II.13})$$

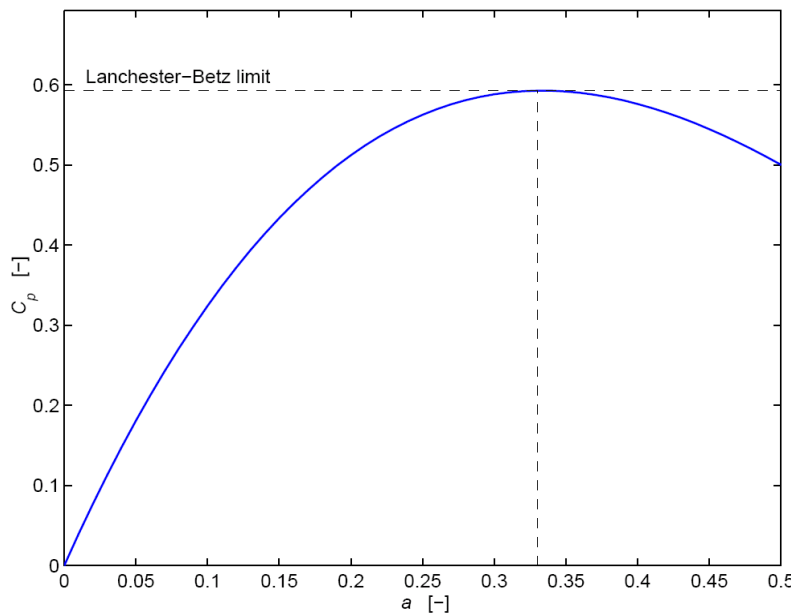


Fig. II.10. Power coefficient C_p as function of the axial induction factor a [68].

Moreover, if this thrust loading is considered as a drag force on the rotor, we can define a drag coefficient as follows.

$$C_{dr} = \frac{D_r}{\frac{1}{2} \rho A V_{tide}^2} = 4a(1-a) \quad (\text{II.14})$$

Since a flat plate has a drag coefficient of about 1.28, we can note that, for $a = 1/3$, we obtain an equivalent drag coefficient of 8/9 for a rotor operating at the maximum C_p condition. Thus the rotor thrust is about 30% less than that of a flat plate equal in diameter to the rotor. Therefore, it is easy to see that the thrust loads generated by continuing operation in high currents can be very large, requiring a very strong rotor and pile.

3.2.3 The BEM Model

BEM theory is one of the oldest and most commonly used methods for calculating induced velocities on wind turbine blades. This theory is an extension of the above studied actuator disk theory. BEM theory assumes that blades can be divided into small elements that act independently of surrounding elements and operate hydrodynamically as two-dimensional airfoils whose hydrodynamic forces can be calculated based on the local flow conditions. These elemental forces are summed along the span of the blade to calculate the total forces and moments exerted on the turbine. The other half of BEM, the momentum theory, assumes that the loss of pressure or momentum in the rotor plane is caused by the work done by the fluid flow passing through the rotor plane on the blade elements. Using the momentum theory, one can calculate the induced velocities from the momentum lost in the flow in the axial and tangential directions. These induced velocities affect the inflow in the rotor plane, and therefore affect also the forces calculated by blade element theory. This coupling of two theories ties together blade element momentum theory and sets up an iterative process to determine the hydrodynamic forces, and also the induced velocities near the rotor.

In practice, BEM theory is implemented by dividing the blades of a marine turbine into many small elements along the span. As these elements rotate in the rotor plane, they trace out annular regions, shown in Fig. II.11, across which the momentum balance takes place.

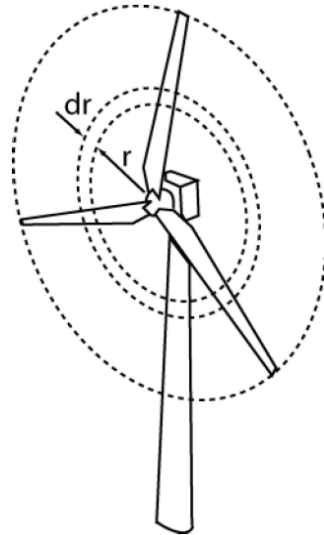


Fig. II.11. Annular plane used in BEM theory.

These annular regions are also the areas where the induced velocities from the wake change the local flow velocity at the rotor plane. BEM can also be used to analyze stream tubes through the rotor disk, which can be smaller than the annular regions and provide more computational fidelity [67], [69].

The contribution of each blade element to the lift and drag force can be derived as follows. Consider an annular cross-section of a rotor blade as depicted in Fig.II.11, and examine an element of length Δr of one blade. The net effect on current flowing through this annular section of the rotor disk results from the forces and moments on all the blades. The instantaneous relative undisturbed flow velocity experienced by a blade element is

$$W = \sqrt{[V_p(1-a)]^2 + [V_t(1+b)]^2} \quad (\text{II.15})$$

$$\text{under an angle } \phi = \arctan\left(\frac{V_p(1-a)}{V_t(1+b)}\right) \quad (\text{II.16})$$

It must be noted that the tangential induction factor b in the above equation is as a rule smaller than the axial induction factor a [26].

Due to the resultant velocity, the blade cross-section exerts a quasi-steady hydrodynamic lift force.

$$\Delta L = \frac{1}{2} \rho c W^2 C_L \Delta r \quad (\text{II.17})$$

and a quasi-steady hydrodynamic drag force

$$\Delta D = \frac{1}{2} \rho c W^2 C_D \Delta r \quad (\text{II.18})$$

where c is the local blade chord, C_L is the blade element 2D lift coefficient, C_D is the blade element 2D drag coefficient, and Δr is the blade section length. The dimensionless hydrodynamic coefficients C_L and C_D – among other things – are functions of the attack angle α and the Reynolds number.

The axial-induced velocity can be determined by expressing the axial thrust ΔF on a blade element as the rate of change of momentum in the annular ring swept out by this element, on one hand. On the other, the tangential induced velocity can be determined by expressing the torque ΔQ on a blade element as the rate of change of angular momentum.

$$\begin{cases} \Delta F = 4\pi r V_p^2 a (1-a) \Delta r \\ \Delta Q = 4\pi r^2 V_t V_p b (1-a) \Delta r \end{cases} \quad (\text{II.19})$$

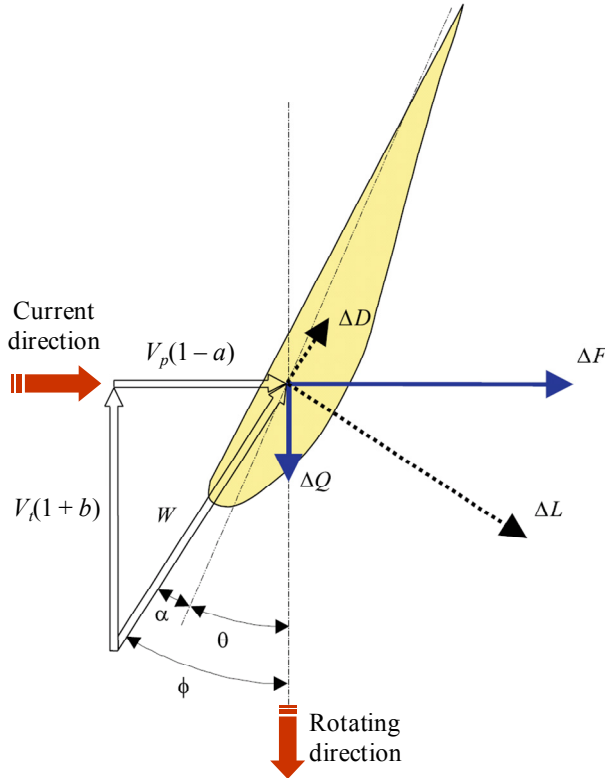
The above equations will lead to the calculation of both axial and tangential coefficients.

$$\begin{cases} a = \frac{\sigma_r C_N}{4 \sin^2 \phi + \sigma_r C_N} \\ b = \frac{\sigma_r C_T}{4 \sin \phi \cos \phi - \sigma_r C_T} \end{cases} \quad (\text{II.20})$$

$$\text{With } \begin{cases} C_N = C_L \cos \phi + C_D \sin \phi \\ C_T = C_L \sin \phi - C_D \cos \phi \end{cases} \quad \text{and} \quad \sigma_r = \frac{N_b c}{2\pi r}$$

Where N_b is the blade number and σ_r is the chord solidity.

Because of its simplicity, the BEM theory does have its limitations. To overcome the restricting assumptions of the above briefly described BEM method, in state of the art aeroelastic codes for wind turbines, a number of semi-empirical corrections are applied [67]. An overview of BEM based rotor aerodynamics in comparison to other computational methods can be found in [70].



- ΔL = Blade element lift force.
- ΔD = Blade element drag force.
- ΔF = Hydrodynamic forces axial components.
- ΔQ = Hydrodynamic forces tangential components.
- Ω = Turbine rotation speed.
- V_p = Local, undisturbed, perpendicular current velocity.
- V_t = Local, undisturbed, tangential current velocity.
- W = Local, undisturbed, current velocity.
- a = Axial induction factor.
- b = Tangential induction factor (swirl velocity).
- α = W angle of attack.
- θ = Rotor blade pitch angle.
- ϕ = W direction related to the rotor plane.

Fig. II.12. Blade element velocities and hydrodynamic forces in the blade local coordinate frame with the chord line as reference.

Two corrections have been adopted for the proposed simulation model. The first one takes into account the so-called blade tip and root effects. In this case, (II.19) becomes

$$\begin{cases} a = \frac{\sigma_r C_N}{4F_L \sin^2 \phi + \sigma_r C_N} \\ b = \frac{\sigma_r C_T}{4F_L \sin \phi \cos \phi - \sigma_r C_T} \end{cases} \quad (\text{II.21})$$

where F_L is Prandtl combined blade tip and blade root loss factor.

The second correction concerns the *turbulent wake state*. In this case, we have adopted the Glauert empirical relation [35].

$$a = 0.143 + \sqrt{0.6427C_{dr} - 0.55106} \quad (\text{II.22})$$

for $C_{dr} > 0.96$.

3.2.4 Rotor Design Options

The choice of 3 blades was made after considering both 2 and 3 blade options (Fig.II.13). Rotors with 3 blades have the advantage of being slightly more efficient, and they are also more balanced, inducing less loads on the gearbox and the structure. The orientation of the rotor is fixed, but the blades can be pitched through 180° so that it can be used for currents in both directions, either on the ebb or the flood tide. The turbine rotor can be changed from operating on a flood tide to an ebb tide simply by reversing the blades, pitching them through 180° (Fig. II.14). The ability to pitch also meant that the blade angle could be optimized in any given current, the blades could be feathered to stop the rotor smoothly, and the maximum power generated could be limited by angling the blades away from the optimum position. It was therefore decided to implement full-length blade pitch control.

Some suitable sections data are applicable from wind turbines [36] and recent cavitation tunnel tests [37]. For the numerical predictions of section performance used for the simulation model, the 2D panel code XFOIL was used. Indeed, XFOIL is a linear vorticity stream function panel method with viscous boundary layer and wake model [38].

Section shape is governed by hydrodynamic performance and structural design. In order to operate over a wide range of conditions, as with a wind turbine, a wide range of lift coefficient (C_L) is desirable with delayed separation and stall. In the case of a marine current turbine, it is also desirable that the section shape is such that cavitations inception is delayed.

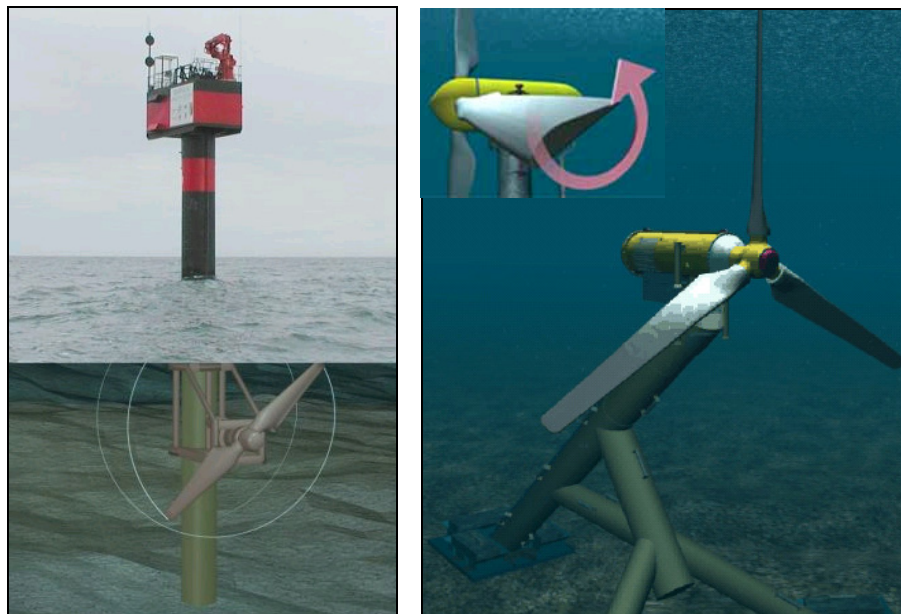
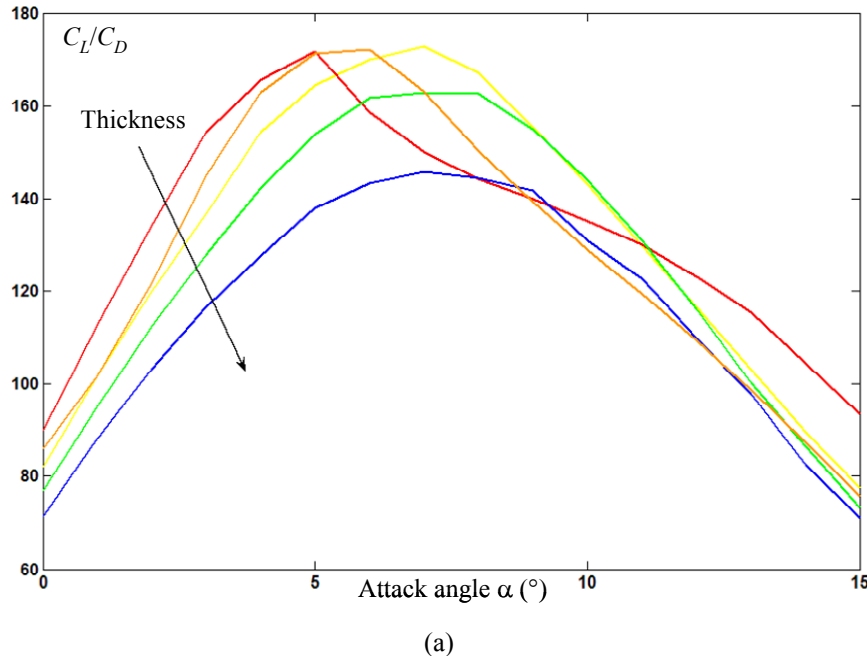
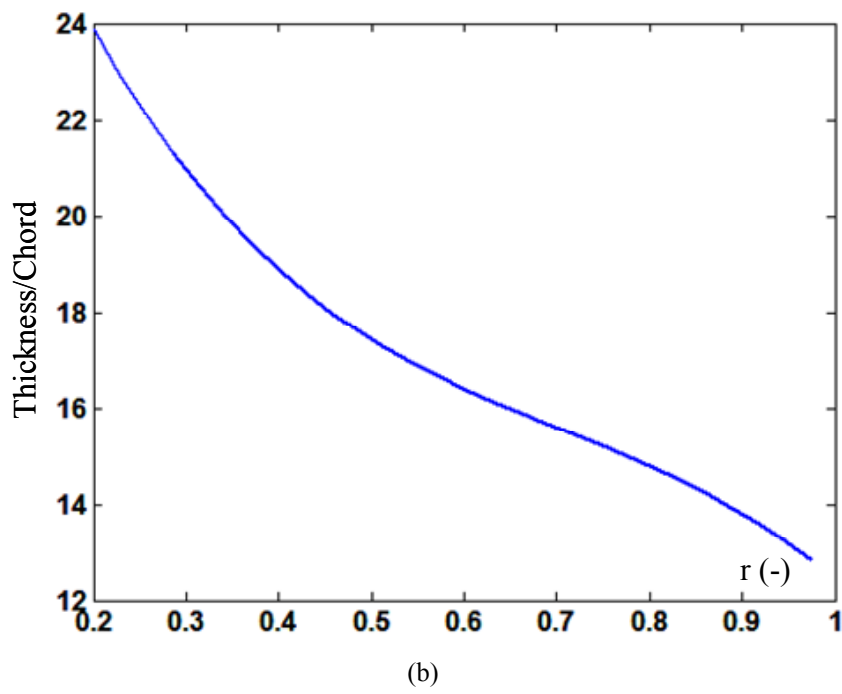


Fig.II.13. 2 (Seaflow) and 3 (E-tide) blades options [© MCT & Strøm AS].

From an efficiency point of view, a low drag coefficient (C_D) is also required. Structural requirements, however, tend to lead to relatively thick sections, particularly near the root, with ensuing higher drag coefficient [29]. We have therefore adopted the NACA 44 profile shape [22]. Figure II.14 shows the main derived characteristics of the above chosen blades. Moreover, the rotor meshes shown by Fig. II.15 has been done using a pre-processor of a code called “*singularités*” developed by the Research Institute of the French Naval Academy.



(a)



(b)

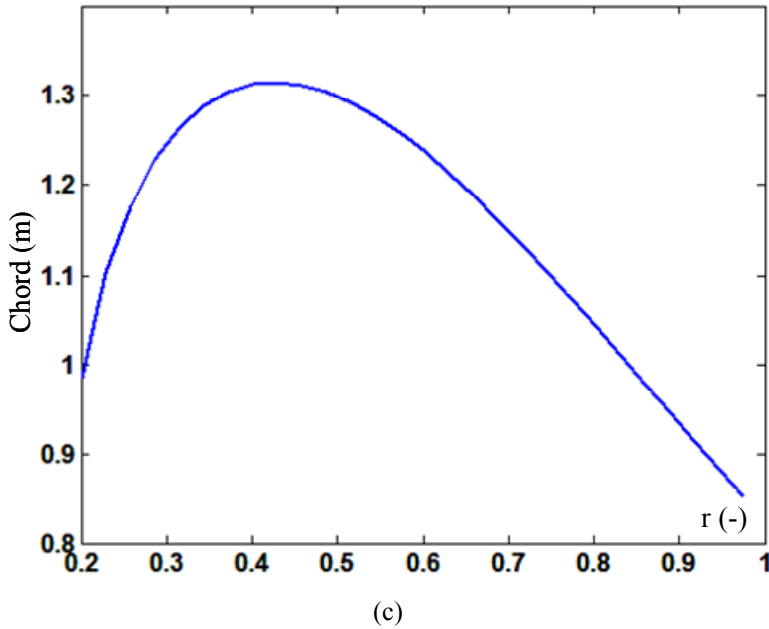


Fig. II.14. NACA 44 blades derived characteristics.

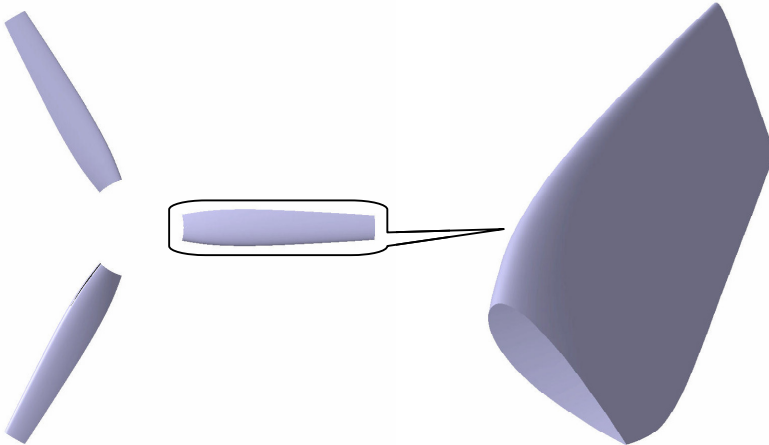


Fig. II.15. Blades mesh using singularities-code.

3.2.5 Validation of the Proposed Model

For validation purposes, we have compared the simulation model output to experimental data from available literature [65], [39]. These data are experimental results for the power coefficient C_p versus TSR (tip speed ratio, $\lambda=R\Omega/V_{tide}$ where R is the turbine radius and Ω is the rotor rotational speed).

The first simulated marine turbine corresponds to the one tested in [71] (Fig. II.16). The obtained power coefficient is shown by Fig.II.17: for a 0.8 m model of a marine current turbine, a current velocity $V_{tide}=1.5$ m/sec, and a pitch angle $\theta = 25^\circ$; a C_p of about 0.349 was found in comparison to 0.375 in the tank test.

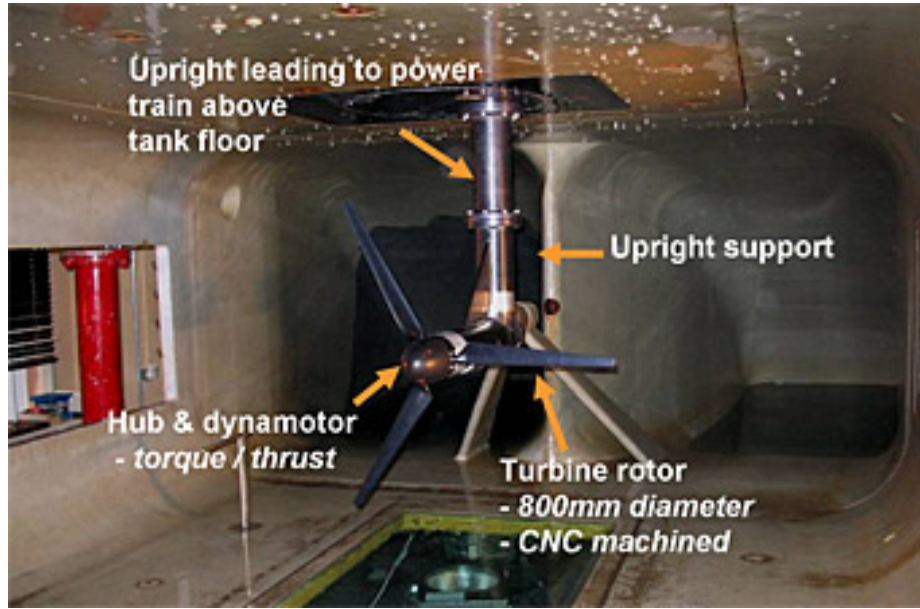


Fig. II.16. The marine turbine tested in [71]
(Illustration reproduced with the kind permission of the authors).

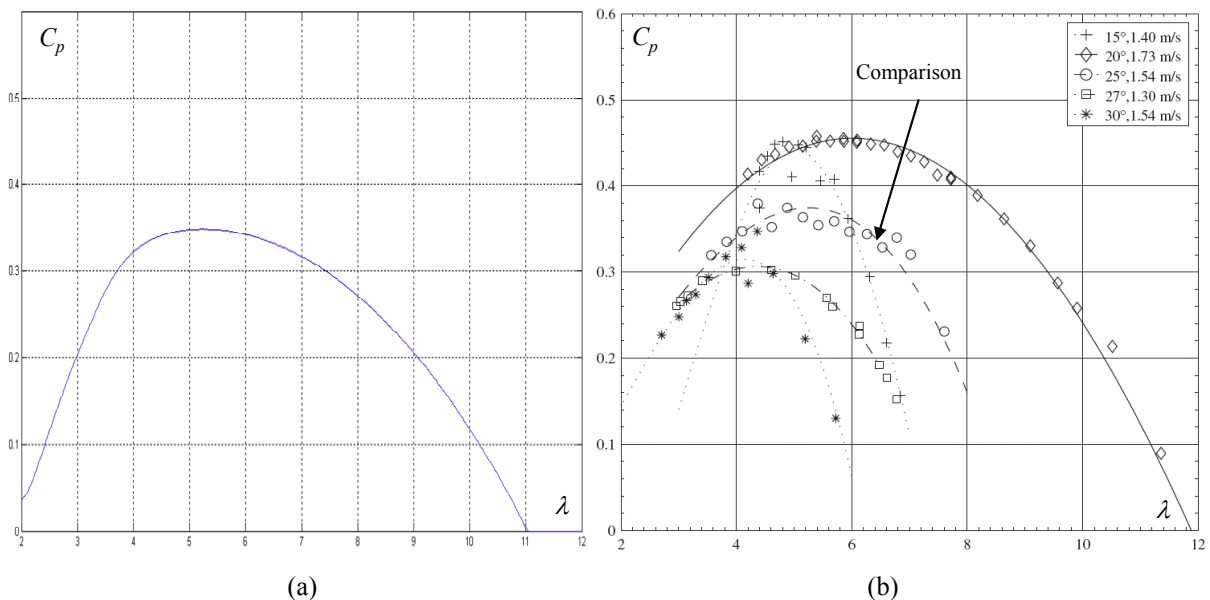


Fig. II.17. Model (a) and experimental (b) C_p curves [71].

This is an encouraging result as it is not possible to reproduce the exact experimental conditions by simulation. Quite the same error was found for others current velocities and pitch angles.

3.2.6 Simulation Results in the Raz de Sein

For the Raz de Sein site, the maximum current velocity is about 3.63 m/sec for 2007. We have therefore adopted a ratio of 75% for economically viable operation of the marine turbine [72-

73]. In fact, it has been shown in [72] and according to wind power experience, that an installed capacity of a site should be rated for a velocity equal to 0.75 (or lower) times the peak velocity at the site for economical reasons. However, if the peak velocity is not clearly defined, rating should be in relation to the velocity V . In our case, this leads to a turbine rotor design with 2.72 m/sec for optimal operation. Moreover, simulations are based on a marine turbine with blades of about 17.4m diameter and of about 1 MW (net electric power) for future marine current converter array deployment. This power rating corresponds to the main projects in the world (MCT, OpenHydro). In this context, the obtained power coefficient C_p curves are shown by Fig. II.18.

Now, the whole simulation tool is used including the resource and the rotor models. The tool input data are those corresponding to optimal operation ($V_{tide} = 2.72$ m/sec). The expected output power of the turbine rotor is about 1.108 MW taking into account gearbox and generator efficiencies as 95% [40]. In this simulation context, the obtained results are shown by Figs. II. 19 and II.20. They are very promising. Indeed, two relevant points are noticed: the maximum output power is about 1.13 MW leading to a relative error of 2%. Moreover, it is well-known that the adopted marine current turbine cannot produce power from water current flow as low as 1 m/sec. This fact is well-taken into account by the simulation model as shown by Fig. II.20 [74].

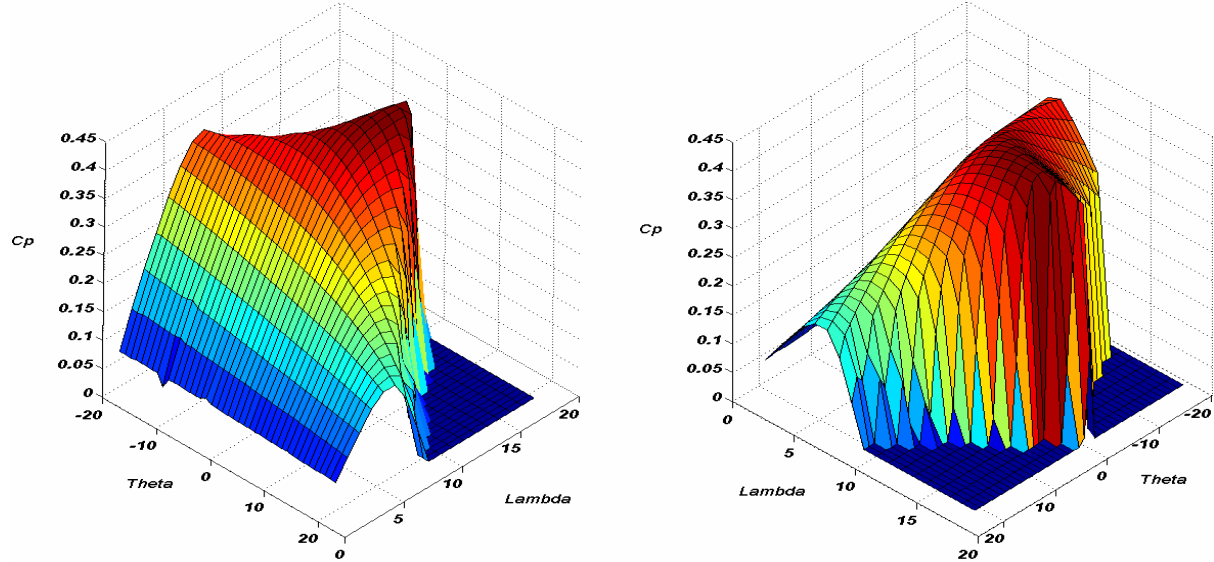


Fig. II.18. $C_p(\lambda, \theta)$ curves.

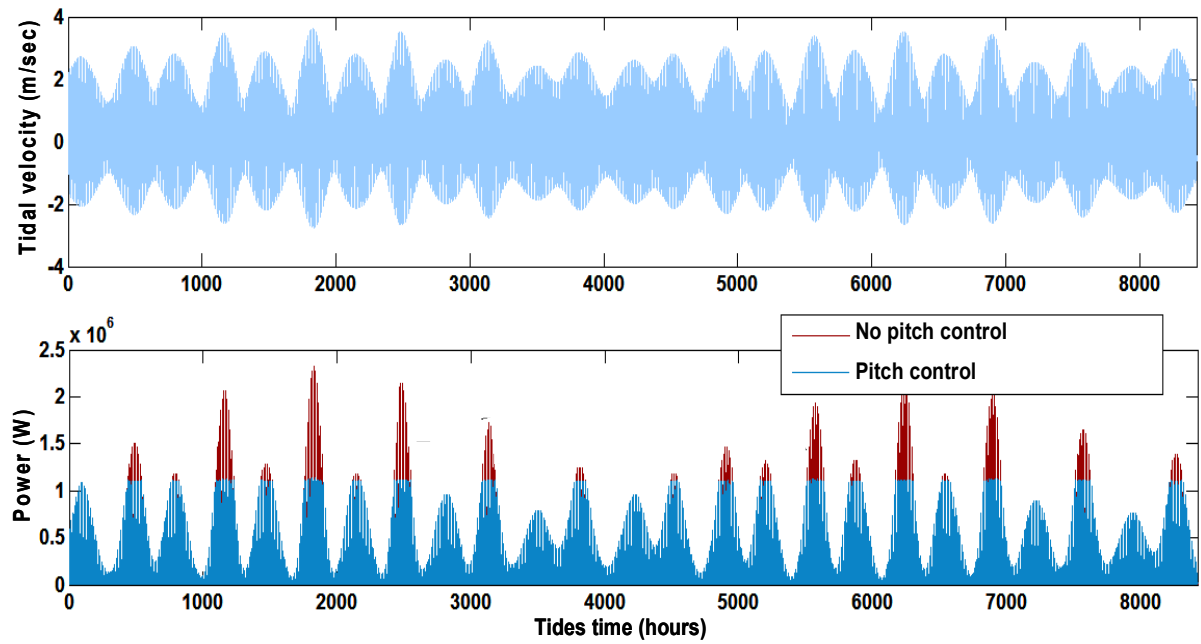


Fig. II.19. The estimated extracted power for year 2007.

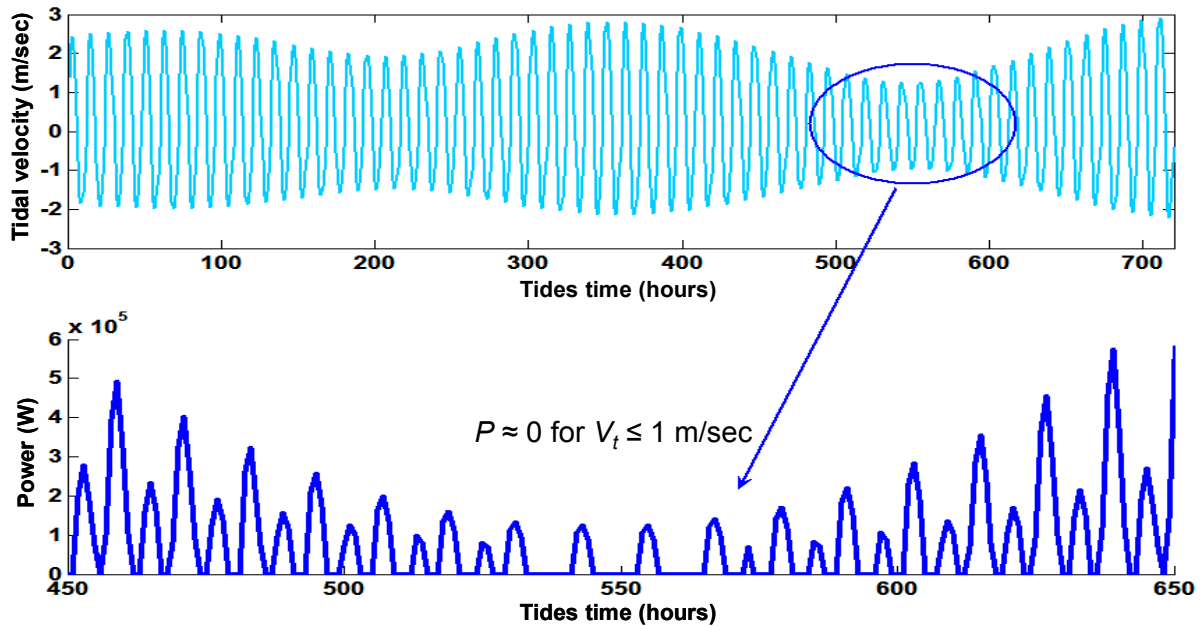


Fig. II.20. The estimated extracted power for July 2007.

II.4 MECHANICAL MODEL

For mechanical modeling, emphasis is put only on those parts of the dynamic structure of the marine current turbine that contribute to the interaction with the grid. Therefore only the drive train is considered, because this part of the marine turbine has the most significant influence on the power fluctuations. The other parts of the MCT structure, as the tower and the flap bending modes, are thus not considered.

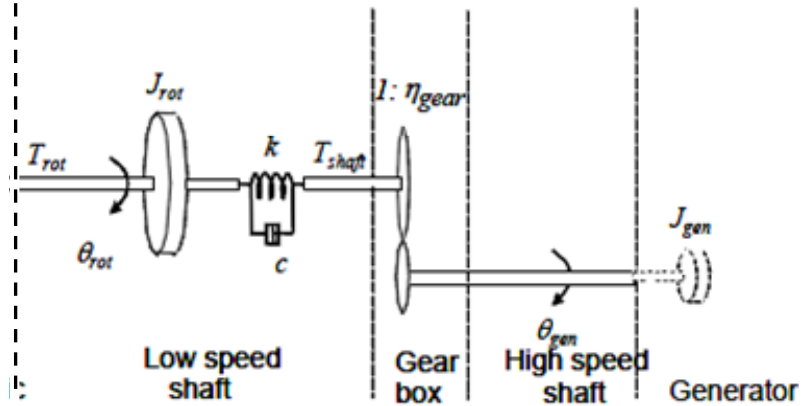


Fig. II.21. Drive train model.

The drive train model is implemented as a mechanical model is implemented as the drive train is a two mass model, namely a large mass corresponding to the rotor inertia J_{rot} and a small mass corresponding to the generator inertia J_{gen} . The low speed shaft is modeled by a stiffness k and a damping coefficient c , while the high-speed shaft is assumed stiff. Moreover, an ideal gearbox with a ratio ($1/1 : \eta_{gear}$) is included (Fig. II.21).

The drive train converts the rotor hydrodynamic torque T_{rot} into the low speed shaft torque T_{shaft} . The mechanical model dynamical description consists of the following equations.

$$\begin{cases} \dot{\theta}_{rot} = \omega_{rot} \\ \dot{\theta}_k = \omega_{rot} - \frac{\omega_{gen}}{\eta_{gear}} \\ \dot{\omega}_{rot} = \frac{(T_{rot} - T_{shaft})}{J_{rot}} \end{cases} \quad (\text{II.23})$$

where θ_k is the angular difference between the two ends of the flexible shaft. The low speed shaft mechanical torque and the generator mechanical power are given by

$$\begin{cases} T_{shaft} = c(\omega_{rot} - \frac{\omega_{gen}}{\eta_{gear}}) + k\theta_k \\ P_t = \omega_{gen} \frac{T_{shaft}}{\eta_{gear}} \end{cases} \quad (\text{II.24})$$

II.5 POWER CONVERTER

The considered power electronics converters are, in the two studied systems (DFIG- and PMSG-based MCT), double-bridge IGBT-VSI. These converters are in first approach modeled as a perfect controlled voltage source with constraints on the voltage maximum value (related to DC-bus voltage) and the maximum frequency. This basic model includes a global efficiency. It has been adopted to limit the computation time. Therefore, the necessary time-steps to take into account the commutation phenomenon are very small in front of the resource timescale (see § II.1).

II.6 TRANSFORMER

The transformer needed to adapt the low-voltage of the generator or power converter to the grid voltage (which is mostly medium voltage) is not modeled at all, as its efficiency is thought to be the same for all concepts under consideration.

II.7 GENERATOR MODEL

Much of the technology that has been suggested for tidal current energy extraction is reminiscent of that used for wind applications. It is then obvious that some wind electric generator topologies could be used for tidal turbines [40]. Table II.1 briefly summarizes the pros and cons of the major generator topologies. In this table, many topologies seem to be exploitable for tidal turbines.

The aim of this section is to set up theoretical models of a doubly-fed induction generator and a permanent magnet synchronous generator suited for both time-domain simulation, and model-based control design.

7.1 Doubly Fed Induction Generator (DFIG)

The wound-rotor induction generator (dubbed as doubly-fed) seems to be an interesting solution for the marine current system. Indeed, the DFIG-based marine turbines, as for wind turbines, offer several advantages including variable speed operation, and four-quadrant active and reactive power capabilities.

As shown in Fig. II. 22, the DFIG may exchange power with the grid not only through the stator but also through the rotor. Consequently, a bidirectional power flow converter is needed in the rotor circuit. The main merit of the doubly-fed IG (DFIG) is its capability to deliver

constant voltage and frequency output for $\pm(20\text{-}40)\%$ speed variation around conventional synchronous speed. Therefore, the power electronic converter has to handle only a fraction (20-40)% of the total power. This means that the losses in the power electronic converter can be reduced compared to a system where the converter has to handle the total power. In addition, the cost of the converter becomes lower [80].

Table II.1. Generator topologies comparison [75].

Type	Pros	Cons
Induction Generator	<ul style="list-style-type: none"> ✓ Full speed range ✓ No brushes on the generator ✓ Complete control of reactive and active power ✓ Proven technology 	<ul style="list-style-type: none"> ✗ Full scale power converter ✗ Need for gearbox
Synchronous Generator	<ul style="list-style-type: none"> ✓ Full speed range ✓ Possibility to avoid gearbox (Direct drive) ✓ Complete control of reactive and active power 	<ul style="list-style-type: none"> ✗ Small converter for field ✗ Full scale power converter
Permanent Magnet Synchronous Generator	<ul style="list-style-type: none"> ✓ Full speed range ✓ Possibility to avoid gearbox (Direct drive) ✓ Complete control of reactive and active power 	<ul style="list-style-type: none"> ✗ Full scale power converter ✗ Low speed generator (big and heavy) ✗ Permanent magnets needed
Doubly-Fed Induction Generator	<ul style="list-style-type: none"> ✓ Limited speed range – Approximately $\pm 30\%$ around synchronous speed ✓ low cost small capacity PWM Inverter ✓ Complete control of reactive and active power 	<ul style="list-style-type: none"> ✗ Need slip rings ✗ Need for gear

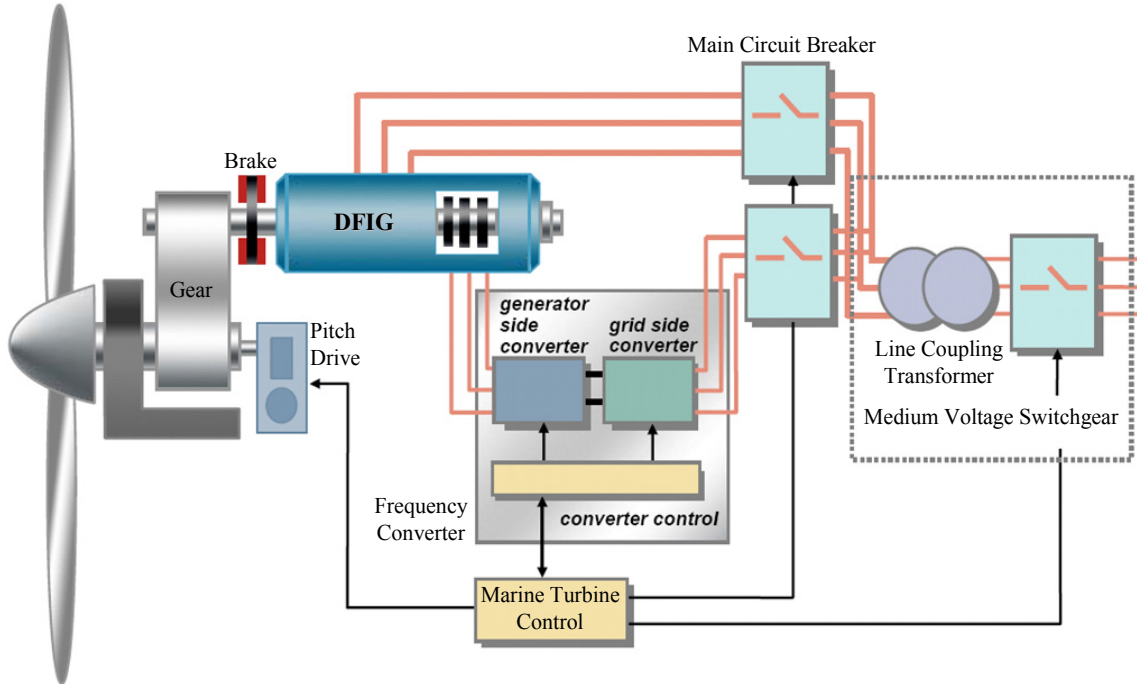


Fig. II.22. Schematic diagram of a DFIG-based generation system.

For bidirectional power flow in the rotor circuit, single stage converters (cycloconverters or matrix converters) or dual-stage back-to-back voltage source PWM inverters have to be used. Independent reactive and active power flow control with harmonics elimination- may be achieved this way for both super and subsynchronous speed operation. Less costly solutions use a unidirectional power flow converter in the rotor when only super or subsynchronous operation as generator is possible.

DFIG-based marine turbines, as for wind turbines, will offer several advantages including variable speed operation, and four-quadrant active and reactive power capabilities. Such system also results in lower converter costs and lower power losses compared to a system based on a fully fed synchronous generator with full-rated converter. Moreover, the generator is robust and requires little maintenance [44], [76-79].

The stator and rotor voltage equations in stationary reference frame are:

$$\begin{cases} [V_s]_3 = R_s[i_s]_3 + \frac{d}{dt}[\phi_s]_3 \\ [V_r]_3 = R_r[i_r]_3 + \frac{d}{dt}[\phi_r]_3 \end{cases} \quad (\text{II.25})$$

The stator and rotor flux are defined as:

$$\begin{cases} [\phi_s]_3 = L_s [i_s]_3 + M [I_r]_3 \\ [\phi_r]_3 = L_r [i_r]_3 + M [I_s]_3 \end{cases} \quad (\text{II.26})$$

To investigate the DFIG the d - q (space – phasor) model is required [Appendix A]. The used Park transform is given by

$$\begin{bmatrix} V_d \\ V_q \end{bmatrix} = \frac{2}{3} \begin{bmatrix} \cos(-\theta_{s,r}) & \cos(-\theta_{s,r} + \frac{2\pi}{3}) & \cos(-\theta_{s,r} - \frac{2\pi}{3}) \\ \sin(-\theta_{s,r}) & \sin(-\theta_{s,r} + \frac{2\pi}{3}) & \sin(-\theta_{s,r} - \frac{2\pi}{3}) \end{bmatrix} \begin{bmatrix} V_a \\ V_b \\ V_v \end{bmatrix} \quad (\text{II.27})$$

The transformation is valid for both stator and rotor. With (II.27), the voltages (II.25) and the fluxes (II.26) become respectively

$$\begin{cases} V_{sd} = R_s i_{sd} + \frac{d}{dt} \phi_{sd} - \omega_s \phi_{sq} \\ V_{sq} = R_s i_{sq} + \frac{d}{dt} \phi_{sq} + \omega_s \phi_{sd} \\ V_{rd} = R_s i_{rd} + \frac{d}{dt} \phi_{rd} - (\omega_s - \omega) \phi_{rq} \\ V_{rq} = R_s i_{rq} + \frac{d}{dt} \phi_{rq} + (\omega_s - \omega) \phi_{rd} \end{cases} \quad (\text{II.28})$$

$$\begin{cases} \phi_{sd} = L_s i_{sd} + M i_{rd} \\ \phi_{sq} = L_s i_{sq} + M i_{rq} \\ \phi_{rd} = L_r i_{rd} + M i_{sd} \\ \phi_{rq} = L_r i_{rq} + M i_{sq} \end{cases} \quad (\text{II.29})$$

The DFIG electromagnetic torque is expressed in the d - q frame as

$$T_{em} = \frac{3}{2} p M (i_{sq} i_{rd} - i_{rq} i_{sd}) \quad (\text{II.30})$$

The mechanical equation is given by

$$J \frac{d\Omega}{dt} = T_{em} - T_m - f \omega \quad (\text{II.31})$$

7.2 Permanent Magnet Synchronous Generator (PMSG)

The PMSG, when used in a grid-connected system, has some advantages over the DFIG. It does not require reactive power from the grid. This results in a better quality of power at the grid interface. This advantage is more pronounced when the MCT farm is connected to a small-capacity grid using a long low-voltage transmission link.

The PMSG is rarely used in gear-driven systems. However, the low-speed design of the synchronous generator is often found advantageous in the direct-drive variable-speed MCT. In such a design, the generator is completely decoupled from the grid by a voltage source power converter (AC/DC/AC) connected to the stator (Fig. II.23).

The stator voltage equations in stationary reference frame are

$$[V_{abc}] = [R][i_{abc}] + [L] \frac{d[i_{abc}]}{dt} + \frac{d\lambda_{abc}}{dt} \quad (\text{II.32})$$

where $[L] = \begin{bmatrix} L_{ss} & M_s & M_s \\ M_s & L_{ss} & M_s \\ M_s & M_s & L_{ss} \end{bmatrix}$

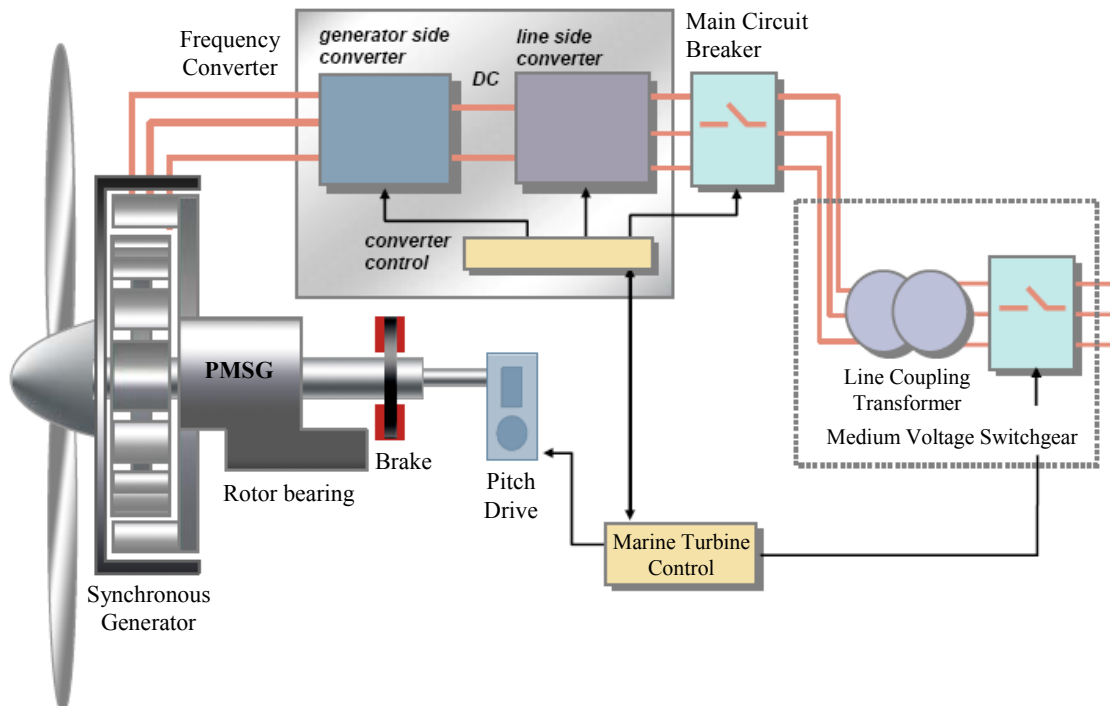


Fig. II.23. Schematic diagram of a PMSG-based generation system.

The PMSG is modeled under the following simplifying assumptions: sinusoidal distribution of stator winding, electric and magnetic symmetry, negligible iron losses and unsaturated magnetic circuit. Under these assumptions, the generator model in the so-called steady-state (or stator) coordinates is first obtained.

Another simpler model can be obtained in d - q rotor coordinates; conversion between (a,b,c) and d - q coordinates can be realized by means of the Park transform [Appendix A]. Then, after neglecting the homopolar voltage u_0 by virtue of symmetry, the d - q PMSG voltages and fluxes become

$$\begin{cases} V_d = Ri_d + L_d \frac{di_d}{dt} - \phi_q \omega_s \\ V_q = Ri_q + L_q \frac{di_q}{dt} + \phi_d \omega_s \end{cases} \quad (\text{II.33})$$

$$\text{and } \begin{cases} \phi_d = L_d i_d + \phi_m \\ \phi_q = L_q i_q \end{cases} \quad (\text{II.34})$$

Thus, (II.32) becomes

$$\begin{cases} V_d = Ri_d + L_d \frac{di_d}{dt} - L_q i_q \omega_s \\ V_q = Ri_q + L_q \frac{di_q}{dt} + (L_d i_d + \phi_m) \omega_s \end{cases} \quad (\text{II.35})$$

The electromagnetic torque is obtained as

$$T_{em} = \frac{3}{2} p(\phi_d i_q - \phi_q i_d) = \frac{3}{2} p[\phi_m i_q + (L_d - L_q) i_d i_q] \quad (\text{II.36})$$

If the permanent magnets are mounted on the rotor surface, then $L_d = L_q$ and the electromagnetic torque becomes

$$T_{em} = \frac{3}{2} p\phi_m i_q \quad (\text{II.37})$$

II.8 CONCLUSION

This chapter has proposed a Matlab/Simulink® based simulation tool for marine current turbines through the modeling of the resource, the rotor and the generator. A part of the proposed simulation tool has been validated by the rare experimental results available in literature.

The developed simulation model has two purposes: performances and dynamic loads evaluation in different operating conditions and control system development for turbine operation based on pitch and speed control. In this case, it is necessary to find a compromise between the simulation model accuracy and the control loop computational speed. In the next chapter, the MCT dynamic performances will be evaluated versus various control techniques.



Chapter
III

**Control Strategies
and Evaluation of the Tested Technologies**

III.1	INTRODUCTION	67
III.2	PRINCIPALS OF MCT OPTIMAL CONTROL.....	67
2.1	CASE OF FIXED-SPEED VARIABLE-PITCH MCT	67
2.2	CASE OF VARIABLE-SPEED FIXED-PITCH MCT	67
III.3	PI CONTROL.....	71
3.1	CONTROLLER DESIGN.....	72
3.2	OPTIMAL CONTROL OF MCT DRIVEN DFIG BY PI SPEED CONTROL	74
3.3	OPTIMAL CONTROL OF MCT DRIVEN PMSG BY PI SPEED CONTROL	78
3.4	DISCUSSION	81
III.4	HIGH-ORDER SLIDING MODE CONTROL	81
4.1	CONTROLLER DESIGN.....	82
4.2	OPTIMAL CONTROL OF MCT DRIVEN DFIG BY HOSM SPEED CONTROL	85
4.3	OPTIMAL CONTROL OF MCT DRIVEN PMSG BY HOSM SPEED CONTROL	92
4.4	HOSM CONTROL ROBUSTNESS AGAINST PARAMETER VARIATIONS	98
III.5	COMPARISON.....	99
III.6	CONCLUSION	104

NOMENCLATURE

C_p	=	Power coefficient;
β	=	Pitch angle;
λ	=	Tip speed ratio;
$s, (r)$	=	Stator (rotor) index (superscripts);
d, q	=	Synchronous reference frame index;
$V(I)$	=	Voltage (Current);
$P(Q)$	=	Active (Reactive) power;
ϕ	=	Flux;
$T_{em} (T_m)$	=	Electromagnetic torque (Mechanical torque);
R	=	Resistance;
$L(M)$	=	Inductance (Mutual inductance);
σ	=	Total leakage coefficient, $\sigma = 1 - M^2/L_s L_r$;
θ_r	=	Rotor position;
$\omega (\omega_s)$	=	Rotor electrical speed (electrical synchronous speed);
ω_r	=	Rotor current frequency ($\omega_r = \omega_s - \omega$);
sl	=	Slip ($\omega_r = sl\omega_s$);
Ω	=	Mechanical speed ($\Omega = \omega/p$);
h	=	Viscosity coefficient;
J	=	Rotor Inertia;
p	=	Pole pair number;
V_{tides}	=	Tidal current speed.
η	=	Mechanical efficiency of the MCT power train

GLOSSARY

MCT	=	Marine Current turbine;
DFIG	=	Doubly-Fed Induction Generator;
PMSG	=	Permanent Magnet Synchronous Generator;
MPPT	=	Maximum Power Point Tracking;
ORC	=	Optimal Regimes Characteristic;
PI	=	Proportional–Integral (controller);
HOSM	=	High-Order Sliding Mode

III.1 INTRODUCTION

The tidal current turbulences and the system parameter drift due to the system wear out can significantly influence the MCT dynamic performance. In this context, various control techniques, suitable to any particular MCT configuration, can be used. In most cases, classical PI or PID control are preferred. However, advanced control techniques can be used in order to ensure better performances, especially for guaranteeing robustness to modeling uncertainties. For example, sliding mode control is a well-performing solution when dealing with dynamical feature uncertainties. In this chapter, a series of control techniques are analyzed, assessed and compared. The main results, based on the developed MCT simulation tools, are presented along with illustration by case studies and Matlab/Simulink® simulation assessment.

III.2 PRINCIPALS OF MCT OPTIMAL CONTROL

2.1 Case of Fixed-Speed Variable-Pitch MCT

In this case, optimization involves using the $C_p(\lambda, \beta)$ characteristic (Fig. III.1). In general, one finds the optimum of $C_p(\lambda, \beta)$ using a look-up table interpolation. Under constant-speed operation (e.g. for a given value of the rotational speed, this curve depends on the pitch angle β and the tidal speed V_{tides} . Optimization is achieved by changing the angle β , such that the operating point to be placed at the maximum of $C_p(\beta)$ corresponds to the current tidal speed value.

2.2 Case of Variable-Speed Fixed-Pitch MCT

Control of variable-speed fixed-pitch MCT aims generally at regulating the power harvested from the tidal currents by modifying the electrical generator speed; in particular, the control goal is to capture the maximum power available from the tidal. For each tidal current speed, there is a certain rotational speed at which the power curve of a given MCT has a maximum (C_p reaches its maximum value).

All these maxima compose what is known as the ORC (Optimal Regimes Characteristic) in the literature (Fig. III.2) [81-82]. By keeping the static operating point of the turbine around the ORC one ensures an optimal steady-state regime. That is, the captured power is the maximal one available from the tidal. This is equivalent to maintain the tip speed ratio at its optimal value λ_{opt} (Fig. III.3). It can be achieved by operating the turbine at variable-speed, according to the tidal speed [81].

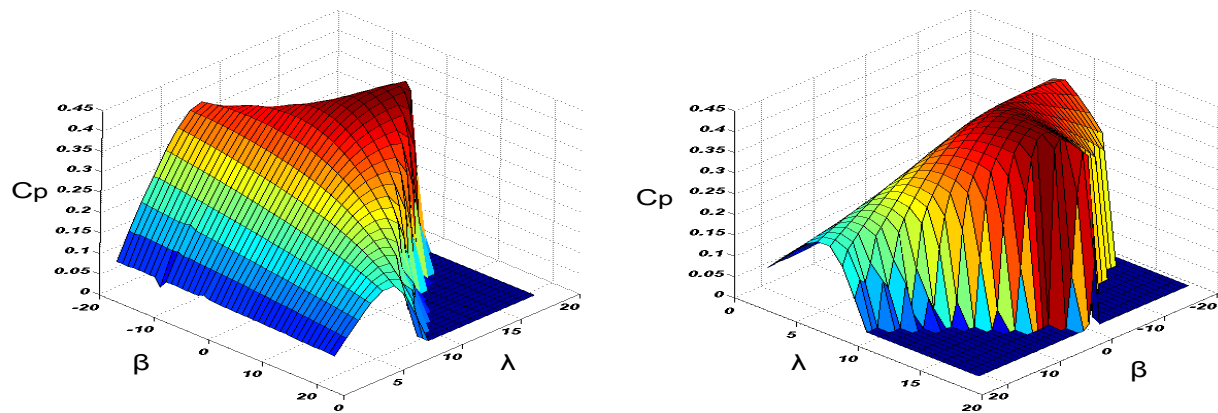


Fig. III.1. $C_p(\lambda, \beta)$ curves.

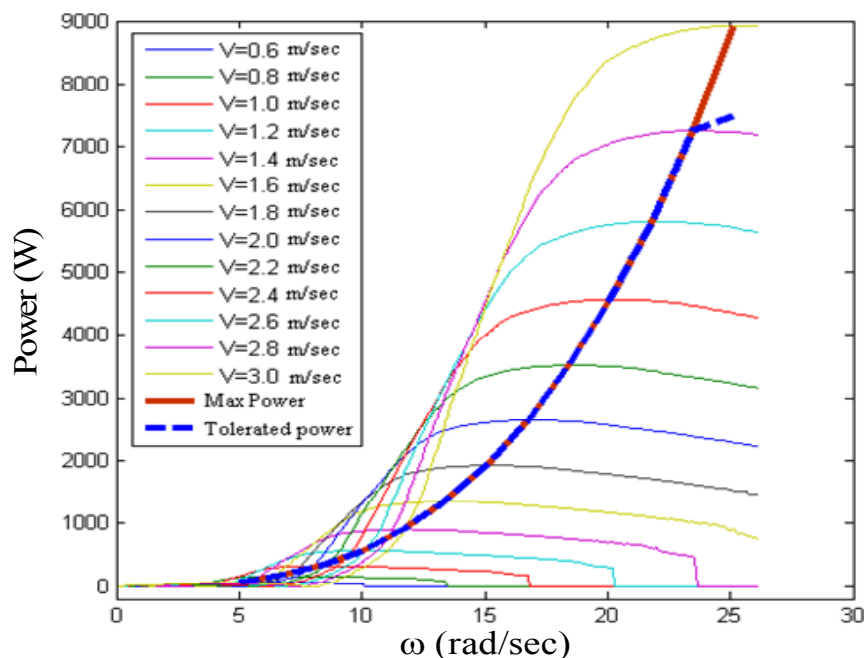


Fig. III.2. Power curves for different tidal current speed.

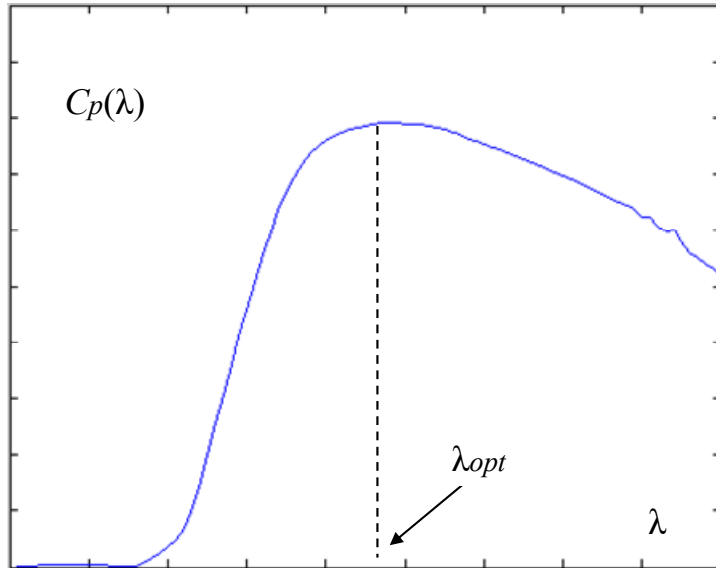


Fig. III.3. Power coefficient curve (hydrodynamic efficiency).

Basically, the control approaches vary in accordance with some assumptions concerning the known models/parameters, the measurable variables, the used control method and the used MCT model. Depending on how rich the information are about the MCT model, especially about its torque characteristic, the optimal control of a variable-speed fixed-pitch MCT is based upon the following approaches.

2.2.1 Maximum Power Point Tracking (MPPT) Strategies

This approach is adequate when parameters λ_{opt} and $C_{pmax}=C_p(\lambda_{opt})$ are unknown. The reference of the rotational speed control loop is adjusted such that the turbine operates around the maximum power for the tidal current speed value [81-82]. To establish whether this reference must be either increased or decreased, it is necessary to estimate the current position of the operating point in relation to the maximum of the $P_{MCT}(\omega)$ curve. This can be done in two ways:

- The speed reference is modified by a variation $\Delta\omega$, the corresponding change in the active power(ΔP_{MCT}) is determined in order to estimate the value $\frac{\partial P_{MCT}}{\partial \omega}$. The sign of this value indicates the position of the operating point in relation to the maximum of $P_{MCT}(\omega)$ characteristic. If the speed reference is adjusted in ramp with a slope proportional to this derivative, then the system evolves to the optimum where $\frac{\partial P_{MCT}}{\partial \omega} = 0$;

- A probing signal is added to the tidal current speed reference. This signal is a slowly variable sinusoid. Its amplitude does not significantly affect the system operation, but still produces a detectable response in the active power evolution. In order to obtain the position of the operating point in relation to the maximum, one compares the phase lag of the probing sinusoid and that of the active power sinusoidal component. If the phase lag is $0/\pi$, then the operating point is placed on the ascending/descending part of $P_{MCT}(\omega)$. Therefore, the slope of the speed reference must increase/decrease. Around the maximum, the probing signal does not produce any detectable response and the speed reference does not have to change.

In this simplified MPPT presentation, factors like the tidal turbulence influences and system dynamics that distort information concerning the operating point position have been neglected. A more detailed description and performances analysis can be found in literature [81].

2.2.2 Shaft Rotational Speed Optimal Control Using a Set-Point from the MCT Data

This solution can be applied if the optimal value of the tip speed ratio λ_{opt} is known. The turbine operates on the ORC if

$$\lambda(t) = \lambda_{opt} \quad (\text{III.1})$$

Which supposes that the shaft rotational speed is closed-loop controlled such that to reach its optimal value.

$$\Omega_{ref} = \frac{\lambda_{opt}}{R} v(t) \quad (\text{III.2})$$

This approach was adopted in the carried-out MCT control simulations.

2.2.3 Active Power Optimal Control Using a Set-Point from the Shaft Rotational Speed Data

This method is used when both λ_{opt} and $C_{pmax} = C_p(\lambda_{opt})$ are known. From the extracted power (I.2), it follows that

$$P_{MCT} = \frac{1}{2} C_p(\lambda) \rho \pi R^2 v^3 = \frac{1}{2} \frac{C_p(\lambda)}{\lambda^3} \rho \pi R^5 \omega^3 \quad (\text{III.3})$$

By replacing λ_{opt} and $C_{pmax} = C_p(\lambda_{opt})$, one obtains the power reference for the second region of the power–tidal speed curve.

$$P_{MCT_{opt}} = P_{ref} = K \omega_{ref}^3 \quad (\text{III.4})$$

$$\text{Where } K = \frac{1}{2} \frac{C_p(\lambda_{opt})}{\lambda_{opt}^3} \rho \pi R^5 \quad (\text{III.5})$$

This approach supposes an active power control loop being used, whose reference is deduced from (III.5). This method is widely employed, especially for medium and high-power wind turbine and can be exploited for marine current turbine [81-82].

III.3 PI CONTROL

The classical PI control is widely used in industry applications. Its design procedure is simple enough, requiring little feedback information and giving rise to easy implemented solution. It can also be employed over most plants having smooth models, in conjunction with other control and modeling techniques such as linearization, gain scheduling, etc.

As stated before, for fixed-pitch turbines, the captured energy maximum available in the tidal current can be achieved if the turbine rotor operates on the ORC. Equivalently, the tip speed ratio must be optimal. This regime can be obtained by tracking some target variables: the rotational speed reference, depending proportionally on the tidal speed, or the optimal rotor power, which proportionally depends on the cubed rotational speed (III.2) and (III.4). Following the same idea, one can fix the mechanical torque proportionally with the rotational speed squared:

$$T_{em_{opt}} = T_{em_{ref}} = K \omega^2 \quad (\text{III.6})$$

with K defined by (III.5).

Some elements for the generator torque PI control are given in literature [81-82]. One can envisage three kinds of control loops for tracking the ORC using the tidal velocity, the rotational speed measurement and an inner torque control loop. The PI controller zeroes the difference between the target and the measured rotational speed and imposes the generator torque reference. One can expect large torque variations, as the torque demand rapidly varies in this configuration.

Using only the rotational speed feedback, a torque control loop can be built by using as (III.6) which is often called the $K\omega^2$ law [81-84]. For an induction generator, the torque PI control can be found in the vector control scheme. If a PMSG is considered, the torque is controlled directly by manipulating the I_q current. An advantage of this control structure is the increased mechanical compliance of the system.

An active power loop can also be built using again the measured rotational speed, the active power and the inner torque control loop. The target power results from (III.4) and the controller output represents the desired torque. By zeroing the power error, the operating point moves to the maximum power point [85-86].

3.1 Controller Design

In this section, we introduce some classical PI design of wind turbines that can be used for the MCT control for the three above-mentioned cases.

3.1.1 Torque Control Loop

In order to improve and maximize the captured energy, the rotor turbine must operate at the maximum power. Equivalently, this means imposing the electromagnetic torque (T_{ref}) which equals the tidal torque corresponding to the maximum available power. The turbine works at maximal efficiency when turning at optimal tip speed ratio λ_{opt} , so the maximum power is proportional to the cubed rotational speed (III.4) and (III.5).

$$T_{ref} = \eta K \omega_{ref}^2 \quad (\text{III.7})$$

As the MCT control structure allows the tidal speed to be tracked within admissible limits of mechanical loads, this method can be used as long as it depends only on slow tidal speed variations. For high dynamics turbulent tidal current, filtering is necessary to ensure sufficiently slow closed-loop dynamics. Moreover, this method is strongly sensitive to parametric variations.

3.1.2 Speed Control Loop

The controller design is based upon the MCT linearized model. The simplified closed-loop structure is shown in Figure III.4.

A high gain K_p will thereby ensure better tracking performance. However, one must take account of control effort (torque) limitations, so K_p values must also be limited. The zero effect of increasing the overshoot is compensated by first-order filtering the reference signal (Fig.III.4). Although the steady-state speed error is zero, there will always be nonzero dynamical errors due to the significantly variable reference signal ω_{ref} .

One must note that the imposed closed-loop performances are guaranteed for the chosen operating point. Both the gain and the time constant of the torque controlled system around a certain steady-state operating point depend on that operating point (through tidal velocity and rotational speed). Therefore, the dynamic performances of the tracking system also vary upon the operating point [81-82].

3.1.3 Power Control Loop

The input of the plant is the electromagnetic torque and its output is the generated active power P . The controller design is based on the parameterization of the system response at step changes in the generator torque for a given tidal speed. In the first moment, the negative torque step results in a step power change, the rotational speed being the initial one.

Then, the difference between the tidal torque and the electromagnetic torque leads to the increasing of the rotational speed, such that the power increases according to the speed dynamics until it reaches the new steady-state value. The generator is controlled by the voltages imposed in the rotor windings by an AC/DC/AC voltage source dual bridge IGBT-inverter (DFIG). One can note that the plant dynamics in the case of the power control loop sensibly differ from those corresponding to the speed control loop case [81-82].

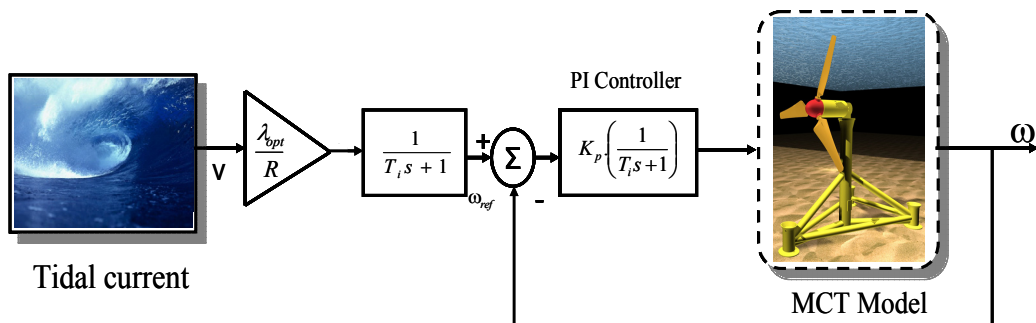


Fig. III.4. MCT PI control structure: speed control loop case.

3.2 Optimal Control of MCT Driven DFIG by PI Speed Control

In order to illustrate the PI speed controller design, a low-power variable-speed fixed-pitch MCT driven DFIG has been used as a case study [113], [118].

The control system is defined in the synchronous d - q frame fixed to either the stator voltage or the stator flux [72]. For the proposed control strategy, the generator dynamic model is written in a synchronously rotating frame d - q with the stator flux given by

$$\begin{cases} \phi_{sd} = \phi_s \\ \phi_{sq} = 0 \end{cases} \quad (\text{III.8})$$

If the stator resistance R_s is neglected, the stator voltage can be expressed in the Park frame by [Appendix A]

$$\begin{cases} V_{sd} = 0 \\ V_{sq} = V_s = \omega_s \phi_{sd} \end{cases} \quad (\text{III.9})$$

From (III.8), the stator current can be written as

$$\begin{cases} I_{sd} = \frac{\phi_s}{L_s} - \frac{M}{L_s} I_{rd} \\ I_{sq} = -\frac{M}{L_s} I_{rq} \end{cases} \quad (\text{III.10})$$

It follows that

$$\begin{cases} \phi_{rd} = \left(L_r - \frac{M^2}{L_s} \right) I_{rd} + \frac{MV_s}{L_s \omega_s} \\ \phi_{rq} = \left(L_r - \frac{M^2}{L_s} \right) I_{rq} \end{cases} \quad (\text{III.11})$$

The rotor voltage is expressed by:

$$\begin{cases} V_{rd} = R_r I_{rd} + \left(L_r - \frac{M^2}{L_s} \right) \frac{dI_{rd}}{dt} - sl\omega_s \left(L_r - \frac{M^2}{L_s} \right) I_{rq} \\ V_{rq} = R_r I_{rq} + \left(L_r - \frac{M^2}{L_s} \right) \frac{dI_{rq}}{dt} + sl\omega_s \left(L_r - \frac{M^2}{L_s} \right) I_{rd} + sl \frac{MV_s}{L_s} \end{cases} \quad (\text{III.12})$$

Using Laplace transformation, we can express the rotor current as

$$\begin{cases} i_{rd}(s) = \frac{1}{R_r + \sigma L_r s} [v_{rd}(s) + sl\omega_s L_r \sigma i_{rq}(s)] \\ i_{rq}(s) = \frac{1}{R_r + \sigma L_r s} [v_{rq}(s) - sl\omega_s L_r \sigma \cdot i_{rd}(s) - slM \frac{V_s}{L_s}] \end{cases} \quad (\text{III.13})$$

The mechanical equation is written in the s -Domain as

$$\Omega(s) = \frac{1}{h + Js} [T_{em}(s) - T_m(s)] \quad (\text{III.14})$$

T_{em} can be expressed in the same Park frame as follows.

$$T_{em} = -\frac{3}{2} p \frac{M}{L_s} \Phi_{sd} i_{rq} \quad (\text{III.15})$$

In those conditions, the DFIG Park model is illustrated by (Fig. III.5).

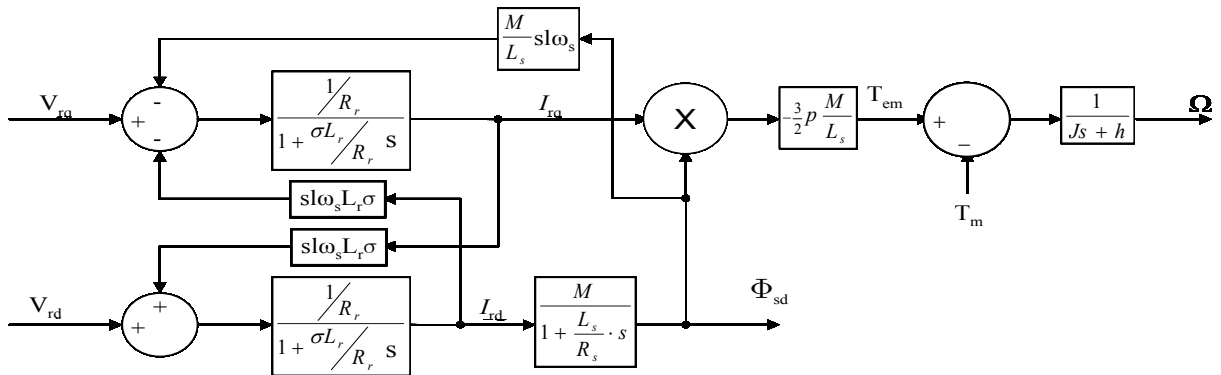


Fig. III.5. DFIG model bloc.

As shown in Fig III.5, the DFIG rotor speed can be controlled through the rotor current I_{rq} . Therefore, an inner loop for current control is needed (Fig. III.6).

Since the electrical and the mechanical dynamics are in different time scales (i.e. the electrical dynamics are faster than the mechanical ones). It might be advantageous to control the generator in a cascade structure. Since the electrical dynamics are the fastest, the current has to be controlled in an inner loop.

Then a speed controller can be added in an outer slower loop (Fig. III.7). If the inner control loop is set faster, than the outer, it is possible to neglect the dynamics of the inner control loop. This assumption will usually make the design of the outer control loop much easier [81-82].

The proposed PI control strategy is tested using tidal current data from the Raz de Sein (Brittany, France) for a marine current turbine of 1.44 m diameter and a 7.5 kW DFIG [Appendix B].

In this first case study, the MCT is simulated considering a resource first-order model (II.1). The resource is assumed to be non-disturbed by sea-surface effects and by other turbulences (Fig. III.8).

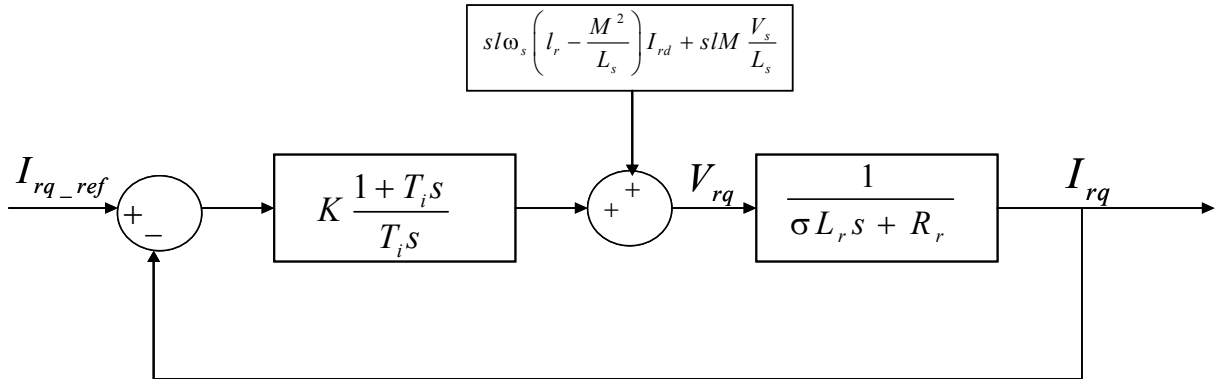


Fig. III. 6. The inner loop of the DFIG speed control.

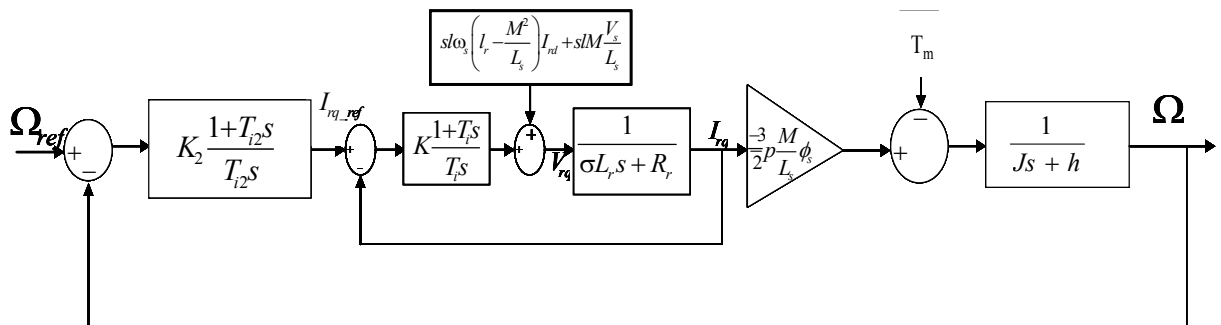


Fig. III.7. The DFIG control cascade.

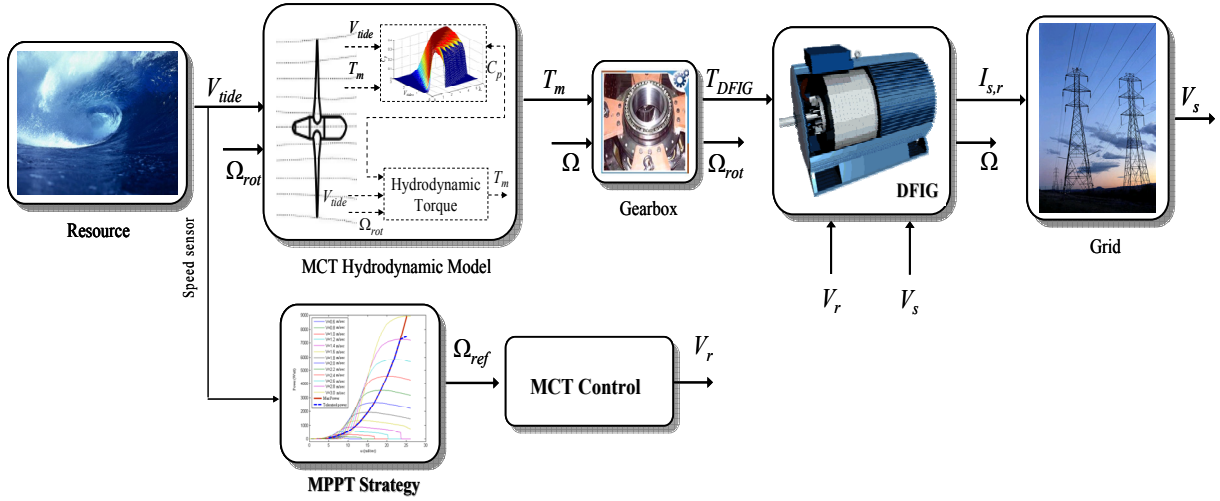


Fig. III.8. Speed-tracking part of the DFIG overall variable speed control scheme.

For speed references given by the MPPT strategy, the DFIG-based MCT control performances are shown in Figs. III.9 and III.10 respectively illustrating the rotor speed tracking performance and the generated active power. The simulation time has been reduced to seconds to limit the computation time to realistic ones. In real-world application, the system mechanical dynamics will be slower than in simulation.

The main merit of the DFIG is its capability to deliver constant voltage and frequency output for $\pm 30\%$ speed variation around conventional synchronous speed. It can be noticed that another choice for the speed variation range is possible (between 30 and 50% are the more often used). This 30% variation speed choice is directly related to a low power sizing of the rotor converter. Therefore, the rotor speed reference generated by the MPPT strategy was limited at $\pm 30\%$ of the conventional synchronous speed. The obtained results show good tracking performances of the DFIG rotor speed [81-82].

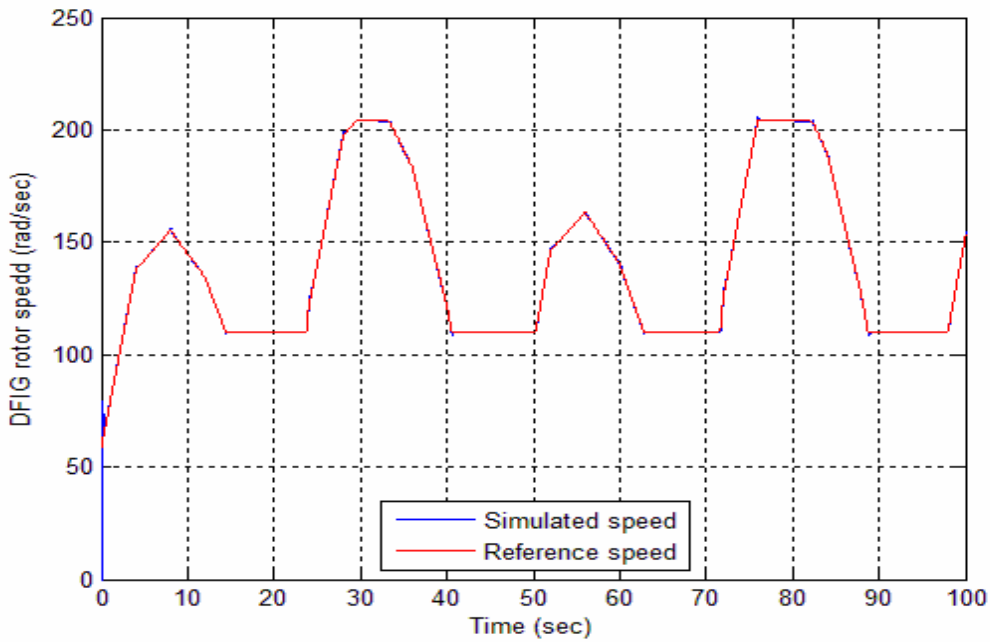


Fig. III.9. The DFIG rotor speed and its reference.

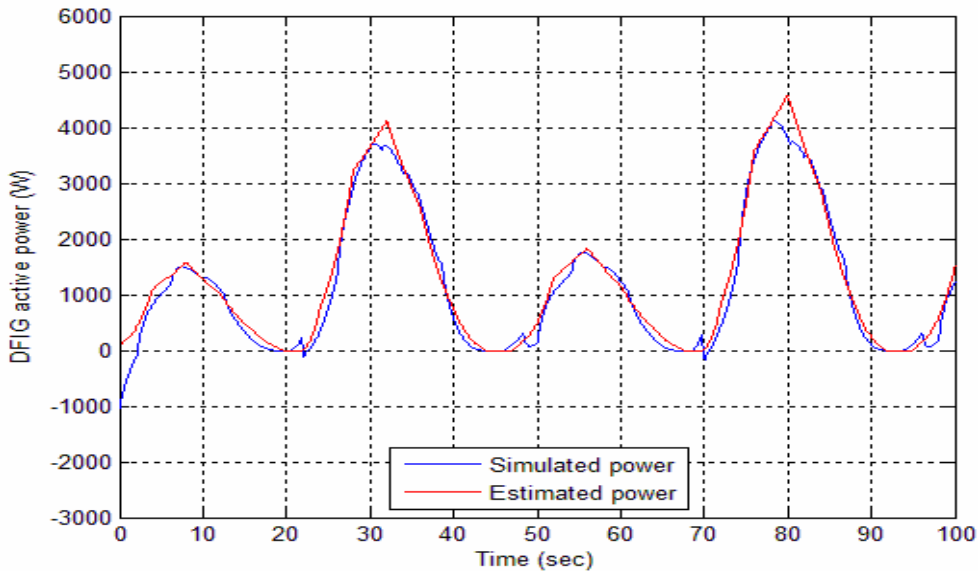


Fig. III.10. The DFIG active power.

3.3 Optimal Control of MCT Driven PMSG by PI Speed Control

In this second case study, an optimal control based on a PI speed controller has been tested for a low-power variable speed fixed-pitch MCT driven PMSG.

The control system is defined in the synchronous d - q frame [Appendix B]. For the proposed control strategy, the permanent magnet synchronous generator dynamic model is written in the s -domain with the stator voltage given by

$$\begin{cases} -(R + L_d s) i_d = V_d - \phi_q \omega_s \\ -(R + L_q s) i_q = V_q + \phi_d \omega_s \end{cases} \quad (\text{III.16})$$

The mechanical equation is expressed by

$$T_{em} - T_m = (J_s + h)\Omega \quad (\text{III.17})$$

The electromagnetic torque T_{em} is defined by

$$T_{em} = \frac{3}{2} p(\phi_d i_q - \phi_q i_d) = \frac{3}{2} p[\phi_m i_q + (L_d - L_q) i_d i_q] \quad (\text{III.18})$$

$$\text{with } \begin{cases} \phi_d = L_d i_d + \phi_m \\ \phi_q = L_q i_q \end{cases}$$

As the used generator for simulation is a permanent magnet synchronous one, therefore $L_d = L_q$ and the electromagnetic torque T_{em} is simplified as

$$T_{em} = \frac{3}{2} p \phi_m i_q \quad (\text{III.19})$$

In those conditions, the PMSG Park model is illustrated by Fig. III.11.

The same strategy adopted for the DFIG was used to control the PMSG-based MCT. Indeed, an inner loop was needed for the current control. Then an outer loop was used to control the MCT shaft speed. As shown in Fig.III.11, the PMSG rotor speed can be controlled through the rotor current I_q .

In this second case, the PMSG-based MCT is simulated in the same condition as the first case. Indeed, The PI control strategy is tested by using a resource first-order model for a marine current turbine of 1.44 m diameter and 7.5-kW PMSG [Appendix B].

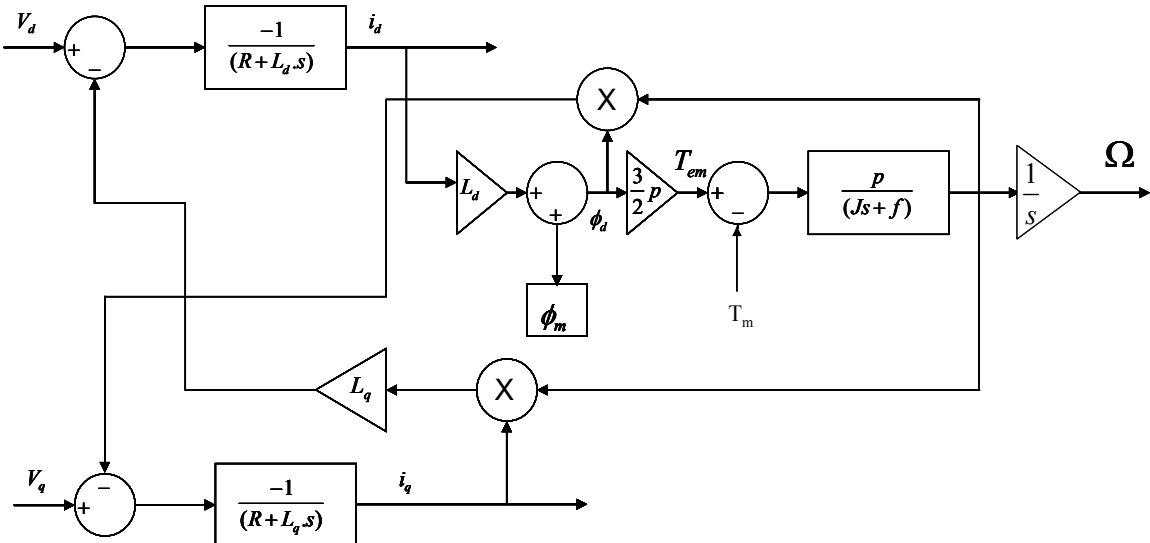


Fig. III.11. The PMSG Park model.

For speed references given by the MPPT strategy, the PMSG-based MCT control performances are shown in Figs. III.12 and III.13 respectively illustrating the rotor speed tracking performance and the generated active power.

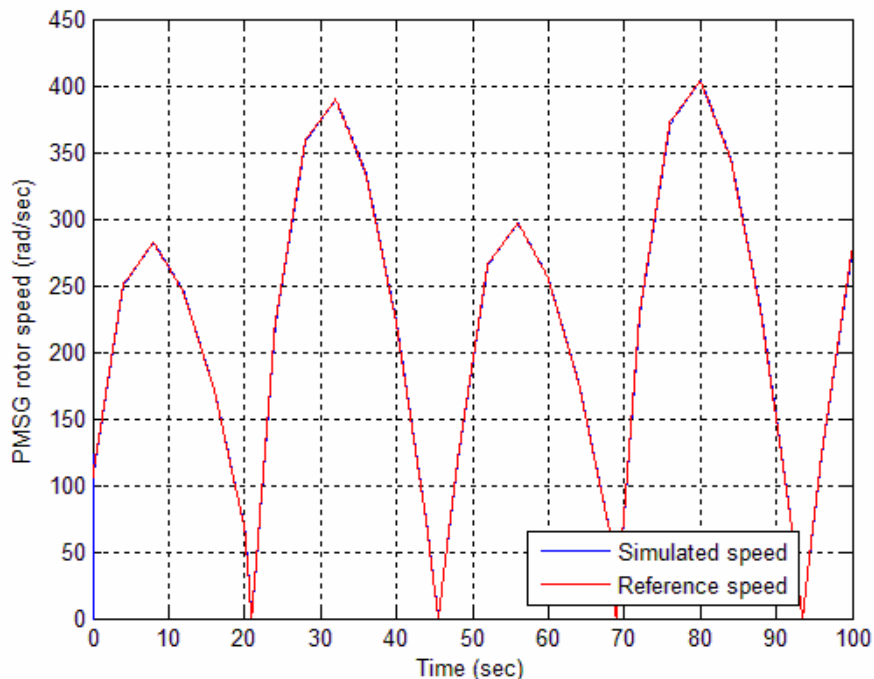


Fig. III.12. The PMSG rotor speed and its reference.

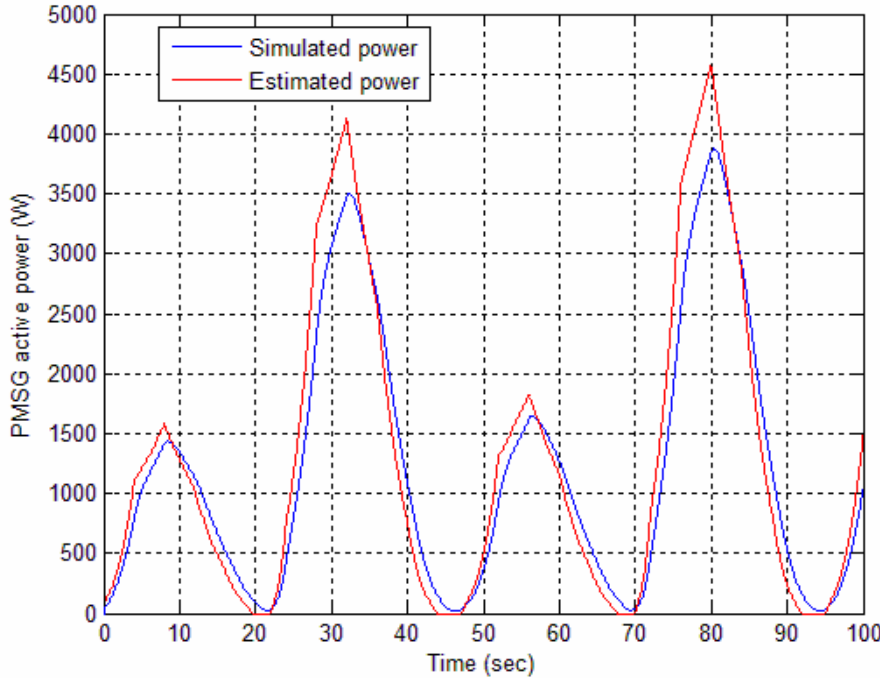


Fig. III.13. The PMSG active power.

The obtained results show good tracking performances of the PMSG rotor speed. [81-82].

3.4 Discussion

In the above section, PI control has been adopted for both DFIG- and PMSG-based MCT speed tracking. This kind of controller is well-known for its simplicity for constant references. Its gains are computed by compensating the larger system time-constant and by guaranteeing a constant tracking error when the reference is a ramp. However, in case of a marine current turbine, the generated reference signals are time-varying and the current sources may be turbulent. These will obviously make the PI feedback not efficient.

III.4 HIGH-ORDER SLIDING MODE CONTROL

Sliding mode control laws for nonlinear systems have been widely investigated and developed since they were introduced by [87]. The objective of this method is, by means of a discontinuous control, to constrain the system to evolve and stay, after a finite-time, on a sliding manifold where the resulting behavior has some prescribed dynamics. Sliding mode control exhibits relative simplicity of design and robustness properties with respect to matched perturbations. However, some problems exist such as the chattering phenomenon (high-frequency oscillations along the sliding motion). This drawback can be very harmful for

the generator since the discontinuous control can cause overheating of the coils and excite some unmodeled high frequency dynamics.

To avoid chattering some approaches were proposed [89-90]. The main idea was to change the dynamics in small vicinity of the discontinuity surface in order to avoid real discontinuity and at the same time to preserve the main properties of the whole system. However, the ultimate accuracy and robustness of the sliding mode were partially lost. Recently invented, the higher order sliding modes (HOSM) generalize the basic sliding mode idea that acts on the high-order time derivatives of the system deviation from the constraint instead of influencing the first deviation derivative as it happens in standard sliding modes. Along with keeping the main advantages of the original approach, they deal with the chattering effect and provide for even higher accuracy in realization. A number of such controllers were described in the literature [91-97].

4.1 Controller Design

The principle of high-order sliding mode control is to constrain the system trajectories to reach and stay, after a finite time, on a given sliding manifold \mathbb{S}^r in the state space [93]. Consider a system whose dynamics is given by

$$x = f(t, x) + g(t, x)u \quad (\text{III.20})$$

where $x \in \mathfrak{R}^n$ is the system state, $u \in \mathfrak{R}$ is the control f and g are sufficiently smooth vector fields. The sliding manifold is defined by the vanishing of a corresponding sliding variable $S : \mathfrak{R}^+ \times \mathfrak{R}^n \longrightarrow \mathfrak{R}$ and its successive time-derivatives up to a certain order, i.e. the r^{th} order sliding set.

$$\mathbb{S}^r = \left\{ (t, x) \in \mathfrak{R}^+ \times \mathfrak{R}^n : S(t, x) = \dot{S}(t, x) = \dots = S^{(r-1)}(t, x) = 0 \right\}$$

A control law u leading to such a behavior will be called an r^{th} order ideal sliding mode algorithm. This discontinuous control law usually acts on the r^{th} time derivative of the sliding variable. Thus, higher order sliding modes can reduce, by far, the chattering phenomenon while preserving the robustness properties. Indeed, assume the fact that the system has relative degree p with respect to the sliding variable. If the sliding mode order r is chosen such

that $p \leq r - 1$, the discontinuous algorithm generating the r^{th} order sliding mode is applied to $u^{(r-p)}$ and thus the actual input of the system is continuous.

An ideal sliding mode does not exist in practice since it would imply that the control commutes with infinite frequency. Because of the technological limitations such as switching time delays and/or small time constants in the actuators, this frequency is finite. Thus, the motion only takes place in a neighborhood of the sliding manifold and is called a real high-order sliding mode. A motion satisfying the following relations

$$|S| = O(\tau^r), |\dot{S}| = O(\tau^{r-1}), \dots, |S^{(r-1)}| = O(\tau)$$

where τ is the sampling period, is said to be a r^{th} order real sliding mode with respect to S . From this definition, it can be seen that the higher the order of the sliding mode is, the more accurate the convergence on $S = 0$ will be.

The problem of interest in the case of the DFIG and PMSG is to generate a second-order sliding mode on an appropriately chosen sliding surface and, thus, to constrain the trajectories system to evolve in finite time on

$$\mathbb{S}^2 = \{x \in \Re^n : S = \dot{S} = 0\} \quad (\text{III.21})$$

It is obtained with a control law acting on the second time derivative of the sliding variable, which can be written in the general form

$$\ddot{S} = \Phi(t, S, \dot{S}) + \varphi(t, S, \dot{S})U$$

Where $U = u$ (resp, $U = \dot{u}$) when the system has relative degree 2 (relative degree 1) with respect to S .

In order to design second-order sliding mode algorithms, it is necessary to establish some assumptions to allow the convergence to the sliding surface and the bound of the variable \dot{S} [91-92]. Particularly, it is assumed that there exist positive constants S_0 , K_m , K_M and C_0 such that $\forall x \in \Re^n$ and $|S(t, x)| < S_0$, the system satisfies the following conditions.

$$0 < K_m \leq |\varphi(t, S, \dot{S})| \leq K_M \text{ and } |\varphi(t, S, \dot{S})| < C_0$$

Different kinds of second order sliding mode algorithms can be found in the literature [91-94], [98]: *Twisting*, *Sampled Twisting*, *Super-Twisting*, *Sub-Optimal*, etc. Hereafter, two algorithms that induce a second-order sliding mode for the system and that will be applied to the DFIG and the PMSG.

Sampled twisting algorithm [99]: This algorithm provides good robustness properties and can be applied when the relative degree is 2. It does not require the knowledge of the time-derivative of the sliding variable and takes into account some practical constraints such as the measurement sampling and the control. The sampling period τ is assumed to be the same for both the control law and the measurements. The sampled twisting algorithm can be written as follows.

$$u = u_{te}(S, \Delta_S) = \begin{cases} -\lambda_M \text{sign}(S) & \text{if } S \Delta_S > 0 \\ -\lambda_m \text{sign}(S) & \text{if } S \Delta_S \leq 0 \end{cases}$$

$$\text{With } \Delta_S = \begin{cases} 0, & k = 0 \\ (S(k\tau) - S((k-1)\tau)), & k \geq 1 \end{cases}$$

Under sufficient conditions,

$$\begin{cases} \lambda_m > 4 \frac{K_M}{S_0} \\ \lambda_m > \frac{C_0}{k_m} \\ \lambda_M > \frac{K_M \lambda_m}{k_m} + 2 \frac{C_0}{k_m} \end{cases}$$

it can be shown that the system trajectories converge onto the real second-order sliding set.

$$\mathbb{S}_{real}^{(2)} = \left\{ |S| = O(\tau^2), |\dot{S}| = O(\tau) \right\}$$

Super-twisting algorithm: This algorithm has been developed for systems with relative degree 1 to avoid the chattering phenomena. The control law comprises two continuous terms that, again, do not depend upon the first time-derivative of the sliding variable. The discontinuity only appears in the control input time-derivative

$$u = u_{st}(S) = v_1 + v_2 \text{ with } \begin{cases} \dot{v}_1 = -\beta \text{sign}(S) \\ v_2 = -\alpha |S|^{\frac{1}{2}} \text{sign}(S) \\ \alpha, \beta > 0 \end{cases}$$

If the control gains satisfy the sufficient conditions [95],

$$\beta > \frac{C_0}{k_m} \text{ and } \alpha > \frac{4C_0(K_M\beta + C_0)}{k_m^2(k_m\beta - C_0)}$$

one can obtain the convergence in finite-time on the sliding surface (III.21).

4.2 Optimal Control of MCT Driven DFIG by HOSM Speed Control

A common practice in addressing DFIG control problem is to use a linearization approach [76], [100-110]. However, due to the inevitable uncertainties inherent in DFIG-based marine current turbines and the tidal resource characteristics such as turbulence and swell effects, such control methods come at the price of poor system performance and low reliability [106]. Hence a nonlinear and robust control is needed to take into account these control problems [107-108], [118-124].

In this context, sliding mode control seems to be an interesting approach and easy to implement [77], [112], [116].

For DFIG-based marine current turbines, sliding mode should provide a suitable control tool for conversion efficiency, torque oscillation smoothing and robustness against electric grid disturbances [110], [79].

The above proposed high-order sliding mode control strategy for a DFIG-based MCT is illustrated by Fig. III.14.

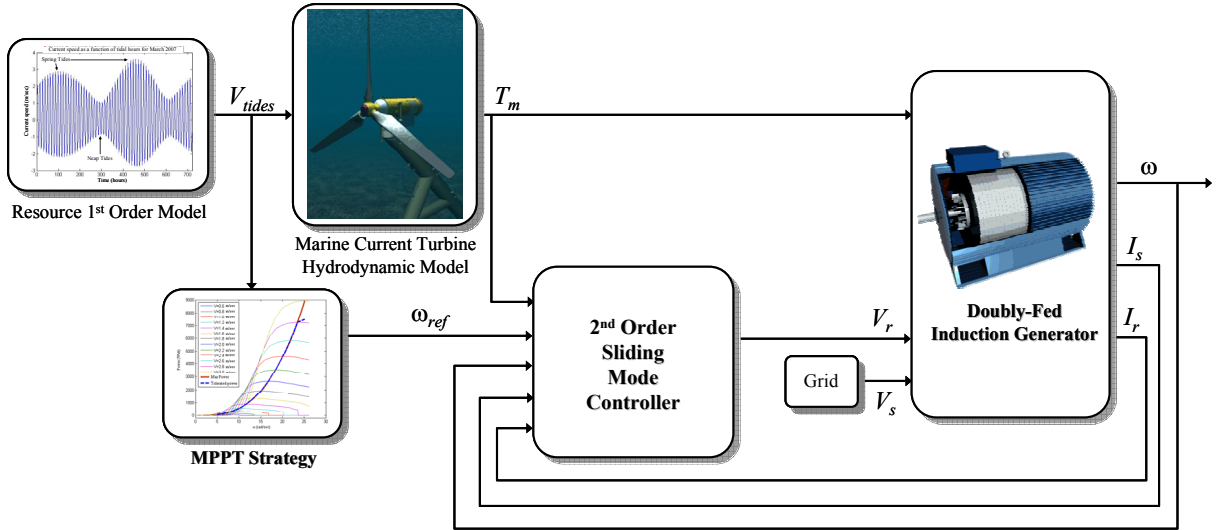


Fig. III.14. The HOSM control scheme for a DFIG-based MCT.

The proposed control strategy is based on a step-by-step procedure: First, the speed reference ω_{ref} is generated by an MPPT strategy [98]. Then, an optimal electromagnetic torque, which ensures the rotor speed convergence to ω_{ref} is computed using the following mechanical equation.

$$T_{em_ref} = T_m + h\omega - \alpha(\omega - \omega_{ref}) + J\dot{\omega}_{ref} \quad (\text{III.22})$$

where α is a positive constant. Afterwards, rotor current references are derived to ensure the DFIG torque and reactive power convergence to the optimal torque and zero, respectively.

$$\begin{cases} I_{qr_ref} = -\frac{L_s}{pM} \frac{T_{em_ref}}{\phi_{sd}} \\ I_{dr_ref} = \frac{1}{M} \phi_{sd} \end{cases} \quad (\text{III.23})$$

In order to ensure the rotor currents converge to their references, a robust high-order sliding mode strategy is used [111]. Let us define the following surfaces.

$$\begin{cases} S_1 = I_{dr} - I_{dr_ref} \\ S_2 = I_{qr} - I_{qr_ref} \end{cases} \quad (\text{III.24})$$

It follows that

$$\left\{ \begin{array}{l} \dot{S}_1 = \frac{L_s}{M^2 - L_r L_s} \left(V_{dr} + R_r I_{dr} - \omega_r (L_r I_{qr} + M I_{qs}) - \frac{M}{L_s} V_{ds} \right. \\ \quad \left. - \frac{MR_s}{L_s} I_{ds} + \frac{M}{L_s} \omega_s (L_s I_{qs} + M I_{qr}) \right) - \dot{I}_{dr_ref} \\ \ddot{S}_1 = \varphi_1(t, x) + \gamma_1(t, x) \dot{V}_{dr} \end{array} \right. \quad (\text{III.25})$$

and

$$\left\{ \begin{array}{l} \dot{S}_2 = \frac{L_s}{M^2 - L_r L_s} \left(V_{qr} + R_r I_{qr} + \omega_r (L_r I_{dr} + M I_{ds}) - \frac{M}{L_s} V_{qs} \right. \\ \quad \left. - \frac{MR_s}{L_s} I_{qs} - \frac{M}{L_s} \omega_s (L_s I_{ds} + M I_{dr}) \right) - \dot{I}_{qr_ref} \\ \ddot{S}_2 = \varphi_2(t, x) + \gamma_2(t, x) \dot{V}_{qr} \end{array} \right. \quad (\text{III.26})$$

Where $\varphi_1(t, x)$, $\varphi_2(t, x)$, $\gamma_1(t, x)$, and $\gamma_2(t, x)$ are uncertain functions which satisfy

$$\left\{ \begin{array}{l} \varphi_1 > 0, |\varphi_1| > \Phi_1, 0 < \Gamma_{m1} < \gamma_1 < \Gamma_{M1} \\ \varphi_2 > 0, |\varphi_2| > \Phi_2, 0 < \Gamma_{m2} < \gamma_2 < \Gamma_{M2} \end{array} \right. \quad (\text{III.27})$$

The proposed control approach is based on the super-twisting algorithm [99]. The proposed high-order (2nd) sliding mode controller contains two parts.

$$\left\{ \begin{array}{l} V_d = u_1 + u_2 \\ V_q = w_1 + w_2 \end{array} \right. \quad (\text{III.28})$$

$$\text{where } \left\{ \begin{array}{l} \dot{u}_1 = -\alpha_1 \text{sign}(S_1) \\ u_2 = -\beta_1 |S_1|^p \text{sign}(S_1) \end{array} \right. \quad (\text{III.29})$$

$$\text{and } \begin{cases} \dot{w}_1 = -\alpha_2 \text{sign}(S_2) \\ w_2 = -\beta_2 |S_2|^\rho \text{sign}(S_2) \end{cases} \quad (\text{III.30})$$

In order to ensure the convergence of the sliding manifolds to zero in finite-time, the gains can be chosen as follows [72], [111].

$$\begin{cases} \alpha_i > \frac{\Phi_i}{\Gamma_{mi}} \\ \beta_i^2 \geq \frac{4\Phi_i}{\Gamma_{mi}^2} \frac{\Gamma_{Mi}(\alpha_i + \Phi_i)}{\Gamma_{mi}(\alpha_i - \Phi_i)}; \quad i=1,2 \\ 0 < \rho \leq 0.5 \end{cases} \quad (\text{III.31})$$

4.2.1 Simulation Results for a Filtered Resource

In this case, the second-order sliding mode control of the DFIG-based marine current turbine was tested. Tidal current data from the Raz de Sein (Brittany, France) have been used to run simulations of a 7.5-kW prototype over various flow regimes.

For speed references given by the MPPT strategy and a filtered resource (Fig. III.15), the DFIG-based MCT control performances are shown in Figs. III.16 and III.17 respectively illustrating the rotor speed tracking performance and the generated active power.

The obtained results show good tracking performances of the DFIG rotor speed and the generated active power.

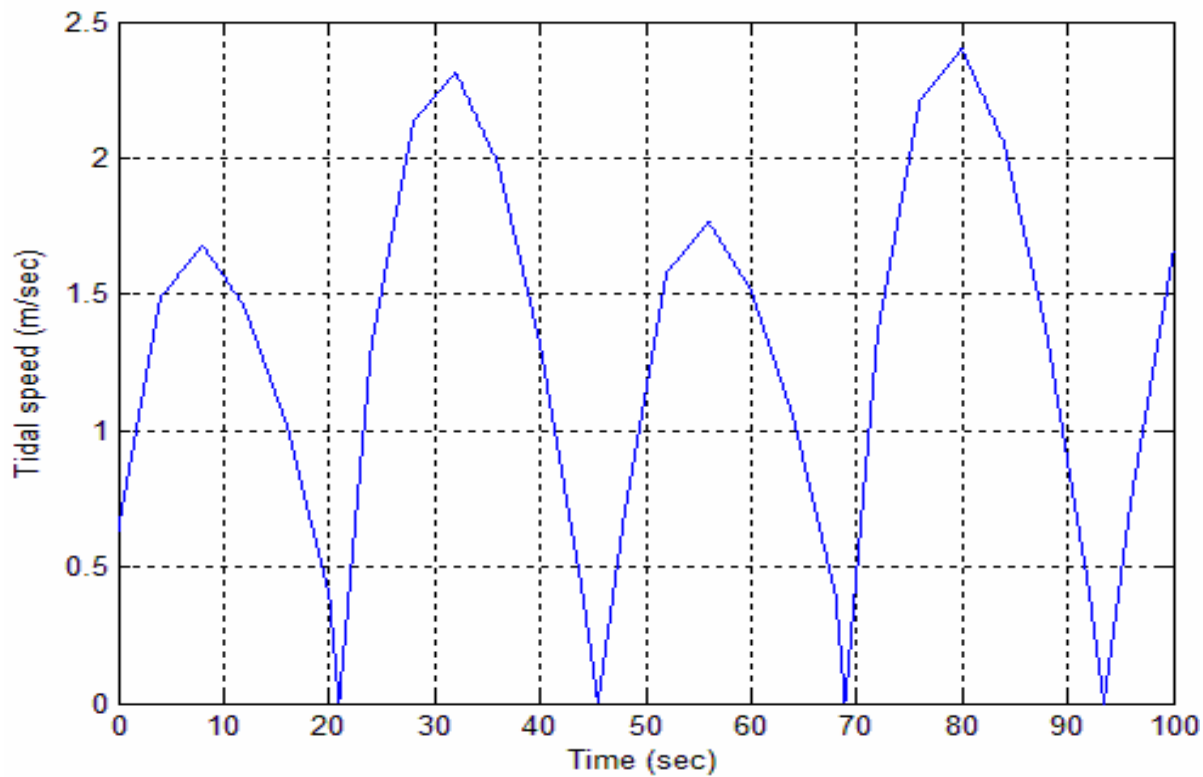


Fig. III.15. Filtered resource speed.

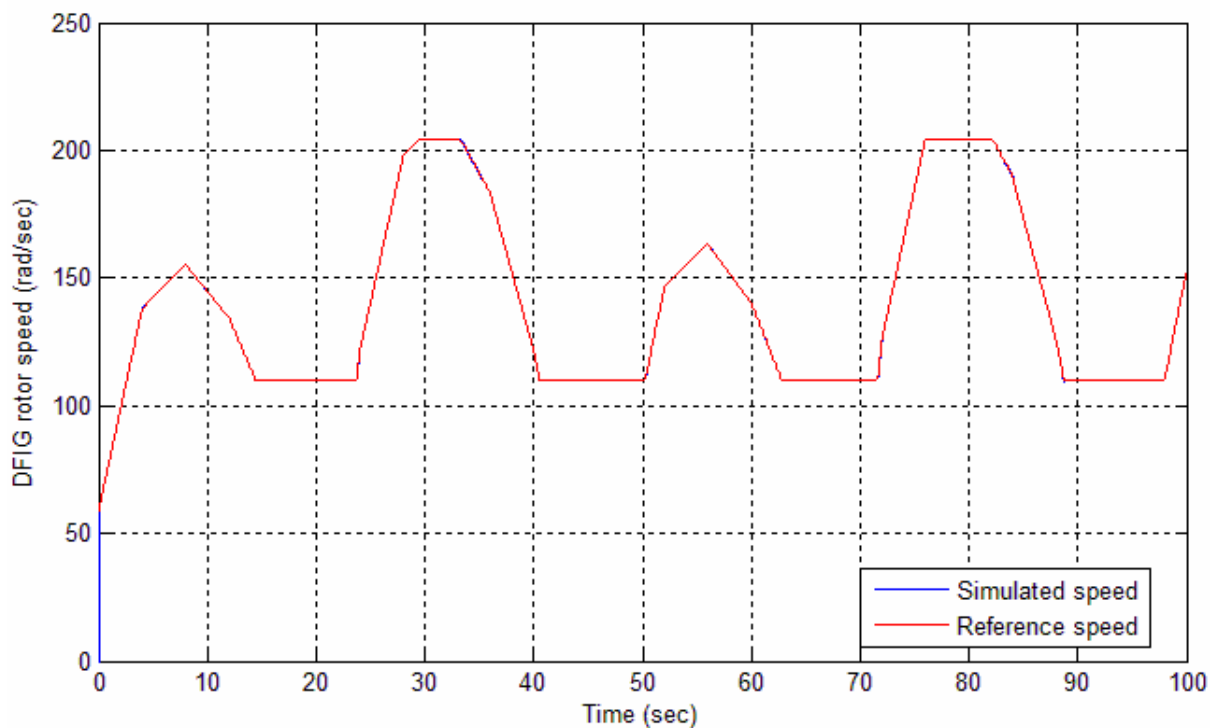


Fig. III.16. The DFIG rotor speed and its reference.

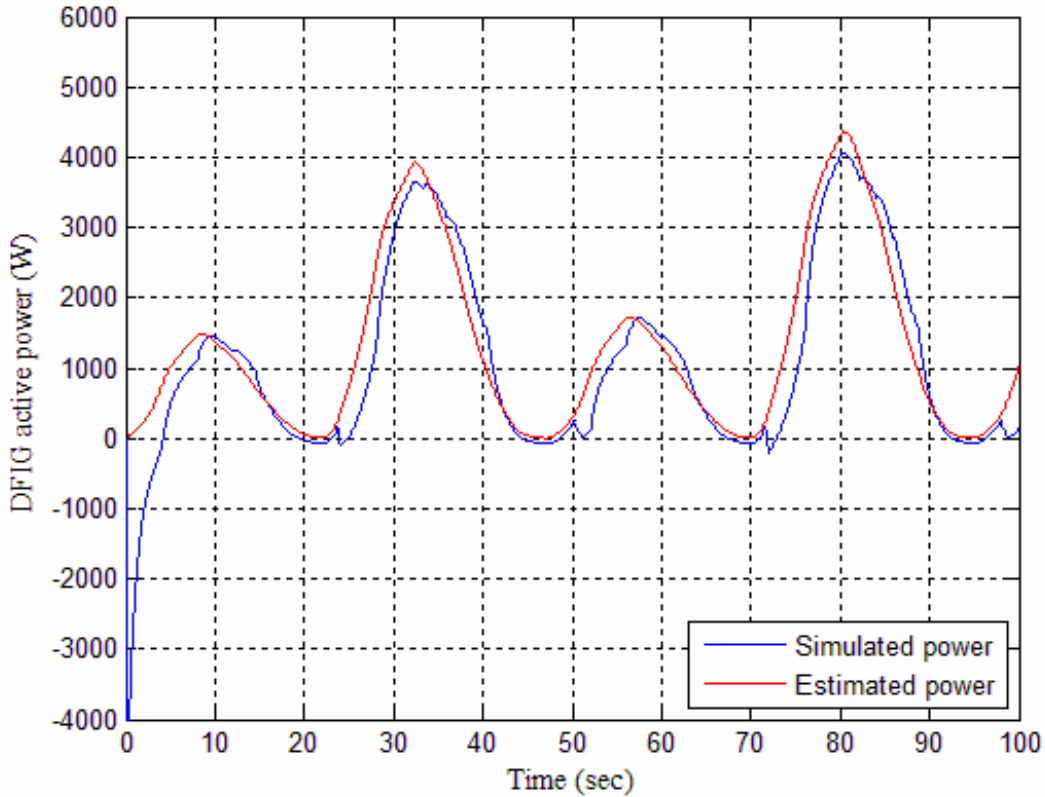


Fig. III.17. The DFIG active power.

4.2.2 *Simulation Results for a Turbulent Resource*

In this second case, the sensibility of the proposed second-order control strategy was analyzed regarding the swell effect. The turbulent resource characteristics are given by Fig. III.18. In this case, the DFIG-based MCT control performances are shown by Figs. III.19 and III.20 respectively illustrating the rotor speed tracking performance and the generated active power. Simulation results shows that the proposed control strategy is effective in terms of speed tracking and power regulation.

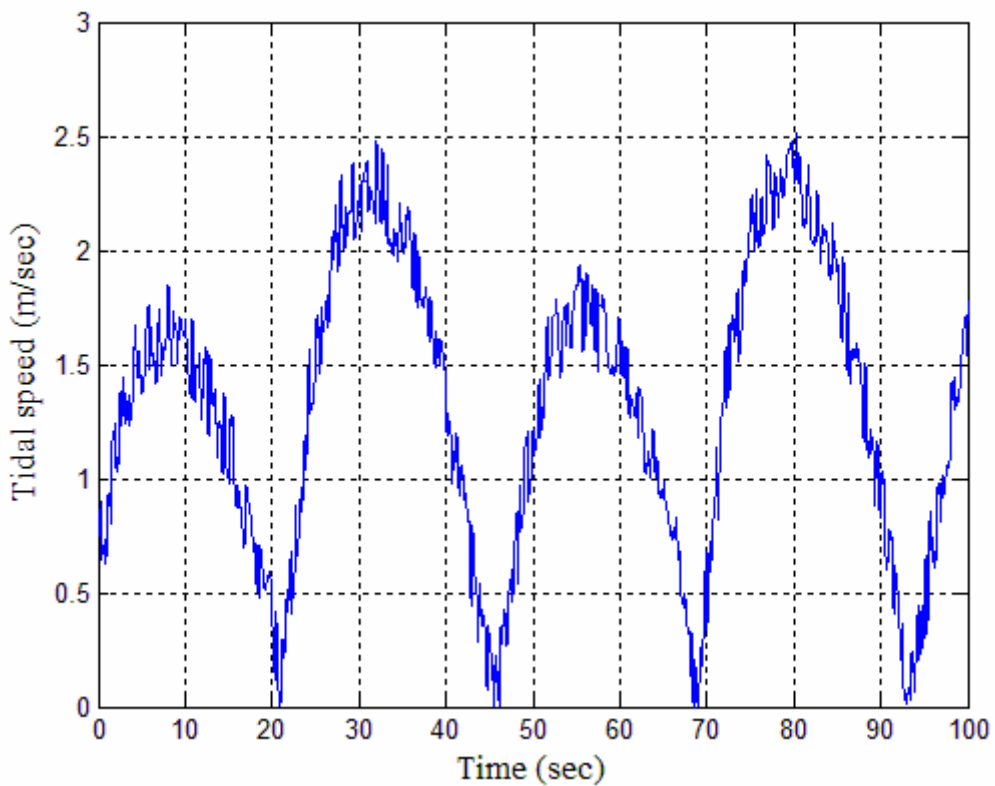


Fig. III.18. Turbulent resource speed.

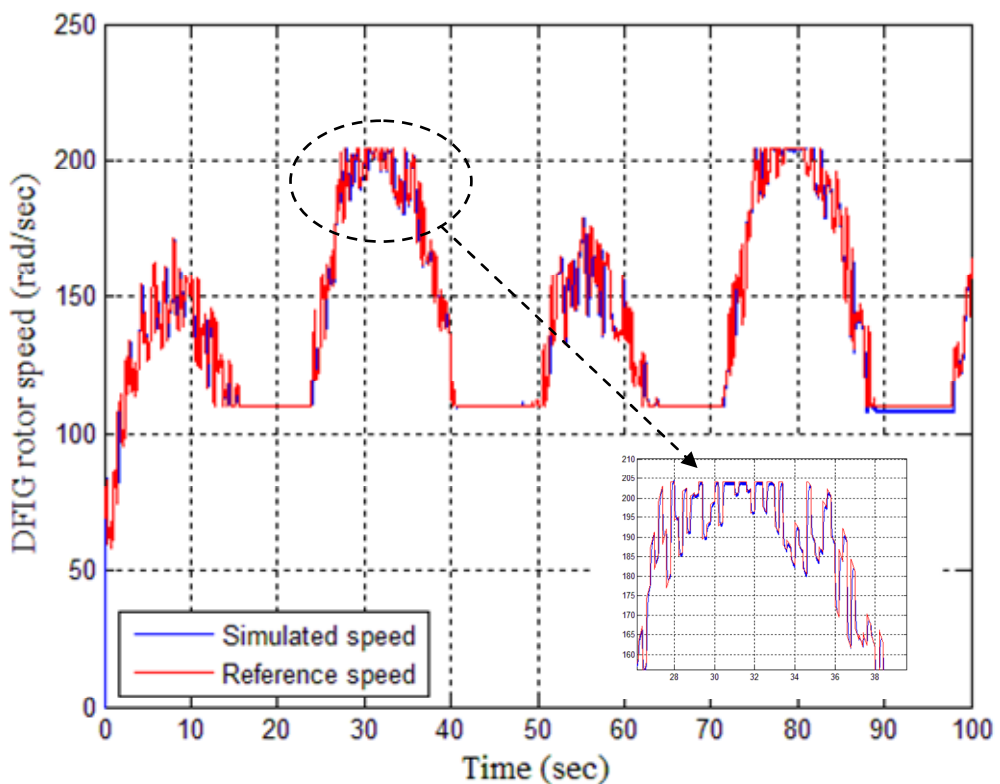


Fig. III.19. The DFIG rotor speed and its reference.

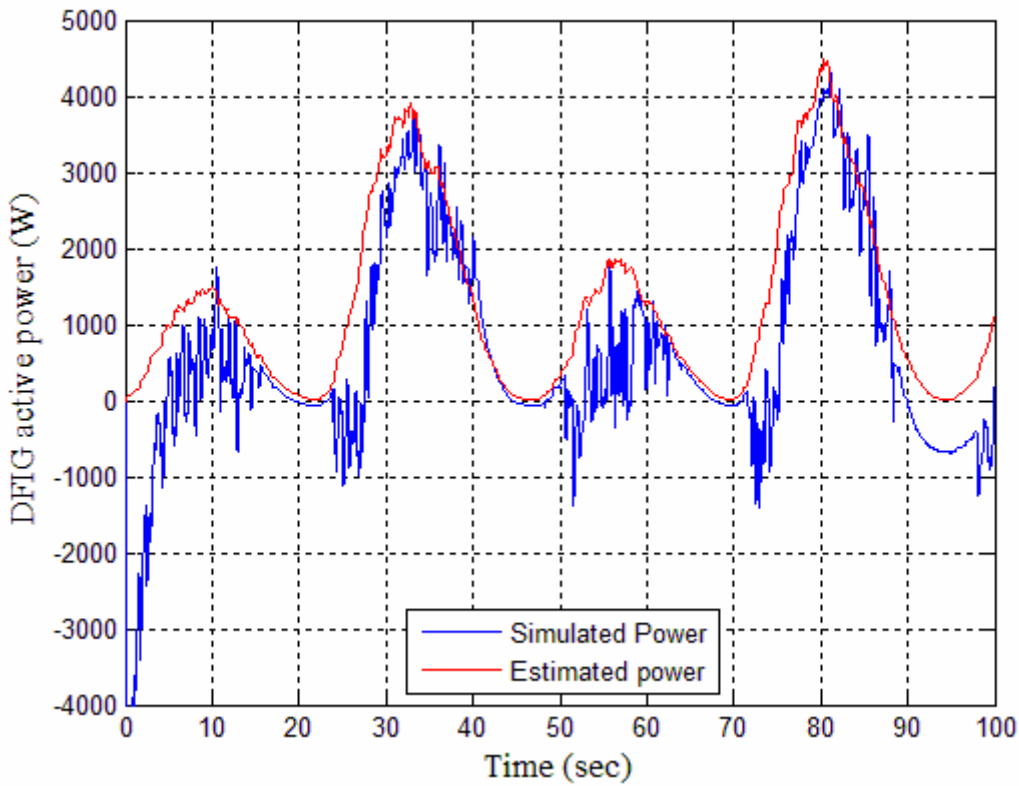


Fig. III.20. The DFIG active power.

4.3 Optimal Control of MCT Driven PMSG by HOSM Speed Control

The above presented second-order sliding mode control strategy has also been tested for a PMSG-based marine current turbine (Fig. III.21) [115].

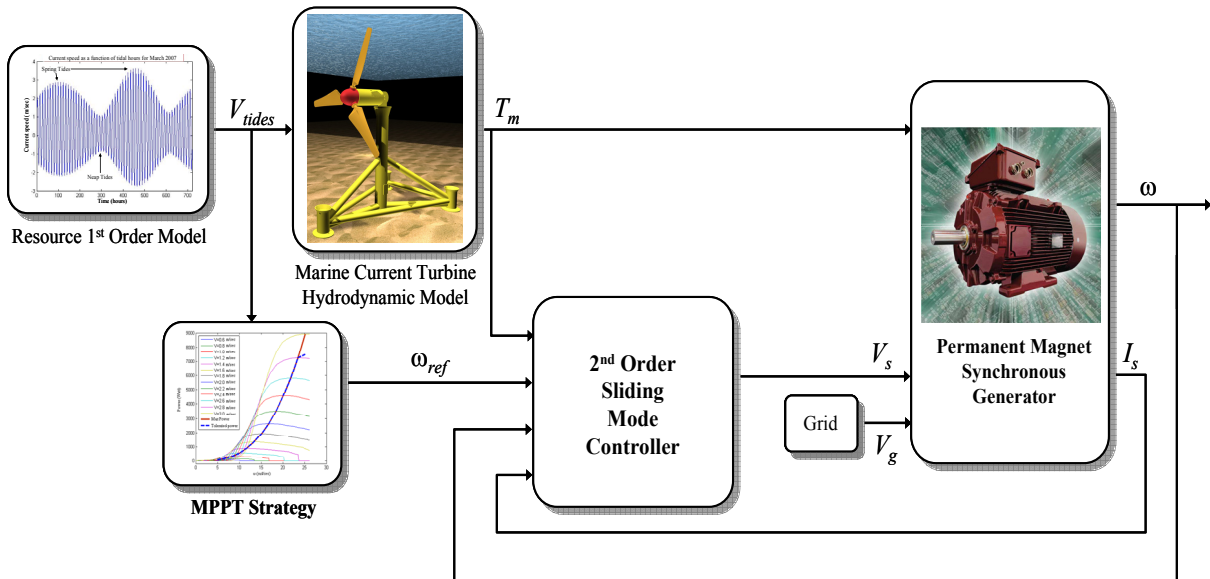


Fig. III.21. The HOSM control scheme for a PMSG-based MCT.

As for a DFIG-based MCT, the proposed control strategy is based on a step-by-step procedure: First, the speed reference ω_{ref} is generated by an MPPT strategy [92]. Then, an optimal electromagnetic torque, which ensures the rotor speed convergence to ω_{ref} is computed using (III.22).

Afterwards, current references are derived to ensure the PMSG torque convergence to the optimal torque.

$$\begin{cases} I_{d_ref} = 0 \\ I_{q_ref} = \frac{2}{3} \frac{T_{em}}{p\phi_f} \end{cases} \quad (\text{III.32})$$

In order to ensure the currents convergence to their references, the second-order sliding mode strategy is used. Let us define the following sliding surfaces.

$$\begin{cases} S_1 = I_d - I_{d_ref} \\ S_2 = I_q - I_{q_ref} \end{cases} \quad (\text{III.33})$$

It follows that

$$\begin{cases} \dot{S}_1 = \dot{I}_d - \dot{I}_{d_ref} \\ \ddot{S}_1 = \varphi_1(t, x) + \gamma_1(t, x)\dot{V}_d \end{cases} \quad (\text{III.34})$$

and

$$\begin{cases} \dot{S}_2 = \dot{I}_q - \dot{I}_{q_ref} \\ \ddot{S}_2 = \varphi_2(t, x) + \gamma_2(t, x)\dot{V}_q \end{cases} \quad (\text{III.35})$$

Where $\varphi_1(t, x)$, $\varphi_2(t, x)$, $\gamma_1(t, x)$, and $\gamma_2(t, x)$ are uncertain bounded functions that satisfy

$$\begin{cases} \varphi_1 > 0, \quad |\varphi_1| > \Phi_1, \quad 0 < \Gamma_{m1} < \gamma_1 < \Gamma_{M1} \\ \varphi_2 > 0, \quad |\varphi_2| > \Phi_2, \quad 0 < \Gamma_{m2} < \gamma_2 < \Gamma_{M2} \end{cases} \quad (\text{III.36})$$

As for a DFIG-based MCT, the super-twisting algorithm was used. The proposed second-order sliding mode controller contains two parts:

$$\begin{cases} V_d = u_1 + u_2 \\ V_q = w_1 + w_2 \end{cases} \quad (\text{III.37})$$

where $\begin{cases} \dot{u}_1 = -\alpha_1 \text{sign}(S_1) \\ u_2 = -\beta_1 |S_1|^\rho \text{sign}(S_1) \end{cases}$ (III.38)

and $\begin{cases} \dot{w}_1 = -\alpha_2 \text{sign}(S_2) \\ w_2 = -\beta_2 |S_2|^\rho \text{sign}(S_2) \end{cases}$ (III.39)

Again, to ensure the convergence of the sliding manifolds to zero in finite-time, the gains can be chosen as follows [106].

$$\begin{cases} \alpha_i > \frac{\Phi_i}{\Gamma_{mi}} \\ \beta_i^2 \geq \frac{4\Phi_i}{\Gamma_{mi}^2} \frac{\Gamma_{Mi}(\alpha_i + \Phi_i)}{\Gamma_{mi}(\alpha_i - \Phi_i)}; \quad i = 1, 2 \\ 0 < \rho \leq 0.5 \end{cases} \quad (\text{III.40})$$

4.3.1 *Simulation Results for a Filtered Resource*

In this case, the second-order sliding mode control of the PMSG-based marine current turbine was tested. Tidal current data from the Raz de Sein (Brittany, France) have been used to run simulations of a 7.5 kW PMSG [Appendix B].

The hydrodynamic loads of the marine current turbine were evaluated for a filtered resource (Fig. III.22). The PMSG-based MCT control performances are shown in Figs. III.23 and III.24 respectively illustrating the rotor speed tracking performance and the generated active power.

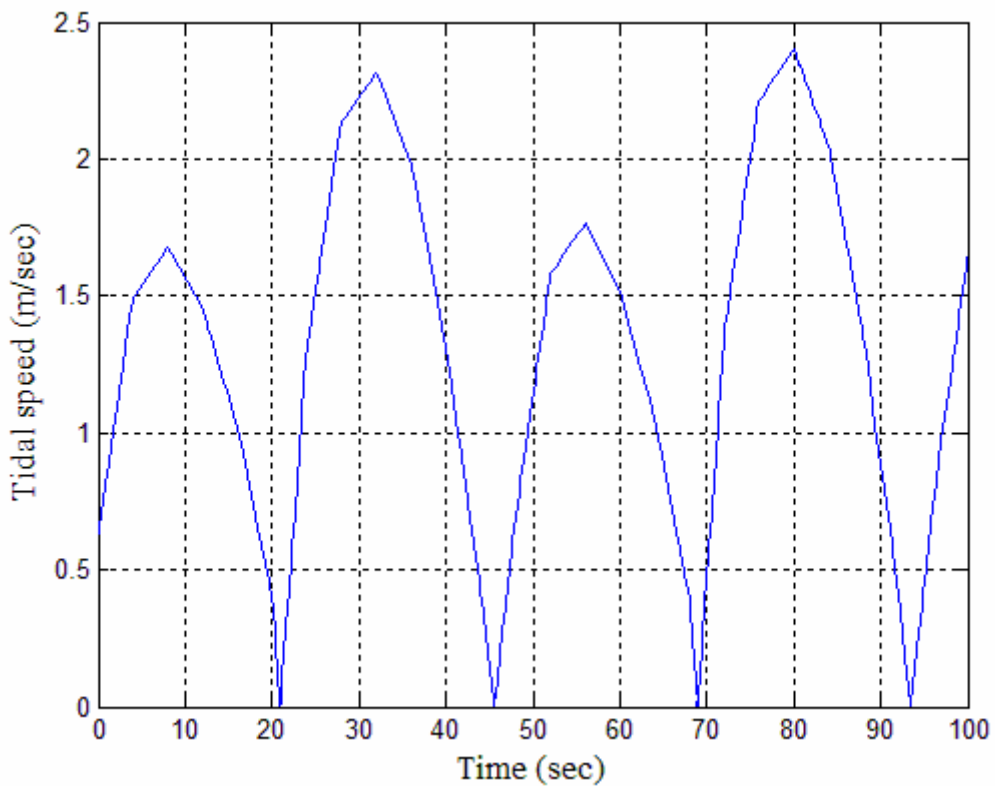


Fig. III.22. Filtered resource speed.

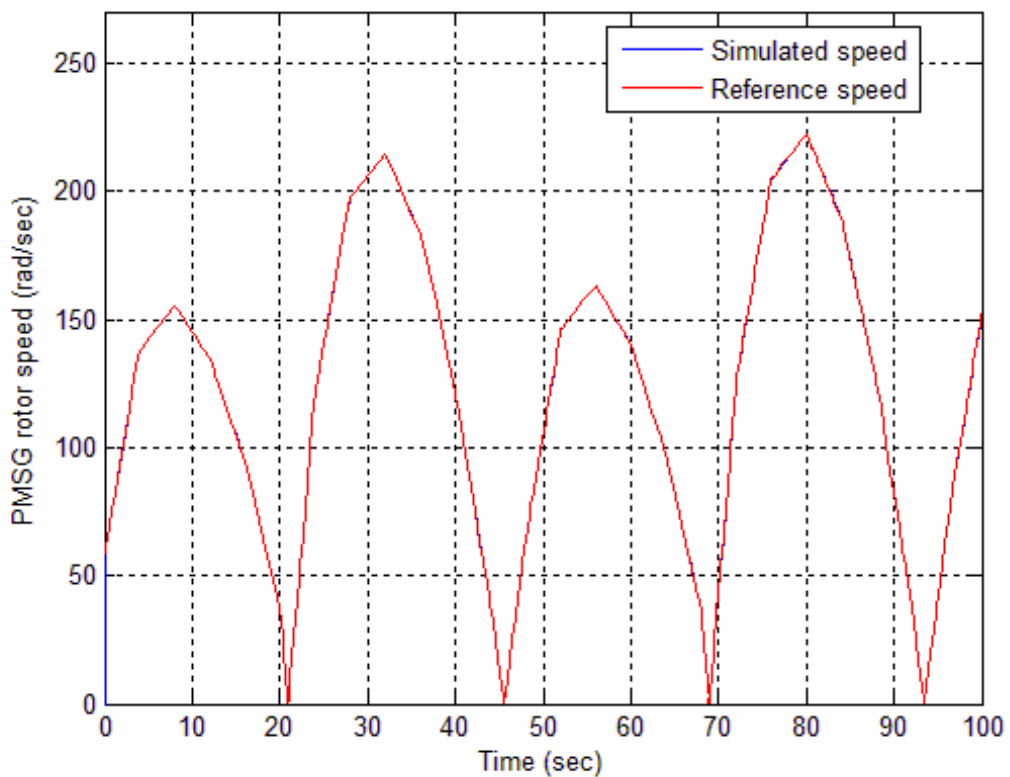


Fig. III.23. The PMSG rotor speed and its reference.

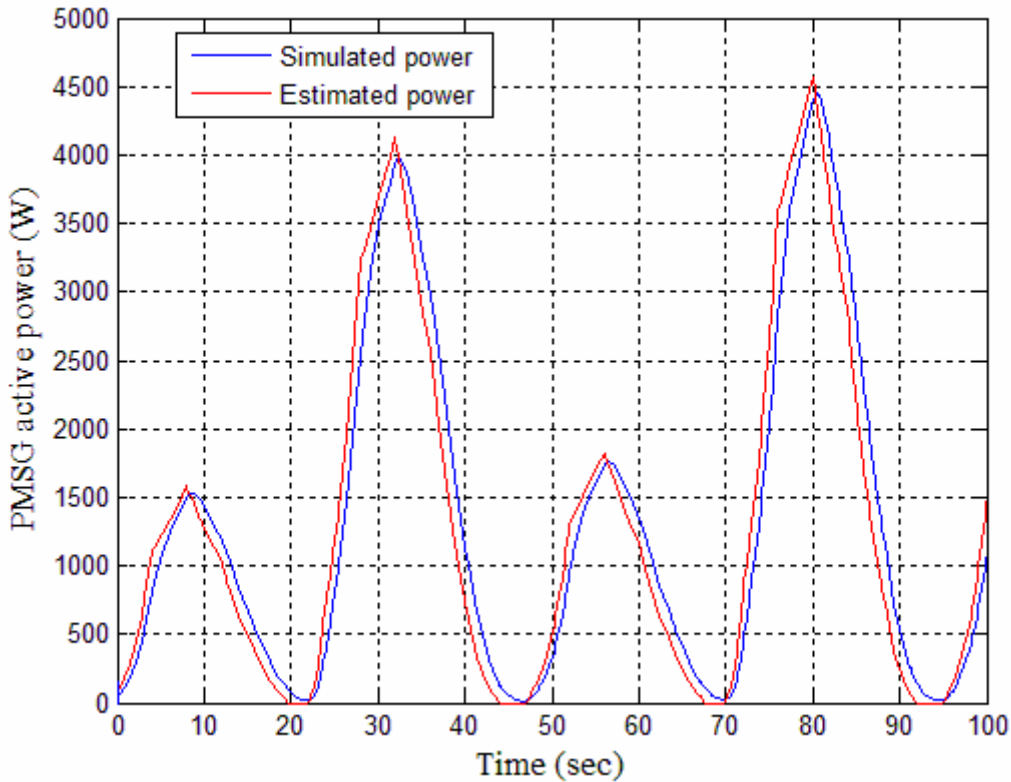


Fig. III.24. The PMSG active power.

The obtained results show good tracking performances of the PMSG rotor speed and the generated active power tracking is greatly improved.

4.3.2 *Simulation Results for a Turbulent Resource*

In this second case, the sensibility of the proposed second-order control strategy was analyzed regarding the swell effect. The turbulent resource characteristics are given by Fig. III.18. In this case, the PMSG-based MCT control performances are shown by Figs. III.25 and III.26 respectively illustrating the rotor speed tracking performance and the generated active power.

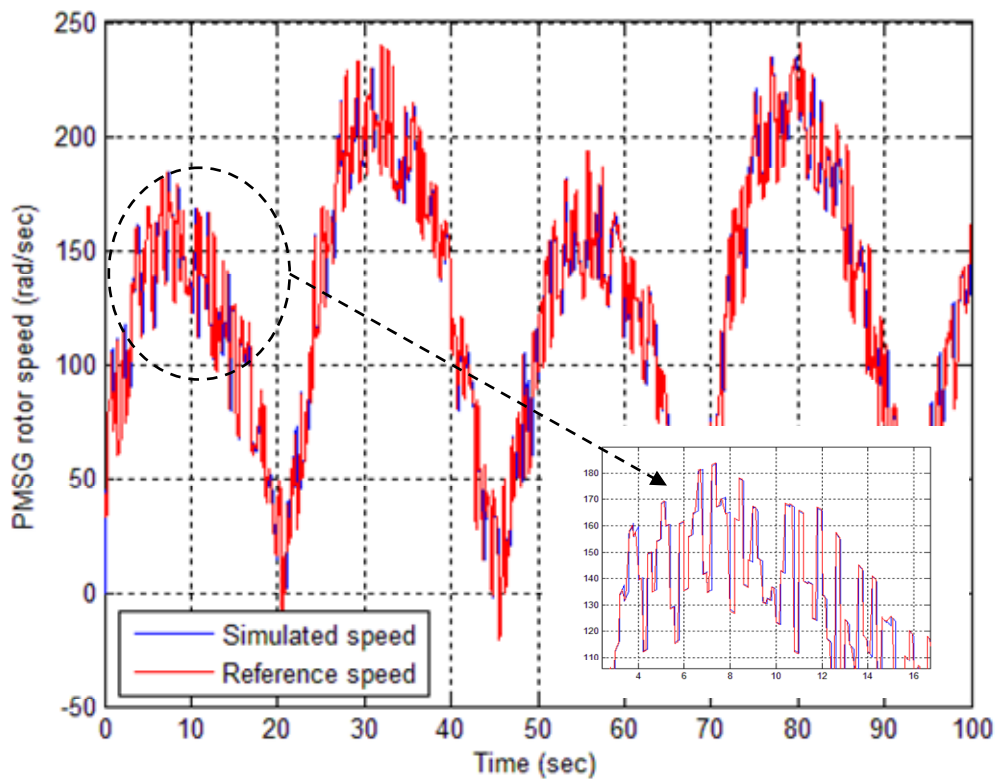


Fig. III. 25. The PMSG rotor speed and its reference.

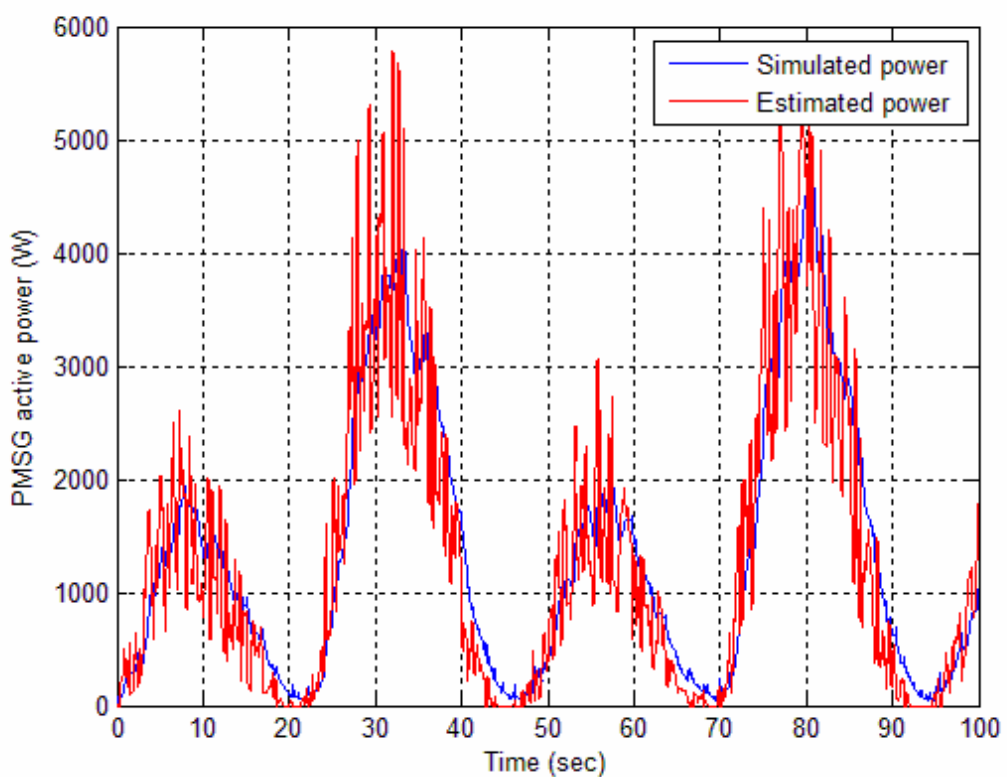


Fig. III. 26. The PMSG active power.

Simulation results shows that the proposed second-order sliding control strategy is effective in terms of speed tracking and power regulation. Moreover, the sensitivity of the proposed control strategy has been analyzed regarding the swell effect.

In Figure III.26, many peaks appeared in the generated power. This is due to the acceleration and deceleration of the turbine speed due to the swell effect. Indeed, any variation of the fluid speed induces consequently a variation of the rotor speed reference which is deduced from the MPPT strategy.

Despite the fact that the control strategy is very efficient in terms of speed tracking, the marine current turbine becomes very sensitive to a high-frequency swell effect. To deal with this problem, the tidal speed must be filtered to avoid such peaks in the generated power.

4.4 HOSM Control Robustness Against Parameter Variations

In this part, the robustness of the high-order sliding mode control is briefly evaluated according to a well-known parameter variation: DFIG stator resistance. Indeed, The DFIG model was modified such as the stator resistance can vary during simulations. The variation of this parameter reaches 200% of its initial value (Fig. III.27).

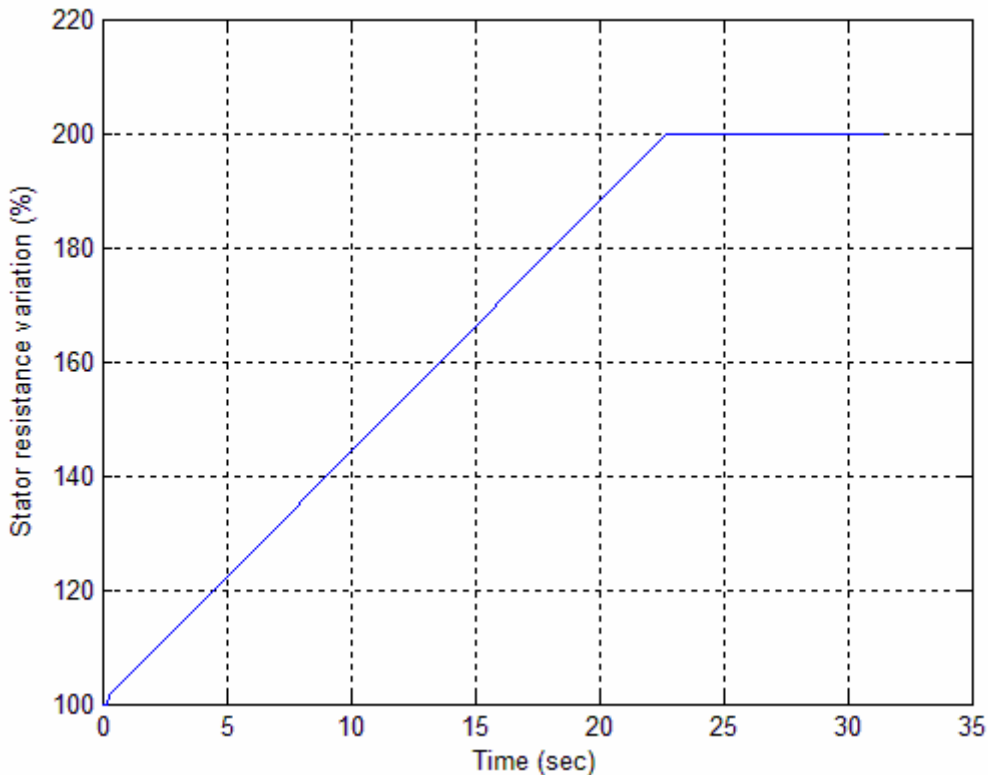


Fig. III. 27. DFIG stator resistance Variation

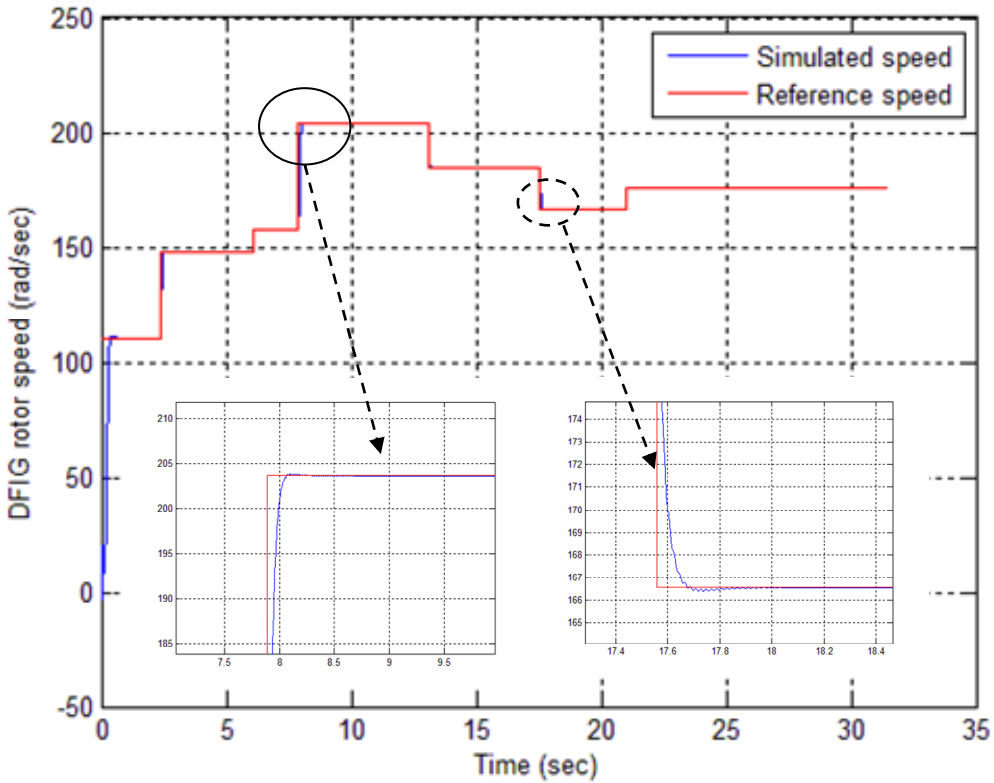


Fig. III.28. DFIG rotor speed and its reference.

In spite of the resistance variation, the DFIG rotor speed shows good tracking performances (Fig. III.28). During simulations, the rotor speed reference was changed many times to evaluate the convergence of the control strategy in terms of acceleration and deceleration. PI control robustness was also evaluated according to parametric variation. Simulations were carried out in the same conditions. However, the simulation results were not relevant. Indeed, the convergence of the control strategy was heavily related to the rotor speed reference variation.

III.5 COMPARISON

In this section, a comparison between both of the control strategies was fulfilled through different case studies for DFIG- and PMSG-based MCT. It should be noted that the carried out simulations will also allow the evaluation of the resource model and its impact on the generated power. Therefore, three types of resources taking into account external disturbance have been simulated in different cases summarized in Table III.1. In the considered cases, the comparison is mainly based on the tidal speed values V_{real} and V_{ref} . Indeed, V_{real} is the tidal

speed used as an input for the marine current turbine model. V_{ref} is the value of the tidal speed used as in input for the MPPT strategies (Fig. III.29).

The simulation time has been chosen to evaluate the influence of swell and sea surface effect disturbances which have time constants or periods of few seconds. In these conditions, the predicted average value of the tidal speed is assumed to be constant and equal to 2 m/sec (4 knots).

In the simulated cases, several waveforms for the tidal speed with and without disturbances have been considered. The three taken resource values are composed by the kinetic speed, the swell disturbance, and a random signal $b(t)$ that represents all the other disturbances.

The simulated cases can be divided in two categories. The first one gathers cases 1 and 2, in which, V_{real} and V_{ref} were set equal. Therefore, it is supposed that the tidal speed is well known. These cases give an idea about the performances of both control strategies in ideal operating conditions.

However, the second category gathers the cases 3, 4 and 5. These cases allow the use of the tidal predicted average speed as a reference for the MPPT calculations and therefore allow a sensorless control (no needs for tidal speed sensor for the MCT). Through these simulations, the robustness of the control strategies was evaluated.

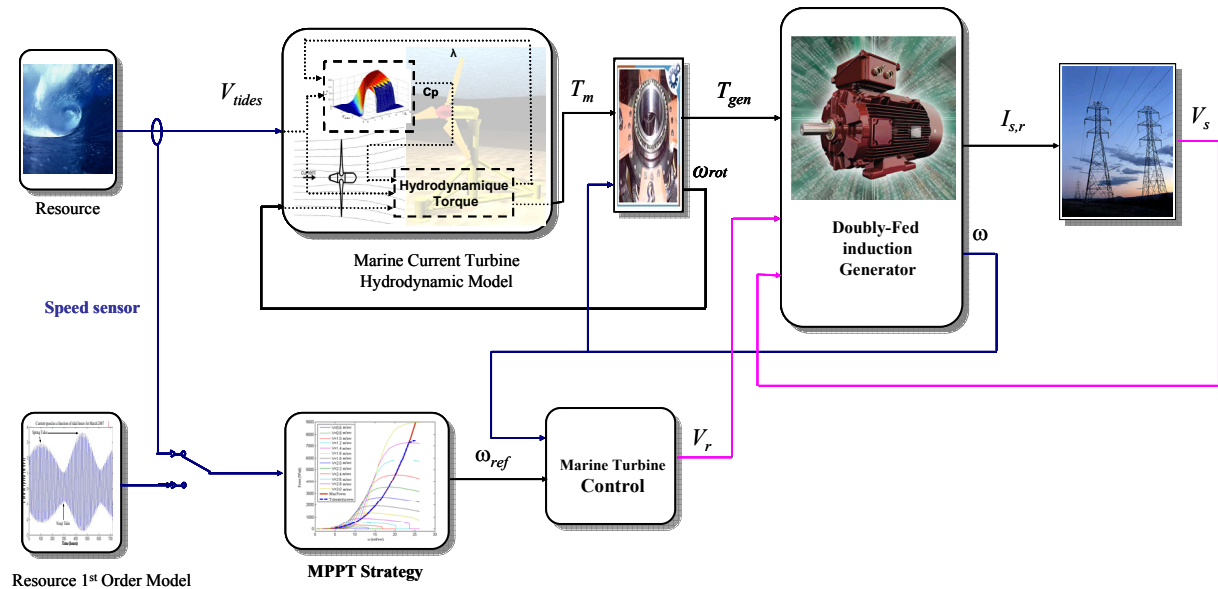


Fig. III.29. DFIG-based MCT control scheme.

Table III. 1. The simulated cases.

Case	Simulation Conditions / Tidal speed (m/sec)	Average Power (kW)			
		DFIG (7.5 kW)		PMSG (7.5 kW)	
		PI	HOSM	PI	HOSM
1	$V_{real} = 2$ $V_{ref} = 2$	2.518	2.483	2.521	2.492
2	$V_{real} = 2 + 0.3252 \cos(0.4189t) + 0.2749 \cos(0.6283t)$ $V_{ref} = 2 + 0.3252 \cos(0.4189t) + 0.2749 \cos(0.6283t)$	2.694	2.565	2.650	2.609
3	$V_{real} = 2 + 0.3252 \cos(0.4189t) + 0.2749 \cos(0.6283t)$ $V_{ref} = 2$	2.449	2.676	2.443	2.692
4	$V_{real} = 2 + 0.3252 \cos(0.4189t) + 0.2749 \cos(0.6283t) + b(t)$ $V_{ref} = 2$	2.397	2.631	2.5452	2.790
5	$V_{real} = 2 + 0.3252 \cos(0.4189t) + 0.2749 \cos(0.6283t) + b(t)$ $V_{ref} = 2 + 0.3252 \cos(0.4189t) + 0.2749 \cos(0.6283t)$	2.573	2.788	2.607	2.811

For all simulations, PI and HOSM parameters are set in such a way that PI control performances are better than the HOSM ones in an ideal condition (cases 1 and 2). The obtained results prove, for both generators, that HOSM control is more adapted when the tidal speed is not well known (cases 3, 4 and 5). Indeed, in these three cases, it can be noted that the generated power is more important than those given by the PI control.

It should be noted, that the average active power is limited under 3 kW due to the use of a small turbine (1.44 m of diameter).

For illustration and for a DFIG-based MCT, Figs. III.30 to III.33 shows the DFIG rotor speeds and the corresponding generated active powers for some of Table III.1 cases. The obtained results prove that the adopted first order model that predicts the resource tidal speed is quite efficient as a reference for the MPPT control block.

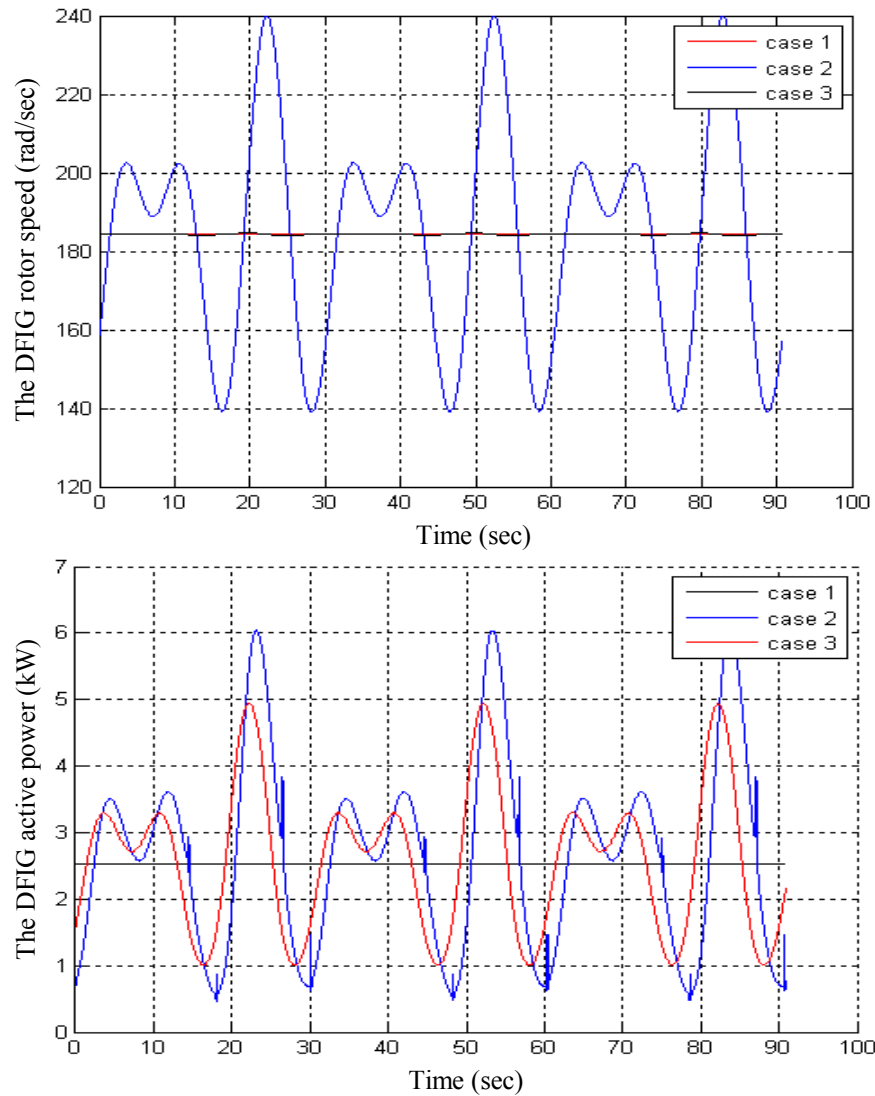
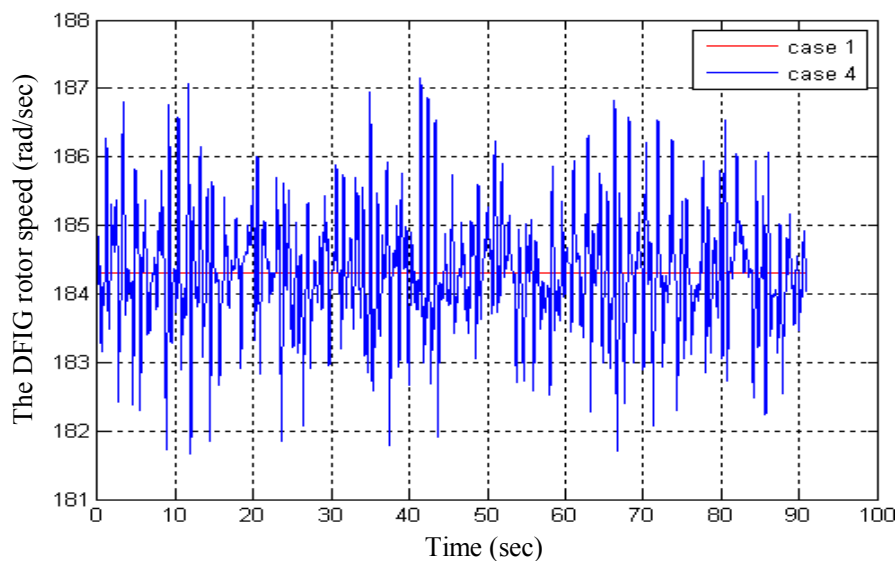


Fig. III.30. The DFIG rotor speed and generated active power
for a turbulent resource for cases 1, 2 and 3 (PI control).



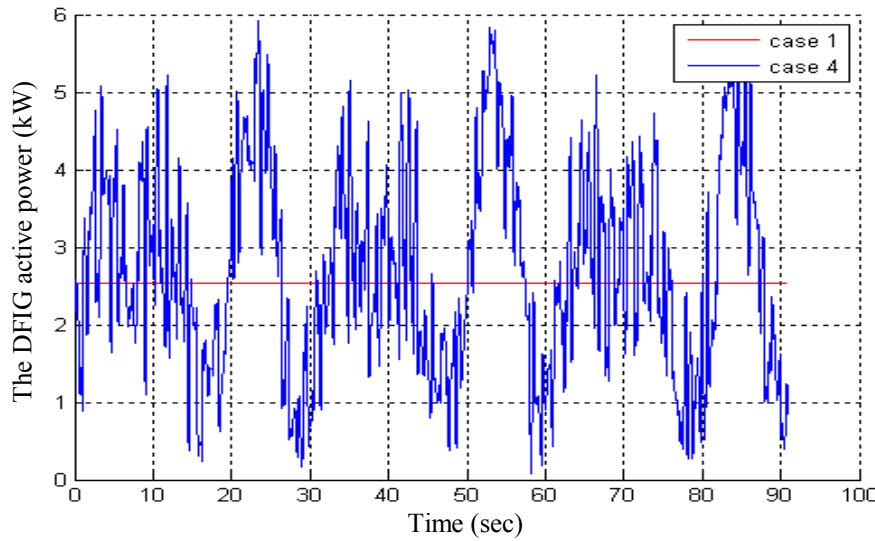


Fig. III.31. The DFIG rotor speed and generated active power for a turbulent resource for cases 1 and 4 (HOSM control).

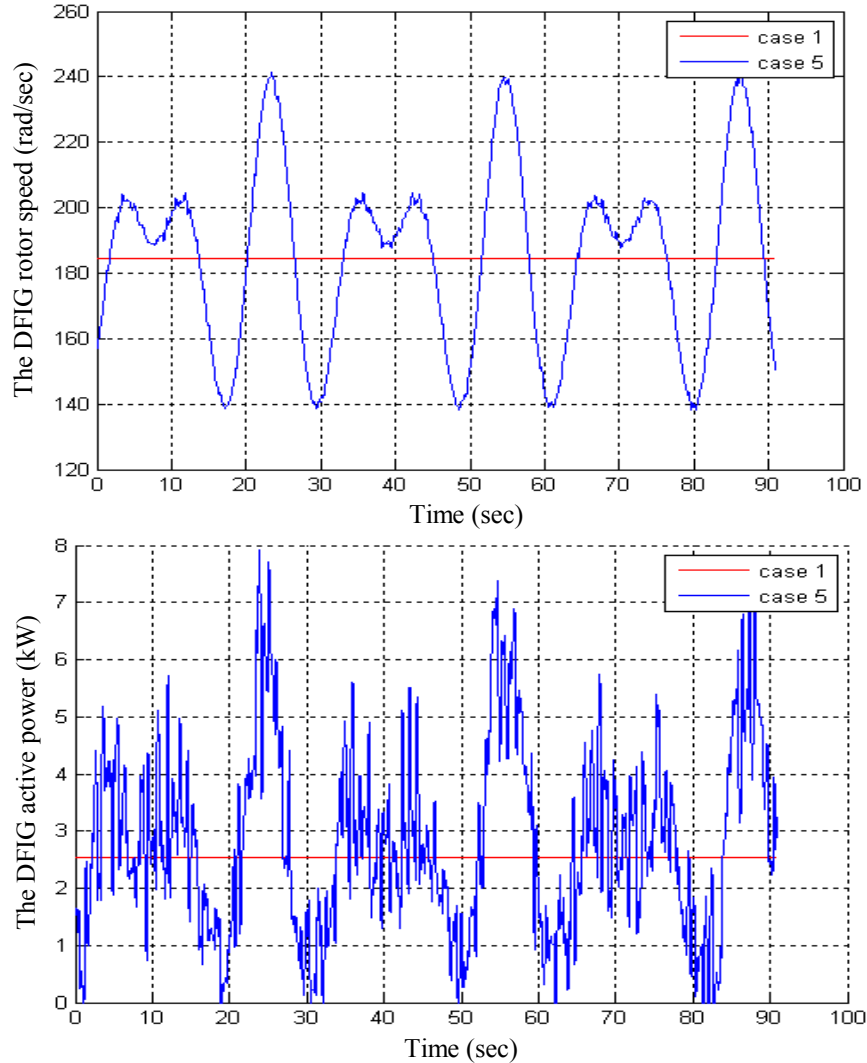


Fig. III.32. The DFIG rotor speed and generated active power for a turbulent resource for cases 1 and 5 (HOSM control).

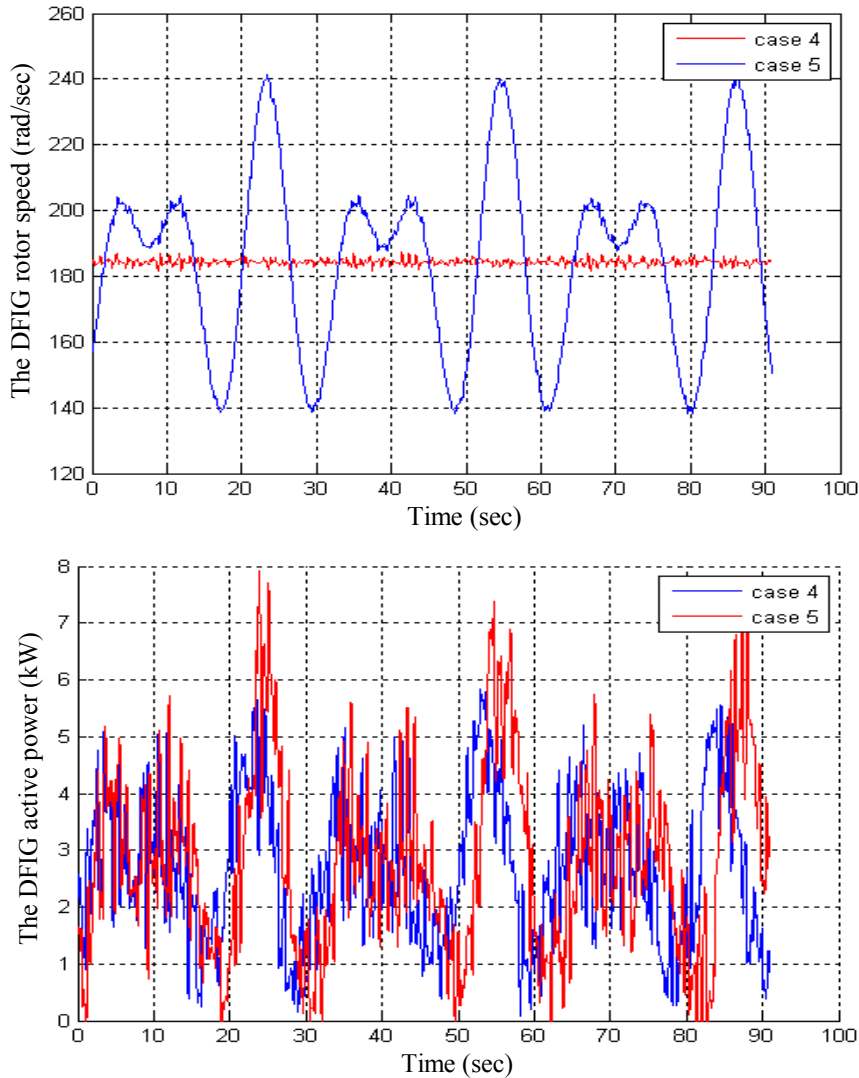


Fig. III.33. The DFIG rotor speed and generated active power for a turbulent resource for cases 4 and 5 (HOSM control).

III.6 CONCLUSION

In this chapter, two control strategy families were evaluated for both DFIG- and PMSG-based marine current turbines: classical PI control and more advanced control techniques, namely high-order sliding mode.

As the swell effect is considered as the most disturbing one for the tidal resource, the sensitivity of the proposed control strategies has been also evaluated.

The obtained results are very encouraging. Indeed, they prove that the adopted first order model that predicts the resource tidal speed is quite efficient as a reference for the MPPT control block. Furthermore, simulation results also show that high-order sliding mode (second-order) control seems to be a good candidate when the resource is not well-known and even if the resource is heavily disturbed.



Chapter
IV

**Validation
and Experimental Analysis**

IV.1	INTRODUCTION	106
IV.2	HARDWARE SPECIFICATIONS	106
IV.3	CONTROL OF A DOUBLY-FED INDUCTION GENERATOR.....	108
3.1	EXPERIMENTAL RESULTS FOR A FILTERED RESOURCE	109
3.2	EXPERIMENTAL RESULTS FOR A TURBULENT RESOURCE	113
IV.4	CONTROL OF A PERMANENT MAGNET SYNCHRONOUS GENERATOR.....	116
4.1	EXPERIMENTAL RESULTS FOR A FILTERED RESOURCE	116
4.2	EXPERIMENTAL RESULTS FOR A TURBULENT RESOURCE	119
IV.5	COMPARISON.....	121
IV.6	CONCLUSION	123

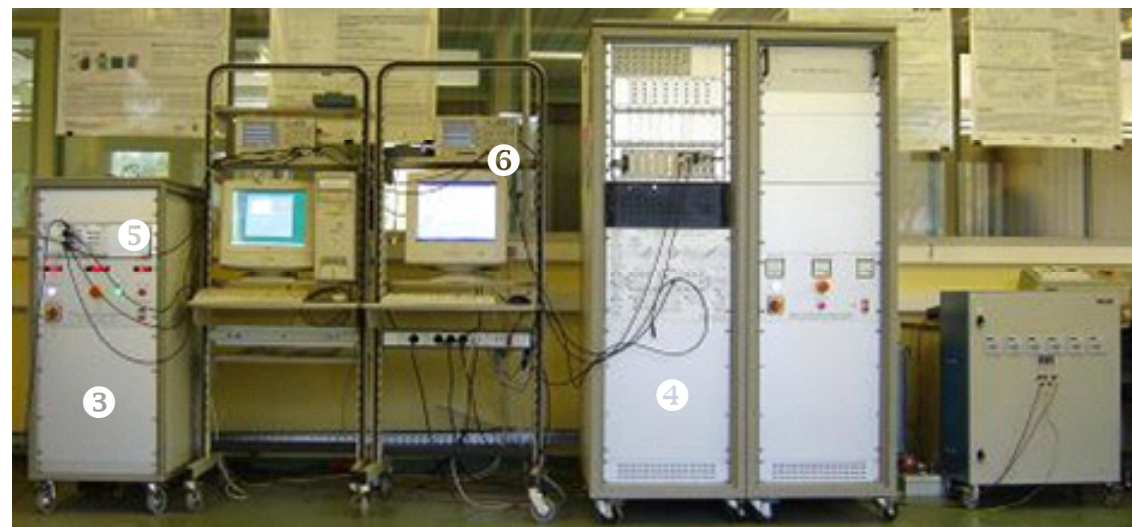
IV.1 INTRODUCTION

For experimental validation of the above-presented control strategies, for both DFIG and PMSG, experiments were carried out using the Grenoble Institute of Technology, France (G2Elab) renewable energy test bench [118-119].

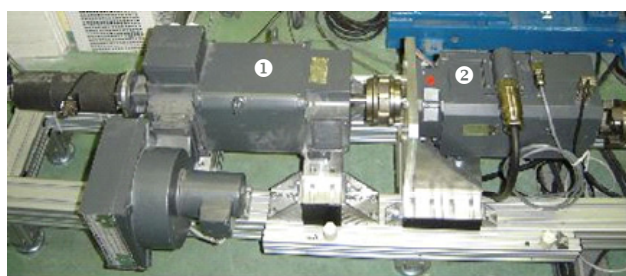
IV.2 HARDWARE SPECIFICATIONS

The test bench presented in Fig. IV.1 allows the physical simulation of the marine power system. The laboratory setup, used to evaluate the MCT performances, consists of 4 parts:

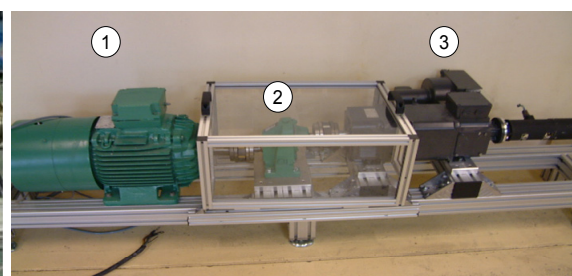
- A DC motor used to emulate the MCT. It reproduces the torque and the inertia with respect to tidal speeds. The DC motor is controlled versus a 4 quadrant inverter by a signal processor DSP TMS 320F240 (Fig. IV.1).



(a)



(b)



(c)

Fig. IV.1. Components of the G2Elab test bench, Grenoble, France:
 (b) ① DC motor, ② PMSG, (c) ① DC motor, ② DFIG, ③ Gearbox (a) ③ Power electronics for driving the DC motor, ④ Power electronics for driving the PMSG, ⑤ DSP TMS320F240 implementing DC motor control, ⑥ DSP DS1005 (dSPACE) implementing DFIG- and PMSG-based MCT control.

- A DFIG and a PMSG are successively used as the MCT generator. Both of the generators are coupled to the DC motor and connected to the grid versus power electronics (Figs. IV.2 and IV.3).
- Power electronics are used in order to control the generators in both topologies and to maintain the DC bus at the desired reference.
- Graphic Interface TESTPOINT: allow the real time modification of the model and the control parameters.

The main advantage of the used test bench is its flexibility [Appendix C]. Indeed, the desired control strategies, already tested in Simulink, can be automatically implemented into the DSP. Moreover, the established and simulated models can be easily modified.

To ensure this flexibility, several software tools are used (Fig. IV.3).

- **Matlab/Simulink[®]** is used for the studied system modeling and the control design and evaluation.
- **RTI** (Real Time Interface) is a dSPACE library including different blocks which allow the implementation of the desired control. These blocks correspond to the Input/Output system and measure block.
- **RTW** (Real Time Workshop) compiles the Simulink files and adapts them to be loaded into the DSP.

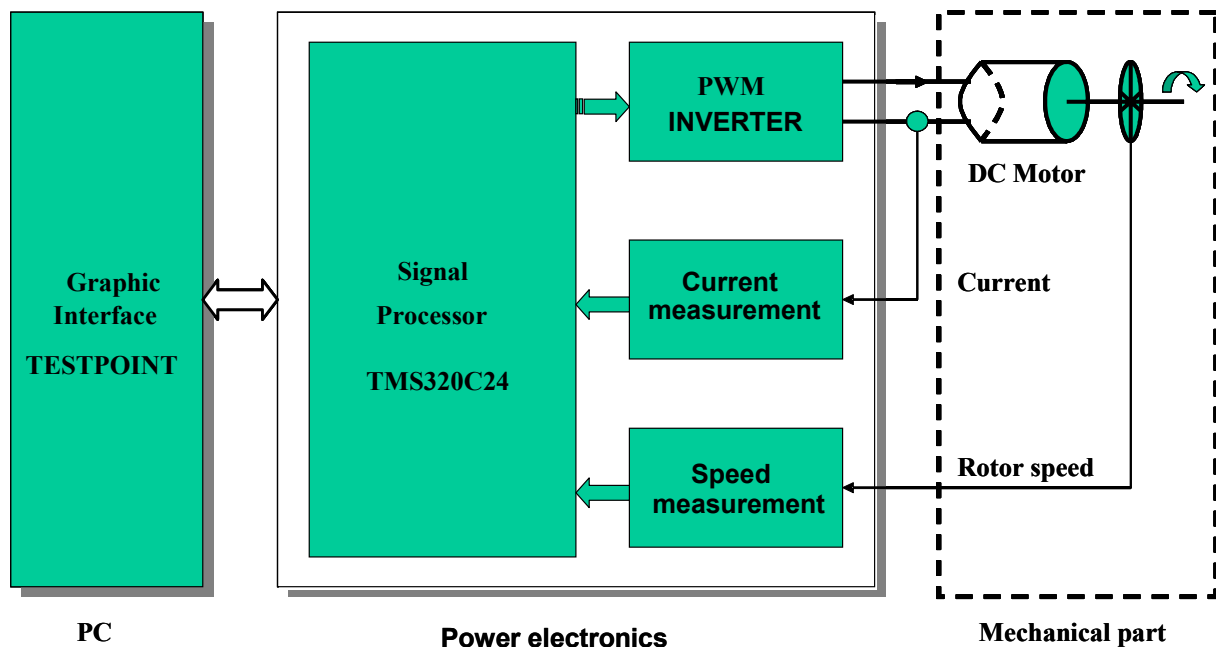


Fig. IV.2. MCT emulator part of the test bench [©G2Elab].

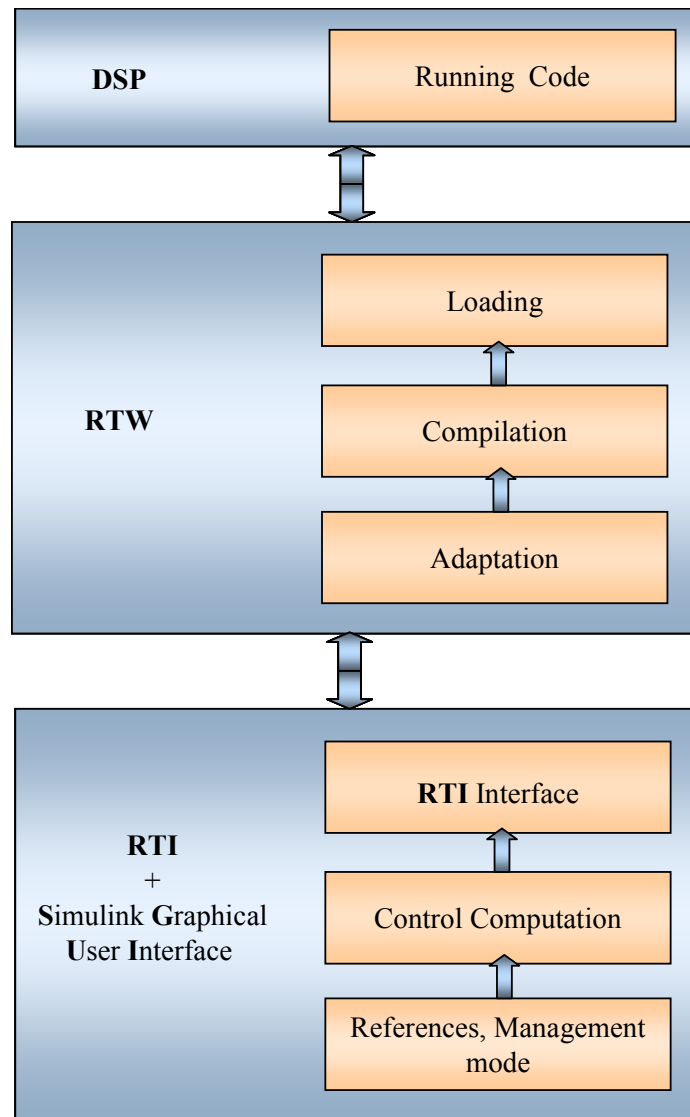


Fig. IV.3. Software tools.

IV.3 CONTROL OF A DOUBLY-FED INDUCTION GENERATOR

The experimental tests were carried out to be as close as possible to the simulation conditions for the marine current turbine described in (§ III.4.2). In these conditions, Fig. IV.4 shows the experimental configuration of the emulated DFIG-based MCT.

In this case, the DFIG-based MCT second-order sliding mode control was tested. To emulate the marine turbine, the DC motor ensures the equivalent mechanical torque of the resource, turbine and gearbox. Indeed, through the hydrodynamic model, already implemented and tested (§ II.2, § II.3 and § II.4), a mechanical torque T_m was generated. It is therefore used as a reference for the direct torque control of the DC motor.

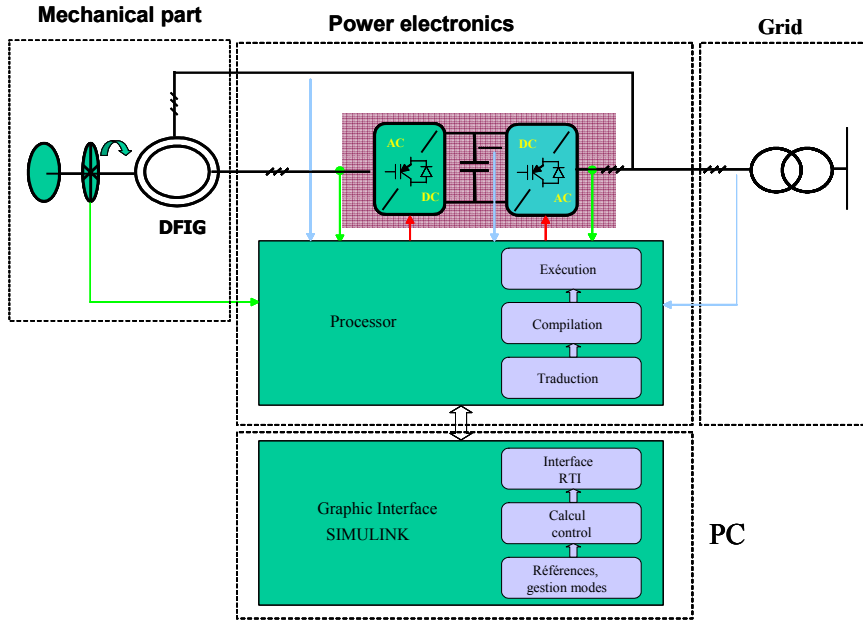


Fig. IV.4. Control of the doubly-fed induction generator [©G2Elab].

3.1 Experimental Results for a Filtered Resource

During experiments, tidal current data from the Raz de Sein (Brittany, France) (Fig. IV.5) have been used to generate the mechanical torque T_m (Fig. IV.6) the DFIG rotor speed variations were limited to $\pm 50\%$ around the rated speed (Fig. IV.7).

For speed references given by the MPPT strategy (§ III.2) and the filtered resource (Fig. IV.5), the DFIG-based MCT control performances are shown by Figs. IV.7 to IV.11 respectively illustrating the rotor speed, currents and the generated active power.

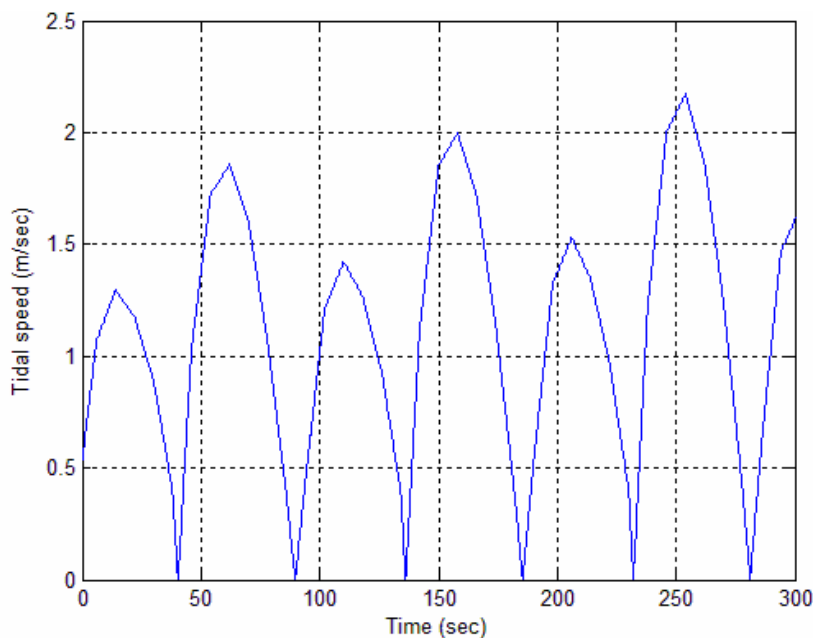


Fig. IV.5. Filtered resource speed.

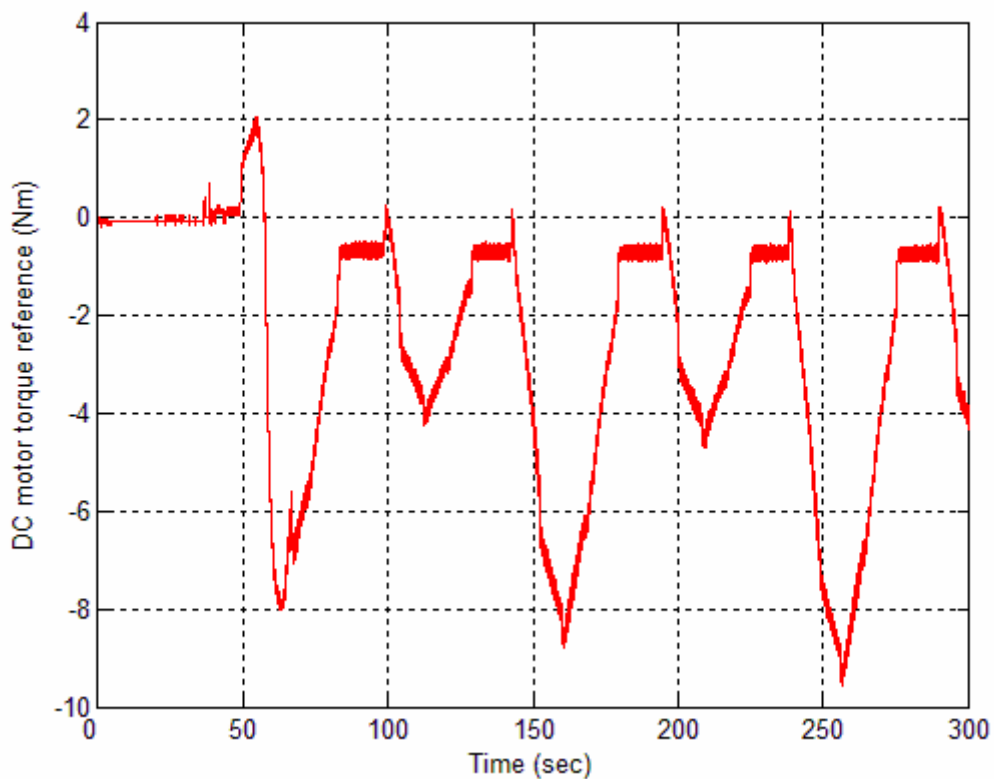


Fig. IV.6. DC motor torque reference.

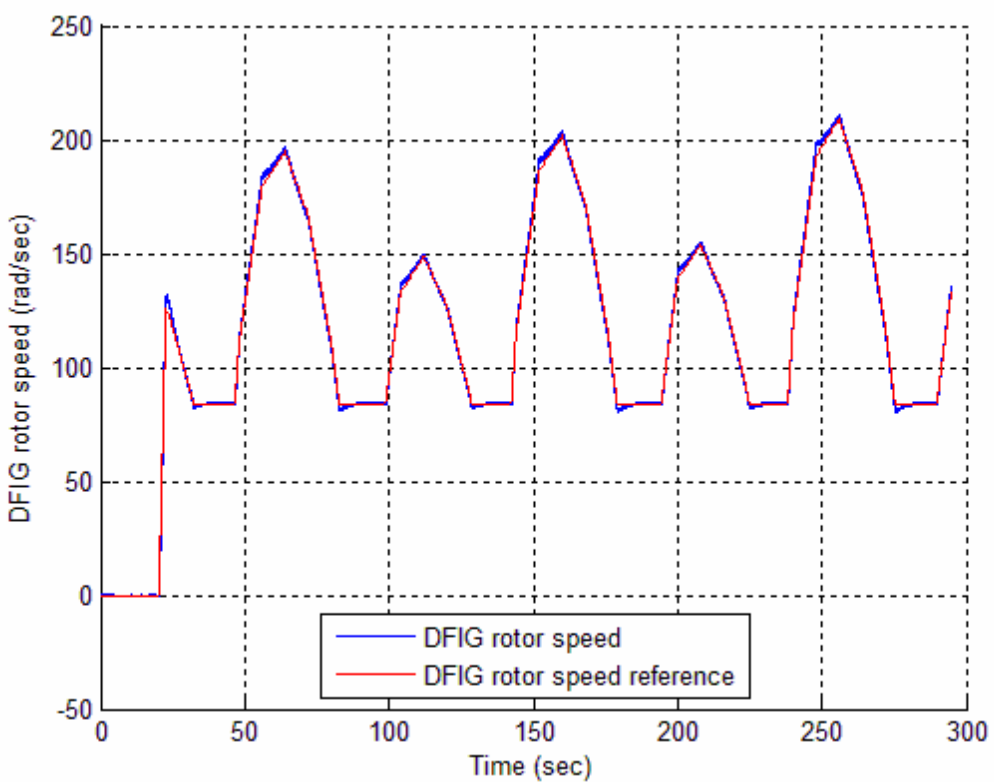


Fig. IV.7. The DFIG rotor speed and its reference.

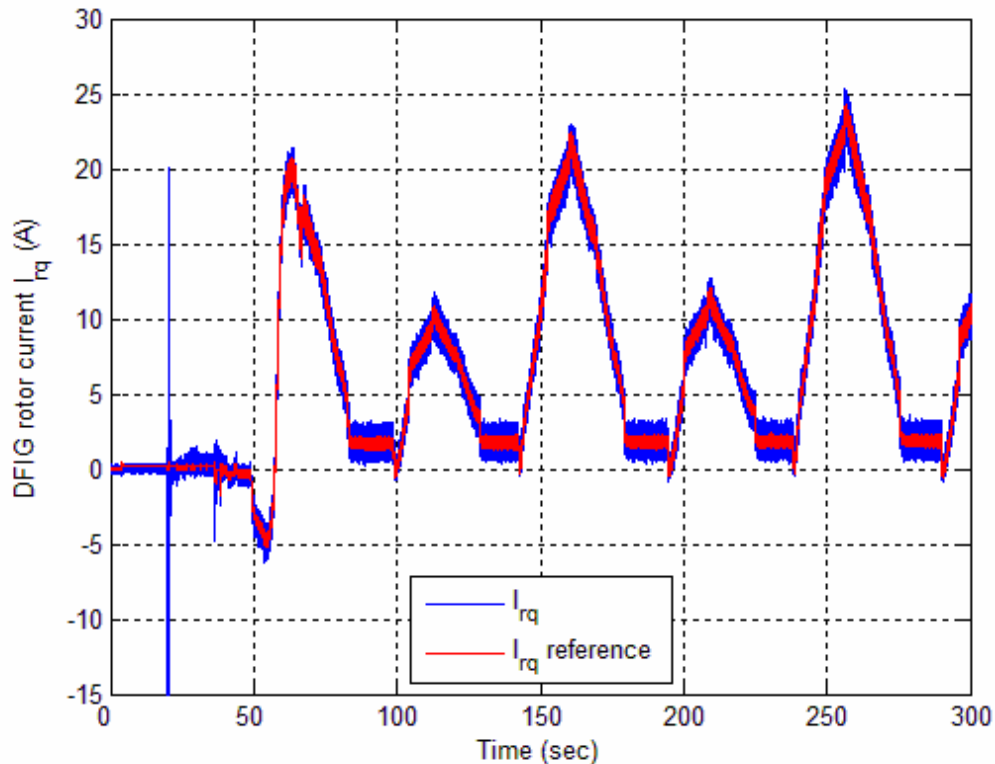


Fig. IV.8. Experimental DFIG I_{rq} current tracking performances.

For security reasons and as shown in Figs. IV.7 and IV.8, a few second are needed to ensure the grid connection. However, the obtained results, as in simulations, show very good tracking performances in terms of the DFIG rotor speed (Fig. IV.7) and current (Fig. IV.8).

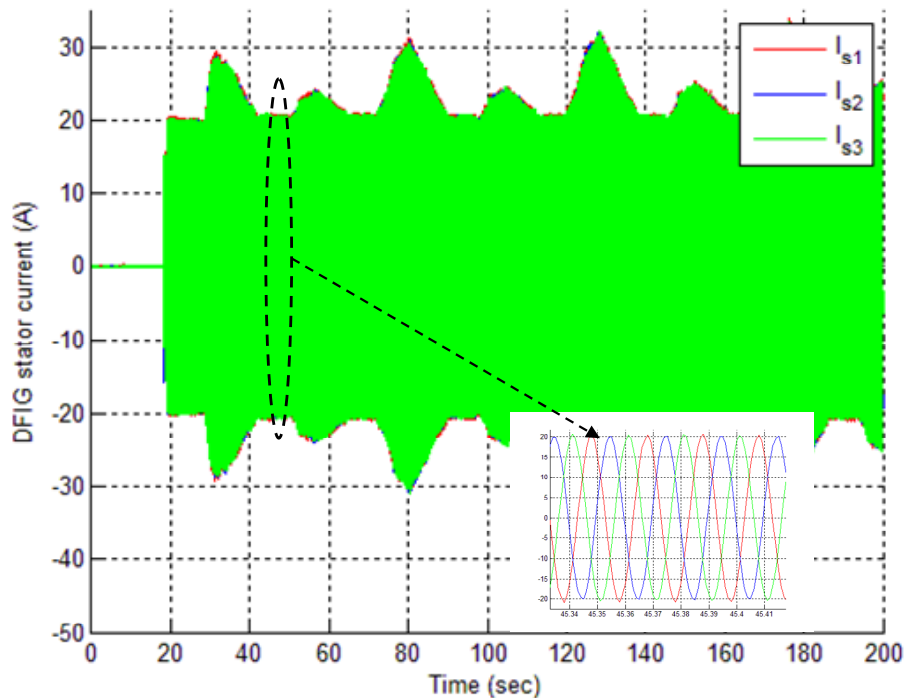


Fig. IV.9. The DFIG stator currents.

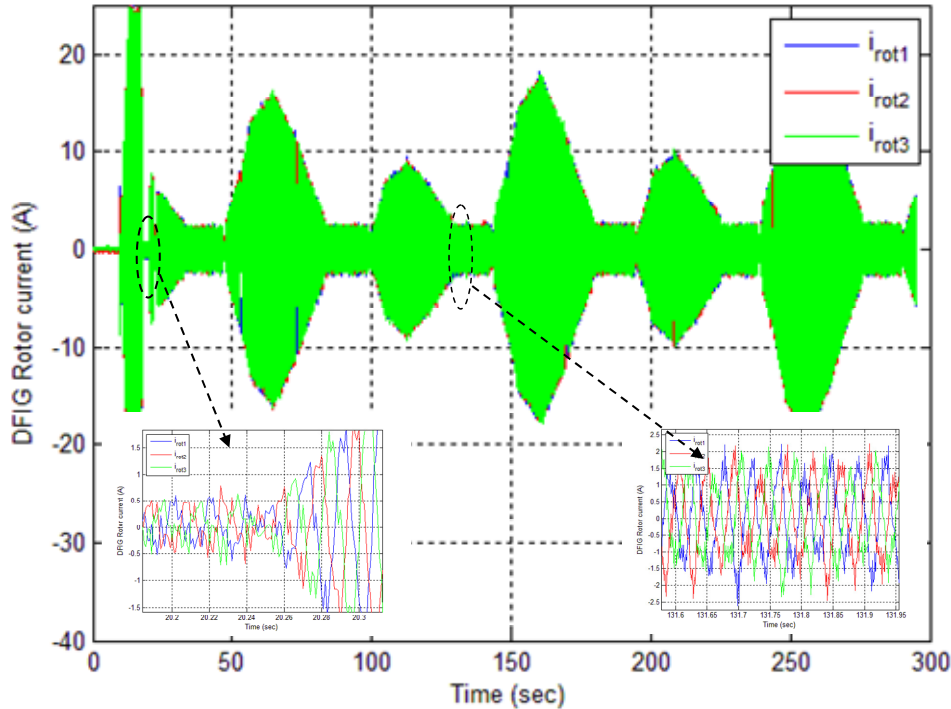


Fig. IV.10. The DFIG rotor currents.

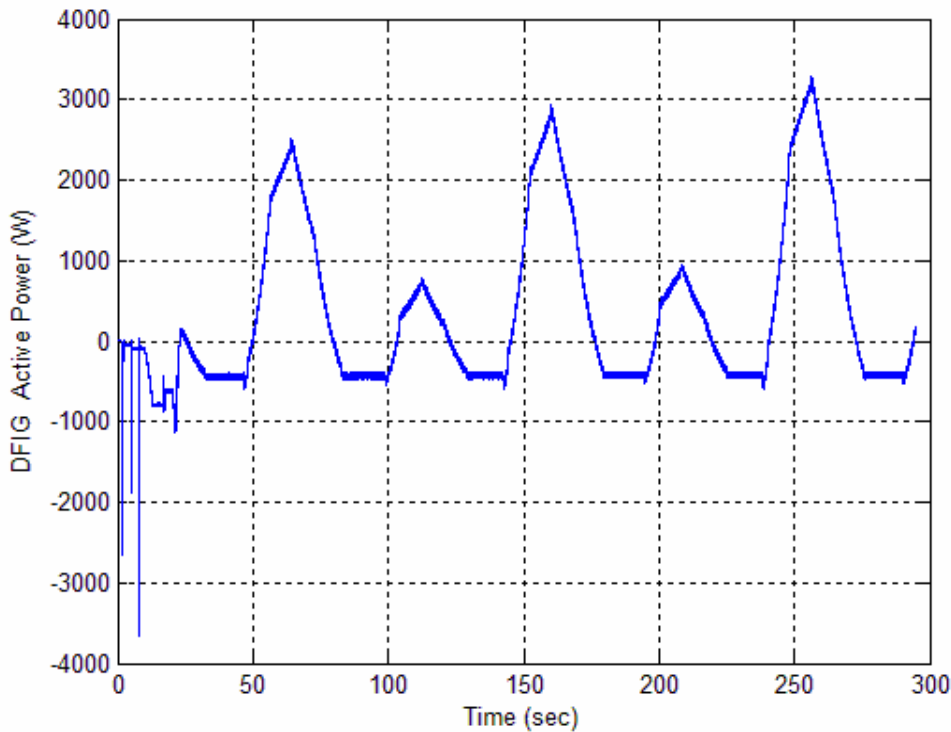


Fig. IV.11. The DFIG active power.

Due to the test bench constraints, the DFIG active power was limited to a maximum of 4 kW (Fig. IV.11). To ensure such limitation, the turbine diameter is set to 1.44 m. Negative powers traduces the existence of test bench mechanical losses and the presence of a low mechanical power input for low speeds.

3.2 Experimental Results for a Turbulent Resource

In this experiment, the swell effect was added to the tidal current data from the Raz de Sein (Brittany, France) (Fig IV.12). Consequently, the mechanical torque T_m has been heavily disturbed (Fig. IV.13).

The DFIG-based MCT control performances are shown in Figs. IV.14 to IV.18 respectively illustrating the rotor speed, currents and the generated active power.

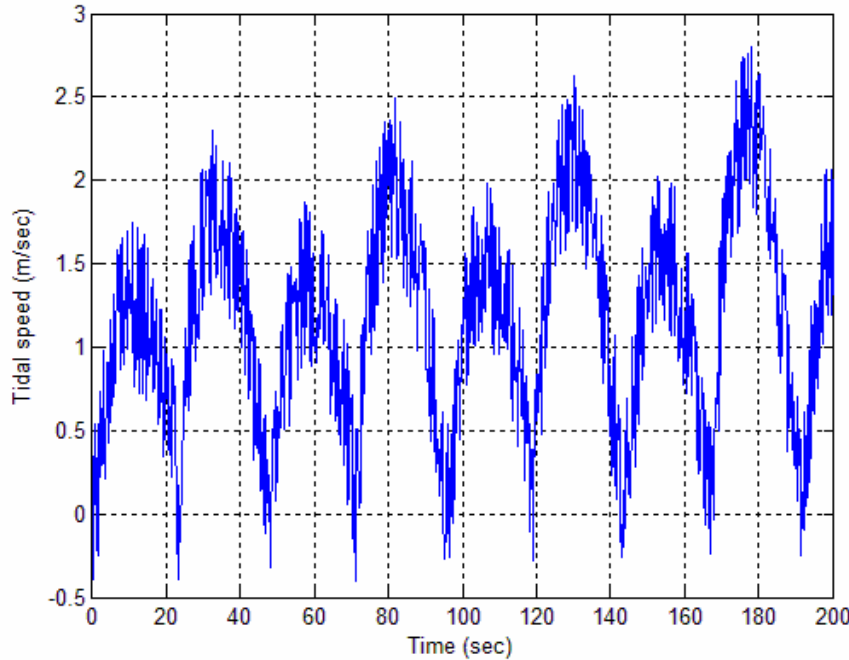


Fig. IV.12. Turbulent tidal speed.

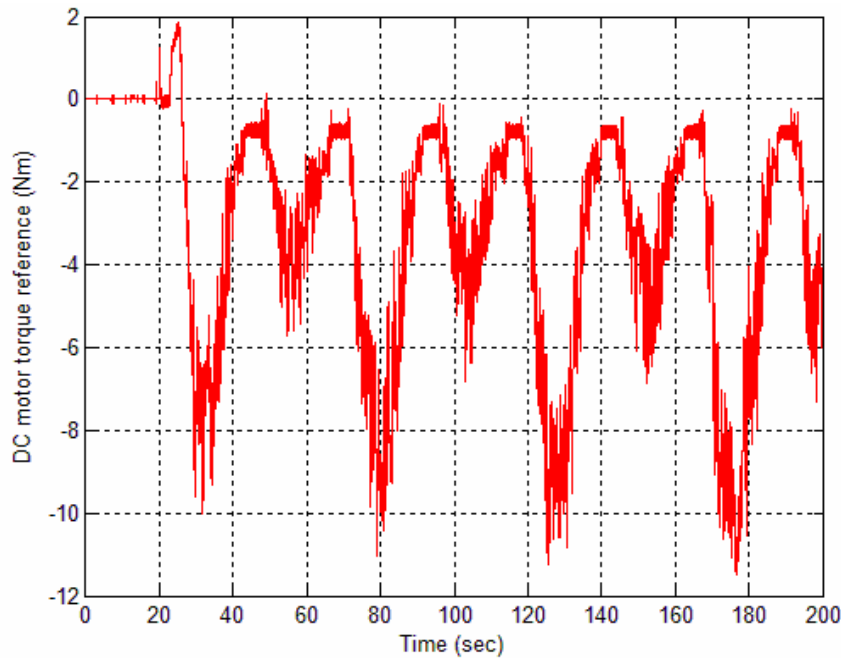


Fig. IV.13. DC motor torque reference.

The obtained results, show very good tracking performances in terms of the DFIG rotor speed (Fig. IV.14) and current (Fig. IV.15).

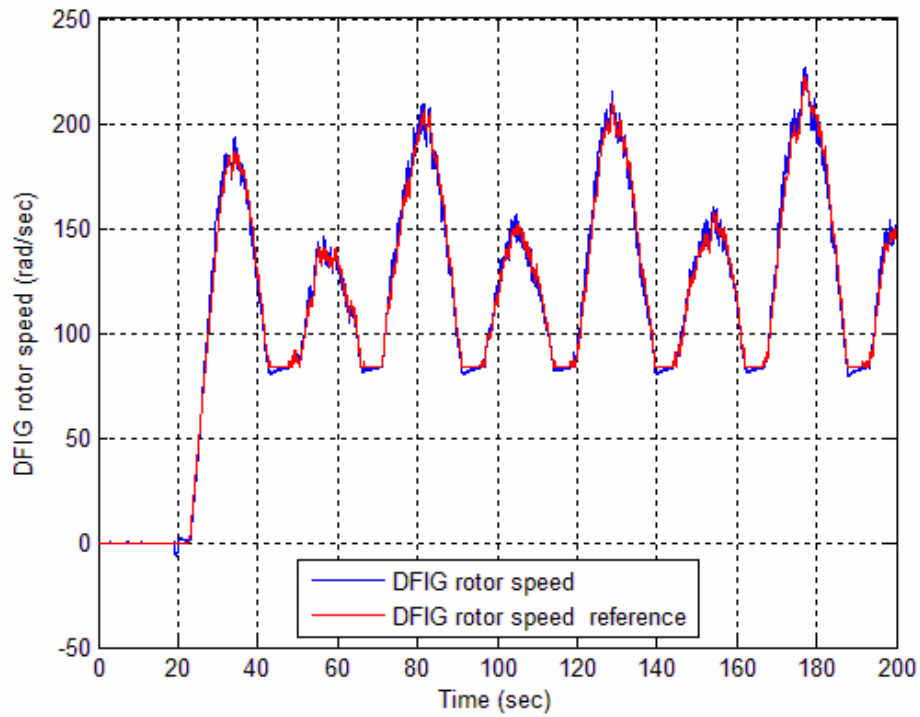


Fig. IV.14. The DFIG rotor speed and its reference.

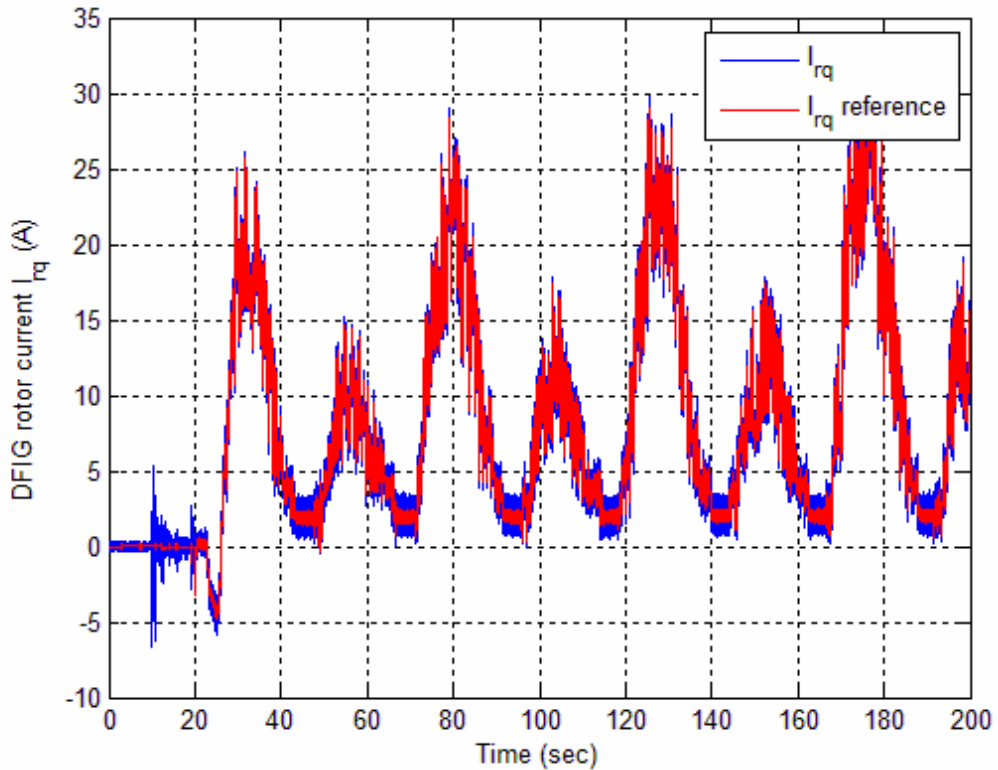


Fig. IV.15. Experimental DFIG I_{rq} current tracking performances.

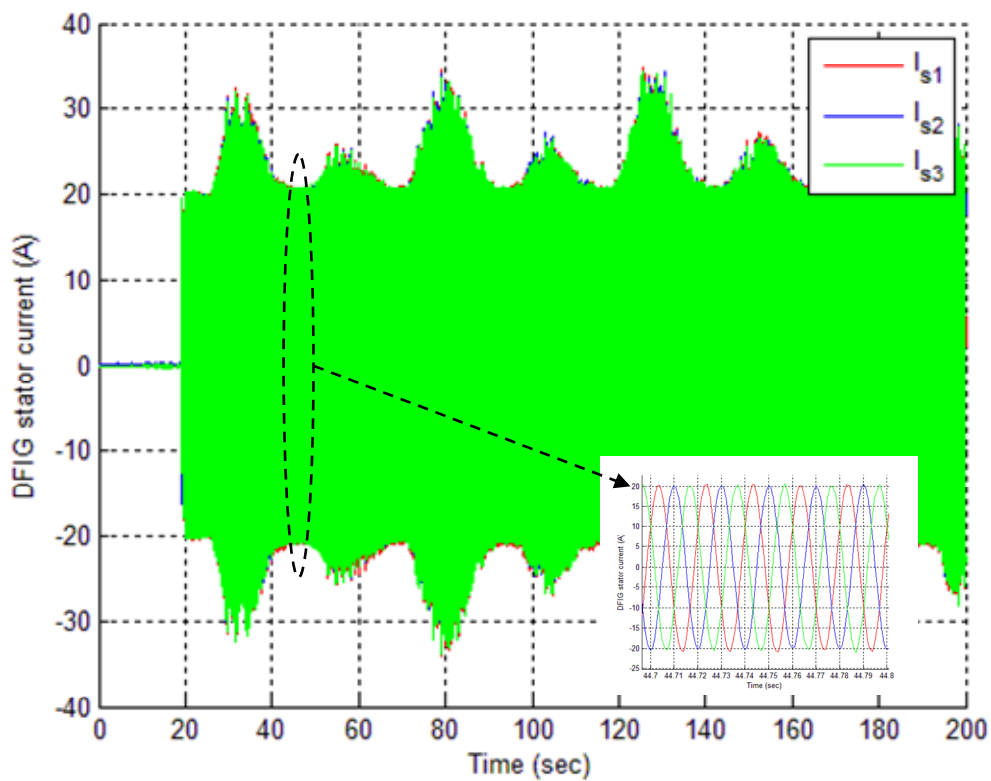


Fig. IV.16. The DFIG stator currents.

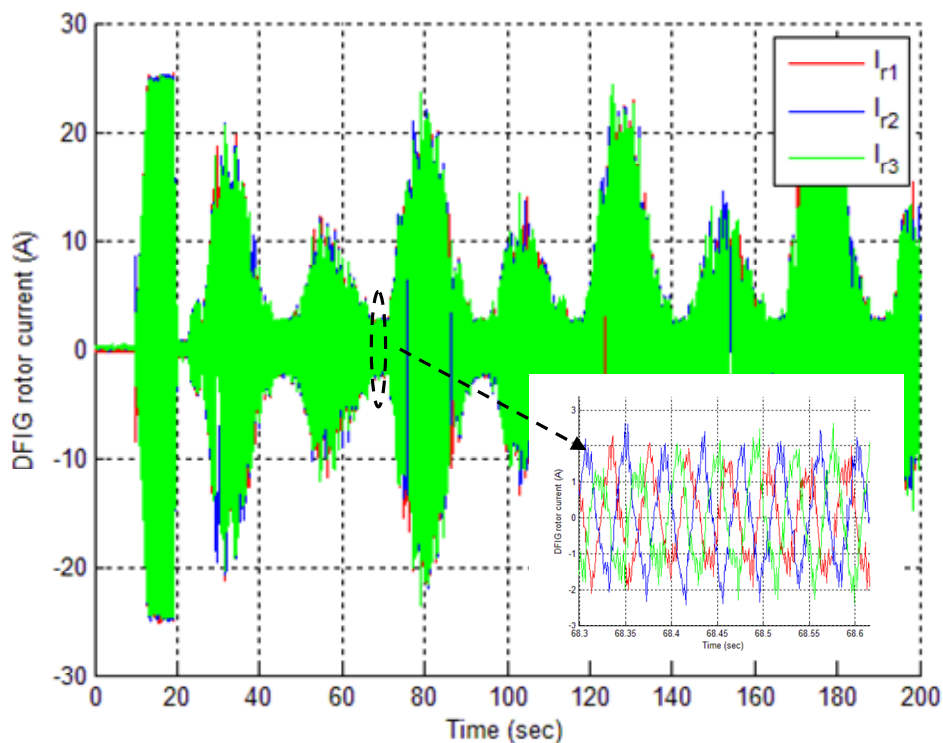


Fig. IV.17. The DFIG rotor currents.

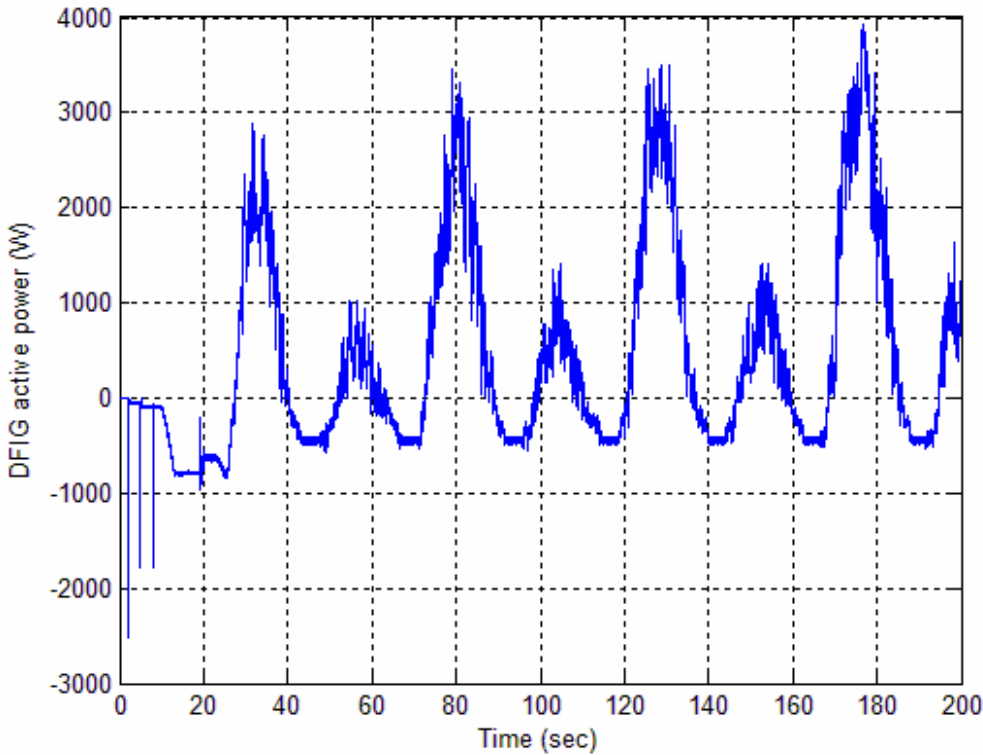


Fig. IV.18. The DFIG active power.

As above-mentioned, the DFIG active power was limited to a maximum of 4 kW.

IV.4 CONTROL OF A PERMANENT MAGNET SYNCHRONOUS GENERATOR

The same experimental tests were carried out to evaluate the PMSG-based MCT control performances. In these conditions, Fig. IV.19 shows the experimental configuration of the emulated PMSG-based MCT. In this case, the second-order sliding mode control of the PMSG-based marine current turbine was tested. To emulate the MCT function, the DC motor ensures the equivalent mechanical torque of the resource, turbine and gearbox.

4.1 Experimental Results for a Filtered Resource

As for the DFIG-based MCT, tidal current data from the Raz de Sein (Brittany, France) (Fig IV.5) have been used to generate the mechanical torque T_m (Fig. IV.6). Therefore, the PMSG-based MCT control performances are shown in Figs. IV.20, IV.21 and IV.22 respectively illustrating the rotor speed, the current, and the generated power. The obtained results show good tracking performances of the PMSG rotor speed and current. Moreover, regarding [109] and as expected, the generated power is smoothest (Fig. IV.22).

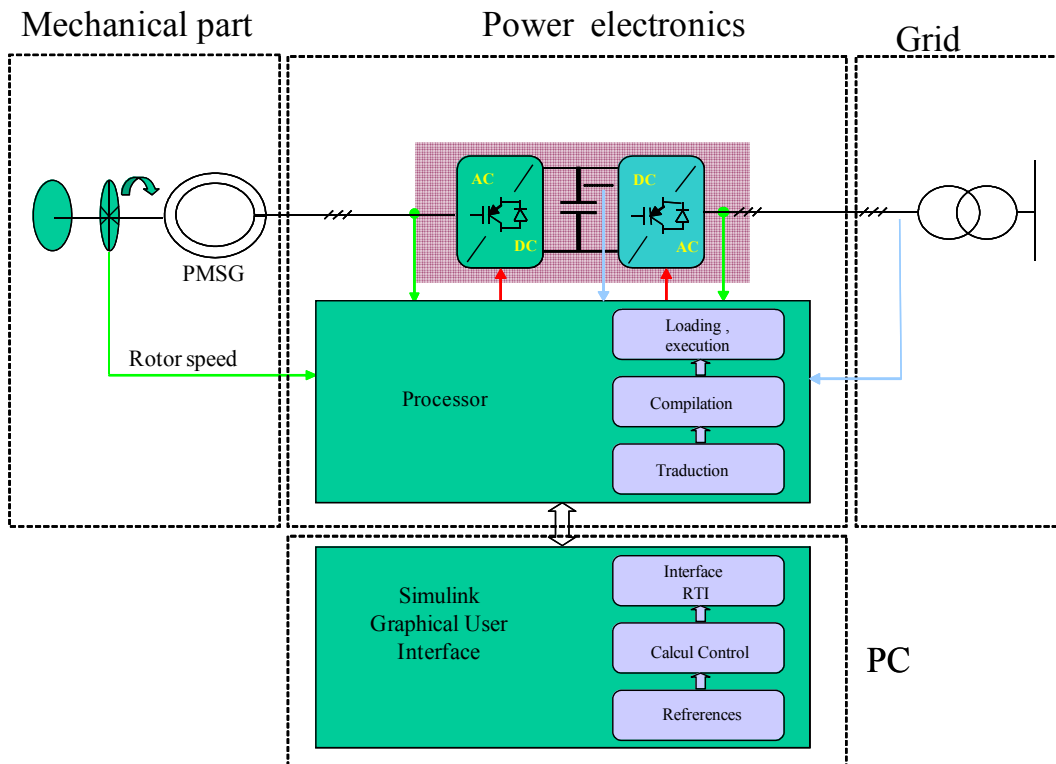


Fig. IV.19. Control of the permanent magnet synchronous generator [©G2Elab].

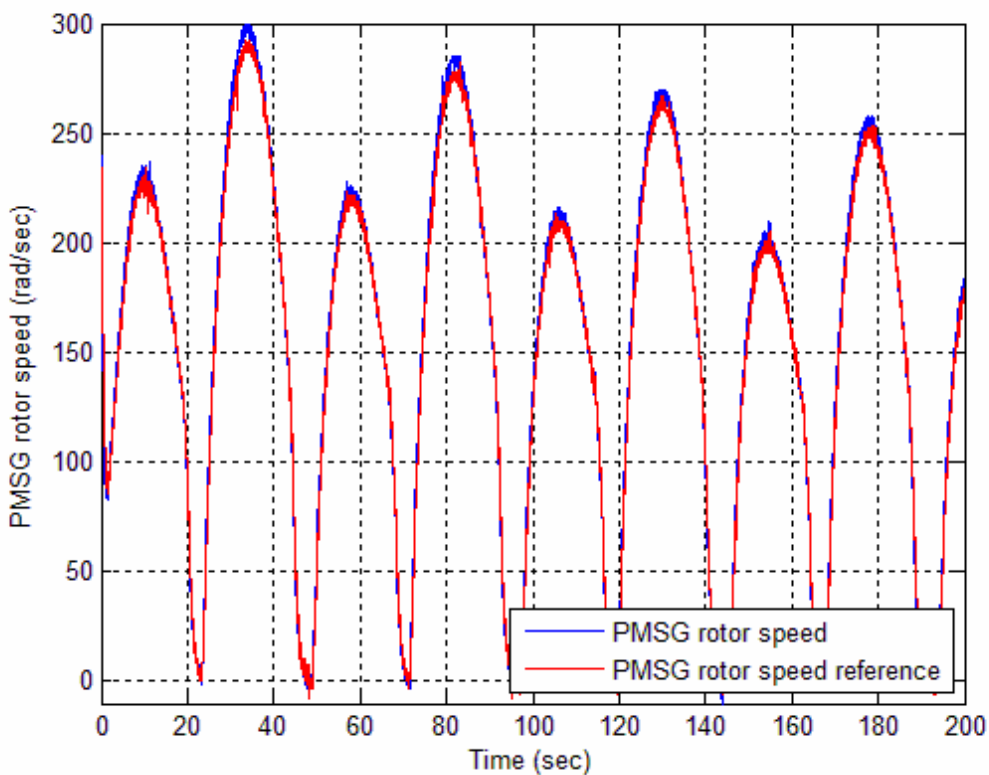


Fig. IV.20. The PMSG rotor speed.

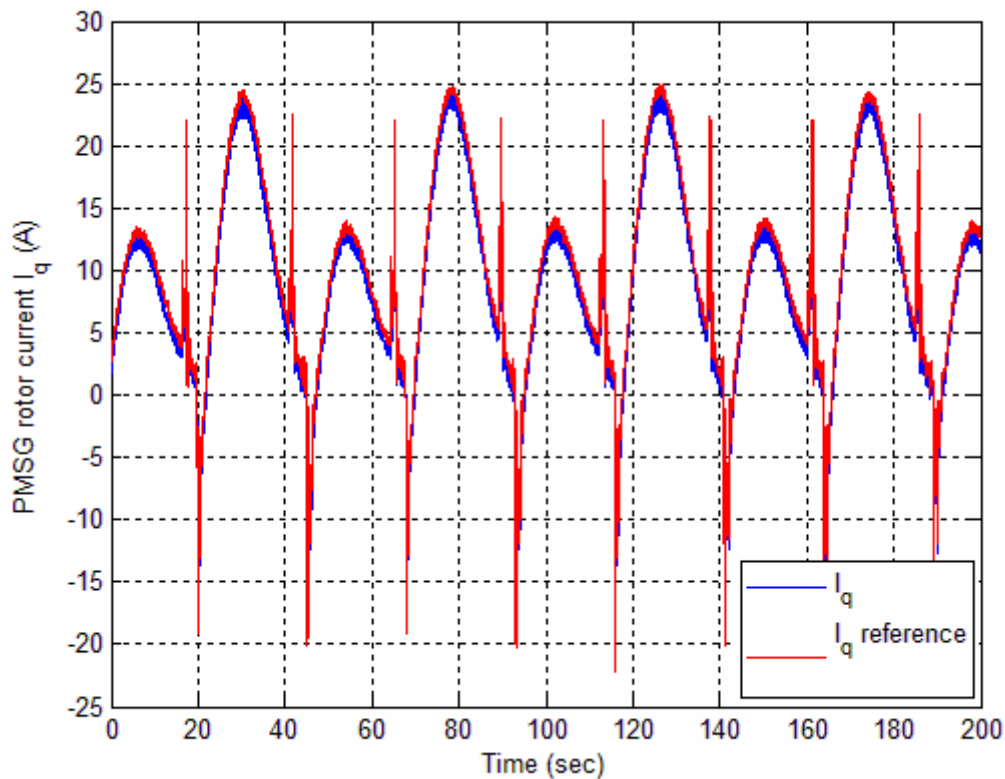


Fig. IV.21 Experimental PMSG I_q current tracking performances.

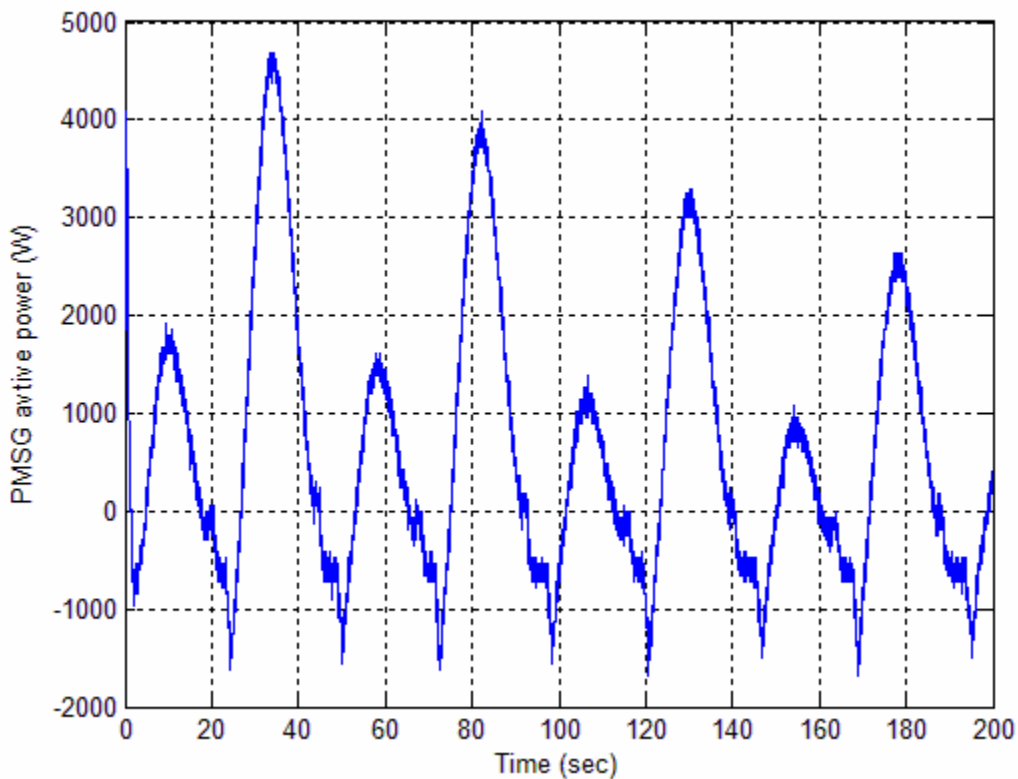


Fig. IV.22. The PMSG active power.

4.2 Experimental Results for a Turbulent Resource

In this experiment, the swell effect was added to a constant value of tidal current equal to 2m/sec (4 knots) (Fig. IV.23). Even with this turbulent resource, the rotor speed and current tracking performances are quite satisfactory (Figs. IV.24 and IV.25).

Since the resource was very turbulent, the generated power has been limited (below 2 kW) to avoid mechanical vibrations of the whole system.

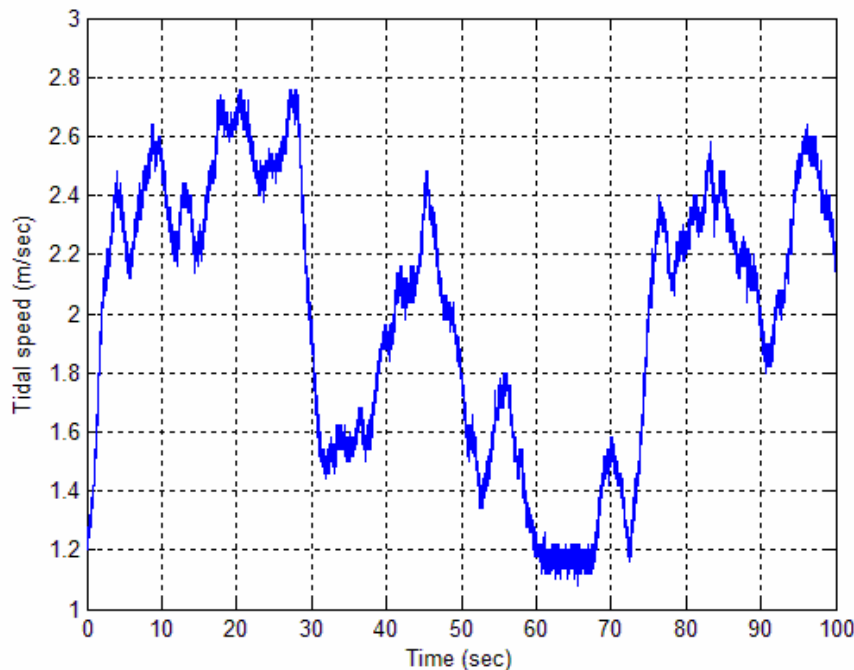


Fig.IV.23. Turbulent tidal speed.

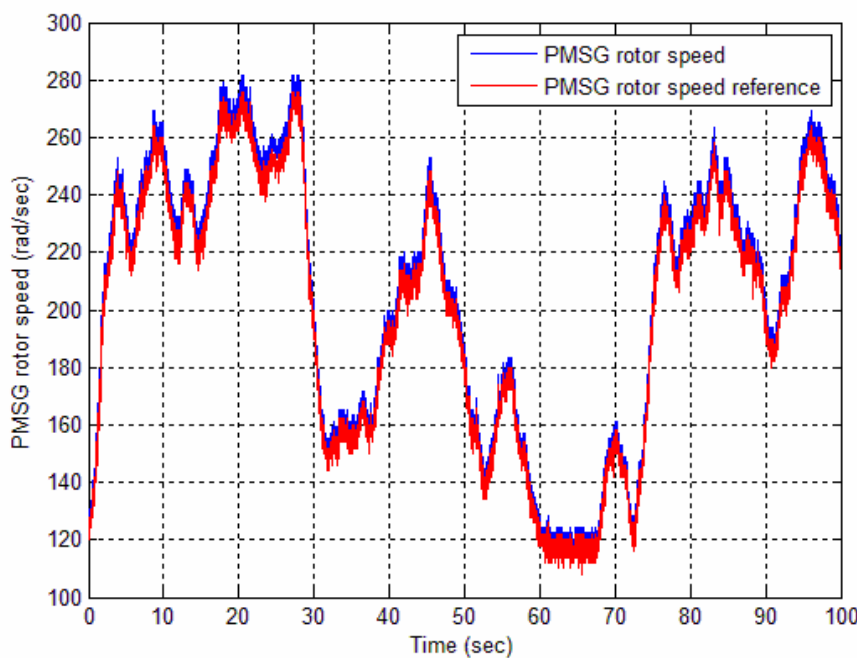


Fig.IV.24. The PMSG rotor speed tracking performances.

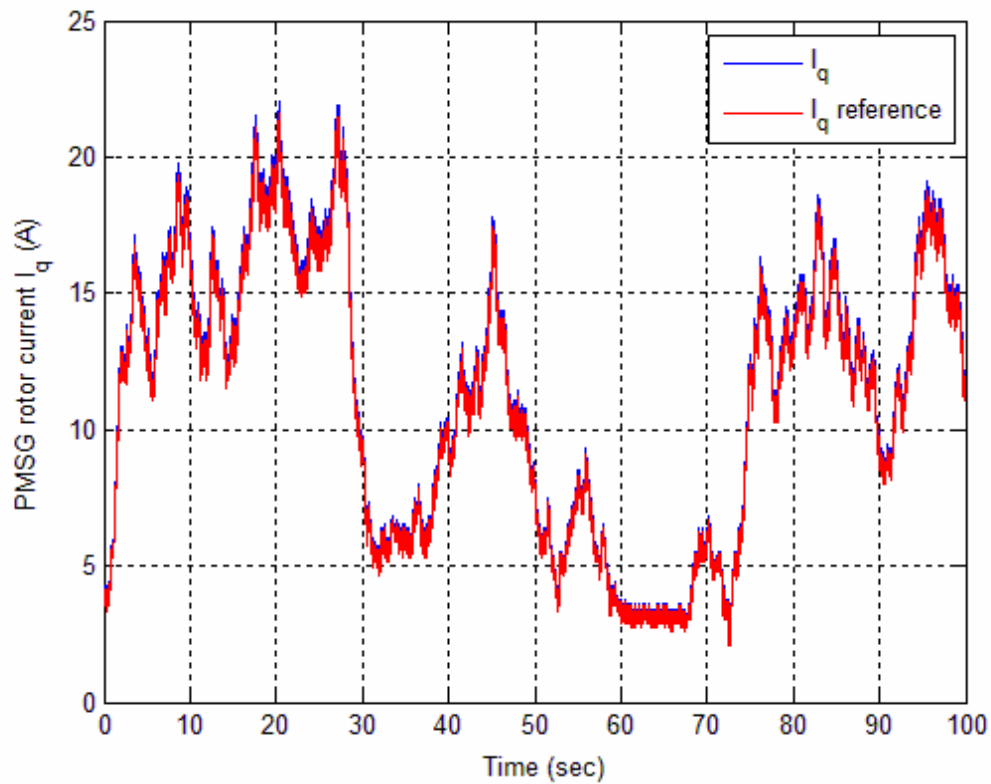


Fig.IV.25. Experimental PMSG I_q current tracking performances.

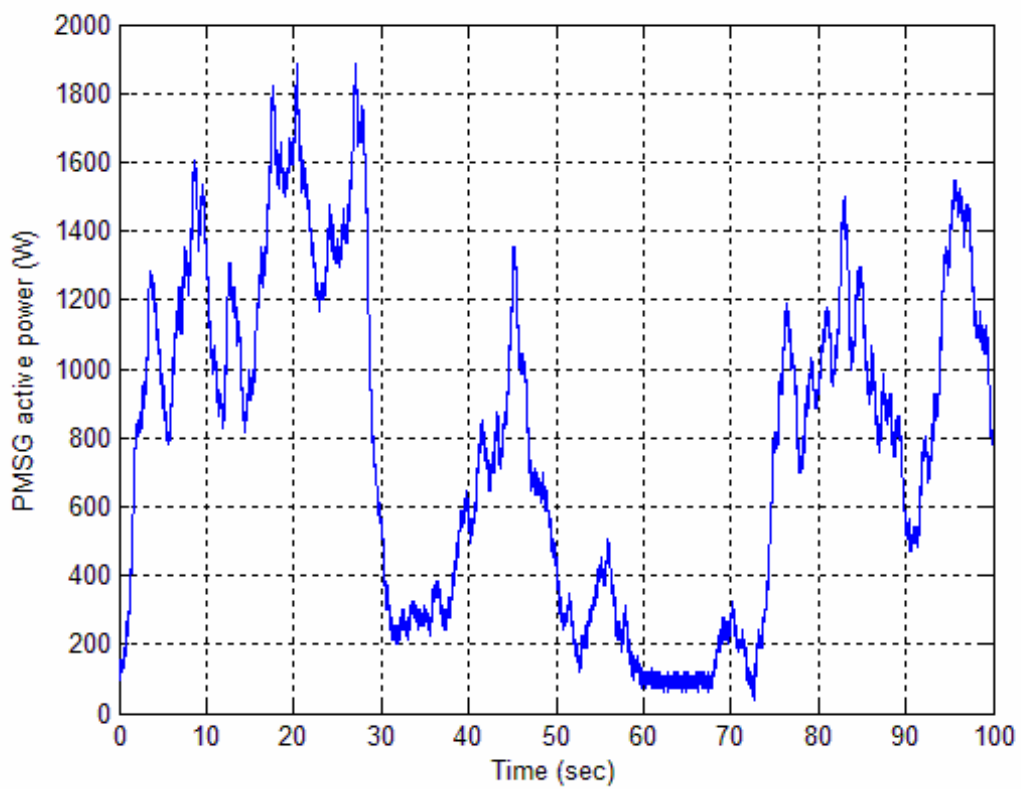


Fig.IV.26. The PMSG active power.

IV.5 COMPARISON

For comparison purposes, Figs. IV.27 to IV.30 show simulation and experimental results of the rotor speed tracking performances and the generated power. Considering real-world marine conditions, the obtained results are satisfactory. The test bench is equipped with current and torque limitations that explain some of Figs IV.28 and IV.30 differences, particularly for high power generation.

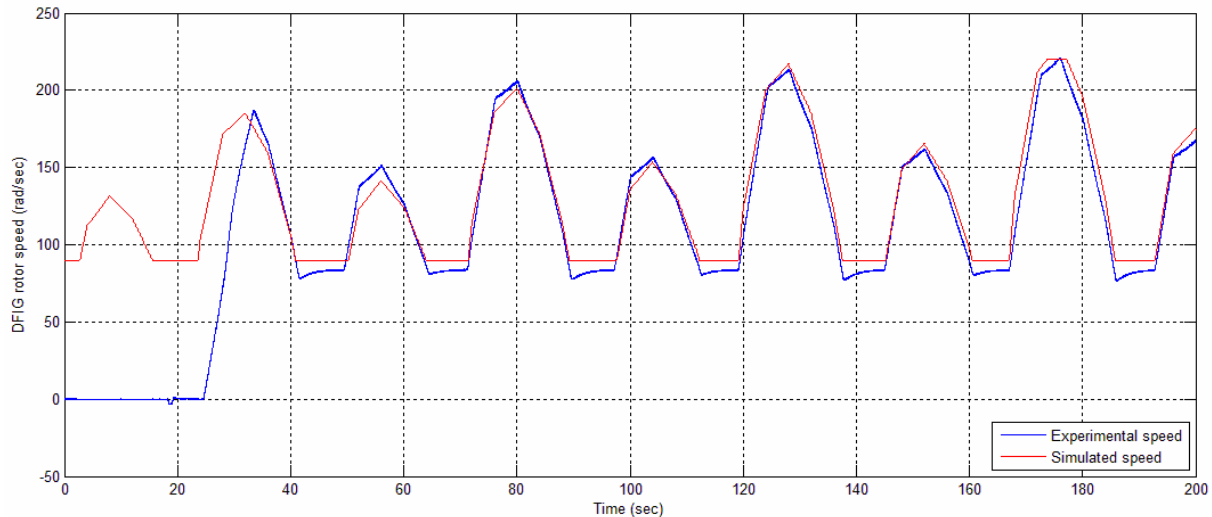


Fig. IV.27. Experimental and simulation DFIG rotor speed tracking performances.

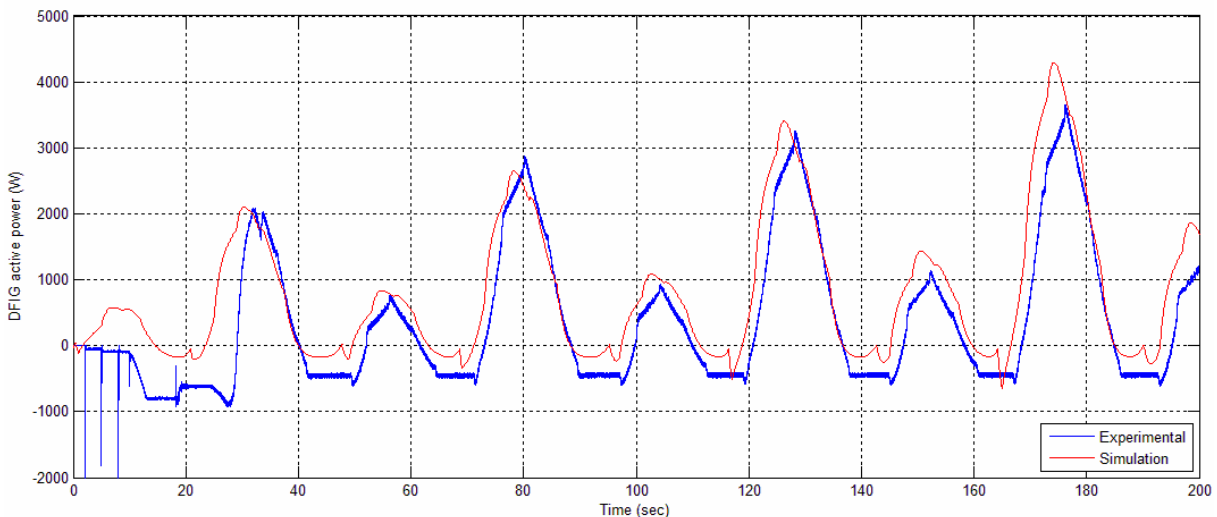


Fig. IV.28. Output power: Experiments vs simulation.

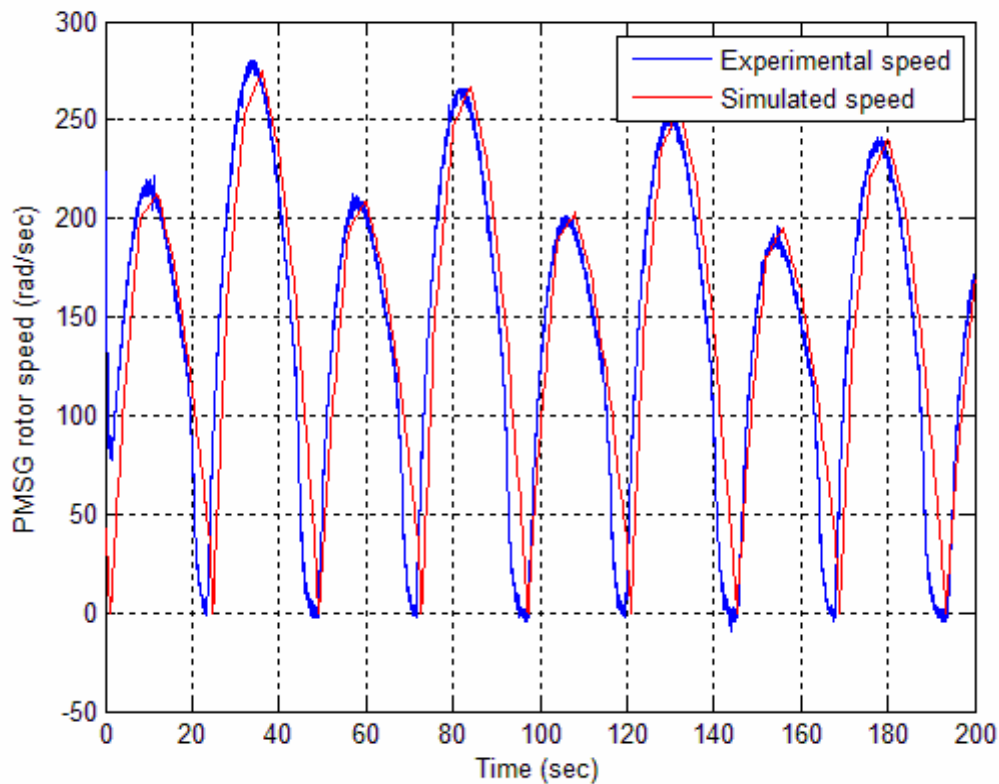


Fig. IV.29. Experimental and simulation PMSG rotor speed tracking performances.

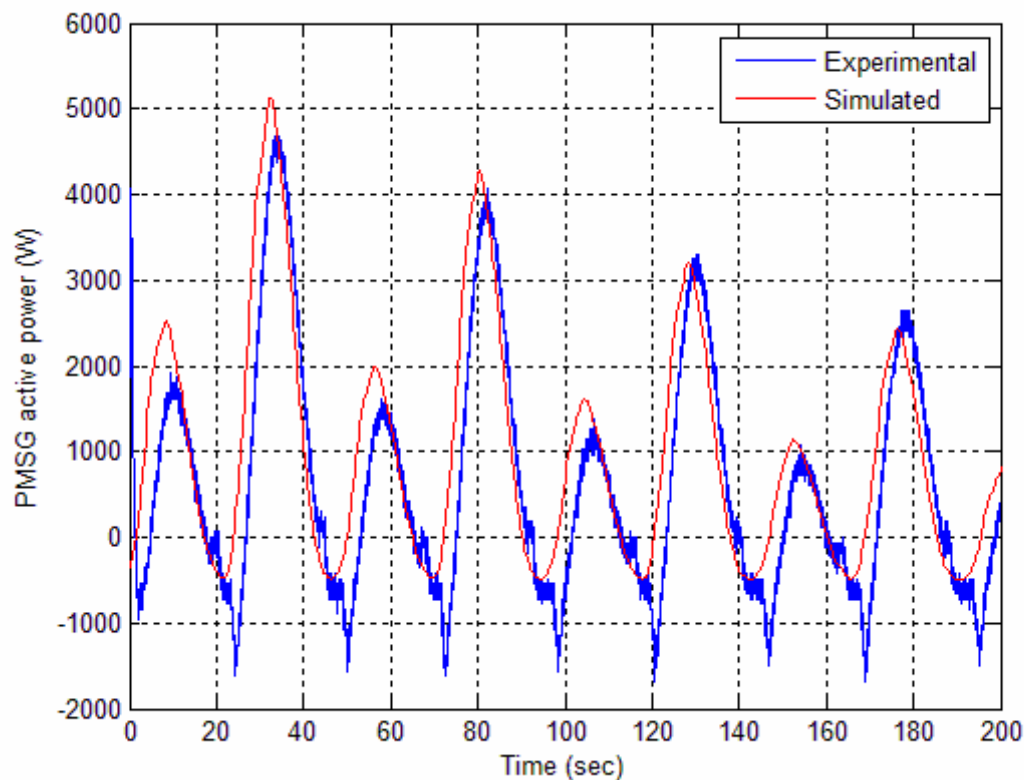
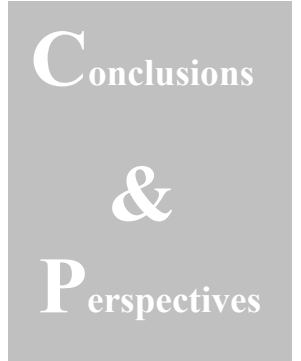


Fig. IV. 30. Output power: Experiments vs simulation.

IV.6 CONCLUSION

This chapter dealt with the experimental validation of a Matlab/Simulink® simulation tool of marine current turbine systems. The simulator was evaluated within the context of speed control of a DFIG- and PMSG-based marine current turbine. For that purpose, a second-order sliding modes control approach has been proposed for the control of a marine current turbine. The experimentally tested control strategy relies on the resource and the marine turbine models. Its main features are a chattering-free behavior, a finite reaching time, and robustness with respect to external disturbances (resource and grid) and unmodeled dynamics. Finally and as an additional justification of such an advanced controller, it should be noted that its practical implementation implies an online computational cost similar to that of PI or PID controllers.

Experimental tests have been carried out on a 7.5 kW real time simulator. The obtained results are satisfactory and very encouraging regarding the validation of the marine current turbine systems simulator.



Conclusions
&
Perspectives

In this thesis, a Matlab/Simulink[®]-based simulation tool for marine current turbines has been proposed. For that purpose, a multiphysics approach has been adopted to model the whole system, including the resource, the rotor, the gearbox and, the generator. The developed tool can evaluate a marine current turbine performances and dynamic loads over different operating conditions. Moreover, it should be used to quantify the potential for generating electricity from various sites and therefore evaluate their cost-effectiveness. Indeed, it has been applied to assess the extractable power from the Raz de Sein. In this case, tidal current data from the Raz de Sein have been used to run the simulation models over various flow regimes and yield the power capture with time. The obtained results were consistent and very promising.

Currently, the marine current turbine simulator incorporates all types of horizontal-axis turbines. Moreover, it includes two different electrical topologies, one based on the doubly-fed induction generator and the other on the permanent magnet synchronous one. For these two technologies, two types of speed control strategies have been proposed. The first one suggests the use of well-known PI controllers. While, the second one proposes a nonlinear control approach based on the so-called high-order sliding mode that should handle torque oscillation smoothing and robustness against resource turbulences and electric grid disturbances.

The various components of the simulator have been tested and experimentally proven in terms of models and speed control performances. Nevertheless, it is crucial to validate the simulator on an experimental benchmark with a more important emulation factor. For this purpose, a 16 kW test bench is being mounted in the Laboratoire Bretois de Mécanique et Systèmes (LBMS) (Fig. 1). The original contribution of the author (most of which have been published in journals and international conference proceedings) could be summarized as follows:

- Development of a first-order model that predicts the resource tidal speed (resource model). The obtained results are very encouraging. Indeed, they prove that the adopted model is quite efficient. It should be noted that this simple model has been already adopted in a recent literature¹.

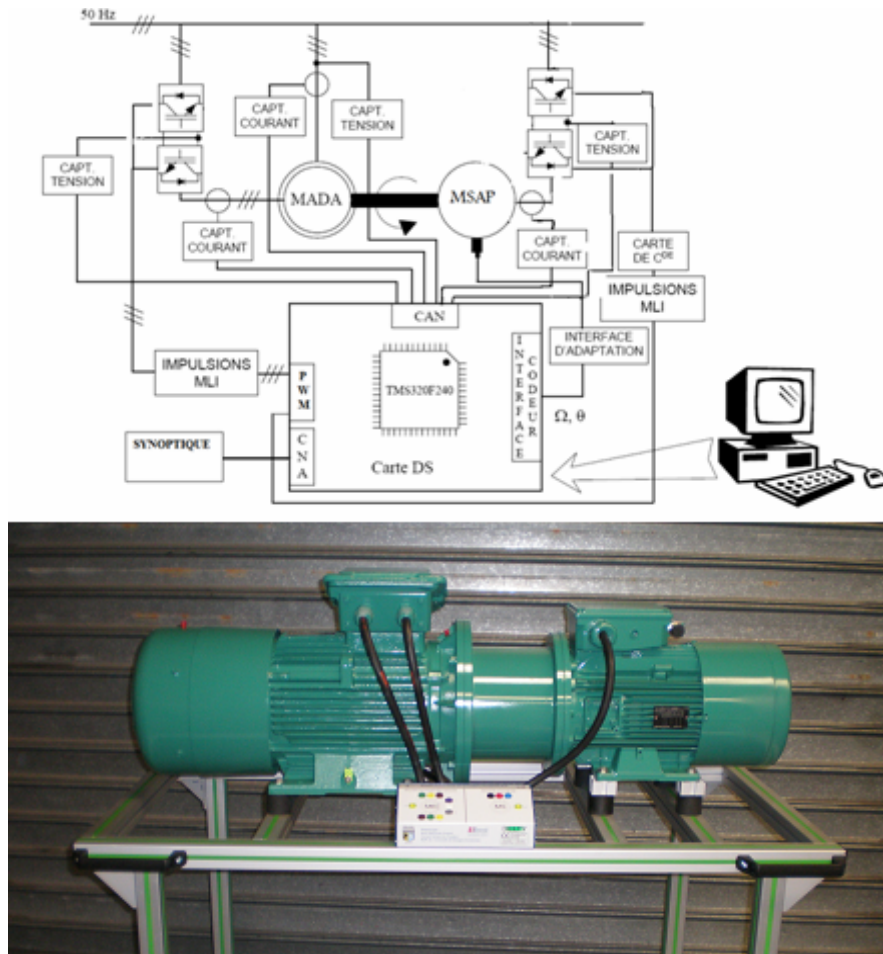


Fig. 1. 16 kW test bench emulator for wind and marine current turbines.

¹ L. Wang et al., "Dynamic stability enhancement and power flow Control of a hybrid wind and marine-current farm using SMES," *IEEE Trans. Energy Conversion*, vol. 24, n°3, pp. 626-639, September 2009.

- Development of a BEM-based model for the turbine modeling. Two corrections have been added to the classical BEM. The first one takes into account the so-called blade tip and root effects and the second one concerns the *turbulent wake state*, where the Glauert empirical relation was adopted. This model is relatively simple and computationally fast meeting the simulation requirements. It should be noted that model has been cited in a very recent specialist report¹.
- Development of a simple PI control strategy associated to an MPPT method for both the DFIG- and PMSG-based marine current turbine. The proposed control strategy relies on the resource and the marine turbine models.
- Development of a second-order sliding mode strategy associated to an MPPT method for both the DFIG- and PMSG-based marine current turbine. As above, the proposed control strategy relies on the resource and the marine turbine models. Its main features are a chattering-free behavior, a finite reaching time, and robustness with respect to external disturbances (resource and grid) and unmodeled dynamics. Moreover, experimental tests have shown that the practical implementation of the proposed second-order sliding mode controller implies an online computational cost similar to that of PI or PID controllers.

The natural continuation of this thesis is mainly due to the marine current turbine simulator configuration. Indeed, due to its modularity, numerous improvements should be promptly considered in future works:

- Include vertical-axis turbine models. This will give opportunities to investigate some of the numerous projects available in the literature; in particular, the vertical-axis marine current turbine prototype called SHIVA at the Research Institute of the French Naval Academy (IRENav);
- Include the converters models;
- Include the grid-connection. This will initiate very interesting works on grid-connection constraints as at the moment there is no real-word feedback;
- Finally, create a user-friendly graphical interface.

Finally, it is obvious that it would be desirable to exploit the simulator modeling bases to extend it to wave energy conversion systems.

¹ Specialist Committee V.4, “Ocean, wind and wave Energy utilization,” in *Proceedings of the 17th International Ship and offshore Structures Congress*, vol. 2, pp. 201-256, August 2009.



Contribution à la Modélisation Multiphysique et à la Commande des Systèmes de Récupérations des Energies des Courants Marins: les Hydroliennes

I. INTRODUCTION	128
II. ETAT DE L'ART SUR LES HYDROLIENNES	129
II.1 PRINCIPE	129
II.2 POTENTIEL ENERGETIQUE ET CHOIX DU SITE	130
II.3 HYDROLIENNE: CONCEPTS ET TOPOLOGIES	131
III. MODELISATION D'UNE HYDROLIENNE	131
III.1 MODELISATION DE LA RESSOURCE	132
III.2 MODELISATION DU CAPTEUR	134
III.3 MODELISATION DE LA CHAINE DE TRANSMISSION MECANIQUE	136
III.4 MODELISATION DE LA GENERATRICE	136
IV. LES STRATEGIES DE COMMANDE.....	138
IV.1 COMMANDE PI.....	138
IV.2 COMMANDE NON LINEAIRE PAR MODE GLISSANT D'ORDRE SUPERIEUR	138
V. VALIDATION EXPERIMENTALE	139
VI. CONCLUSIONS ET PERSPECTIVES	140

I. INTRODUCTION

Face au problème de la gestion des déchets nucléaire et aux émissions de gaz à effet de serre, les énergies renouvelables occupent une place avancée parmi les énergies d'avenir grâce à leur faible impact sur l'environnement ; d'autant plus que ces énergies jouent un rôle important dans la lutte contre le changement climatique et dans le développement économique de certains pays. Ces atouts, alliés à des technologies de plus en plus performantes, favorisent le développement des énergies renouvelables mais de manière encore très inégale selon le type de ressources considérées. Une de ces énergies renouvelables, l'énergie hydrolienne, suscite depuis quelques années un intérêt particulier du fait de ses nombreux avantages. En effet, la force et la vitesse des courants de marée, phénomène prédictible, peuvent être connues des décennies à l'avance. Pour une hydrolienne placée à un endroit donné, il est donc possible, par opposition aux autres énergies renouvelables, dépendant des conditions météorologiques, de connaître à tout moment quelle sera, au premier ordre, la puissance extractible par les gestionnaires de réseaux d'énergie afin d'alimenter ses consommateurs. De plus, les pays d'Europe de l'Ouest et en particulier le Royaume Uni et la France possèdent de nombreux sites près des côtes où cette énergie est exploitable dans de bonnes conditions économiques.

Le but des travaux de thèse est la modélisation de la chaîne de conversion de systèmes de récupération d'énergie hydrocinétique (courants marins) et de génération d'énergie électrique dans leur environnement. L'objectif est de concevoir et d'implanter un modèle multiphysique capable de prévoir le comportement d'une hydrolienne dans son environnement. L'outil ainsi obtenu pourra être utilisé pour le dimensionnement et l'évaluation de la rentabilité d'installations hydroliennes.

Dans **le premier chapitre** de ce mémoire de thèse, un état de l'art sur les différentes technologies des hydroliennes a été présenté.

Le deuxième chapitre de la thèse porte sur la modélisation d'une hydrolienne. Chaque partie du système a été modélisée sous forme d'un bloc indépendant favorisant le test et l'évaluation de différentes topologies d'hydroliennes.

Le troisième chapitre rappelle le principe de la commande optimale des hydroliennes et introduit deux types de commandes ; les régulateurs classiques PI et les régulateurs par mode glissant de deuxième ordre. Ces deux stratégies de commande ont permis d'évaluer et de comparer les performances de deux topologies d'hydroliennes basées sur la Générateur Synchrone à Aimants Permanents et la Générateur Asynchrone à Double Alimentation.

Enfin, le **quatrième chapitre** est dédié à la validation expérimentale de différents cas de fonctionnement de l'hydrolienne.

Dans ce résumé, chaque section présente d'une manière succincte les principaux éléments de chaque chapitre.

II. ETAT DE L'ART SUR LES HYDROLIENNES

Les océans forment un milieu fluide riche en flux énergétiques qui peuvent être exploités sous des diverses formes. Dans la suite, nous présentons l'énergie des courants de marées ainsi que les technologies nécessaires pour son exploitation [61].

II.1 Principe

L'énergie hydronienne provient de l'énergie cinétique de l'eau. En effet, si nous considérons une masse d'eau m qui se déplace à la vitesse v , l'énergie cinétique de cette masse vaut alors :

$$E_c = \frac{1}{2}mv^2 \quad (1)$$

Si cette énergie pouvait être complètement récupérée à l'aide d'une hélice qui balaie une surface A , située perpendiculairement à la direction de la vitesse des courants marins, la puissance instantanée fournie serait alors :

$$P_t = \frac{1}{2}\rho Av^3 \quad (2)$$

où ρ est la masse volumique de l'eau. Cependant, le dispositif de conversion extrait une puissance P_e (puissance extraite) inférieure à la puissance incidente P_t (puissance totale), à cause de la vitesse non nulle des masses d'eau derrière la turbine. On définit alors le coefficient de puissance de la turbine.

$$C_p = \frac{P_e}{P_t}; \quad C_p < 1 \quad (3)$$

Ce coefficient caractérise l'aptitude de la turbine à capter de l'énergie hydronienne. La puissance correspondante est donc donnée par :

$$P_e = \frac{1}{2} \rho \pi R^2 v^3 C_p \quad (4)$$

où R est le rayon de l'hélice. On peut estimer la valeur maximale de ce coefficient C_p , donc la puissance maximale qui peut être récupérée avec une turbine, en s'appuyant sur la théorie de Rankine-Froude dans un fluide incompressible. C'est la valeur maximale de ce coefficient qui correspond à la limite, dénommée limite de Betz, du coefficient de puissance $C_{P_{MAX}} = 16/27 \approx 0.593$.

II.2 Potentiel Energétique et Choix du Site

Pour l'installation d'une hydrolienne, il est crucial de bien sélectionner le site d'implantation. C'est pourquoi une bonne connaissance des courants marins est très importante. Il existe deux principaux types de courants. Les courants *globaux* : ils sont dus aux différences de température et de salinité de masses d'eau voisines. Ils se divisent en deux catégories : les courants locaux liés aux vents et les courants réguliers comme le Gulf Stream. Les courants dits *de marée* (ou de marnage) que l'on rencontre près des côtes ou aux embouchures des fleuves. Leur origine est gravitationnelle et ils sont liés aux déplacements d'eau associés aux marées. Au large, ils sont giratoires mais se transforment à l'approche des côtes en courants alternatifs. Les courants de marées se trouvent généralement accélérés suivant la topographie du fond notamment aux alentours des caps et des détroits entre les îles. Ce sont ces derniers qui intéressent les industriels. En effet, situés près des côtes (moins de 5 km), ils garantissent un acheminement plus aisé de l'électricité. Les ressources énergétiques associées à ces courants marins sont très importantes au niveau mondial. En effet, les courants de marée techniquement exploitables ont un potentiel de près de 100 GW.

Cette énergie hydrocinétique présente l'avantage d'être prévisible et indépendante des variations météorologiques, comme le soleil ou la force du vent. Le Service Hydrographique et Océanographique de la Marine (SHOM) est ainsi capable de prédire pour un lieu donné les fluctuations du courant des années à l'avance grâce à l'étude des marées et de la bathymétrie du site. Certaines zones présentent un intérêt particulier grâce à leur topographie sous-marine qui permet d'avoir des vitesses de courant relativement élevées. En effet, l'équation (4) montre que la puissance dépend du cube de la vitesse, d'où l'intérêt de choisir des sites avec des vitesses les plus élevées possible. Pour des contraintes d'ordre technologique et économique à la fois, la valeur seuil minimale exploitabile est établie à ce jour à 1 m/sec soit environ 2 nœuds [13-15]. Cette valeur seuil minimale est susceptible d'être abaissée au gré

des évolutions technologiques. Néanmoins, pour éviter d'éventuels surcoûts, il faut aussi considérer la valeur de courant maximale, prépondérante dans le dimensionnement de l'installation.

Le choix du site d'installation des hydroliennes se fait également par rapport à la profondeur du fond marin. Les valeurs de courant exploitables supposent des profondeurs d'eau qui oscillent entre 30 et 40 m [16-20]. Il faut tenir compte aussi des variations de niveaux dues aux vagues. C'est ainsi que trois sites privilégiés ont pu être identifiés en France (Fig. I.3).

- Le Raz Blanchard avec des vitesses pouvant atteindre 12 nœuds (6.2 m/sec) ;
- Le Fromveur près d'Ouessant, 9 nœuds (4.1 m/sec) ;
- Le Raz de Sein, courant Nord sud de 8 nœuds (3.1 m/sec) ;

Il est à noter qu'un grand nombre de sites des côtes de Bretagne sont le siège de courants entre 0.5 à 3 m/sec.

Avec une ressource hydrocinétique avoisinant les 6 GW répartie entre le Raz Blanchard (3 GW), Fromveur (2 GW) et Raz de Sein (1 GW), la France est le pays le plus prometteur en Europe, en termes de potentiel, après le Royaume Uni (10 GW).

La consommation instantanée d'électricité française est d'environ 50 GW. Ainsi, l'hydrolienne pourrait répondre à la demande nationale à hauteur de 12%. En réalité ce chiffre correspond au maximum de production, le taux nominal serait de 8 à 10% soit l'équivalent de trois réacteurs nucléaires.

II.3 Hydrolienne: Concepts et Topologies

L'exploitation de l'énergie cinétique des courants de marée présente des similitudes avec l'exploitation de l'énergie cinétique du vent, il n'est pas donc étonnant que les systèmes hydroliens proposés soient majoritairement semblables dans un premier temps aux systèmes éoliens. Néanmoins, on retrouve un retour vers certaines technologies déjà abandonnées ou peu utilisées dans le domaine de l'éolien. Tel est le cas des turbines à axe verticale de grande dimension ou les turbines à battement caudal. Selon les technologies utilisées, trois grandes familles d'hydrolienne peuvent être identifiées (Fig. I.6) [61].

III. MODELISATION D'UNE HYDROLIENNE

Afin d'être capable d'une part de choisir une technologie adaptée à un site particulier et de tester des lois de régulation d'un système hydrolien d'autre part, il apparaît nécessaire de disposer d'un outil de simulation capable de modéliser l'ensemble de la chaîne de conversion

d'énergie et de prévoir ces performances. Dans un premier temps, un modèle de la ressource est conçu à partir de données océanographiques classiques. Ce modèle permet de modéliser finement la vitesse du courant dans un site particulier. Cette approche est présentée sur l'exemple du site du Raz de Sein pour l'année 2007. Dans un deuxième temps, un premier type de capteur hydrodynamique basé sur une hélice à axe horizontal (technologie la plus utilisée actuellement) est modélisé par la méthode BEM (Blade Element Momentum). Cette méthode éprouvée qui permet d'évaluer les performances d'une hélice est très utilisée dans l'industrie pour simuler les charges aérodynamiques d'hélices en particulier pour les applications éoliennes. La mise en œuvre de cette méthode permet de modéliser au sein de la chaîne de simulation les performances hydrodynamiques de l'hélice. Ensuite, un modèle de la chaîne de transmission mécanique a été développé dans la perspective de son utilisation avec des génératrices à entraînement indirecte. Finalement, deux types de machines candidates à équiper les hydroliennes ; Générateur Synchrone à Aimants Permanents (GSAP) et la Générateur Asynchrone à Double Alimentation (GADA) [74].

III.1 Modélisation de la Ressource

III.1.1 Courants de Marée

Les courants marins exploitables sont principalement créés par le phénomène des marées et à une moindre échelle par des phénomènes liés à des différences de densité ou de température au sein des masses d'eau. La marée provoque le mouvement de grande quantité d'eau vers le large (jusant) ou vers les côtes (flot) avec une périodicité principale d'une demi journée (cycle semi-diurne de 12 heures et 24 minutes) ou d'une journée (cycle diurne de 24 heures et 48 minutes) selon les sites. Dans la plupart des sites, le phénomène est une combinaison de ces 2 cycles majeurs. L'amplitude des marées et des courants qu'elles génèrent dépendent de la position de la lune et du soleil par rapport à la terre (Fig. I.4). L'influence en terme de force d'attraction de la lune est d'environ 68 % contre 32 % pour le soleil. Dans les endroits où le cycle semi-diurne est prépondérant les maxima d'amplitudes de courants correspondent à la nouvelle et à la pleine lune (lors de ces marées dites de "vives eaux", le soleil, la lune et la terre sont alors pratiquement alignés et conjuguent leurs effets). Les minima d'amplitudes se produisent lors du 1^{er} et du 3^{ème} quartier (marées dites de "mortes eaux" où les effets du soleil et de la lune se compensent partiellement). A des endroits où le cycle principal est un cycle diurne, l'amplitude des marées dépend de la déclinaison de la lune (hauteur de l'astre par rapport à l'équateur), les plus fortes marées correspondent alors à des grandes déclinaisons et

les plus faibles à des déclinaisons nulles. Ces variations en termes d'amplitude correspondent à des périodicités de 2 semaines, un an, et à des périodes plus longues. Ces amplitudes sont entièrement prédictibles plusieurs mois voire plusieurs années à l'avance [6], [16].

Les caractéristiques de la ressource sont généralement calculées à partir de bases de données océanographiques avec un maillage géographique de résolution donnée. Pour chacune des mailles d'espace, il est possible de disposer des principales données suivantes : vitesse en fonction de l'heure pour les marées de vives eaux, profondeur, houle centennale et moyenne, distance de la côte. Les 2 premières données permettent de reconstituer facilement la vitesse probable du courant en fonction de la date et de l'heure. Les autres données donnent des indications précieuses sur les contraintes liées à l'exploitation du site et sur les caractéristiques des perturbations possibles [12], [17-18]. Pour illustrer l'exploitation de ce type de données, l'évolution théorique de la valeur des courants de marées dans le Raz de Sein pour l'année 2007 et pour mars 2007 est donnée par la Fig. II.4.

III.1.2 Lieu d'Implantation

Il était judicieux de modéliser la ressource en Bretagne dans un des deux sites potentiellement intéressants : le passage du Fromveur au large d'Ouessant et le Raz de Sein situé entre l'île de Sein et la pointe du Raz. En effet, le SHOM possède des données (courant, bathymétrie, nature du fond) sur ces lieux fréquemment empruntés par le trafic maritime. Notre choix s'est ainsi porté sur le Raz de Sein. Les valeurs des courants y sont en effet suffisamment importantes, comprises environ entre 0.5 m/sec et 4 m/sec. Le choix d'implantation d'une hydrolienne dans cette zone est cependant limité. En effet, des courants rotationnels sont présents à l'Ouest de cette zone et même si leur intensité n'est pas négligeable, ils ne sont pas exploitables pour la majorité des technologies d'hydroliennes existantes.

III.1.3 Modélisation du Courant

Le principe de la programmation sous Matlab/Simulink® repose sur l'équation (II.1). Pour chaque heure marée, on calcule ainsi la valeur du courant.

La modélisation de la ressource a permis de mettre en évidence des pics de courant qui sont peu fréquent pendant l'année et qui devraient être pris en compte lors du dimensionnement de la turbine et de la génératrice.

Le modèle de simulation, ainsi mis au point, permet une certaine modularité : le choix du site n'est pas fixe, la valeur du courant utile est adaptable, et la plage de temps considérée peut

également varier (de un mois à un an). Ce modèle de courant au premier ordre est désormais utilisable en entrée du modèle de la chaîne de conversion hydrodynamique.

Afin d'affiner la modélisation de la ressource, un modèle de Stockes a été utilisé pour estimer l'effet de la houle (II.2). Cette dernière est considérée comme la perturbation la plus influente sur la vitesse de la marée (Fig. II.5) [114].

III.2 Modélisation du Capteur

La modélisation du capteur consiste à préétablir des courbes de performance en fonction des caractéristiques géométriques des profils hydrodynamiques composant le système mécanique de récupération d'énergie afin de pouvoir les intégrer dans un environnement de simulation dynamique. Afin de pouvoir modéliser rapidement et précisément le capteur d'une hydrolienne en gardant néanmoins des temps de calcul acceptables, des techniques similaires à celles employées dans l'industrie éolienne ont été adoptés [35].

III.2.1 Théorie des Quantités de Mouvement Appliquées à un Élément de Pale

Le modèle de simulation du capteur est basé sur la théorie des quantités de mouvement développée par Glauert. Cette théorie est une extension de la théorie de Rankine-Froude.

En considérant le rotor de l'hydrolienne comme une surface circulaire d'épaisseur nulle soumise à une différence de pression, le modèle de Rankine-Froude fournit une estimation des vitesses dans le sillage et de la puissance récupérée.

La Figure II.9 montre l'effet d'une extraction de puissance sur une masse d'eau par une hydrolienne ainsi que la frontière avec le milieu extérieur. Le débit est conservé dans la veine fluide aussi bien en amont qu'en aval de la turbine. Le fluide est d'abord ralenti en amont par la présence de la turbine puis en aval par l'extraction d'énergie cinétique. Du fait de son incompressibilité, il y a une expansion de la veine de courant dans le sillage. La différence entre la vitesse du courant arrivant sur la turbine et celle au niveau de la turbine est nommée vitesse induite. En appliquant les théorèmes d'Euler, de Bernoulli et un bilan de la quantité de mouvement en amont et en aval du disque, il ressort que la vitesse au niveau du disque est la moyenne des vitesses amont et aval.

En divisant radialement les pales du rotor en plusieurs éléments distincts, comme le flux de courant en sections annulaires, on considère chaque section de pale comme un profil en deux dimensions soumis à une veine de courant selon un certain angle d'attaque et dont les données de portance et de traînée sont connues. Le calcul des forces totales est obtenu en sommant les

forces élémentaires sur chaque section selon la théorie de Rankine-Froude, chacune d'elles étant considérée indépendante de sa voisine sur la pale (Fig. II.11).

La fraction puissance récupérable est représentée par un coefficient de puissance C_p . ce coefficient peut être défini en fonction d'un facteur d'induction axial a , qui représente le pourcentage de réduction de la vitesse entre le courant amont et le plan du rotor (II.11).

III.2.2 Domaine Limite de Fonctionnement

Lorsque le facteur d'induction axial a excède 0.5, le domaine de validité de la théorie est dépassé. Pour des vitesses induites élevées, la théorie n'est plus applicable en raison d'un retour de flux dans le sillage de la turbine. Cet état de fonctionnement intermédiaire entre un fonctionnement générateur et propulseur se caractérise par un sillage turbulent ayant de fortes interactions avec le courant circulant autour de l'hydrolienne qui affecte le débit du courant passant dans l'hydrolienne. Dans cet état, le coefficient de poussée ne suit plus l'évolution prédictive par la Théorie de Rankine-Froude mais continue à augmenter. Plusieurs corrections semi-empiriques existent alors pour corriger les résultats au-delà de cette valeur seuil. Nous avons ainsi choisi d'appliquer la correction semi-empirique dite de Glauert pour notre modèle de simulation (II.22).

III.2.3 Maillage du Capteur

Pour obtenir l'allure du profil créé, le préprocesseur d'un code de calcul, développé par l'Institut de Recherche de l'Ecole Navale, dit code-singularités, a été utilisé. Ce module, écrit en FORTRAN 77, permet d'obtenir un maillage précis du capteur à partir de lois géométriques. Pour le profil NACA 44, avec les lois géométriques que nous avons adoptées, nous obtenons le maillage en 3D représenté par la Fig. II.15.

III.2.4 Obtention de la Courbe $C_p(\lambda, \theta)$

Afin de valider la modélisation du capteur, nous avons comparé les résultats fournis par le programme aux rares données expérimentales disponibles à ce jour (Fig. II.17). Ces données sont issues d'essais réalisés sur l'hydrolienne de la Fig. II.16. En paramétrant notre modèle de simulation sur les données de cette hydrolienne, nous obtenons, pour un angle d'inclinaison des pales de 25° et avec une vitesse de courant de 1.5 m/sec et un rayon de 0.4 m, un C_p de 0.349 contre 0.375 en bassin d'essais.

On constate alors que la valeur de C_p respecte bien la limite de Lanchester-Betz avec une valeur maximale de 0.4436. Cette valeur est due notamment aux pertes en extrémités de pale, à la traînée et aux phénomènes de décrochage aux faibles valeurs de λ .

III.2.5 Résultats de Simulation

La courbe $C_p(\lambda, \theta)$ obtenue peut désormais être utilisée dans un modèle Matlab/Simulink®. Le coefficient de puissance C_p est variable suivant l'angle d'inclinaison des pales θ et la vitesse du courant marin (Fig. II.18). Lorsque la ressource est reliée au bloc capteur, la simulation peut alors être lancée après avoir convenablement configuré ses différents paramètres (échelle de temps, début et fin de la simulation, etc.).

La puissance de l'hydrolienne étant proportionnelle au coefficient C_p , son domaine de fonctionnement doit se situer, autant que possible, sur le sommet de cette courbe.

III.3 Modélisation de la Chaîne de Transmission Mécanique

Dans le cas d'une hydrolienne équipée d'une génératrice classique (vitesse d'environ 1500 trs/min), l'utilisation d'un multiplicateur est obligatoire. Ce dernier permettra la transmission de la puissance mécanique captée par la turbine tournant à faible vitesse à l'arbre de la génératrice (Fig. II.21). Les équations (II.23) à (II.27) définissent l'ensemble des interactions entre les deux cotés de la chaîne de transmission.

III.4 Modélisation de la Générateur

Dans le contexte lié à l'extraction de l'énergie des courants marins, il nous semble intéressant de modéliser les 2 génératrices les plus employées pour les systèmes éoliens que sont les systèmes à base de GADA et GSAP. A cet effet, le tableau I présente des éléments comparatifs concernant ces 2 systèmes [113].

Tableau I : Comparatifs GSAP-GADA.

GSAP	GADA
<u>Avantages</u> <ul style="list-style-type: none"> ➤ Rendements élevés ➤ Pas de balais donc nécessite moins de maintenance ➤ Fonctionnement possible en entraînement direct sans multiplicateur ➤ Fonctionnement à vitesse variable sur toute la plage de puissance ➤ Puissance massique élevée 	<u>Avantages</u> <ul style="list-style-type: none"> ➤ Electronique de puissance dimensionnée à une fraction de la puissance nominale ➤ Connexion de la génératrice plus facile à gérer
<u>Inconvénients</u> <ul style="list-style-type: none"> ➤ Electronique de puissance dimensionnée pour la puissance nominale de la génératrice ➤ Grand diamètre de génératrice ➤ Prix de l'électronique de puissance ➤ Prix des aimants permanents 	<u>Inconvénients</u> <ul style="list-style-type: none"> ➤ Rendement faible ➤ Contrôle commande complexe ➤ Contacts glissants bagues balais ➤ Puissance massique faible ➤ Plage de vitesse limitée ➤ Nécessité d'un multiplicateur (maintenance régulière)

L'hélice étudiée au paragraphe précédent est employée avec une génératrice de 7.5 kW qui peut être asynchrone à double alimentation associée à un double convertisseur MLI à puissance réduite connecté au rotor (GADA) (Fig. II.22) ou synchrone à aimants permanents associée à un double convertisseur MLI de puissance nominale (GSAP) (Fig. II.23).

La GADA est modélisée par un modèle électromécanique classique de type Park. Les équations électriques liant les différents courants ($i_{si}, i_{ri}, i \in (d, q)$) aux flux ($\phi_{si}, \phi_{ri}, i \in (d, q)$) statoriques et rotoriques qui interagissent dans la machine sont définies par les équations (II.28) à (II.31).

La GSAP est elle aussi modélisée par un modèle de type Park présentées par les équations (II.32) à (II.37).

Les convertisseurs MLI sont considérés comme des sources de tensions idéales commandables. Vu leur grande importance, il serait intéressant de les modéliser plus finement au niveau des commutations dans de futurs travaux.

IV. LES STRATÉGIES DE COMMANDE

IV.1 Commande PI

La commande en vitesse des systèmes repose sur l'utilisation classique de régulateurs linéaires de type PI. Nous avons choisi au niveau de la GADA de limiter la puissance rotorique à un tiers de la puissance nominale. Ce choix, classique dans le domaine de l'éolien a priori proche des problématiques de l'hydriole, conduit à une limitation de la vitesse de la machine entre 0.5 et 1.5 fois sa vitesse de synchronisme.

Au niveau la GSAP la machine est contrôlée de manière très classique en vitesse par le biais d'une boucle de vitesse associée à une boucle de courant (contrôle de couple) interne. Le courant dans l'axe direct est alors maintenu à 0 (minimisation des pertes joules dans la GSAP), le courant dans l'axe q servant au contrôle du couple de la machine. Que ce soit pour la GADA ou pour la GSAP des régulateurs linéaires de type PI sont utilisés au niveau des boucles de courant et de vitesse [113-114].

Les résultats de simulation pour les deux types de machines sont très satisfaisants en terme de suivie de la consigne de vitesse (Fig. III.9) et (Fig. III.12).

IV.2 Commande Non Linéaire par Mode Glissant d'Ordre Supérieur

Dans toute formulation d'un problème de commande, le modèle mathématique développé dans le but d'établir la loi de commande ne reflète pas exactement le processus réel. Ces différences peuvent par exemple être dues à des dynamiques non modélisées, à des variations des paramètres du système ou à une modélisation trop approximative de comportements complexes du processus. On doit néanmoins s'assurer que, malgré toutes ces incertitudes, la loi de commande résultante permet d'atteindre les objectifs prédéfinis. Ceci a conduit à un important intérêt pour la synthèse de contrôles dits robustes capables de pallier à ce problème. L'approche par des correcteurs linéaires, du type PID, a vite montré ses limites. En effet, ceux-ci sont soumis à la loi de Bode qui veut que les effets d'amplitude et les effets de phase soient couplés et antagonistes. Par exemple, toute avance de phase, qui est l'effet bénéfique recherché, va de pair avec une augmentation du rapport dynamique. De fait, les possibilités de compensation et d'utilisation de gains élevés s'en trouvent réduites.

Pour palier à ces inconvénients, on peut envisager des techniques non linéaires, telles que les méthodes adaptatives ou de stabilité absolue, mais également la technique des modes glissants. Cette dernière s'inscrit dans la théorie des systèmes à structure variable. Les lois de commande par modes glissants sont réalisées de manière à conduire et contraindre le système à rester dans le voisinage d'une surface de commutation. Il y a deux principaux avantages à une telle approche. Tout d'abord, le comportement dynamique résultant peut être déterminé par le choix d'une surface adéquate. Ensuite, la réponse du système en boucle fermée est totalement insensible à une classe particulière d'incertitudes, ce qui fait de cette méthode une candidate sérieuse dans la perspective de l'élaboration de commandes robustes des systèmes hydroliens.

Les travaux réalisés, dans cette partie, visent essentiellement à améliorer les résultats obtenus avec les régulateurs PI et à augmenter la robustesse du système vis-à-vis des perturbations. Dans ce cadre, le mode glissant d'ordre supérieur a été élaboré pour les deux types de génératrices.

Dans le but de réaliser une commande en vitesse variable basée sur la stratégie MPPT, il était nécessaire de générer un couple électromagnétique de référence C_{em-ref} à partir de la vitesse de rotation ω_{ref} (III.22). Ensuite, les surfaces de glissement S_1 et S_2 sont définies de manière à assurer la commande de la vitesse de rotation et de la puissance réactive. La commande de la GADA (respectivement de la GSAP) sont décrites par les équations (III.23) à (III.31) (respectivement (III.32) à (III.40)). Les résultats de la commande en vitesse sont très satisfaisants pour les deux types de génératrices [116-117].

Un essai de robustesse de la commande non linéaire, vis-à-vis d'une variation paramétrique de la génératrice, a été également effectué. Les résultats obtenus sont plus que satisfaisants (Fig. III.27) et (Fig. III.28).

V. VALIDATION EXPERIMENTALE

La validation expérimentale est réalisée sur un banc d'essai au laboratoire G2lab de l'INP Grenoble. Le banc expérimental comporte deux parties essentielles :

- ***Le simulateur de couple hydrodynamique.*** La génération du couple hydrodynamique de l'hydrolienne est réalisée à l'aide d'un moteur à courant continu (MCC) dont le couple est programmable, via un DSP. L'ensemble est piloté par une interface TESTPOINT. L'utilisateur intègre le modèle de la turbine, du multiplicateur éventuel ainsi que les vitesses de courant marin.
- ***La génératrice.*** Deux types de génératrices ont été testés:

- La Générateur Synchrone à Aimant Permanent (GSAP) pour laquelle le stator est connecté au réseau via l'interface d'électronique de puissance AC-DC-AC. Les commandes des deux onduleurs de tension sont générées par un système dSPACE.
- La Générateur Asynchrone à Double Alimentation (GADA) pour laquelle le stator est directement connecté au réseau. Cependant, le rotor est connecté via l'interface d'électronique de puissance AC-DC-AC. Les commandes des deux onduleurs de tension sont également générées par le même système dSPACE.

Les résultats expérimentaux ont permis de valider à la fois la partie électrique du modèle de l'hydrolienne et les stratégies de commandes choisies [116].

VI. CONCLUSIONS ET PERSPECTIVES

Les travaux développés durant cette thèse, ont permis la mise au point d'un simulateur qui permet de prévoir le comportement d'une hydrolienne dans son environnement. A cet effet, une approche multiphysique a été adoptée pour la modélisation de l'ensemble de la chaîne de conversion d'énergie. L'environnement de simulation ainsi développé peut également être utilisé pour le dimensionnement et l'évaluation de la rentabilité d'installations hydroliennes.

A l'heure actuelle, l'outil développé permet de simuler tous les types de turbines à axe horizontal. De plus, il permet de choisir entre deux topologies électriques différentes ; une basée sur la générateur asynchrone à double alimentation et une sur la générateur synchrone à aimants permanents. Pour ces deux technologies, deux types de commande en vitesse ont été proposés. La première stratégie est consacrée l'utilisation des régulateurs linéaires PI. La deuxième, quant à elle, propose une commande non linéaire dite *mode glissant d'ordre supérieur*.

Les différents composants du simulateur ont été testés et éprouvés expérimentalement en termes de modèles et en termes de performances de régulations de vitesse. Il est néanmoins indispensable de valider le simulateur sur un système avec un facteur d'émulation plus important. A cet effet, un banc expérimental de 16 kW est en cours de finalisation au Laboratoire Bretois de Mécanique et Systèmes (LBMS).

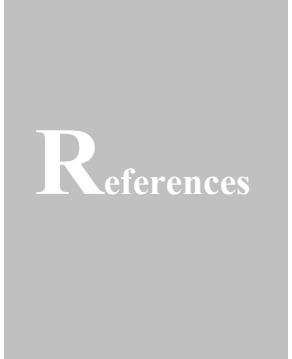
Les développements présentés dans ce mémoire restent cependant perfectibles ouvrant ainsi la voie à d'intéressantes perspectives. En effet, le développement modulaire (blocs) de l'outil de simulation fait que les perspectives suivantes doivent être rapidement envisagées :

- Inclure les modèles de turbines à axe Vertical. Ceci permettra d'étudier la capacité d'un certain nombre de projets en cours. Entre autres, le prototype à axe vertical a cinématique

paramétrable d'hydrolienne appelé SHIVA de l'Institut de recherche de l'Ecole Navale IRENav ;

- Inclure le modèle des convertisseurs ;
- Inclure la connexion au réseau. Ceci permettra d'initier des travaux sur les contraintes dues à la connexion réseau sachant que pour le moment il n'y a aucun retour d'expérience ;
- Enfin créer une interface graphique pour une utilisation plus conviviale.

De plus il pourrait être très intéressant d'exploiter la base du simulateur présenté pour développer des outils dédiés à la simulation des systèmes de récupération des énergies des vagues.



References

- [1] A.T. Jones et al., "Recent progress in offshore renewable energy technology development," in *Proceedings of IEEE PESGM'05*, vol. 2, pp. 2017-2022, San Francisco (USA), June 2005.
- [2] R. Ramakumar et al., "Economic aspects of advanced energy technologies," *Proc. IEEE*, vol. 3, n°8, pp. 318-332, March 1993.
- [3] G.T. Heydt, "An assessment of ocean thermal energy conversion as an advanced electric generation methodology," *Proc. IEEE*, vol. 3, n°8, pp. 409-418, March 1993.
- [4] C.M. Johnstone et al., "EC FPVI co-ordinated action on ocean energy: A European platform for sharing technical information and research outcomes in wave and tidal energy systems," *Renewable Energy*, vol. 31, pp. 191-196, 2006.
- [5] L.B. Bernshtein, "Tidal power development – A realistic, justifiable and topical problem of today," *IEEE Trans. Energy Conversion*, vol. 10, n°3, pp. 591-599, September 1995.
- [6] T.J. Hammons, "Tidal power," *Proc. IEEE*, vol. 3, n°8, pp. 419-433, March 1993.
- [7] S. Seth et al., "Tidal energy in electric power systems," in *Proceedings of IEEE PESGM'05*, vol. 2, pp. 630-635, San Francisco (USA), June 2005.
- [8] J.P. Frau, "Tidal energy: Promising projects. La Rance, a successful industrial-scale experiment," *IEEE Trans. Energy Conversion*, vol. 8, n°3, pp. 552-558, September 1993.

- [9] 2005 IEEE Power Engineering Society General Meeting Panel Session, "Harnessing the untapped energy potential of the oceans: Tidal, wave, currents and OTEC," San Francisco (USA), June 2005.
- [10] Technomare SpA and IT Power Ltd., "Non Nuclear Energy—JOULE II, Wave energy project results: The Exploitation of tidal marine currents," *Non-Nuclear Energy R&D Component*, EU JOULE Contract JOU2-CT94-0355, 1996.
- [11] P.W. Ullman, "Offshore tidal power generation – A new approach to power conversion of the oceans' tides," *MTS Journal*, vol. 36, n°4, pp. 16-24, 2002.
- [12] I.G. Bryden et al., "Choosing and evaluating sites for tidal current development," *Proc. IMechE, Part A: Journal of Power and Energy*, vol. 218, n°8, pp. 567-578, 2004.
- [13] B.V. Davis, "Low head tidal power: A Major source of energy from the world's oceans," in *Proceedings of IECEC'97*, vol. 3, pp. 1982-1989, Honolulu (USA), July-August 1997.
- [14] I.G. Bryden et al., "An assessment of tidal streams as energy sources in Orkney and Shetland," *Underwater Technology*, vol. 21, n°2, 1995.
- [15] I.G. Bryden, "Tidal stream power for Orkney and Shetland?," *Underwater Technology*, vol. 9, n°4, 1993.
- [16] T.G. Pugh, *Tides, Surges and Mean Sea-Level*. London, UK: Wiley, 1987.
- [17] L.S. Bluden et al., "Initial evaluation of tidal stream energy resources at Portland Bill, UK," *Renewable Energy*, vol. 31, pp. 121-132, 2006.
- [18] I.G. Bryden et al., "Assessing the potential of a simple tidal channel to deliver useful energy," *Applied Ocean Research*, vol. 26, pp. 198-204, 2004.
- [19] J.S. Couch et al., "Tidal current energy extraction: Hydrodynamic resource characteristics," *Proc. IMechE, Part M: Journal of Engineering for the Maritime*, vol. 220, n°4, pp. 185-194, 2006.
- [20] A.S. Bahaj et al., "Fundamentals applicable to the utilisation of marine current turbines for energy production," *Renewable Energy*, vol. 28, pp. 2205-2211, 2003.
- [21] L. Myers et al., "Power output performance characteristics of a horizontal axis marine current turbine," *Renewable Energy*, vol. 31, pp. 197-208, 2006.
- [22] P.L. Fraenkel, "Power from marine currents," *Proc. IMechE, Part A: Journal of Power and Energy*, vol. 216, n°1, pp. 1-14, 2002.
- [23] I.G. Bryden et al., "ME1 – Marine energy extraction: Tidal resource analysis," *Renewable Energy*, vol. 31, pp. 133-139, 2006.
- [24] <http://www.marineturbines.com/home.htm> (last accessed January 2009).
- [25] <http://www.e-tidevannsenergi.com/> (last accessed January 2008).
- [26] <http://www.pontediarchimede.com/> (last accessed January 2008).
- [27] <http://www.engl.com/> (last accessed January 2008).
- [28] <http://www.teleos.co.uk/Home.htm> (last accessed January 2008).
- [29] <http://www.smdhydrovision.com/> (last accessed January 2008).
- [30] <http://www.lunarenergy.co.uk/> (last accessed January 2008).
- [31] <http://www.hydrohelix.fr/> (last accessed January 2008).
- [32] <http://www.Cleancurrent.com/> (last accessed October 2009).

- [33] <http://www.lunarenergy.co.uk/> (last accessed October 2009).
- [34] <http://www.sabella.fr/> (last accessed October 2009).
- [35] S. Kiho et al., "The power generation from tidal currents by Darrieus turbine," *Renewable Energy*, vol. 9, n°1-4, pp. 1242-1245, 1996.
- [36] <http://www.bluenergy.com/> (last accessed January 2008).
- [37] <http://www.gcktechnology.com/GCK/> (last accessed January 2008).
- [38] A.M. Gorlov, "The Helical Turbine and its applications for tidal and wave power," in *Proceedings of IEEE OCEANCS'03*, vol. 4, pp. 1996, San Diego (USA), September 2003.
- [39] <http://www.legi.hmg.inpg.fr/cavit/Data/Harvest.html> (last accessed January 2008).
- [40] <http://www.biopowersystems.com/> (last accessed September 2008).
- [41] S.R. Turnock et al., "Development of a floating tidal energy system suitable for use in shallow water," in *Proceedings of EWTEC'07*, Porto (Portugal), September 2007.
- [42] J.A. Clarke et al., "Regulating the output characteristics of tidal current power stations to facilitate better base load matching over the lunar cycle," *Renewable Energy*, vol. 31, pp. 173-180, 2006.
- [43] M.E.H. Benbouzid et al., "The state of the art of generators for wind energy conversion systems," in *Proceedings of ICEM'06*, Chania (Greece), September 2006.
- [44] J.W. Park et al., "Wide speed operation of a doubly-fed induction generator for tidal current energy," in *Proceedings of IEEE IECON'04*, vol. 2, pp. 1333-1338, Busan (Korea), November 2004.
- [45] H. Polinder et al., "Comparison of direct-drive and geared generator concepts for wind turbines," *IEEE Trans. Energy Conversion*, vol. 21, n°3, pp. 725-733, September 2006.
- [46] S.M. Abu Sharkh et al., "Performance of an integrated water turbine pm generator," in *Proceedings of IEE PEMD'02*, vol. 2, pp. 486-491, Bath (UK), April 2002.
- [47] Ø. Krøvel et al., "Design of an integrated 100 kW permanent magnet synchronous machine in a prototype thrusters for ship propulsion," in *Proceedings of ICEM'04*, Krakow (Poland), September 2004.
- [48] <http://www.openhydro.com/home.html> (last accessed January 2009).
- [49] J.R. Bumby et al., "Axial-flux permanent-magnet air-cored generator for small-scale wind turbines," *IEE Proc. Electric Power Applications*, vol. 152, n°5, pp. 1065-1075, September 2005.
- [50] M. P. Papadopoulos et al., "Voltage quality change by grid-connected wind turbines," in *Proceedings of EWEC'99*, Nice (France), pp. 783-785, March 1999.
- [51] A. Petersson, "Analysis, modeling and control of doubly-fed induction generators for wind turbines," *Licentiate Thesis*, Chalmers University of Technology, Göteborg (Sweden), 2003.
- [52] A. Larsson et al., "Grid impact of variable speed wind turbines," in *Proceedings of EWEC'99*, Nice (France), pp. 1-5, March 1999.
- [53] L.H. Hansen et al., "Conceptual survey of generators and power electronics for wind turbines," *Technical Report Risø-R-1205(EN)*, Risø National Laboratory, Roskilde (Denmark), December 2001.

- [54] I. Boldea and S. A. Nasar, *Electric Drives*. CRC Press, 1999.
- [55] L. Harnefors, *Control of Variable-Speed Drives*. Mälardalen University: Västerås (Sweden), 2002.
- [56] W. Leonhard, *Control of Electrical Drives*. Springer-Verlag, 2nd Edition, 1996.
- [57] EU Commission, “The exploitation of tidal marine currents,” *Report EUR16683EN*, 1996.
- [58] L. Myers et al., “Simulated electrical power potential harnessed by marine current turbine arrays in the Alderney Race,” *Renewable Energy*, vol. 30, pp. 1713-1731, 2005.
- [59] G.M Masters, *Renewable and Efficient Electric Power Systems*. Wiley-IEEE Press, 2004.
- [60] I.G. Bryden et al., “ME1 – Marine energy extraction: Tidal resource analysis,” *Renewable Energy*, vol. 31, pp. 133-139, 2006.
- [61] S.E. Ben Elghali et al., “Marine tidal current electric power generation technology: State of the art and current status,” in *Proceedings of IEEE IEMDC'07*, Antalya (Turkey), vol. 2, pp. 1407-1412, May 2007.
- [62] E. Bossanyi, *Wind Energy Handbook*. New York: Wiley, 2000.
- [63] J.S. Carlton, *Marine Propellers and Propulsion*. Oxford: Butterworth-Heinemann (2nd Ed.), 2007.
- [64] W.M.J. Batten et al., “Experimentally validated numerical method for the hydrodynamic design of horizontal axis tidal turbines,” *Ocean Engineering*, (2006), doi:10.1016/j.oceaneng.2006.04.008.
- [65] W.M.J. Batten et al., “Hydrodynamics of marine current turbines,” *Renewable Energy*, vol. 31, pp. 249-256, 2006.
- [66] H. Glauert, *The elements of Airfoil and Airscrew Theory*. Cambridge University Press (2nd Ed.): 1959.
- [67] G. Mattarolo et al., “Modelling and simulation techniques applied to marine current turbine,” in *Proceedings of the 2006 International Conference on Ocean Energy*, Bremerhaven (Germany), 2006.
- [68] D. Molenaar, “Cost-effective design and operation of variable speed wind turbine,” *PhD Thesis*, Delft University Press, Delft (The Netherlands), 2003.
- [69] P.J. Moriarty et al., “AeroDyn theory manual,” NREL/TP-500-36881, January 2005.
- [70] H. Snel, “Review of the present methods of rotor aerodynamics“, *Wind Energy*, vol. 1, pp. 46-69, 1998.
- [71] A.S. Bahaj et al., “Power and thrust measurements of marine current turbines under various hydrodynamic flow conditions in a cavitation tunnel and a towing tank,” *Renewable Energy*, vol. 32, pp. 407-426, 2007.
- [72] S. Müller et al., “Doubly fed induction generator systems,” *IEEE Industry Applications Magazine*, vol. 8, n°3, pp. 26-33, May-June 2002.
- [73] DTI UK, “Commercial prospects for tidal stream power,” Report ETSU T/06/00209/REP, 2001.

- [74] S.E. Ben Elghali et al., "A Simulation model for the evaluation of the electrical power potential harnessed by a marine current turbine", *IEEE Journal of Oceanic Engineering*, vol. 32, n°4, pp. 786-797, October 2007.
- [75] M.E.H. Benbouzid et al., "The state of the art of generators for wind energy conversion systems," in Proceedings of ICEM'06, Chania (Greece), September 2006.
- [76] G. Tapia et al., "Proportional–integral regulator-based approach to wind farm reactive power management for secondary voltage control," *IEEE Trans. Energy Conversion*, vol. 22, n°2, pp. 488-498, June 2007.
- [77] T.K.A. Brekken et al., "Control of a doubly fed induction wind generator under unbalanced grid voltage conditions," *IEEE Trans. Energy Conversion*, vol. 22, n°1, pp. 129-135, March 2007.
- [78] A. Tapia et al., "Modeling and control of a wind turbine driven doubly fed induction generator," *IEEE Trans. Energy Conversion*, vol. 18, n°2, pp. 194-204, June 2003.
- [79] E. Koutroulis et al., "Design of a maximum power tracking system for wind-energy-conversion applications," *IEEE Trans. Industrial Electronics*, vol. 53, n°2, pp. 486-494, April 2006.
- [80] I. Boldea et al., *The Induction Machine Handbook*. CRC Press, 2001.
- [81] I. Munteanu, "Contribution to the optimal control of wind energy conversion systems," *PhD Thesis*, University of Galaty, 2006.
- [82] I. Munteanu et al., *Optimal Control of Wind Energy Systems: Towards a Global Approach*. Springer, 2008.
- [83] W.E. Leithead, "Dependence of performance of variable speed wind turbines on the turbulence, dynamics and control," *IEE Proc. Generation, Transmission and Distribution*, vol. 137, n°6, pp. 403-413, November 1990.
- [84] W.E. Leithead, et al., "Role and objectives of control for wind turbines," *IEE Proc. Generation, Transmission and Distribution*, vol. 138, n°2, pp. 135-148, March 1991.
- [85] E. Muljadi et al., "A conservative control strategy for variable-speed stall-regulated wind turbines," Technical Report NREL/CP-500-24791, 2000.
- [86] T. Burton, et al., *Wind Energy Handbook*. Wiley, 2001.
- [87] V.I. Utkin, "Variable structure systems with sliding modes," *IEEE Trans. Automatic Control*, vol. 22, n°2, pp. 212-222, April 1977.
- [88] V.I. Utkin, *Sliding Modes in Control and Optimization*. Springer, 1992.
- [89] S.V. Emelyanov et al., "Applying the principle of control by deviation to extend the set of possible feedback types," *Soviet Physics*, vol. 26, n°6, pp. 562-564, 1981.
- [90] J.J.E. Slotine, "Sliding controller design for nonlinear systems," *Int. J. of Control*, vol. 40, n°2, 1984.
- [91] G. Bartolini et al., "Applications of a sub-optimal discontinuous control algorithm for uncertain second order systems," *Int. J. of Robust and Nonlinear Control*, vol. 7, n°4, pp. 299-310, 1997.
- [92] G. Bartolini et al., "Chattering avoidance by second-order sliding mode control," *IEEE Trans. Automatic Control*, vol. 43, n°2, pp. 241-246, February 1998.

- [93] S.V. Emelyanov et al., "Higher order sliding modes in the binary control systems," *Soviet Physics*, vol. 31, n°4, pp. 291-293, 1986.
- [94] A. Levant, *Second Order Sliding Algorithms: Their realization*. In "*Dynamics of Heterogeneous Systems*," pp. 32-43, 1985.
- [95] A. Levant, "Sliding order and sliding accuracy in sliding mode control," *Int. J. of Control*, vol. 58, n°6, pp. 1247-1263, 1993.
- [96] A. Levant, "Arbitrary-order sliding modes with finite time convergence," in *Proceedings of IEEE MCC'98*, Alghero (Italy), June 1998.
- [97] A. Levant, "Robust exact differentiation via sliding mode technique", *Automatica*, vol. 34, n°3, pp. 379-384, 1998.
- [98] L. Fridman and A. Levant, *Sliding Mode Control in Engineering*. Chap. 3 *Higher Order Sliding Modes*, pp. 53-101, Marcel Dekker, 2002.
- [99] F. Nollet et al., "Observer-based second order sliding mode control laws for stepper motors," *Control Engineering Practice*, vol. 16, pp. 429-443, 2008.
- [100] F. Bonnet et al., "Dual direct torque control of doubly fed induction machine," *IEEE Trans. Industrial Electronics*, vol. 54, n°5, pp. 2482-2490, October 2007.
- [101] G. Iwanski et al., "Sensorless direct voltage control of the stand-alone slip-ring induction generator," *IEEE Trans. Industrial Electronics*, vol. 54, n°2, pp. 1237-1239, April 2007.
- [102] L. Xu et al., "Direct active and reactive power control of DFIG for wind energy generation," *IEEE Trans. Energy Conversion*, vol. 21, n°3, pp. 750-758, September 2006.
- [103] R. Cardenas et al., "MRAS observer for sensorless control of standalone doubly fed induction generators," *IEEE Trans. Energy Conversion*, vol. 20, n°4, pp. 710-718, December 2005.
- [104] A. Mirecki et al., "Architecture complexity and energy efficiency of small wind turbines," *IEEE Trans. Industrial Electronics*, vol. 54, n°1, pp. 660-670, February 2007.
- [105] M.M. Hand et al., "Advanced control design and field testing for wind turbines at the National Renewable Energy Laboratory," *NREL/CP-500-36118*, May 2004.
- [106] Y.D. Song et al., "Variable speed control of wind turbines using nonlinear and adaptive algorithms," *Journal of Wind Engineering and Industrial Aerodynamics*, vol. 85, pp. 293-308, 2000.
- [107] K.D. Young et al., "A control engineer's guide to sliding mode control," *IEEE Trans. Control Systems Technology*, vol. 7, n°3, pp. 328-342, May 1999.
- [108] B. Beltran et al., "Sliding mode power control of variable-speed wind energy conversion systems," *IEEE Trans. Energy Conversion*, vol. 23, n°2, pp. 551-558, June 2008.
- [109] S.E. Ben Elghali et al., "Modeling and MPPT sensorless control of a DFIG-based marine current turbine," in *Proceedings of the ICEM'08*, Vilamoura (Portugal), September 2008.
- [110] A. Levant et al., "Integral high-order sliding modes," *IEEE Trans. Automatic Control*, vol. 52, n°7, pp. 1278-1282, July 2007.
- [111] H.K. Khalil, *Nonlinear Systems*. McMillan, 1992.

- [112] S.E. Ben Elghali et al., "High-order sliding mode control of a marine current turbine driven doubly-fed induction generator," *IEEE Journal of Oceanic Engineering*, To Appear in June 2010.
- [113] S.E. Ben Elghali et al., "Modeling and control of a marine current turbine driven doubly-fed induction generator," *IET Renewable Power Generation*, vol. 4, n°1, pp. 1-11, January 2010.
- [114] S.E. Ben Elghali et al., "Modélisation et commande d'une hydrolienne équipée d'une génératrice asynchrone double alimentation", *European Journal of Electrical Engineering – EJEE*, April 2010.
- [115] S.E. Ben Elghali et al., "High-order sliding mode control of a marine current turbine driven permanent magnet synchronous generator", in *Proceedings of the IEEE IEMDC'09*, Miami, Florida (USA), pp. 1541-1546, May 2009.
- [116] S.E. Ben Elghali et al., "High-order sliding mode control of DFIG-based marine current turbine", in *Proceedings of the IEEE IECON'08*, Orlando, Florida (USA), pp. 1228-1233, November 2008.
- [117] S.E. Ben Elghali et al., "Modeling and control of a marine current turbine using a doubly-fed induction generator", in *Proceedings of the ICOE'08*, Brest (France), October 2008.
- [118] I. Munteanu et al., "Conception systématique des simulateurs temps réel Hardware-in-the-Loop. Application aux systèmes de conversion éolienne," *Journal Européen des Systèmes Automatisés*, vol. 41, pp 1139-1164, Octobre/Novembre 2007.
- [119] I. Munteanu et al., "Energy-reliability optimization of wind energy conversion systems by sliding mode control," *IEEE Trans. on Energy Conversion*, vol. 23, n°3, pp. 975-985, September 2008.
- [120] I. Munteanu et al., "Sliding mode control laws for variable speed wind power systems", in *Proceedings of the EPE'03*, Toulouse (France), September 2003.
- [121] M. Andreica et al., "Micro-hydro water current turbine control for grid connected or islanding operation," in *Proceedings of the IEEE PESC'08*, Rhodes (Greece), June 2008.
- [122] M. Andreica et al., "Stand-alone operation of cross-flow water turbines," in *Proceedings of the IEEE ICIT'09*, Gippsland (Australia), February 2009.
- [123] M. Andreica et al., "Intégration d'une hydrolienne au réseau, MPPT et qualité de l'énergie," *Revue des Energies Renouvelables*, vol.11, n°4, pp. 493-502, Décembre 2008.
- [124] M. Andreica et al., "Cross-flow water turbines control under grid disturbances," in *Proceedings of the IEEE Power Tech'09*, Bucharest (Romania), June/July 2009.

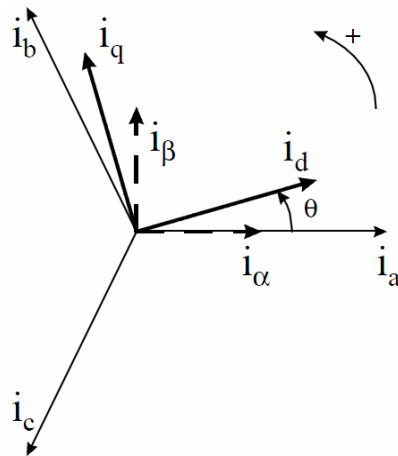


Appendices

Appendix A: The Park Transform.....	150
Appendix B: The Electric Machines Parameters	152
Appendix C: The G2Elab Test Bench Layout	153

Appendix A: The Park Transform

Clarke and Park transforms are used in high performance drive architectures (vector control) related to permanent magnet synchronous and induction machines. Through the use of the Clarke transform, the real (I_{ds}) and imaginary (I_{qs}) currents can be identified. The Park transform can be used to realize the transformation of the I_{ds} and the I_{qs} currents from the stationary to the moving reference frame and control the spatial relationship between the stator vector current and rotor flux vector.



Stator current in the d - q rotating reference frame
and its relationship with the (a,b,c) stationary reference frame.

The Clarke Transform

The mathematical transformation called Clarke transform modifies a three-phase system to a two-phase orthogonal system.

$$\begin{cases} i_a = \frac{2}{3}i_a - \frac{1}{3}(i_b - i_c) \\ i_\beta = \frac{2}{\sqrt{3}}(i_b - i_c) \\ i_o = \frac{2}{3}(i_a + i_b + i_c) \end{cases}$$

The Park Transform

The two-phase α - β frame representation calculated with the Clarke transform is then fed to a vector rotation block where it is rotated over an angle θ to follow the frame d - q attached to the rotor flux. The rotation over an angle θ is done according to the formula.

$$\begin{cases} i_d = i_\alpha \cos \theta + i_\beta \sin \theta \\ i_q = -i_\alpha \sin \theta + i_\beta \cos \theta \end{cases}$$

Park and Clarke Inverse Transforms

The vector in the $d-q$ frame is transformed from $d-q$ frame to the two-phase $\alpha-\beta$ frame representation calculated with a rotation over an angle θ according to the formula.

$$\begin{cases} i_\alpha = i_d \cos \theta - i_q \sin \theta \\ i_\beta = i_d \sin \theta + i_q \cos \theta \end{cases}$$

The modification from a two-phase orthogonal $\alpha-\beta$ frame to a three-phase system is done by the following equations.

$$\begin{cases} i_a = i_\alpha \\ i_b = -\frac{1}{2}i_\alpha + \frac{\sqrt{3}}{2}i_\beta \\ i_c = -\frac{1}{2}i_\alpha - \frac{\sqrt{3}}{2}i_\beta \end{cases}$$

Appendix B: The Electric Machines Parameters

B.1. DFIG Parameters

TABLE B.1. PARAMETERS OF THE SIMULATED AND TESTED DFIG.

Parameters	Values
Rated Power : P	7.5 kW
R_s	0.455 Ω
L_s	0.084 H
R_r	0.62 Ω
L_r	0.081 H
M	0.078 H
J	0.3125 kg.m ²
h	6.73 10 ⁻³ Nms ⁻¹

B.2. PMSG Parameters

TABLE B.2. PARAMETERS OF THE SIMULATED AND TESTED PMSG.

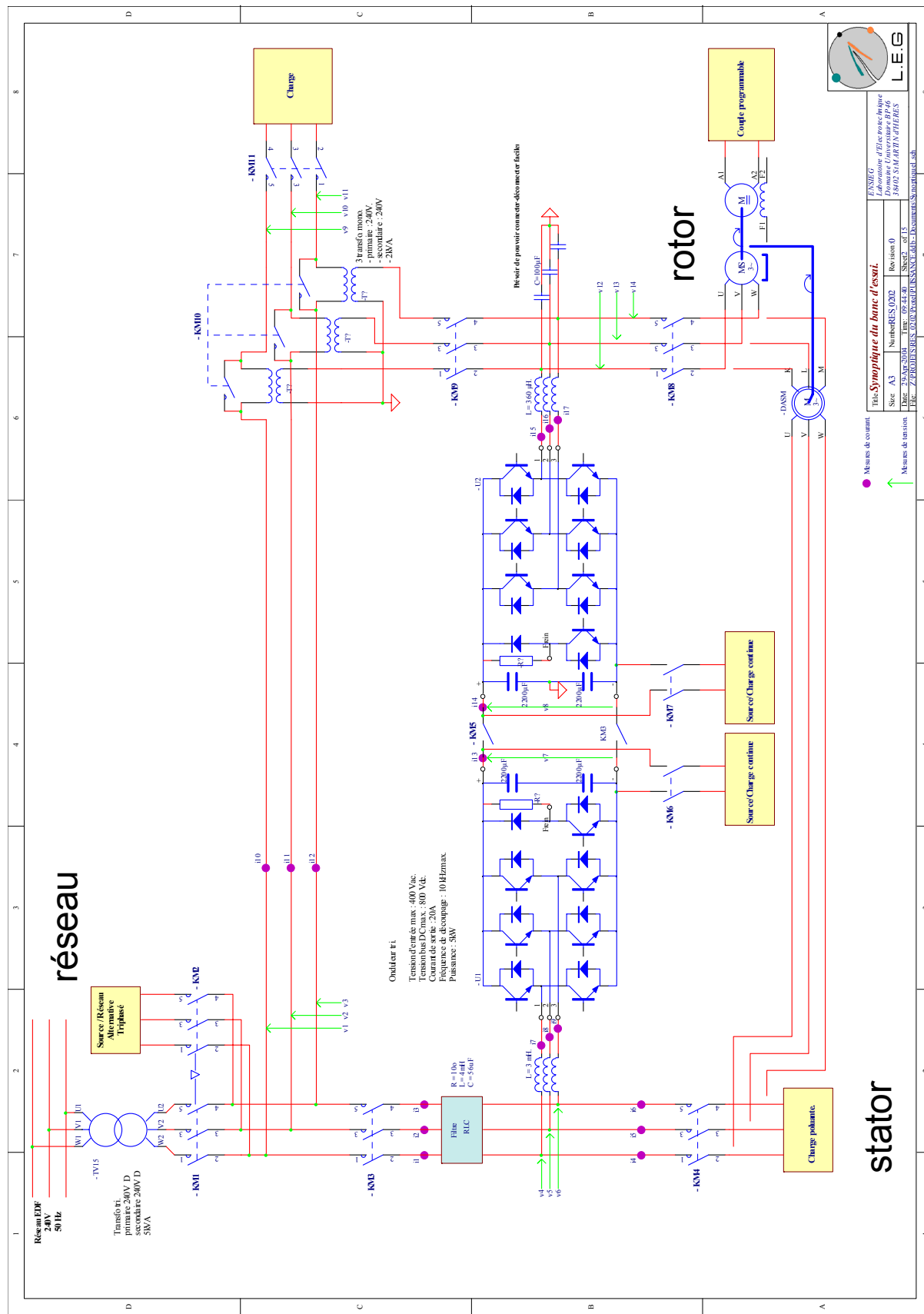
Parameters	Values
Rated Power	7.5 kW
Rated Speed	3000/ 6000 rpm
Rated Torque	22 Nm/ 17 Nm
Rated Voltage	135V/ 270V
Rated Current	31A/ 25.5A
p	4
R	0.173 m Ω
L_d	0.085 mH
L_q	0.951 mH
ϕ_m	0.112 Wb
J	0.0048 kg.m ²
h	8.5 10 ⁻³ Nms ⁻¹

B.3. DC Motor Parameters

TABLE B.3. PARAMETERS OF THE DC MOTOR.

Parameters	Values
Rated Power : P	6.5 kW
Rated Speed	3850 rpm
R_s	78 Ω
R_r	0.78 Ω
L_r	3.6 H
J	0.02 kg.m ²

Appendix C: The G2Elab Test Bench Layout



Contribution à la Modélisation Multiphysique et à la Commande des Systèmes de Récupérations des Energies des Courants Marins: les Hydroliennes

Résumé—Les travaux développés durant cette thèse, ont permis la mise au point d'un simulateur qui permet de prévoir le comportement d'une hydrolienne dans son environnement. A cet effet, une approche multiphysique a été adoptée pour la modélisation de l'ensemble de la chaîne de conversion d'énergie. L'environnement de simulation ainsi développé peut également être utilisé pour le dimensionnement et l'évaluation de la rentabilité d'installations hydroliennes.

A l'heure actuelle, l'outil développé permet de simuler tous les types de turbines à axe horizontal. De plus, il permet de choisir entre deux topologies électriques différentes ; une basée sur la génératrice asynchrone à double alimentation et une sur la génératrice synchrone à aimants permanents. Pour ces deux technologies, deux types de commande en vitesse ont été proposés. La première stratégie consacre l'utilisation des régulateurs linéaires PI. La deuxième, quant à elle, propose une commande non linéaire dite modes glissants d'ordre supérieur.

Les différents composants du simulateur ont été testés et éprouvés expérimentalement en termes de modèles et en termes de performances de régulations de vitesse. Les développements présentés dans ce mémoire restent cependant perfectibles ouvrant ainsi la voie à d'intéressantes perspectives.

On Multiphysics Modeling and Control of Marine Current Turbine Systems

Abstract—In this thesis, a Matlab/Simulink®-based simulation tool for marine current turbines has been proposed. A multiphysics approach has been adopted to model the whole system, including the resource, the rotor, the gearbox, and the generator. The developed tool can evaluate a marine current turbine performances and dynamic loads over different operating conditions. Moreover, it should be used to quantify the potential for generating electricity from various sites and therefore evaluate their cost-effectiveness. Currently, the marine current turbine simulator incorporates all types of horizontal-axis turbines. Moreover, it includes two different electrical topologies, one based on the doubly-fed induction generator and the other on the permanent magnet synchronous one. For these two technologies, two types of speed control strategies have been proposed. The first one suggests the use of well-known PI controllers. While, the second one proposes a nonlinear control approach based on the so-called high-order sliding mode that should handle torque oscillation smoothing and robustness against resource turbulences and electric grid disturbances.

The various components of the simulator have been tested and experimentally proven in terms of models and speed control performances. The obtained results were consistent and very promising.